A THZ FOCAL PLANE IMAGING ARRAY USING METAMATERIAL-INSPIRED BOLOMETER AND WAFER-LEVEL INTEGRATED FOCUSING ELEMENTS

By

Kyoung Youl Park

A DISSERTATION

Submitted to
Michigan State University
in partial fulfillment of the requirements
for the degree of

Electrical Engineering – Doctor of Philosophy

2014

ABSTRACT

A THZ FOCAL PLANE IMAGING ARRAY USING METAMATERIAL-INSPIRED BOLOMETER AND WAFER-LEVEL INTEGRATED FOCUSING ELEMENTS

By

Kyoung Youl Park

There is substantial interest in terahertz (THz) for applications in communications, sensing, spectroscopy, imaging, and security. Existing THz systems are built using quasi-optical setups. To reduce cost and make THz integrated circuits a reality, approaches to wafer level integration of components is critically needed. Among the many THz systems, imagers are most desirable as they can be immediately adopted for applications in medical-imaging, security, and non-destructive evaluation (NDE). Many types of detectors have been studied in the design and fabrication of THz focal plane arrays such as Schottky diode rectifiers and bolometers. A typical focal plane array (FPA) pixel element consists of a read-out circuitry, detector device and an antenna or a lens element. A 100×100 element FPA will require 10,000 of these individual elements. Pick-and-place of such a large number of elements within a small foot print is cost prohibitive and technically challenging. Wafer level integration of these elements is desirable to overcome this challenge.

Among the many detector elements, bolometers are desirable as they are simple to implement and has the potential to provide high sensitivity. At THz frequencies a bolometer has to be directly coupled to an antenna element to achieve high coupling efficiency. However, antennas thermally load the bolometers and reduce the overall sensitivity. Thus, new approaches to integrating bolometer with antenna elements are needed to achieve high sensitivity. Furthermore, new approaches to improving intrinsic sensitivity of a bolometer in the THz spectral region are needed.

Key focus of this research is towards the design and demonstration of THz metamaterial based absorbing structures and their utilization in the design of absorbers for packaging and bolometers for focal plane arrays (FPAs), with major research focus on the design and implementation of THz focal plane arrays. A range of bolometer designs based on metamaterial structures are investigated, including cross, circles, Minkowski, and slit ring resonator which are implemented using high resistive thin metal films. Minituarized unitcells are designed, fabricated and tested in order to improve the sensitivity of the bolometers.

For beam focusing and enhanced coupling efficiency to the detector elements (bolometers), wide-band micro-lens array are designed and demonstrated. These microlens arrays can be fabricated at the wafer level using 3D printing. Furthermore, a new plasmonic antenna element is demonstrated that can also be utilized in place of the conventional micro-lens design. This antenna element is integrated in close proximity to the bolometer structures while avoiding thermal loading the detector element. Performance of this antenna element is presented in comparison to conventional antenna elements. A THz imaging array that integrates the detector elements and lens element at the wafer level is demonstrated as part of this research work. Apart from imaging array, under this research work, approaches to fabricating 3D THz components at the wafer level have been demonstrated through the use of 3D printing and deep metal etching processes.

To my wife, Hee Young and lovely son, Jun-Beom
and
Parents

ACKNOWLEDGEMENTS

It is time to finish the long journey to the doctoral degree. Many people have supported and helped me in completing my dissertation, whether directly or indirectly. I would like to express my heartfelt gratitude to them for their contributions.

First of all, I would like to thank my advisor, Dr. Premjeet Chahal, for his guidance, and support. His understanding and passion has helped me overcome many research challenges during my pursuit of Ph.D. Also, he has taught me so many interdisciplinary theories related to materials, microfabrication, optics and electromagnetics to broaden my engineering knowledge and vision.

I would like to thank my committee members Dr. Edward Rothwell, Dr. Tim Hogan, and Dr. Jeff Sakamoto, for the time they invested in helping me complete this dissertation. Additionally, I received help and guidance along the years from Dr. Shanker Barasubramanian. I send many thanks to lab-mates past and present: Dr. Nophadon Wiwatcharagoses, Dr. Jose Hejase, Xianbo Yang, Joshua Myers, Amanpreet Kaur, Ifwat Ghazali, Steve Zajac, Cecila Acosta and Jennifer Byford. Also, I would like to thank members of EM and NDE research groups. Also, special thanks to Brian Wright, Gregg Mulder, and Karl Dersch for their avail to my teaching class, experiments and microfabrication.

Furthermore, I would like to express my thanks to the Agency for Defense Development, Republic of Korea for providing me the financial and moral support for my Ph.D studies in the United States.

And, finally my deepest gratitude goes out to my family, who has always supported me, my wife, Hee Young and my great son, Jun-Beom.

TABLE OF CONTENTS

LIST OF TABLES

LIST OF FIGURES

CHAPTER 1. THZ IMAGING ARRAY TECHNOLOGY

1. 1. Introduction

Over the last decade significant interest has grown in the area of terahertz (THz). The THz electromagnetic spectrum lies between millimeter wave (mmWave) and infrared (IR) band. Broadly, it is defined by the frequency range of 0.1 to 10 THz with corresponding free space wavelength (λ_0) between 3 mm to 30 μm [1]. Classically, another definition is that, the frequency range is applied to 300 GHz to 3 THz (λ_0= 1 mm to 1 μm) [2]. THz frequency range has several advantages; in comparison to mmWaves; 1) higher resolutions, 2) miniaturization of components sizes (antenna, passive and active circuits), in comparison to IR and X rays; 1) non-ionizing radiation (unlike X-rays), 2) better transmission under poor visibility environments such as smoke, fog, clouds, and sandstorms [3]. Based on these unique characteristics, a large number of applications have evolved in this spectral range. In particular, THz imaging systems are being developed for applications including concealed weapon and explosive detection for security and the radiation spectral of interstellar for radio astronomy [2, 4, 5]. THz imaging systems are also being investigated as a complement to existing screening methods such as X-rays, magnetic resonance imaging (MRI) and ultrasonography for biomedical applications [6]. In particular THz imaging systems are attractive for screening skin cancer and tooth decay where X-rays are commonly used. Use of THz imaging will reduce exposure of patients to high energy X-ray radiation.

For communications, despite the high attenuation of THz radiation through atmosphere in compare to RF frequencies, there is growing interest its use for high bandwidth communication for short range point to point communications [8]. This includes communications within a building or from a computer to computer. Using THz carrier frequency, the usable bandwidth can be increased manifold, it can help transmit enormous amount of data (5 % of 300 GHz=15 GHz * 1 bps/Hz=15 Gbps at QPSK) and for military applications it enhances the jamming capability using conventional spread spectrum techniques. Furthermore, due to natural small wavelength, the physical size of sub-system components can be significantly reduced in size and thus saving cost and reducing weight of most systems. The components needed for THz systems are non-existent, and the ones that are commercially available are cost-prohibitive and limited in their functions. Similar to RF and millimeter wave systems, the components needed for most system (e.g. antenna, phase shifters, polarizers, and so on) are similar in nature. Thus, THz component will find applications in a broad range of systems. In order to narrow down the focus, this research focuses on components that are needed in the design of a THz imaging system. In particular an imaging system built using bolometer detectors. Components demonstrated for imaging array will find utilization in a host of other THz circuit designs (e.g., communication links).

As mentioned above, THz imaging is being studied for many applications ranging from security to medical imaging. Thus, there is significant interest in the development of THz imaging systems [9-13]. There are various approaches to designing a THz system, and one approach is through the use of a focal plane array (FPA) chip. This approach allows in the use of existing micro- and nano-fabrication infrastructure utilized in the manufacture of high performance front-end RF components.

The FPA chip is an integral part of a THz imaging system. In particular, THz components designed from periodic structures are studied. Components include THz detectors, beam focusing elements and antenna. Detector elements that work similar to a bolometer detector element that is commonly used in the infrared region are studied. Beam focusing elements includes lens array designs and also beam focusing through surface plasmonics and dielectric lenses. All of these components are designed to operate in the THz frequency region (> 100 GHz). Also, all of proposed components are designed, fabricated, and tested under this study.

1. 2. THz Imaging system

In this section, existing THz imaging systems that have been presented in literature and their respective sub-components are presented. A THz imaging system can fundamentally be divided into two separate groups: i) passive and ii) active imaging system. Passive imaging systems directly detect the natural radiation from the objects or the reflection from the environment; the concept is analogous to radiometry to measure the electromagnetic radiation to be characterized by difference in temperature and emissivity [14-16]. The architecture of passive imaging systems (depicted in Figure1.1) is quite similar to a visible camera structure that consists of detectors, focusing elements. In passive imaging system, there are two methods to monitor the THz radiation: heterodyne detecting and direct detecting. For heterodyne detection, the semiconductor (Schottky diode mixer), superconductor (cryogenic cooling), and hot electron bolometers (HEB) have been extensively investigated over the past decade [2, 17-19]. One of the basic configurations of direct detection approaches comprises of bolometers and an antenna element. The antenna elements directly or indirectly couple to the bolometer element providing an impedance match between the bolometer element and the free space. Although coupling efficiency is enhanced but the antenna element thermally loads the detector and thus reducing sensitivity. The bolometer detectors are also broadband in nature and thus utilized where frequency resolution is not required. Frequency bandwidth is limited by the antenna element utilized.

An active imaging system has a source to illuminate the object with the electromagnetic wave and subsequently detect the reflected electromagnetic wave. These are, in general, narrow band systems because narrow band generation of radiation is simpler. Furthermore, sensitivity can be enhanced through heterodyning. This operating principle is similar to that of radars. This imaging system has been in the spotlight for indoor security application where the detection range is limited [20] and also for environment monitoring for hazardous plumes during a fire. Practically, in order to achieve sufficient signal to noise ratio (SNR) to detect an object in an indoor environment, where the background noise level is close to natural radiation level from the sample, the active imaging system shows better performance than the passive imaging system. To be specific, compared to the passive system, although both of the fundamental structure of power detecting are same, the active imaging system can increase the capabilities such as higher sensitivity. Due to this characteristic, the active imaging system has been used in remote scanning applications.

In a passive imaging system, the system has to be designed to be wide band to capture ambient signal over a wide frequency range to achieve good detection capability (i.e., capture black body radiation reflected from the objects over a wide spectral range). On the other hand, an active imaging system is typically made to be narrow band as the illumination signal used is generally at a fixed frequency or over a narrow band. Thus, the components to be designed should cater specifically to this need.

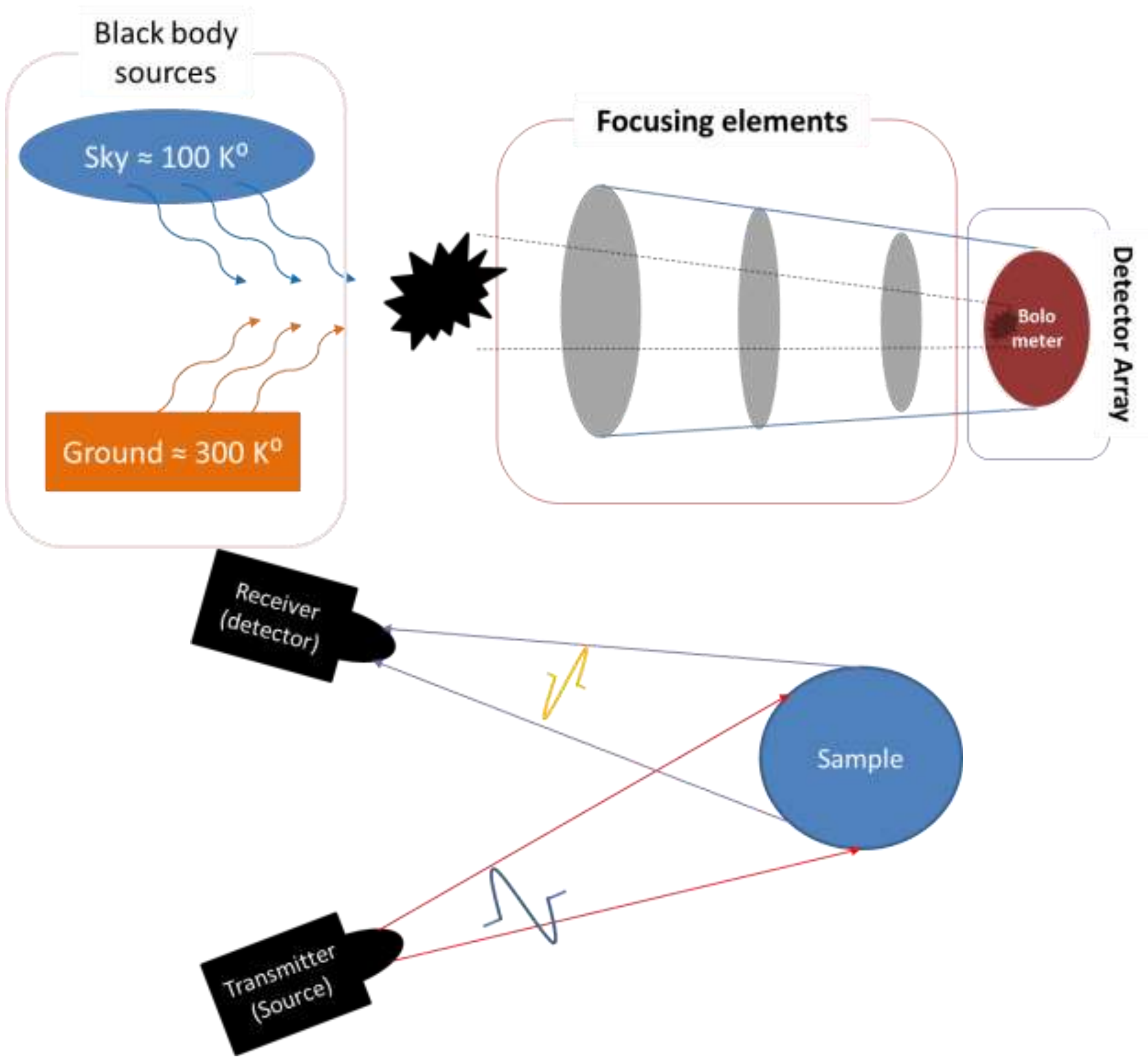

Figure 1.1 The simplified schematics of THz imaging systems; top: passive imaging system, bottom: active imaging system (reflection mode).

1. 3. Components for THz imaging system

In this section, two essential sub-components for THz imaging systems are introduced: detectors and focal plane array.

1.3.1THz detectors

THz detectors play a significant role in order to measure the incident signal in a THz imaging system. THz detectors can be divided into two categories: heterodyne and direct detectors [2]. Heterodyne detectors are the most common THz detectors using semiconductors and superconductors. In a heterodyne detection approach, both a RF source and a local oscillator (LO) are needed. Detection is carried out by mixing the RF and LO signals. The key advantage of this approach is that phase information can be preserved. Direct detectors have been studied in order to replace heterodyne detection methods in imaging arrays where phase information is not necessary. Also, this is because a system based on heterodyne detectors consumes significantly more total DC power than a system based on a direct detector. Furthermore, the design of a heterodyne imaging system where a large number of pixels are utilized becomes difficult to design as the local oscillator (LO) power distribution on a chip becomes challenging. Illumination of LO can be utilized; however, for a large number of pixels the total LO power required will be significantly high. Typically, LO power of 3 – 10 dBm per pixel is required for good sensitivity.

For heterodyne detection, the semiconductor (Schottky diode mixer), superconductor (cryogenic cooling), and hot electron bolometers (HEB) have been widely used [2, 17-19]. Conventionally, the Schottky diode mixer has been utilized in applications where the sensitivity of room-temperature is acceptable. Also, it offers sufficient radiometric sensitivities near 0.5 K at 0.5 THz and 0.5 K at 2.5 THz. In superconducting detectors, in order to achieve high sensitivity cryo-cooling is required which makes the overall system large and bulky. These detectors have been developed based on the Josephson-effect, superconductor-semiconductor barriers, superconductor-insulator-superconductor (SIS) tunnel junction mixer, and bolometers [2, 19]. Hot electron bolometer (HEB) mixer is an alternative to THz SIS mixers that can work at very high speeds owing to fast phonon or electron diffusion cooling [21]. Recent HEB mixers essentially based on tiny microbridges of niobium (Nb), NbN, and aluminum (Al) that respond thermally to THz radiation [22]. Heterodyne approach provides significant advantage of the ability to track the IF up to several gigahertz with the fast voltage responsivity (picoseconds range) [23]. Table 1 summarizes the properties of the heterodyne semiconductor, superconductor, and hot electron bolometers.

Table 1.1 The properties of heterodyne detecting components

	Semiconductors (Schottky diode mixer)	Superconductors (SIS mixer)	Hot electron bolometers (HEB mixer)
Advantages	• High SNR • Working at room temp. • High sensitivity	• Low LO power (μW) • High sensitivity(0.05K/GHz) • High operating frequency	• Fast voltage responsivity (pS range) • Low LO power (nW range) • Schematics and materials for THz
Disadvantages	• High LO power(mW)	• Superconductor: NbN/AlN/NbN • Cryogenic cooling system needed	• Noise performance related to the material critical temperature and operating temperature
Applications	• Earth science • Planetary observation • Plasma diagnostics	• Earth science • Space observation	• Space observation

In the case of direct detectors, there is a rising need to replace the heterodyne detecting in some applications that necessitate relatively low spectral resolution compared to the ultrahigh resolution of heterodyne detectors and also to reduce overall DC power needed for detection [2,6]. There have been several types of detection approaches used including GaAs-Schottky diodes with antenna coupled, bolometers using thermal absorbing materials such as bismuth (Bi) and vanadium oxide (VO_x), compound bolometers consist of thermometer or readout circuits integrated with the radiation absorber, microbolometers with focusing elements to couple incident power, acoustic bolometer, a fast calorimeter, etc. [2,6]. However, these detectors based on the bolometer have challenging problems to solve including a calibration (mode matching) problem in antenna coupled detectors (diode and bolometers) and slow response time (the order of seconds) of an acoustic bolometer and a fast calorimeter [6]. In order to resolve this problem, the cooled detector based on He-cooled Si, Ge, or InSb bolometers have been used for THz detection.

Table 1.2 Summary of direct detecting sensing elements

	Schotty diode antenna coupled	Bolometer	Cooled detector
Advantages	• Room temperature • Fast response	• Direct thermal absorption • Simple readout circuitry	• Fast response time (microsecond scale)
Disadvantages	• Circuit biasing (for non-zero bias diodes) • Expensive substrate	• Thermal loading from antenna • Calibration • Slow response time	• Cryogenic cooling • Cryogenic cooled readout circuits
Applications	• Focal plane array • Security (passive and active imaging system) • Non-destructive evaluation (active imaging system) • Biomedical imaging and microscopy		

Here, more detail information of detectors is presented, starting with a bolometer. Bolometers were introduced by S.P. Langley in 1878. His invention, the bolometer, works as a radiant-heat detector that is very sensitive to temperature variation (temperature resolution=0.00001 °C) [24]. The operating concept of the bolometer is to measure the electrical resistance of the material (Bi, VOx) responds to the incident power of electromagnetic waves. Fig 1-2 demonstrates the general scheme of the bolometer [25]. Absorbers are normally realized using thin metal/semiconductor film. The thermistor is in direct contacts with the thin film. In this configuration, the thermistor is in direct thermal contact and thus decreases thermal capacitance [26]. Second, there is a detector using photoconductive response with certain composite material, Gallium doped Germanium (Ge:Ga). It has a distinct characteristic that the cut-off wavelength is roughly 120 μm under the unstressed configuration and 4.2 k; however, when the stress is induced to a detector crystal layers, the wavelength of it increases up to 200 μm [27]. The stress can be induced through thermal loading. This type of detector has been utilized in astronomy and laboratory applications.

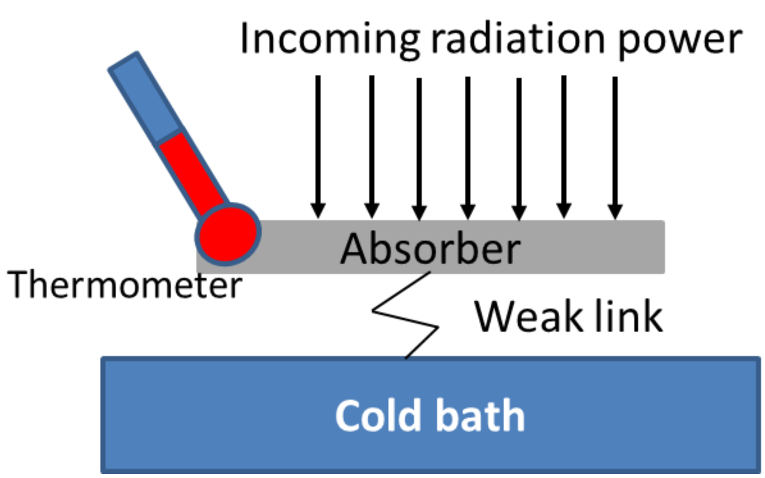

Figure 1.2 The operating principle of the bolometer [26].

In order to analyze the bolometer operating mechanism, the basic theory bolometer is introduced. A bolometer is conventionally composed of an absorber and a thermometer of heat capacity *C*, connected by a thermal conductance *G* (substrate and circumstance of a bolometer), to a heat sink retained at a certain fixed temperature T_0 in shown as Figure 1.3 (a) [28]. The power of incident wave, P is transferred to heat in the absorber. This causes the temperature to rise, $\Delta T = T - T_0 = P/C$, until the radiation power going to the absorber is identical to the power running into the heat sink through the weak thermal linkage. Figure 1.3 (b) shows a typical bolometer measurement setup. The bolometer element is placed in series with a large stable resistor (low noise and low TCR) and biased using a DC voltage source [28, 29].

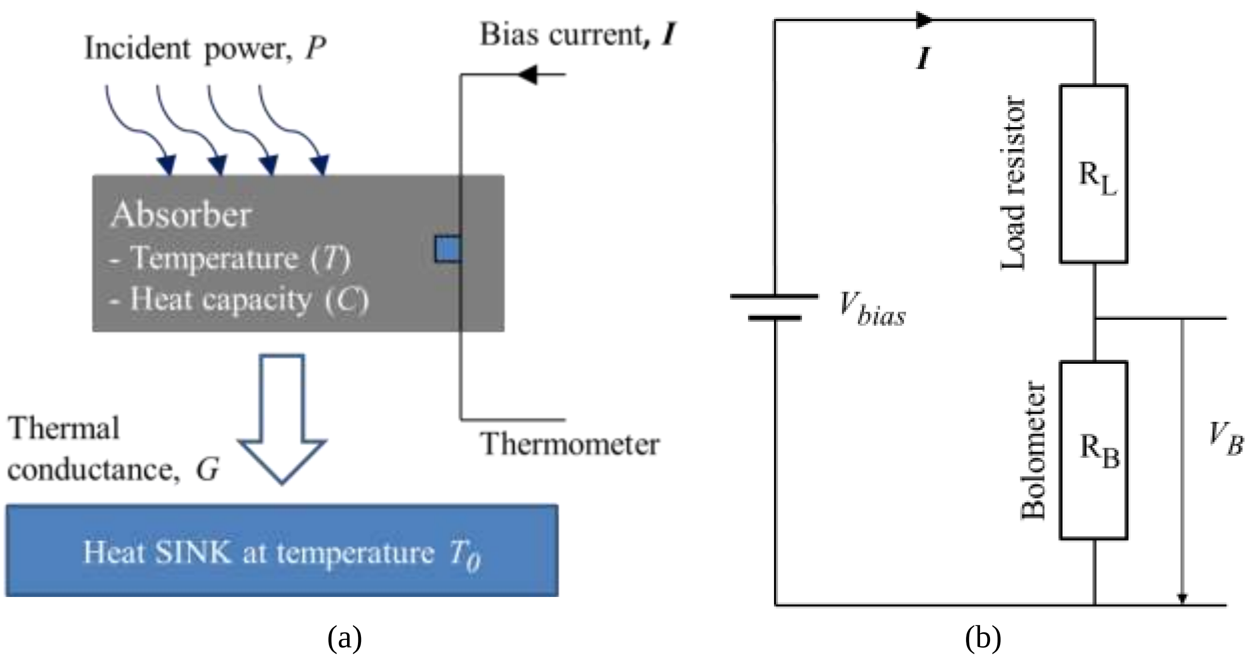

Figure 1.3 The layout and block diagram of bolometer biasing circuit.

From the bias source V_{bias} and the load resistor R_L, the current *I* flows constantly runs through the bolometer. The incident power causes the bolometer temperature (*T*) to increase and increasing its resistance value. This relation can express the equation,

$$T = T_0 + (P_{incident} + P_{bias})/G \qquad 1\text{-}(1)$$

T, the temperature rise has an influence on change in the resistance of the bolometer and thus the voltage, V_B across a bolometer changes which is measured using a readout circuitry [28, 29].

Conventionally, there are several critical parameters that affect the performance of a bolometer. The performance is described through key parameters such as noise equivalent power (NEP), noise equivalent temperature difference (NEΔT), time constant (τ), and detectivity (D*). NEP is a fundamental parameter, it describes the sensitivity of a bolometer and is the minimum detectable power (signal to noise ratio SNR of 1) over a bandwidth of 1 Hz [29,30]. Theoretically, the NEP per unit Hz bandwidth of a bolometer is defined as [30]

$$NEP = 4\sqrt{\frac{A\sigma k T^5}{\epsilon}} \qquad 1\text{-}(2)$$

Where, A = area of a bolometer (m^2), σ = Stefan-Boltzmann constant (=5.67×10^{-8} $J/(m^2\cdot S\cdot K^4)$), k = Boltzmann constant, T = temperature, ε = emissivity. These parameters can be optimized to achieve high sensitivity, a low NEP value is desired (i.e., high sensitivity). To achieve high sensitivity, small bolometer area, low-thermal conductivity, high absorptivity and strong temperature dependence of the bolometer film is desired. From thermal point of view, sensitivity can be express as NEΔT,

$$NE\Delta T = \frac{\sqrt{AB}}{D^*(\frac{dP}{dT})} \qquad 1\text{-}(3)$$

Where, B is the system bandwidth and dP/dT is the change in power on the bolometer per unit change in temperature in the spectral band. The detectivity and responsivity can be expressed [28, 30]

$$D^* = \frac{\sqrt{\epsilon}}{4\sqrt{\sigma k T^5}} \tag{1-(4)}$$

The response time (τ) of a bolometer is given by

$$\tau = \frac{C}{G} \tag{1-(5)}$$

From this equation, we can recognize the relation between the heat capacity and thermal conductance. In order to increase response time, thermal capacity C should be made small and thermal conductance to the substrate G should be made large. However, increase in thermal conductance leads to poor NEP. Thus, there is an optimum solution between sensitivity and response time.

1.3.2 THz focal plane arrays

THz focal plane array is the use of the microbolometer (or other detection elements) arrays which are fabricated by integrating the microbolometers with planar antennas, for instance, bow-tie antenna and log periodic antenna onto a common substrate. As an example, in [31], a 120 element antenna coupled microbolometer FPA for concealed weapons detection was introduced. Here niobium (Nb) films are utilized for the bolometer element and slot ring antenna for coupling the incoming radiation to these elements. For applications in an indoor environment, the operating signal level is low because of natural radiation level is close to the background noise power level. In this case, the active imaging system is preferred for higher sensitivity over the passive imaging systems. Active imaging is achieved by including an illuminator along with these detection elements. The FPA introduced in [31] is manufactured on a high resistivity silicon wafer (D=75mm), and integrates 120 Nb microbolometers coupled to slot-ring antennas, see Figure 1.4. The operating mechanism is that the antennas focus the incident sub-THz radiation and a voltage difference is produced across the Nb bolometer depending on the amount of incident power. In this system, in order to generate the signal, three IMPATT pulsed noise oscillators are used (rated power = 1W, frequency=95GHz) configured to illuminate the scene from three directions. Illumination from multiple angles assists signal detection regardless of the orientation of typical targets.

As discussed here, significant progress has been made in the design and fabrication of bolometer based THz imaging system. However, there are many advances that need to be made to make this technology viable to everyday use. This includes: i) enhancing sensitivity of the bolometer element, ii) integration of micro lens for further enhancement of sensitivity. Also, there is a need for CMOS based readout circuitry that needs to accompany the individual pixels and thus the processes developed should be compatible with CMOS fabrication or CMOS post processing.

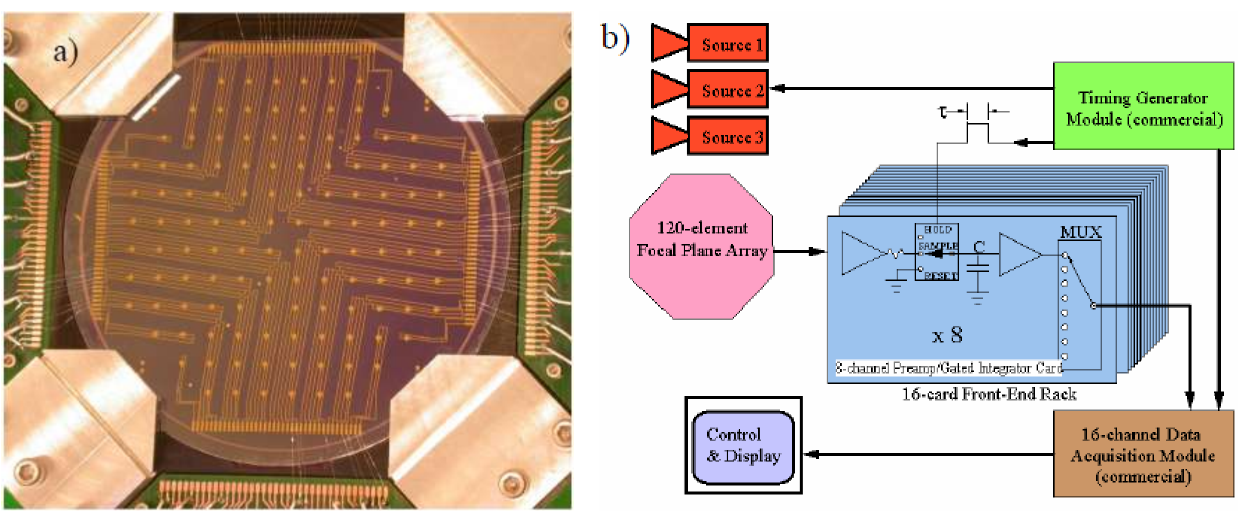

Figure 1.4 Photograph and system layout of 120 element antenna-coupled microbolometer focal plane array [31].

1. 4. Goals of the dissertation

First, detectors based on frequency dependent periodic structures are investigated. Compared to other bolometer design, in place of an antenna element, periodic structures are incorporated to enhance sensitivity, see Figure 1.5. Furthermore, skin-effect losses are taken advantage of to further enhance sensitivity. Thus, use of a lossy metal coupled with patterned structures is implemented in THz direct detecting sensors. The absorbing film is made from a periodic metallization, which combines the loss of the metal due to surface resistance with the field enhancement near the structural resonance to achieve absorption losses similar to a bolometer. Existing microbolometers have been replaced with a simple fabrication and low cost metamaterial-inspired bolometer.

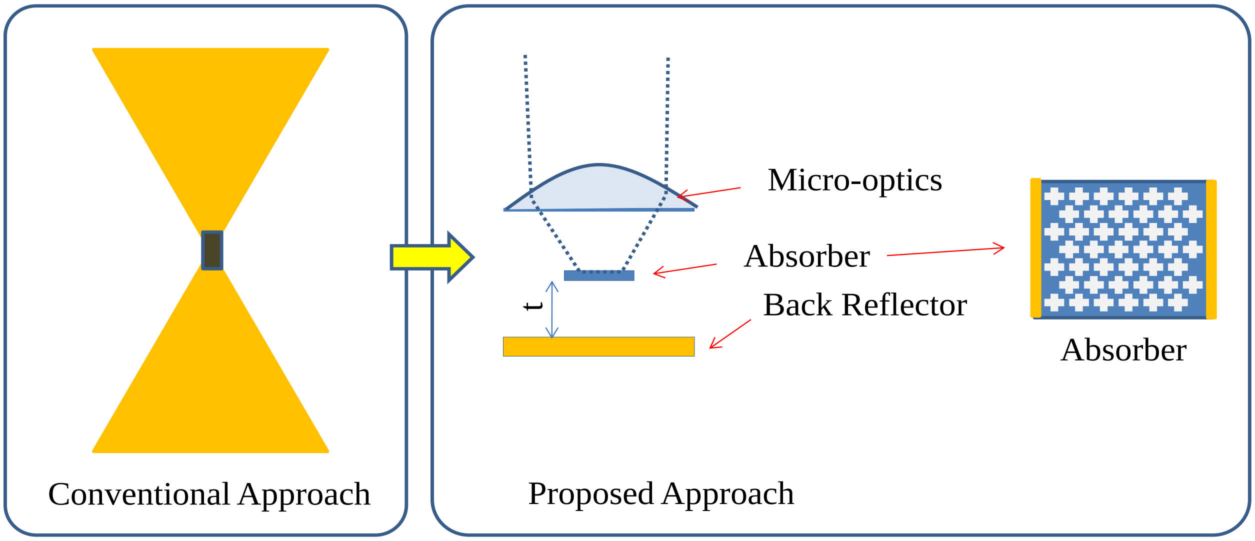

Figure 1.5 Proposed bolometer detector utilizing a direct metamaterial-inspired absorber replacing a conventional antenna element based pixel.

Second, microbolometers have been used in conjunction with various antenna designs to achieve improved coupling efficiency. The electromagnetic energy heats the microbolometer, altering its electrical resistance, thus altering the applied current or voltage. These systems boast small length scales and heightened sensitivity to small changes in the incident electromagnetic energy. However, the coupling of these two systems can lead to unwanted thermal loading, negatively affecting the overall sensitivity of the sensor. Also, small size bolometers are desirable to improve signal to noise ratio. Thus, a sensor which not only captures a large amount of incident electromagnetic energy, but also efficiently converts this to a usable electrical signal, is desirable. This takes advantage of not only the thermal sensitivity of the bolometer, but also improves its coupling efficiency with the frequency selective surface. The focal plane array (FPA) forms the heart of the THz imaging system. The challenge is in the fabrication of beam focusing elements at the individual pixel element level. For current imaging systems, built using single pixel elements, silicon micro lenses are used. However, Si lenses are made from high resistivity Si that is expensive and difficult to fabricate in a large array format on a single wafer. A simple fabrication that allows simultaneous fabrication of multiple lenses in an array format is desirable which will help reduce complexity in assembly. In this research, in order to realize the focal plane array (FPA) with improving coupling efficiency and integrating with the proposed bolometers, surface plasmon antenna and micro-lens array are studied.

Finally, in view of system level, the way to integrate all of proposed components such as the detector using periodic structures and beam focusing antenna together and characterize the system level performance has been carried out. In order to measure the system performance, diverse measuring methods such as quasi-optic measurement, time-domain measurements has been considered. Through this process, the performance of proposed THz imaging system has been characterized.

1. 5. Overview of the dissertation

This dissertation is organized as follows:

Chapter 1 introduces THz imaging array and introduces existing approaches. Chapter 2 explains theoretical methods to analyze the proposed periodic absorbing structures using periodic analysis method. The fundamental properties of periodic structures such as frequency selective structure and metamaterial are studied.

Chapter 3 demonstrates several types of THz absorber based on periodic structures that operate at THz frequency spectrum range. The detail information of design, EM simulation and fabrication of THz absorbers are not only introduced, but also the measurement results using time and frequency domain testing setups are explained in this chapter.

Chapter 4 describes a novel THz power detector using designed THz absorber. The proposed power detector is demonstrated for W-band application and used in the construction of designed periodic structures. The material properties of nickel are characterized using measuring setup of temperature coefficient of resistance (TCR). Quasi-optic measurement has been utilized to examine the power meter at designed operating frequency.

In Chapter 5, in order to improve the incident power intensity to the imaging sensor, the beam focusing elements (bulls eye antenna) based on surface plasmonic are investigated. Two well-known simulation methods, finite element method (FEM) and finite difference time-domain (FDTD) have been utilized in the design of bulls eye structures. For the fabrication, two methods are investigated: i) metal etching and ii) 3D plastic printing. Deep trench wet-etching of copper (Cu) is introduced and utilized instead of the conventional micromachining techniques. A new plastic based bulls-eye structure using three-dimensional printing is investigated. For antenna measurement, the relative gain of the bull’s eye structure is measured relative to pinhole in a Cu substrate.

Chapter 6 presents different types of beam focusing elements (dielectric lens) that can be used to improve the sensitivity of the detector elements. A novel approach to integrate large number of lens element at the wafer-level is introduced and demonstrated. Detailed simulations using HFSS is carried out for a range of dielectric lens designs. Simulations are carried out for near-field and far-field radiation pattern analysis. Using similar setup as utilized for the characterization of bull’s eye structure, the micro-lenses are characterized.

Chapter 7 introduces a novel THz imaging array that integrates the above elements together to fabricate focal plane arrays (FPAs). This includes the integration of metamaterial absorber structure along with micro-optics at the wafer-level. To miniaturize the size of the pixel elements to enhance sensitivity, a range of metamaterial inspired structures are designed, fabricated and characterized. An imaging array is demonstrated by imaging a concealed object in a paper envelope.

Chapter 8 concludes the finding of this research work, and future research topics and potential applications using a THz imaging array are discussed.

.

CHAPTER 2. PERIODIC STRUCTURES: FREQUENCY SELECTIVE AND METAMATERIAL

This chapter introduces the periodic structures utilized and their theoretical analysis. Periodic structures such as frequency selective surfaces (FSS) and metamaterials, normally have been used in filter application in electronic or RF devices. Unlike a conventional filter, which normally studies only the frequency response (resonant frequency and reflection and transmission response), the periodic structure must poses bandpass or bandstop characteristics for varying incident angles and polarization. There is significant interest in periodic structures (FSS) for a variety of applications such as the radome structures, reflector antenna for dual bands, and stealth technology in order to decrease the radar cross section (RCS) of a flying object and sea ferrying vessels [32-34]. Typically, the periodic structure is defined as an infinite assembly of unitcells, showing the uniform structures, which may consist of one-, two-, and three dimensional array. These schematics are typically composed of two layers; one is a metallic patterned layer and the other is a dielectric layer forming a substrate or a superstrate. The performance of the periodic structure is totally characterized by the schematic of the unit cell and its arrangement in a semi-infinite pattern.

2. 1 Periodic structure

2.1.1 Properties of periodic structure

Originally, the periodic structure consists of an arrangement of either wire or slot shapes. Wire type, the periodic structure is composed of randomly shaped conducting components, which help guide the electric currents in a complex pattern. Compliment to these structures, the slot shape of periodic structure consists of arbitrary shaped holes in a metallic plate, which can support magnetic currents [32]. The former acts as a bandstop filter because the components are reflective at a resonant frequency and they pass through electromagnetic waves below and above the resonant frequency [33]. Circuit theory can be utilized to carry out simple analysis. An equivalent circuit for a wire periodic structure is composed of a series LC pair resonant, in a short circuit, it is that reflects the energy at the resonant frequency, alternatively, on the rest of frequencies, the LC pair work to pass the electromagnetic wave same as open circuits. The latter works as a bandpass filter, because the slot components are transparent at the resonant frequency and they reflect the incident waves the rest of frequencies located on above and below the resonant frequency. It can be analyzed same as the bandpass filter which is composed of the inductor and capacitor that combined parallel. At the resonant frequency, the configuration of the inductor and capacitor works an open circuit response, while the other frequencies work a short circuit [32].

Also, many case of periodic structure use hybrid configurations that are composed of metallic layers and dielectric layers. These schematics are typically composed of two layers; one is a metallic patterned layer and the other is a dielectric layer forming a substrate or a superstrate. The performance of the periodic structure is totally characterized by the schematic of the unit cell and its arrangement in a semi-infinite pattern. A periodic array of dipole elements is depicted in Figure 1.2. Independent of FSS shapes, the resonance mechanism of most FSS structure is similar. In relation to resonance, consider an array of FSS structures on a dielectric substrate. Assume a plane wave in free space impinges upon the FSS structure. The unit cell of the FSS structure resonates at an effective electrical length of the unit cell that is a multiple of the resonance half wavelength [33, 34]. Harmonizing to the phase front of the wave, these unit cells have a certain phase delay. As a result, the radiation of the EM wave is scattered by individual unit cells and the effective length of FSS leads to resonate the frequency associated with the length. It provides bandstop or bandpass filter characteristics.

2.1.2 Analysis of periodic structure

Traditionally, in order to analyze the periodic structure, there are two fundamental methods, 'the plane wave expansion' and 'the mutual impedance' to characterize the electrical properties such as the scattering and impedance of designed periodic structures. Here is the example to characterize the periodic structure to utilize both of ways that were mentioned above. There is the finite array that is composed of two dimensional elements shown in Fig 2.1. In order to analyze the periodic structure, Tsao's and Mittra's works [35, 36] are referred in this dissertation. Based on these references, the analysis starts by considering the geometry of a free-standing periodic structure as shown in Fig 2.1.

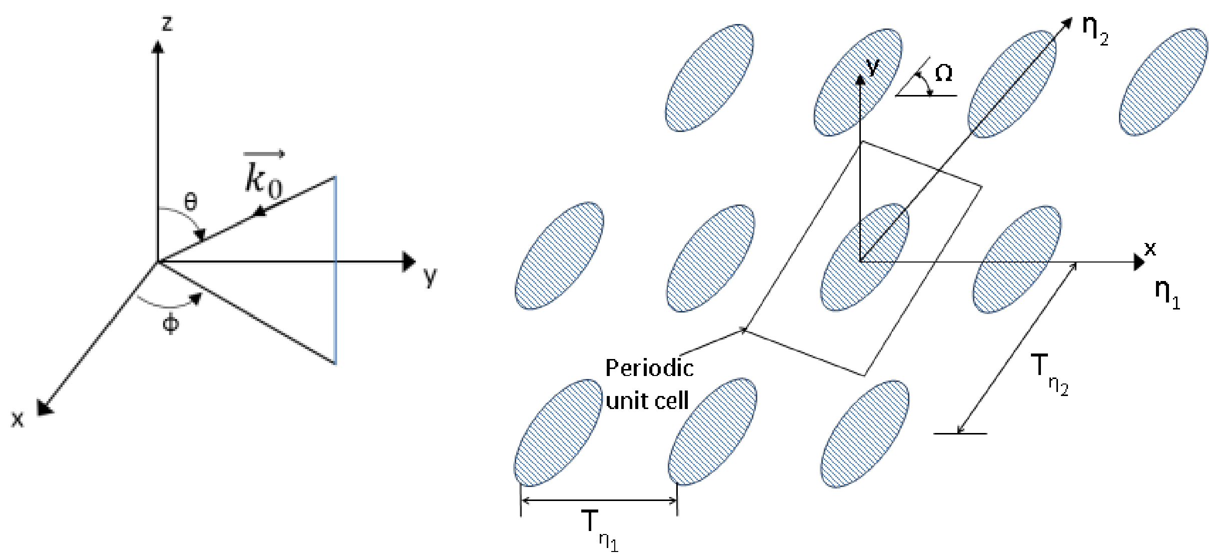

Figure 2.1 FSS radiated by plane wave propagating in k_0 direction.

First, in order to analyze the periodic structure, there is an assumption that the periodic structure is infinite in size and the metal is much thinner than the wavelength [35]. In order to analyze the periodic structure, there are the parameters; $\vec{J}$, the current induced on the FSS structure due to the incident field and $\vec{A}$, the magnetic vector potential due to the induced current ($\vec{J}$). Also, assuming the time conventional is $e^{j\omega t}$, at the z = 0 plane, the components associated with the transverse (z-axis) can be written as [33, 35, 36];

$$\begin{bmatrix} A_x(x,y) \\ A_y(x,y) \end{bmatrix} = \bar{\bar{G}}(x,y) * \begin{bmatrix} J_x(x,y) \\ J_y(x,y) \end{bmatrix} \qquad 2-(1)$$

where

$$\bar{\bar{G}} = \frac{e^{-jk_0 r}}{4\pi r}\bar{\bar{I}}, \quad r = (x^2 + y^2)^{1/2}$$

$\bar{\bar{I}} = identity\ tensor,$ k_0= free space wavenumber

The transverse components of scattered electric field $\vec{E}^s$ at z=0 can be obtained from the transverse components, $\vec{A}$ [33, 35].

$$E^s(x,y) = \frac{1}{j\omega\epsilon}\begin{bmatrix} \frac{\partial^2}{\partial x^2} + k_0^2 & \frac{\partial}{\partial x}\frac{\partial}{\partial y} \\ \frac{\partial}{\partial x}\frac{\partial}{\partial y} & \frac{\partial^2}{\partial y^2} + k_0^2 \end{bmatrix}\begin{bmatrix} A_x \\ A_y \end{bmatrix} \qquad 2-(2)$$

Using the Fourier transform, and then the following equation is derived in the spectral domain [35].

$$\begin{bmatrix} \tilde{E}_x^s(\alpha,\beta) \\ \tilde{E}_y^s(\alpha,\beta) \end{bmatrix} = \frac{1}{j\omega\epsilon_0}\begin{bmatrix} k_0 - \alpha^2 & -\alpha\beta \\ -\alpha\beta & k_0 - \beta^2 \end{bmatrix}\tilde{\bar{\bar{G}}}(\alpha,\beta)\begin{bmatrix} \tilde{J}_x(\alpha,\beta) \\ \tilde{J}_y(\alpha,\beta) \end{bmatrix} \qquad 2-(3)$$

Where

$$\bar{\bar{\tilde{G}}}(\alpha,\beta) = \frac{-j}{2(k_0^2 - \alpha^2 - \beta^2)^{1/2}} \bar{\bar{I}}$$

In this equation, the transform variables, *a* and *b*, are related to the *x, y* on the cartesian coordinate system. When the FSS structure is stringently periodic, the induced current $\vec{\mathrm{J}}(x, y)$ can be transformed to $\vec{\mathrm{J}}(\alpha, \beta)$ is nonzero (using Fourier transform) for discrete values of the spectral variables α and β [33, 35]. The discrete of spectral variables, α_{mn} and β_{mn} are related with the Floquet harmonics for the periodic structure. The explicit expression for α_{mn} and β_{mn} are

$$\alpha_{mn} = \frac{2\pi m}{a} + k_0 \sin\theta \cos\phi$$
$$\beta_{mn} = \frac{2\pi n}{b \sin\Omega} - \frac{2\pi m}{a} \cot\Omega + k_0 \sin\theta \sin\phi \qquad 2\text{–}(4)$$

where θ, φ are the angle of the incident plane waves .

Using the inverse transform and applying the boundary condition, it can be calculated that the sum of the scattered field and the incident field is zero; $\vec{E}^s + \vec{E}^i = 0$ on the conduction surface of the FSS structure. The following equation shows the relation for the unknown induced currents on the FSS structure [33, 35, 36].

$$\frac{1}{j\omega\epsilon_0} \sum_m \sum_n \begin{bmatrix} k_0 - \alpha_{mn}^2 & -\alpha_{mn}\beta_{mn} \\ -\alpha_{mn}\beta_{mn} & k_0 - \beta_{mn}^2 \end{bmatrix} \bar{\bar{\tilde{G}}}(\alpha_{mn}, \beta_{mn}) \begin{bmatrix} \tilde{J}_x(\alpha_{mn}, \beta_{mn}) \\ \tilde{J}_y(\alpha_{mn}, \beta_{mn}) \end{bmatrix} e^{j(\alpha_{mn}x + \beta_{mn}y)}$$

$$= \sum_m \sum_n \begin{bmatrix} \tilde{G}_{xx} & \tilde{G}_{xy} \\ \tilde{G}_{yx} & \tilde{G}_{yy} \end{bmatrix} \begin{bmatrix} \tilde{J}_x(\alpha_{mn}, \beta_{mn}) \\ \tilde{J}_y(\alpha_{mn}, \beta_{mn}) \end{bmatrix} e^{j(\alpha_{mn}x+\beta_{mn}y)} =$$

$$- \begin{bmatrix} E_x^i(x,y) \\ E_y^i(x,y) \end{bmatrix}$$

2−(5)

Above equation 2-(5) can be solved with the Galerkin's method. The unknown induced current $\vec{J}$ is represented in relation to a set of basis function $\vec{f_i}$ [35];

$$\vec{J} = \sum_i C_i \vec{f_i}$$

2-(6)

Where C_i is still unknown coefficients to be calculated. Substituting 2-(6) into 2-(5) and using $\vec{f_i}$ as the testing functions, 2-(5) is changed the equation as the matrix form and can be calculated the C_i. After calculating C_i, The unknown induced current $\vec{J}$ is obtained from the equation 2-(6). The plane wave expansion is based on the scattering problem by the theory of antenna array where receive the incident power and then reflect or transmit it. In order to analyze this theory, here is the two-dimensional where is located in the XZ - plane.

CHAPTER 3. TERAHERTZ ABSORBERS

3. 1. Metamaterial structure

Conventionally, metamaterial structures are designed by placing various periodic structures [37] to have two or three dimensional patterns in a metallic or a dielectric substrate. In general, the metamaterial structure (unit cell) is much smaller than conventional frequency selective structures (FSS, $\lambda/2$ element) at the wavelength of wanted frequency. The operation mechanism of metamaterial resembles the traditional FSS and both are based on the resonant elements. Simply stated, the idea is that plane-wave illuminates an array of metamaterial elements, thus exciting electric current on the surface of metamaterial structure. The amplitude of the generated current depends on the strength of the coupling of energy between the incident wave and the structure. Traditionally, on the FSS, the coupling reaches its highest level at the half wavelength of operating frequency, however, on metamaterial, the physical size of the structure can be reduced significantly by utilizing a variety of LC (inductive-capacitive) resonant structures.

Previous metamaterial-based absorbers are, in order to effectively absorb electromagnetic radiation in the terahertz frequency regime, utilize thin periodic structures suspended above a metallic backing [38, 39]. These two metallic layers sandwich a thick dielectric layer. The purpose of the system is to absorb incoming electromagnetic radiation at a particular frequency regardless of polarization or incident angle. The periodic metamaterial unit cell is chosen to correspond to roughly one half of a wavelength. This ensures resonance mode build up across the structure. In order to demonstrate applications of metamaterials for absorption, three-dimensional finite element method (FEM) simulation was performed.

Simulations are based on the Floquet theorem [32-35]. Figure 3.1 shows the unitcells structures and the side view of the stacked layer.

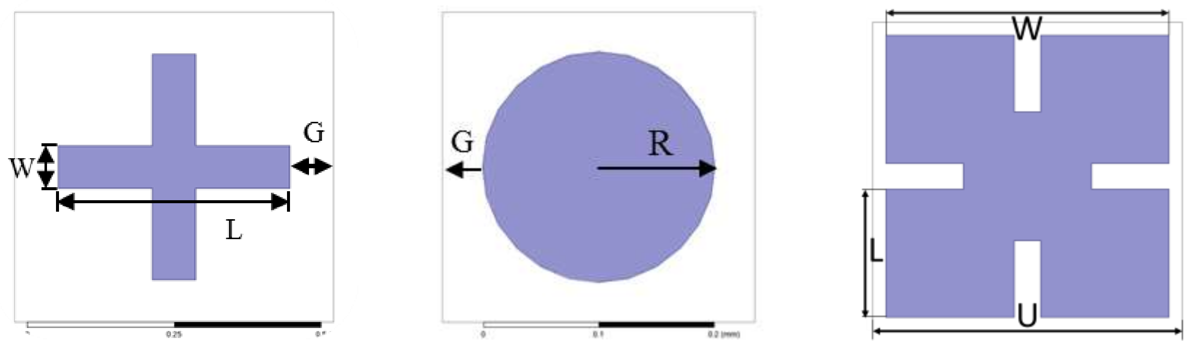

Cross　　Circle　　Minkowski

(a)

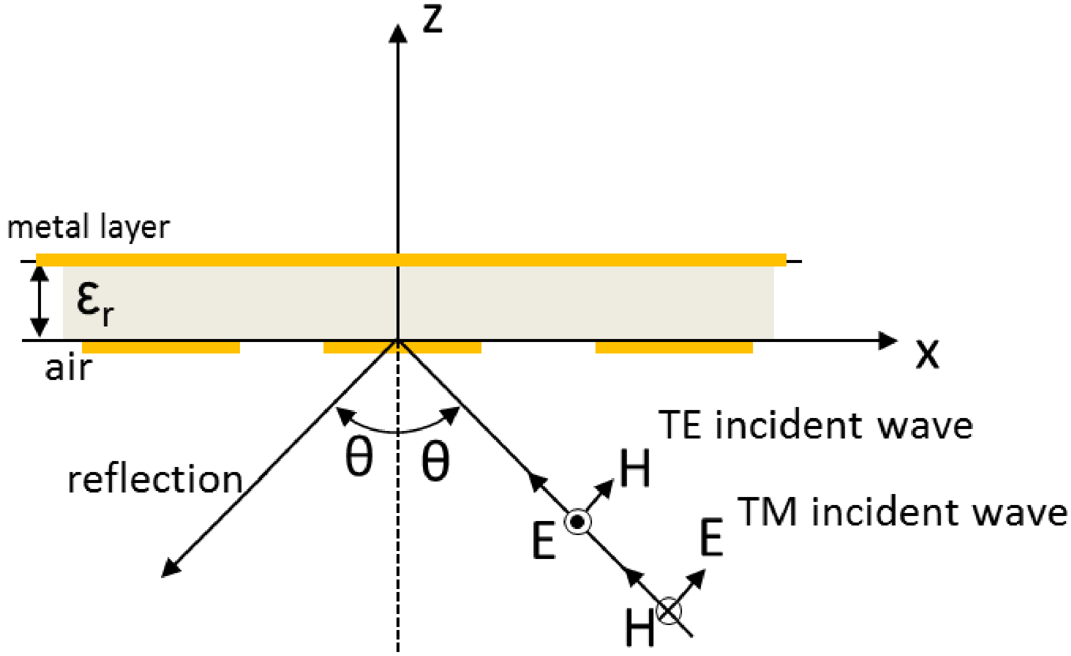

(b)

Figure 3.1 The geometries of proposed metamaterial structures (a): Cross, Circle, and Minkowski (from left), and analysis method of Floquet theorem (b).

3. 2. Skin Effect

The terminology of skin depth, normally, used in order to express the relative intensity quantitatively to which the electromagnetic wave can penetrate into the metal conductor. The skin effect causes the effective resistance of the conductor to increase at higher frequencies where the skin depth is smaller, thus reducing the effective cross-section of the conductor. In this research, we studied the effect of the metal used to make the patterns of the terahertz metamaterial-inspired absorber. Equation 3-(1) shows the expression for skin depth (δ) [40]. Which is dictated by conductivity (ρ) and permeability (μ_r) of the material and frequency (f) of operation.

$$\delta = \sqrt{\frac{2}{\omega\mu\sigma}} = \sqrt{\frac{\rho}{\pi f \mu_r \mu_0}} \qquad 3-(1)$$

It is well known that the smaller the skin depth, the more lossy the metal is to a propagating wave. From Equation 3-(1), it is clear that a small skin depth can be achieved through the use of a large permeability or a low conductivity material. On the other hand, in order to make lossy conductors, there are two ways to be considered. First, a metal can be forced to be lossy by enforcing a thickness of the metal film that is thinner than its skin depth at the desired frequency. Second, the surface impedance of a metal can be expressed the relationship between the resistivity and skin-depth shown as equation 3-(2) [41]. In this equation, the real and imaginary parts are the resistance and the inductance of a surface conductor. If the skin-depth is made small, it leads to higher surface resistance with the same bulk resistivity.

$$Z_s(f) = (1+i)\frac{\rho}{\delta_s} \qquad 3-(2)$$

Leading on from these two ideas, two different studies were conducted. First, the effect of using high-conductivity copper (Cu) and low conductivity titanium (Ti) were studied. In this case, the thickness of metal was chosen to be smaller than the skin depth in order to use the high surface resistance at resonance, and hence, increase the loss of the absorber. Second, a ferromagnetic metal, nickel (Ni) was considered. This metal has a high permeability, albeit unknown in THz region, which is related to skin depth. The small skin depth of nickel makes the surface highly resistive. This high surface resistance interferes with the wave propagation, which results in resonance absorption losses. The properties of metals related to the skin effect are summarized in Table 3-1.

Table 3.1 Properties of metals used in simulations

		Nickel	Titanium	Copper
Conductivity (S/m)		1.45×10^{7}	1.82×10^{6}	5.8×10^{7}
Permeability(μ_r)		100	1	1
Skin depth (δ)	0.1 THz	0.042 μm	1.16 μm	0.20 μm
	0.2 THz	0.030 μm	0.80 μm	0.14 μm
	0.4 THz	0.021 μm	0.57 μm	0.10 μm

In order to verify these distinguished properties, the absorption characteristic of each metal is simulated using a commercial electromagnetic simulation tool, Ansoft HFSS based on finite element method (FEM). Using this simulation tool, the S-parameter can be produced to be able to characterize and calculate the absorption ($A = 1 - |S_{11}|^2 - |S_{21}|^2$) of the absorber. Figure 3.2 (a) illustrates the scheme of the simulated dipole structure to analyze the correlation between skin effect and metal properties. It is composed of a conductor layer, a dielectric layer, and ground plane (a single port network due to ground plane). The simulated dipole structure has the dimensions, in micrometers (μm), of: width (W) = 75, length (L) = 400, and conductor thickness (t) = 0.2, respectively. Simulation results of return loss of different metals are shown as Figure 3.2 (b). As mentioned above, the high permeability metal, Ni, has a significant absorption characteristic under same conductor thickness compared to other metals due to the thinner skin depth. Figure 3.2 (c) illustrates the simulated return loss of a Ni dipole to analyze the absorption ratio on different thickness. The results show that thinner Ni layer absorbs large amount of the incident power, the peak absorption is close to 0.99 at t=0.01μm. Figure 3.2 (b), (c), and (d), it is clear that the high permeability and thin conductor thickness enable to achieve perfect absorption of the proposed absorbers due to high surface resistivity.

(a)

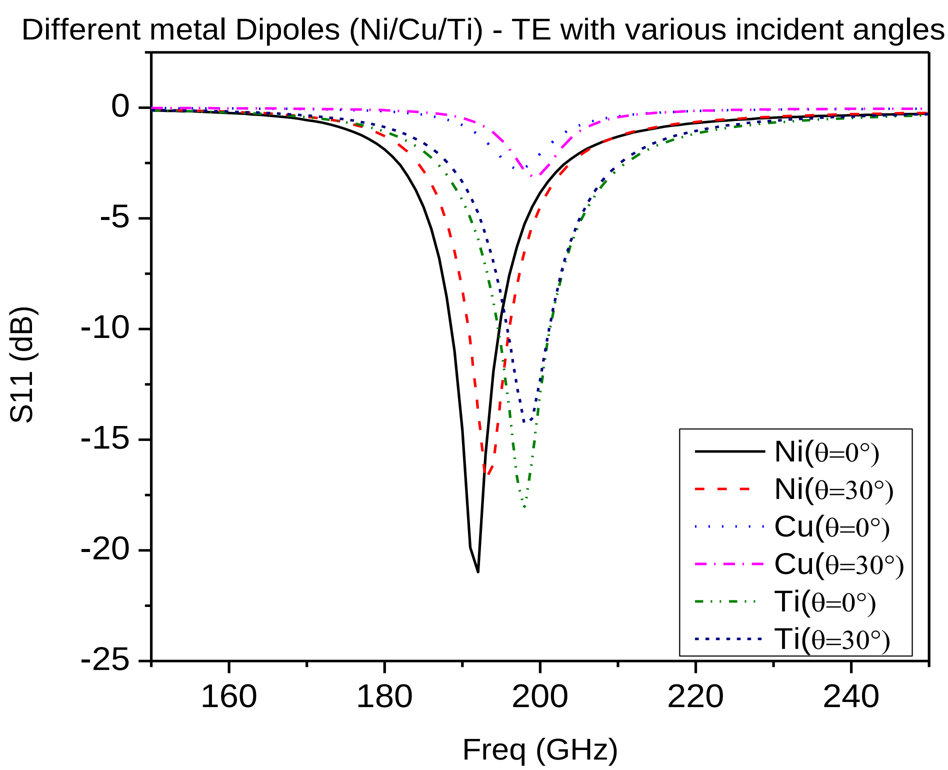

(b)

Figure 3.2 The simulation results of skin effect and permeability, (a) simulation schematic, (b) different metals, (c) the reflection of Ni changing the thickness, and (d) the reflection of various permeability.

Figure 3.2 (cont'd)

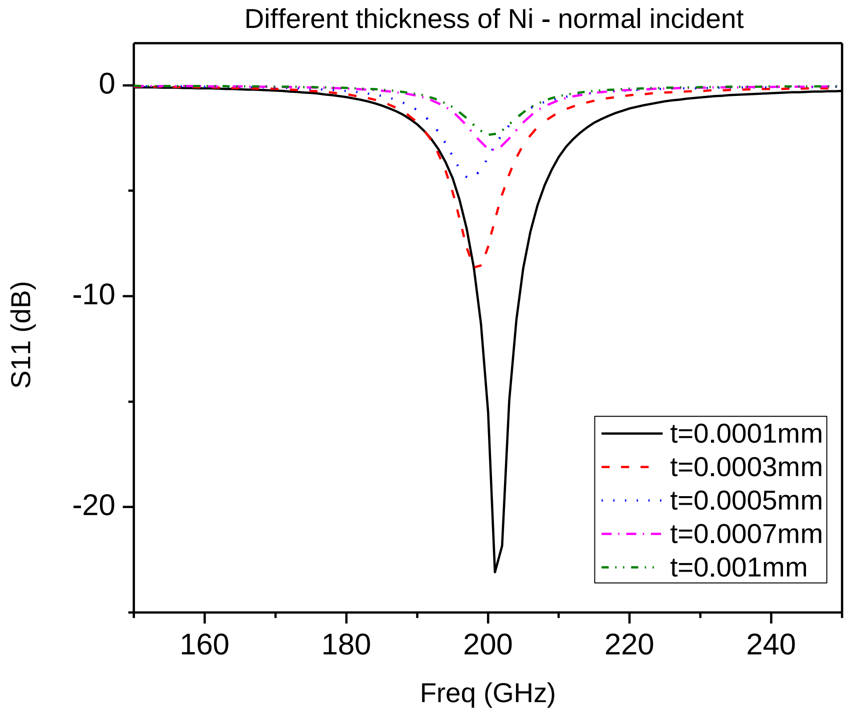

(c)

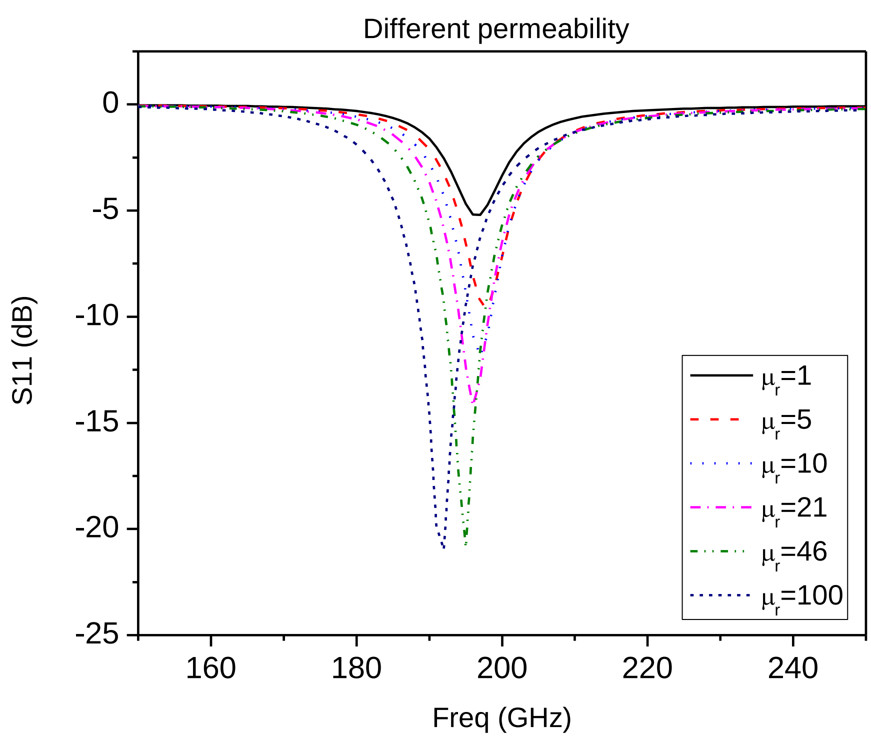

(d)

Another simulation has been carried out that the transmission properties of a rectangular waveguide coated with different metals mentioned above. Figure 3.3 shows the simulated transmission (S_{21}) of rectangular waveguides. The physical size of waveguide is set as WR-4 (operating frequency: 170 to 260 GHz), W × H=1.0922 mm × 0.5461 mm. The coated thickness of metals is 100 μm.

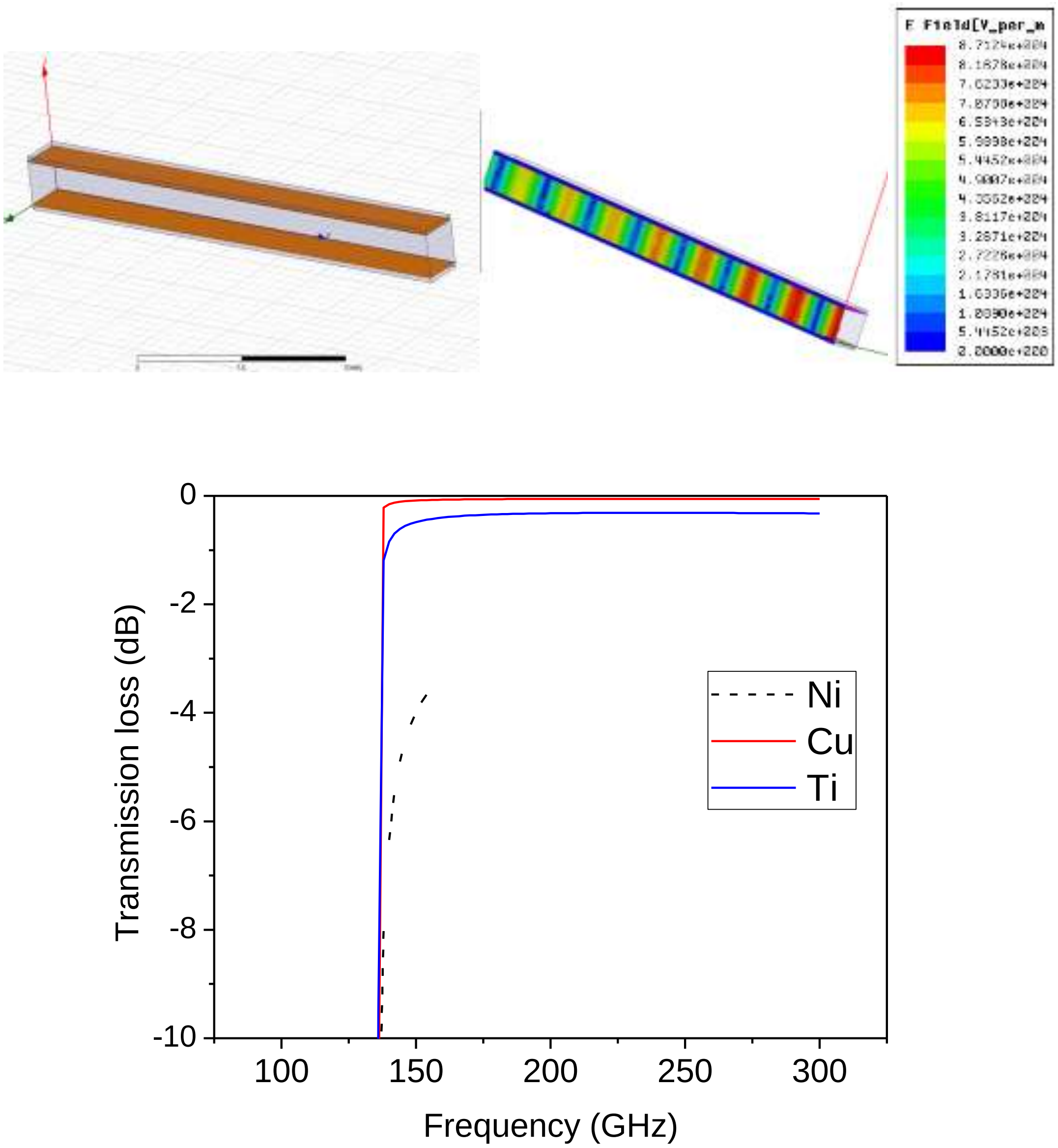

Figure 3.3 Waveguide transmission simulation with different metals.

All of the simulations show that nickel, a ferromagnetic material, has higher absorption and wider bandwidth than the other metals considered. On the other hand, the higher conductivity material, copper (Cu), showed the narrowest absorption bandwidth. Hence, nickel (Ni) was chosen for the design and fabrication of absorbing structures. Nickel is also a preferred metal for fabrication of packaging devices, because it is a low-cost material and can easily be deposited using electroless- and electro-plating [42].

3. 3. Designs and simulations

3.3.1 Single layer proposed metamaterial arrays

For the actual device design and testing, 0.2 THz and 0.4 THz were chosen as the center frequencies. The exact shapes of the metamaterial unit cell were chosen to emulate a regular cross, circle, and Minkowski as shown in Figure 3.1. All of proposed structures were considered to produce the polarization independent form it of incident wave. The widths (W) of each cross arm were chosen as 75 μm and 37.5 μm, while the length (L) of each arm was chosen as 400 μm and 200 μm, respectively. Additionally, the gap (G) between each unitcell was set as 150 μm and 75 μm. In the circle layout, the radius (R) of it was designed as 204 μm and 102 μm, the gap (G) set 72 μm and 36 μm, separately. For Minkowski structure, the width (W) of the structure was designed as 760 μm, the length (L) of a leg was 345 μm, and the entire physical size of unitcell (U) is 830 μm. Likewise, the thickness of the metallic layer was chosen to be 0.5 μm and 0.25 μm, while the thickness of the dielectric was 50 μm and 25 μm, respectively. Rogers® ULTRALAM liquid crystalline polymer (LCP, ε_r= 3.5 and tan δ= 0.05) was chosen as the substrate based on its relatively good dielectric properties in the THz spectral region [43].

Figure 3.4 demonstrates the simulation results of cross-dipole absorbers using Floquet port in HFSS. To be specific the simulation, the electromagnetic wave is excited from a port on top side of z-axis, which is able to radiate TE/TM mode. Also, different incident angles (θ) are considered from 0 to 90°. Then, the simulated structure can be only computed the reflection (S_{11}) because of a single port. From simulated the reflection, the absorption can be inverted. In Figure 4 (a) and (b), 0.2 and 0.4 THz cross absorber simulation results are shown. Reflection is plotted on the left side and absorption is the right side with two exiting modes and changed incident angles. In Figure 3.4 gives the reflection and absorption as different incident angles in the TM and TE, respectively. Both cross absorbers, the simulated frequencies of maximum absorbing show 0.198/0.197 THz (TE/TM mode) and 0.387/0.389 THz at a normal incident angle. The calculated absorption of maximum absorbing frequencies is 88.3/88.1 % at 0.2 THz and 78/78.3 % at 0.4 THz, respectively. In simulation results, the absorbing results of TE and TE mode, both are well matched each other. It is because this scheme (cross) has a structural advantage which is less dependent on the polarization of incident electromagnetic wave. Moreover, up to the incident angle, θ=60° (not shown), the absorption of a cross absorber works well both of transmitting modes (peak absorption of TE=62.3 %, TM=86 %). The simulated full width at half maximum (FWHM) of each frequency is calculated 15.6% (at 0.2 THz) and 19.3 % (at 0.4 THz) at normal incident angle. The E-field and surface current distributions are illustrated in Figure 3.4 (c) and (d), respectively.

Simulated results of circle absorbers are depicted in Figure 3.5. Generally, the schematic of circle is independent from the polarization of incident wave. At normal incident angle, the peak absorption and FWHM of TE are identical with it of TM (peak absorption=93.8 % at 0.201 THz, 99 % at 0.395 THz).

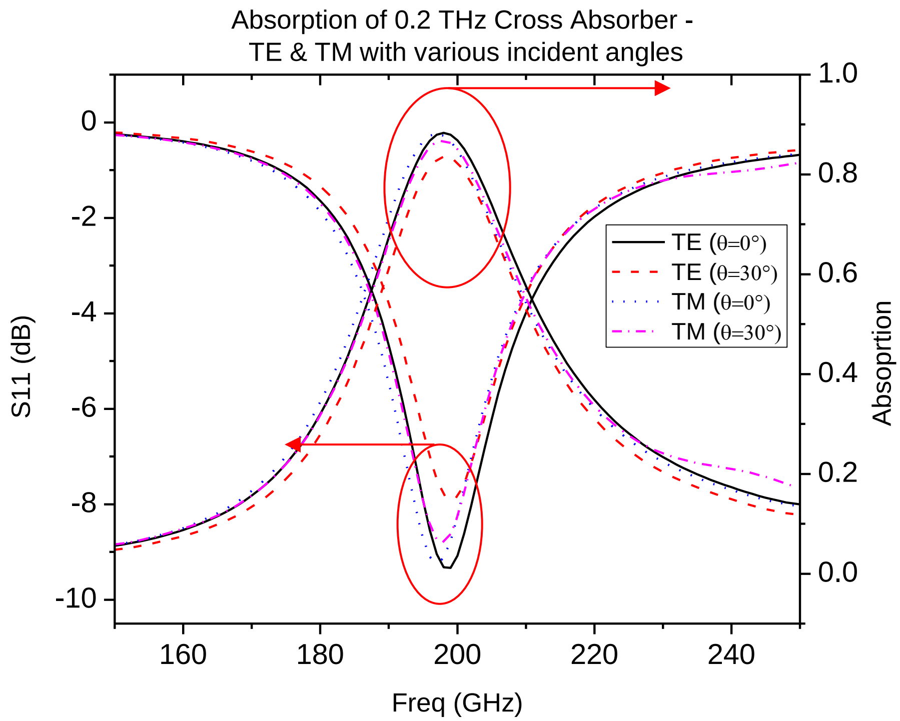

(a)

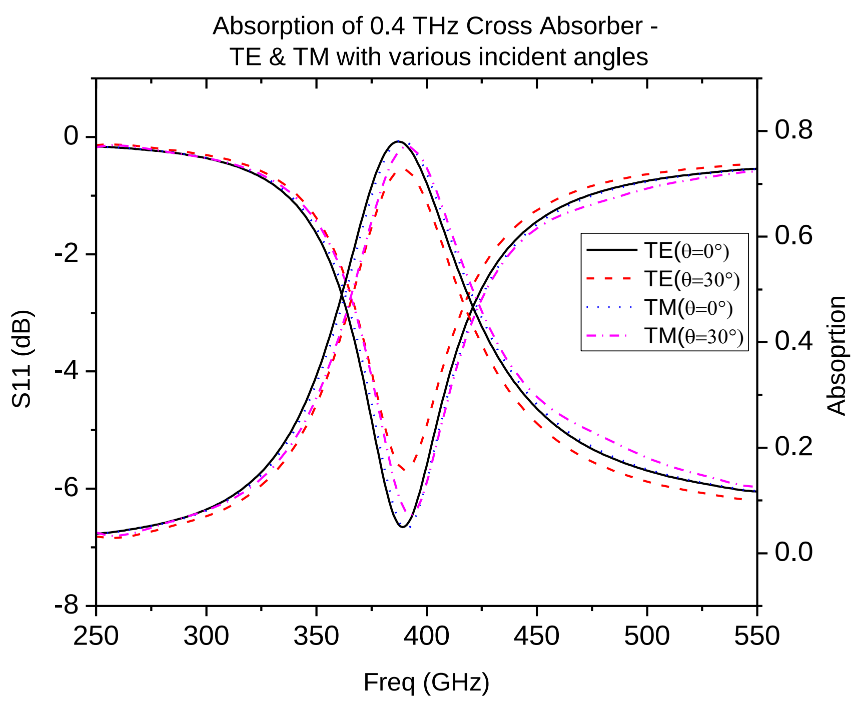

(b)

Figure 3.4 Simulation results(using Floquet's port) of 0.2/0.4 THz cross dipole absorbers with various incident angles (θ); (a),(b) Return loss/Absorption of 0.2/0.4 THz cross absorber, (c),(d) Field distribution(E-field)/surface current of a cross absorber.

Figure 3.4 (cont'd)

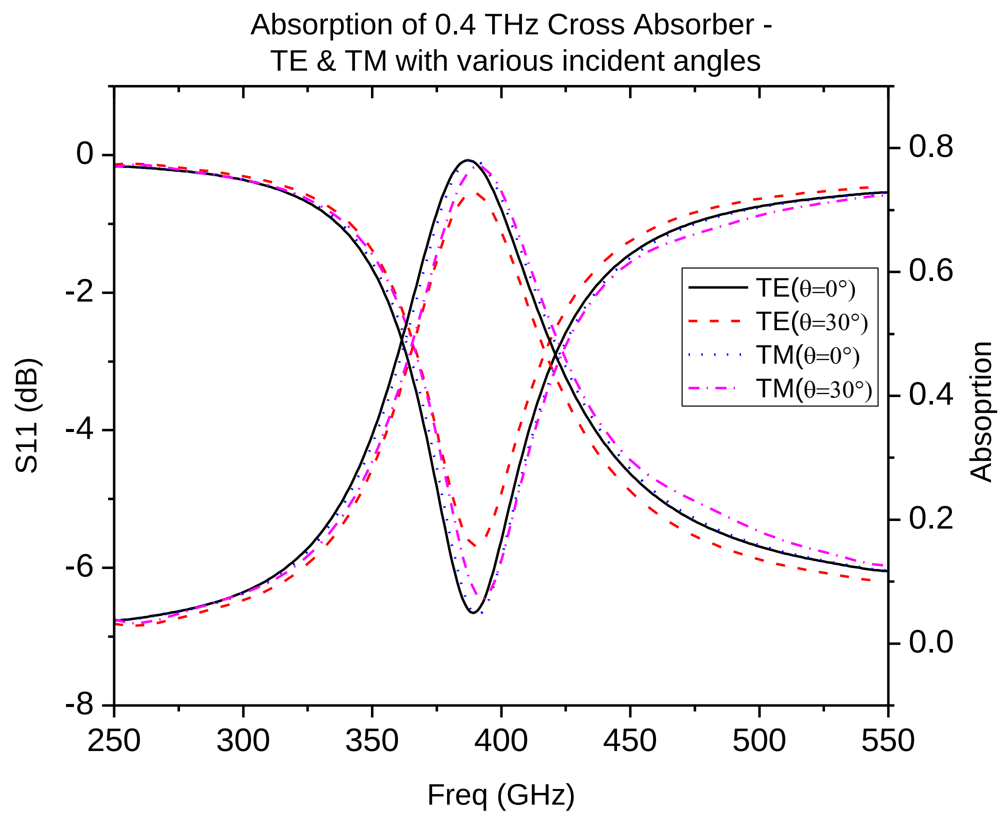

(b)

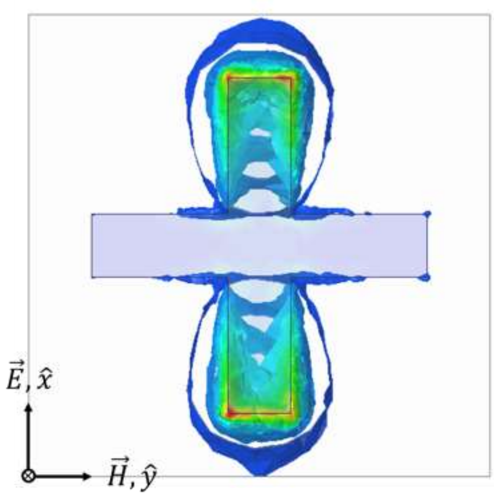

(c) E-field

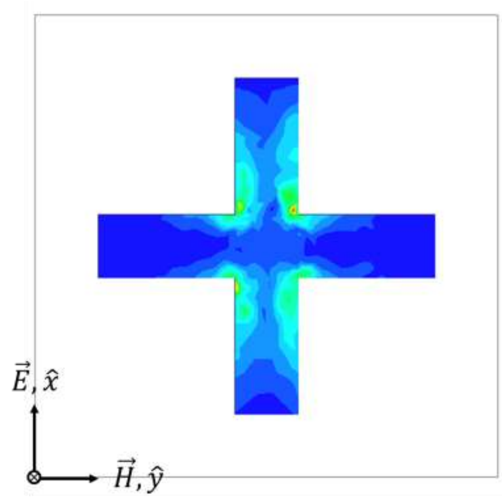

(d) Surface current

In the incident angle, θ=30° of 0.4 THz absorber, the reflection of TE shows very deeply comparing to other TE/TM simulation. However, as converts to the absorption, the value of it was calculated as 100% absorption. The deviation between normal angle and this angle is only 1%. Compared to the cross type absorber, the FWHM of circle absorber is shown wider absorption bandwidth, 19.7 % at 0.2 THz and 22.6 % at 0.4 THz, respectively. Figure 3.5 (c) and (d) demonstrate the field distribution of E-field and surface current density on the surface of the circle absorber.

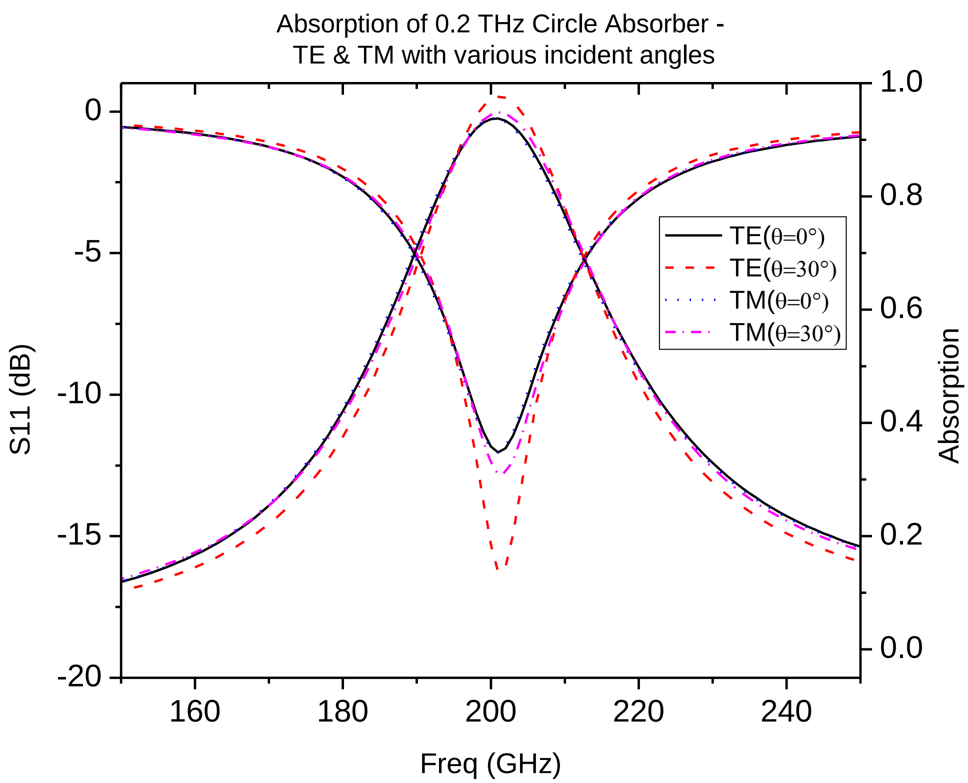

(a)

Figure 3.5 Simulation results of a 0.2/0.4 THz circle absorber with various incident angles; (a),(b) Return loss/Absorption of 0.2/0.4 THz circle absorber, (c),(d) Field distribution(E-field)/surface current of a circle absorber.

Figure 3.5 (cont'd)

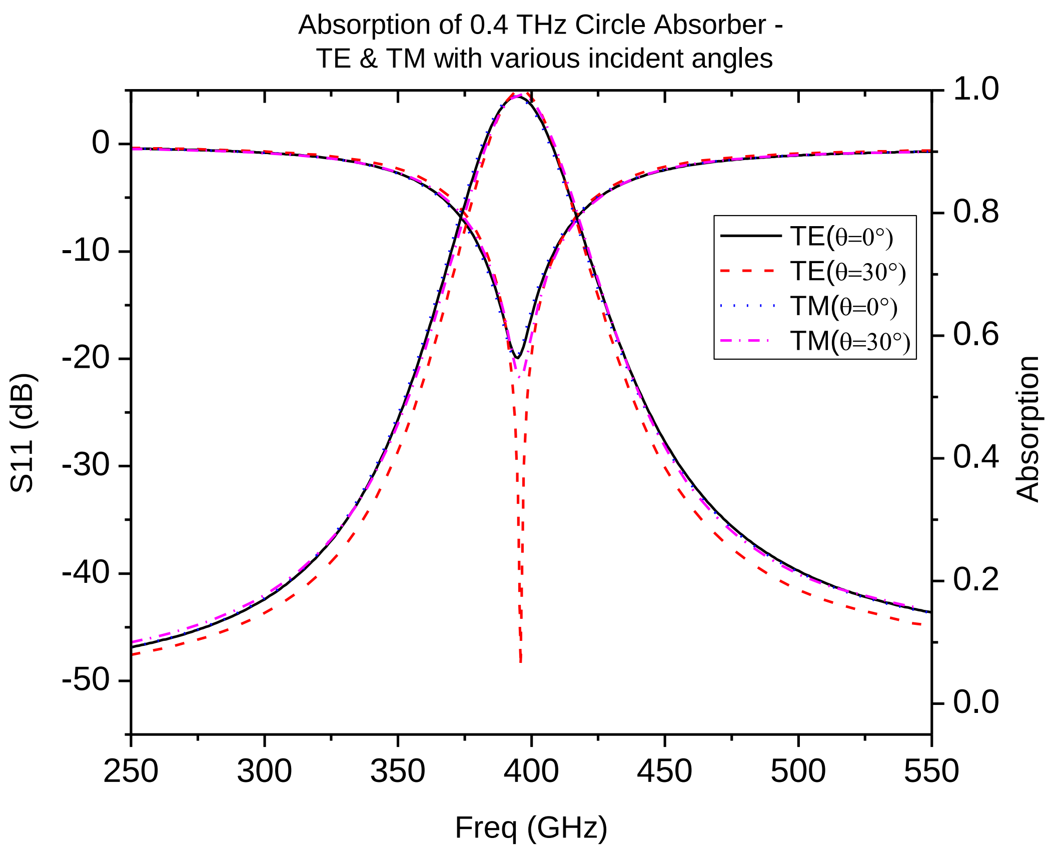

(b)

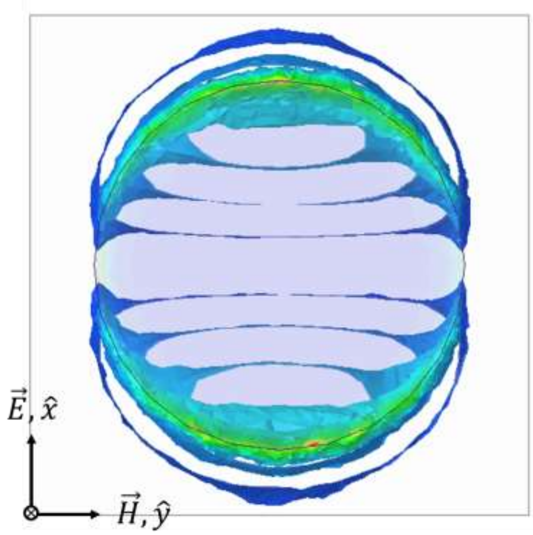

(c)

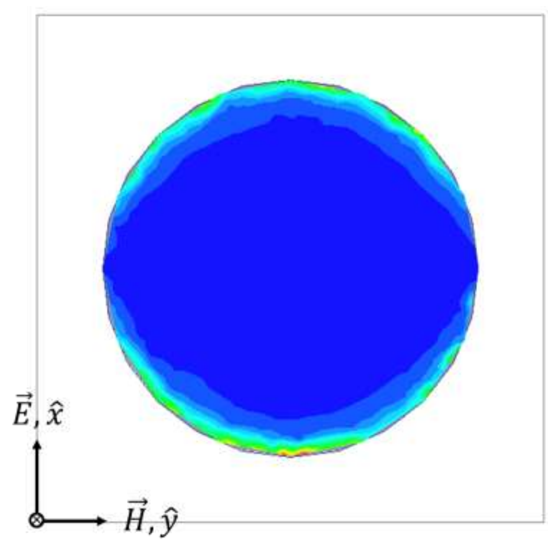

(d)

Figure 3.6 demonstrates simulated results of Minkowski structure that is designed to operate at 0.2 THz. The distinct characteristic of Minkowski has multiple resonant frequencies due to the shape [64]. The frequencies of strong absorption peaks are approximately at 0.21 THz (main), 0.243 THz (second) and 0.074 THz (third). Maximum absorption frequency, the amount of $S_{11,}$ is 15.5 dB. It is clear that the absolute density of absorption is 97.2 % at the main frequency. Absorptions at second and third frequency are 80 % and 79 %, respectively. All of the peaks can be utilized for absorption in incident ration. From simulation results, the FWHMs of absorption peaks are approximately 28.6 % (0.061THz between 0.193 and 0.254 THz including main and second peak) and 18.2 % of third peak. The bottom of Figure 3.6 shows simulated E-field and surface current distributions for the Minkowski structure. It is clear that strong E-field appears in the edge of structure and the EM wave penetrates the space between the metallic layers leading to desired absorption. These geometrical parameters play a significant role in tuning the desired frequency.

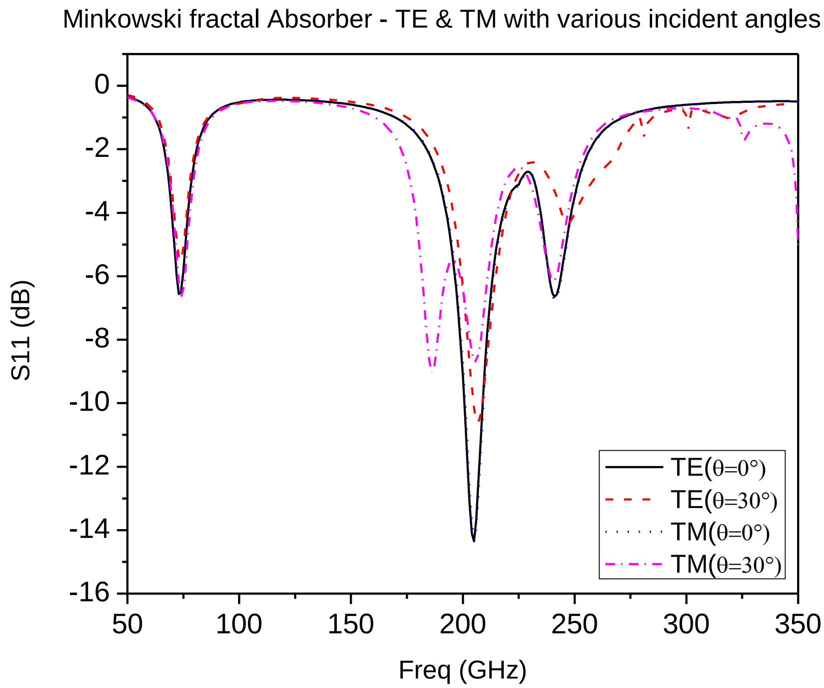

(a)

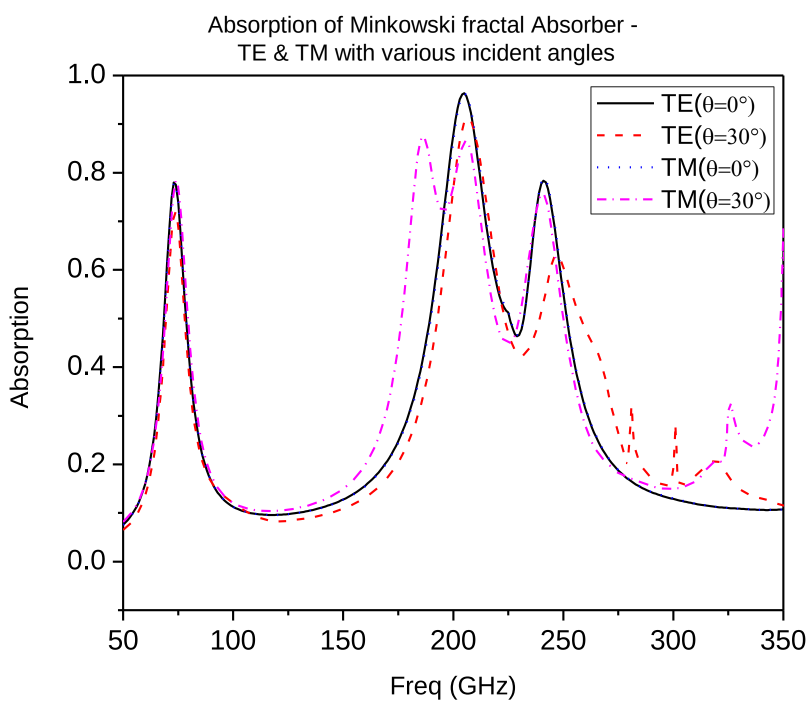

(b)

Figure 3.6 Simulation results of a THz Minkowski absorber with various incident angles (θ); (a), (b) Return loss/Absorption; (c), (d) Field distribution (E-field)/surface current.

Figure 3.6 (cont'd)

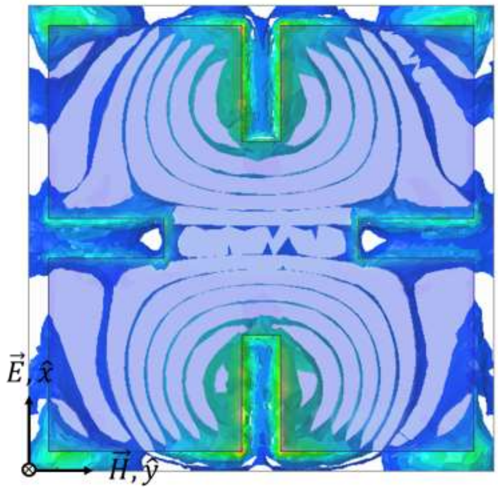

(c)

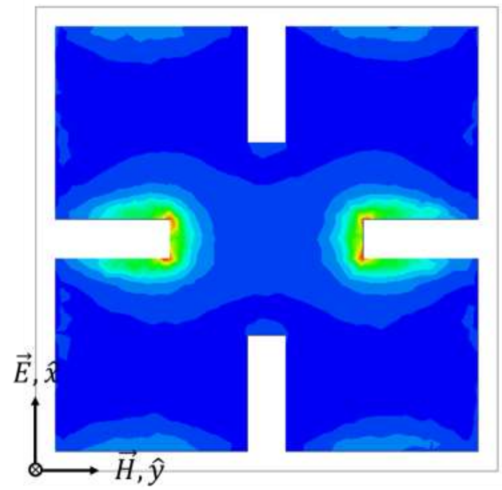

(d)

3.3.2 Double layers of proposed metamaterial arrays

In order to increase the absorption strength and bandwidth, multi-stacking of layers was analyzed. In the first case, two of same layers were stacked on top of each other. This approach provides dual advantage, the inherent resonant frequency is maintained and furthermore the interaction between these layers provide enhancement in bandwidth. In the second configuration, two layers having different resonance frequencies are stacked on top of each other. This arrangement provides a significant enhancement in bandwidth. Figure 3.7 summarized the simulation results of multi-layer of a cross absorber. In Figure 3.7 (a) shows the simulated results of double 0.2 THz cross absorbers. Compared to a single layer 0.2 THz cross absorber, the maximum absorbing frequency shifted slightly down to 0.185 THz due to mutual coupling between top and bottom absorber layer. With overlapping the same resonant frequency, the operating bandwidth is higher than a single layer absorber. Specifically, the peak absorption was analyzed as 99.9 % at 0.185 THz and the FWHM is 30.8 % (absorption: 88.3 % and FWHM: 15.6 % of a 0.2 THz cross absorber).

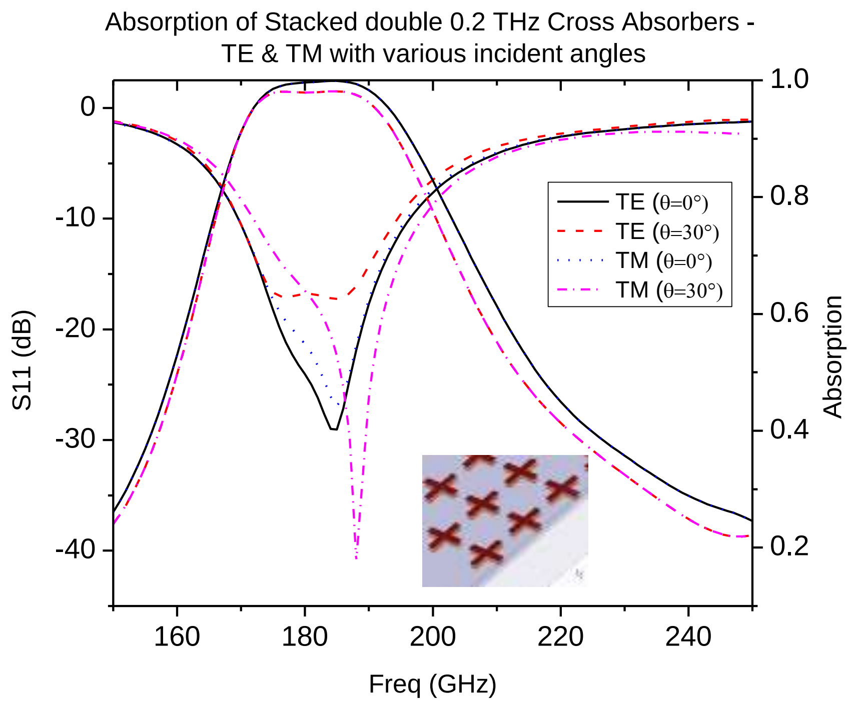

(a)

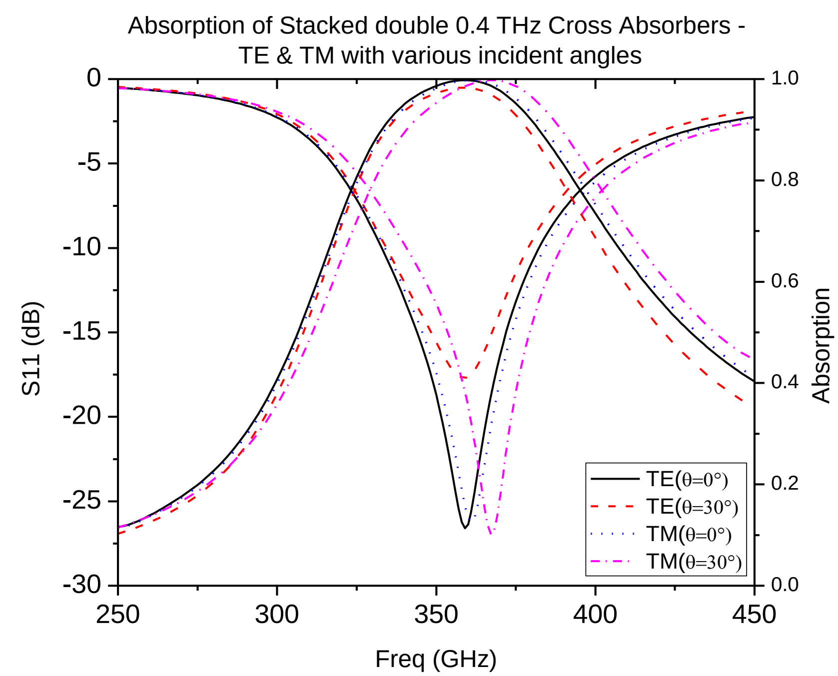

(b)

Figure 3.7 Simulated absorption results of double stacked cross absorbers, (a) double layers of 0.2 THz absorbers, (b) double layers of 0.4 THz absorbers, and (c) 0.2/0.4 THz absorbers hybrid configuration.

Figure 3.7 (cont'd)

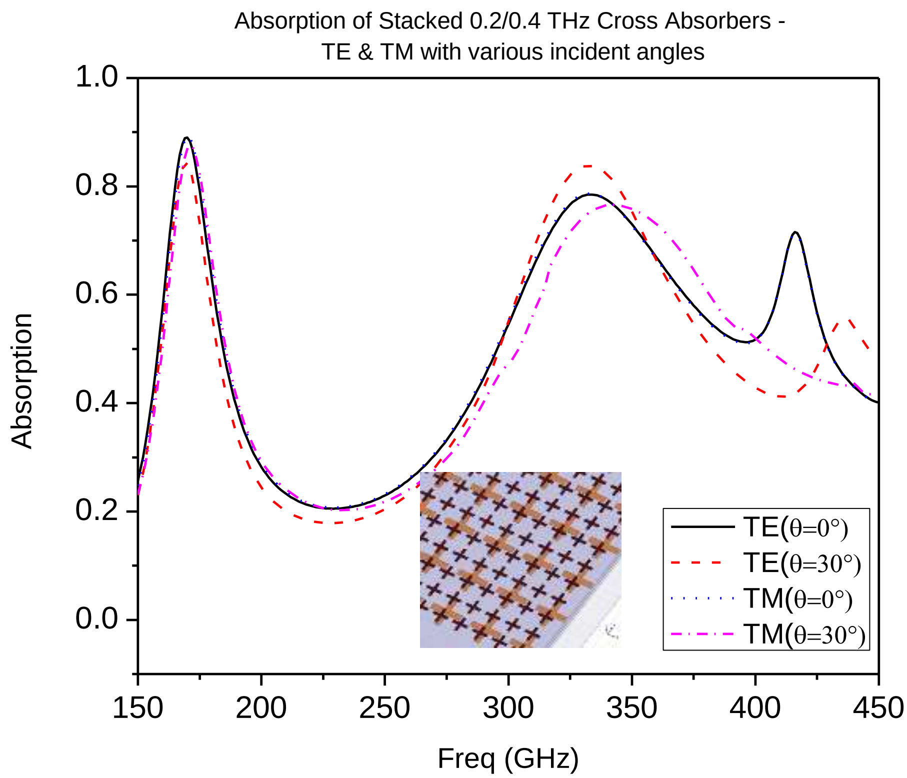

(c)

Likewise, double 0.4 THz cross absorbers show similar performances. The peak absorption was computed as 99.7 % at 0.362 THz and the FWHM is 34%. This assembly provides wider bandwidth and higher absorption than a single absorber. Figure 3.7 (c) demonstrates the simulated results of a hybrid configuration that is composed of a 0.2 THz cross and a 0.4 THz cross. In this simulation, the peak frequencies can be recognized as multiply resonating. First peak is at 0.17 THz with 89 % of absorption and the second peak is at 0.334THz with 78.5 % absorption. In case of The FWHM, multi peak absorptions lead to increase in the usable FWBH significantly, for first case it is 17.6 % and 46.4 % for the second case.

Figure 3.8 illustrated the simulation results of multi-layer circle absorber design. Simulated results of double 0.2 THz circle absorbers were shown as a maximum absorption analyzed at 0.169 THz with 71.6 %, the FWHM of it was 50.4 % (usable bandwidth 0.085 THz). On double layers of 0.4 THz, the centered frequency was simulated at the peak absorption of 80.3 % at 0.332 THz and the FWHM was 52.1 % as well. It is clear that a double stacked absorber plays a significant role towards improving operating usable absorbing bandwidth. However, comparing to the single 0.2 THz circle absorber, the maximum absorption ratio reduced slightly, it is due to the spatial impedance mismatch between top and bottom layer. It can be matched to adjust the thickness of the dielectric substrate. In Figure 3.8 (c), simulation results of the hybrid alignment - 0.2/0.4 THz absorbers were shown. Similar to stacked hybrid cross absorber, there are multiple absorbing resonant frequencies calculated. The peak absorptions were simulated: first peak placed at 0.164 THz with 88.3 % absorption and second peak shown 95.5 % at 0.361 THz. The FWHM were 25.1 % and 28.9 %, respectively.

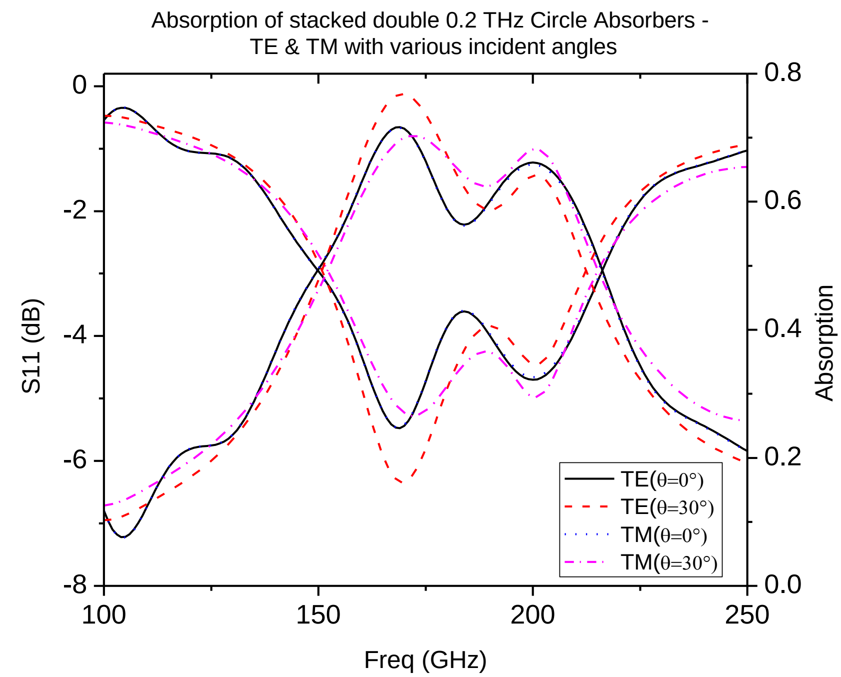

(a)

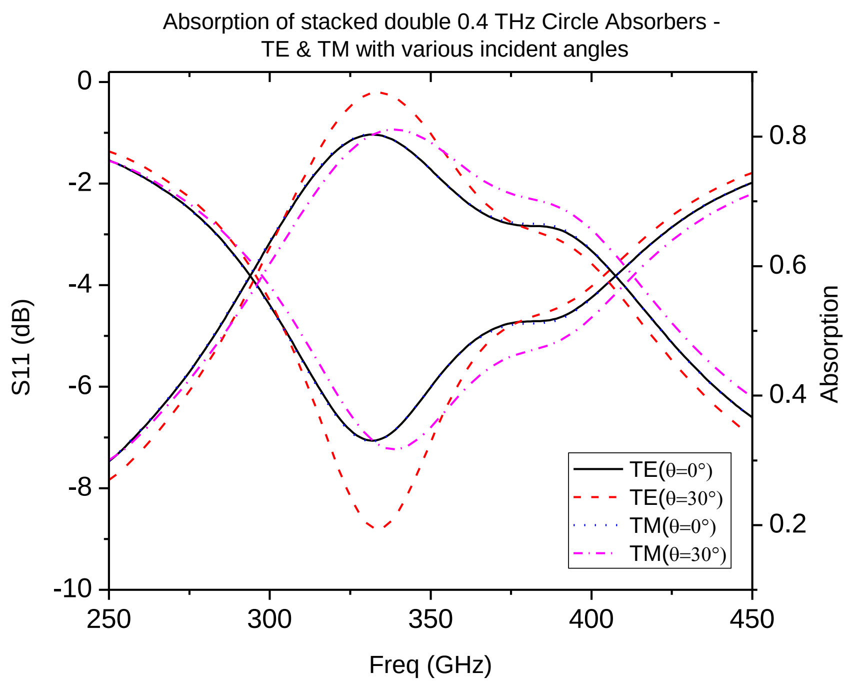

(b)

Figure 3.8 Simulated absorption results of double stacked circle absorbers, (a) double layers of 0.2 THz absorbers, (b) double layers of 0.4 THz absorbers, and (c) 0.2/0.4 THz absorbers hybrid configuration.

Figure 3.8 (cont'd)

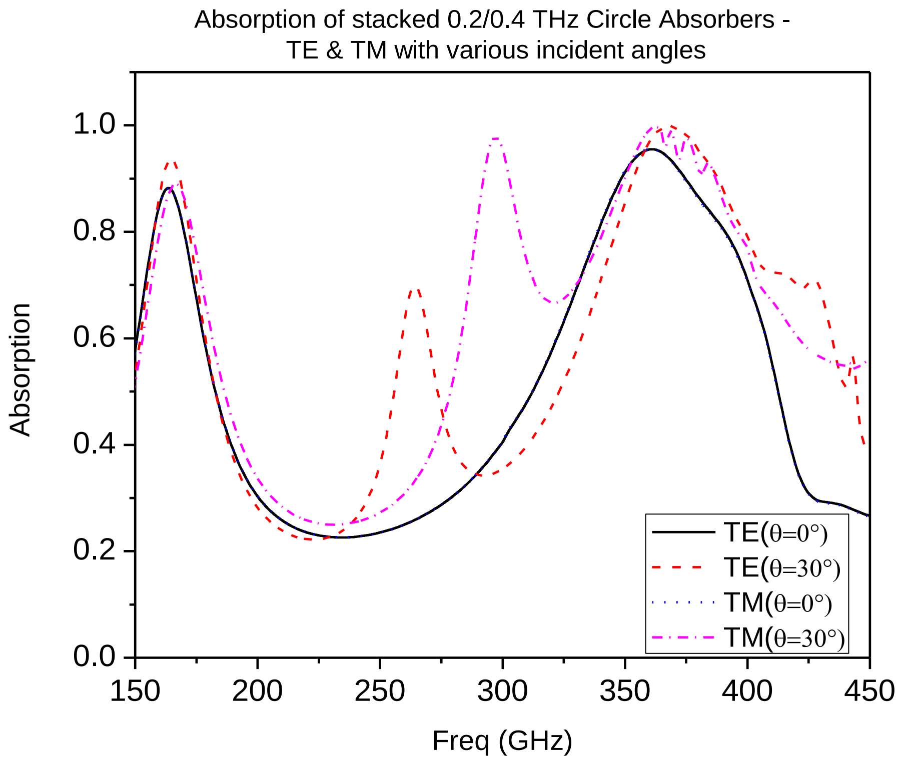

(c)

3. 4. Fabrication

Terahertz absorbers were fabricated using a conventional micro-fabrication approach. A liquid crystalline polymer (LCP) substrate was chosen as it shows well behaved dielectric characteristics in the THz range. Fine metal patterns were achieved using a lift-off process. After spin-coating and developing the photoresist (PR, Microposit® S1800® series) layer on top of LCP, nickel was evaporated via an e-beam process to pattern the metamaterial-inspired absorbers in the cast. Followed by removal (and lift-off) of photoresist using acetone. Figure 3.9 summarizes the process flow.

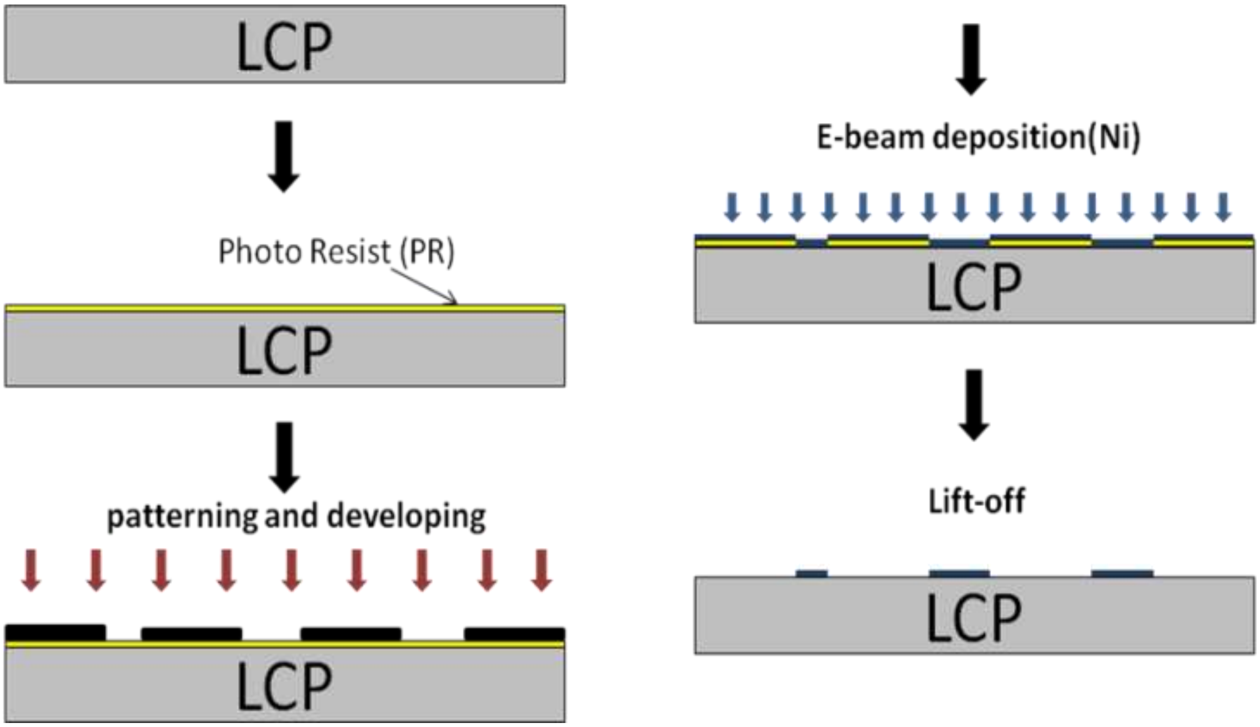

Figure 3.9 Fabrication process flow of THz absorbers.

Nickel thicknesses of 0.5, and 0.25 μm were used for 0.2 THz and 0.4 THz absorber designs, respectively. These thicknesses are larger than the skin depth and much thinner than the wavelength at these respective frequencies. Figure 3.10 shows a photomicrograph of a sample fabricated using Ni on LCP substrate using the process outlined in Figure 3.9.

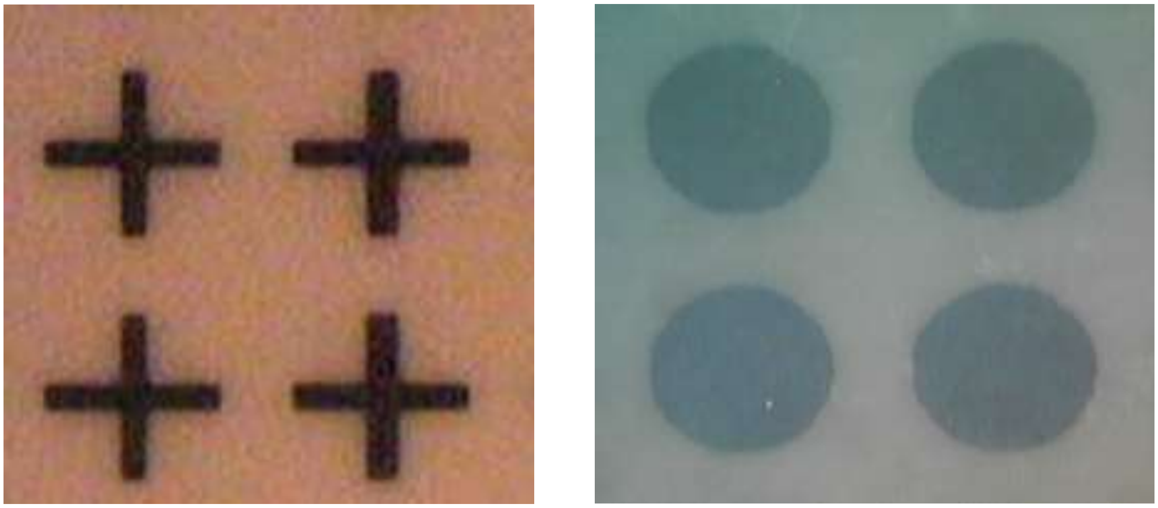

Figure 3.10 Photomicrographs of fabricated absorber structures: cross and circle using Ni on LCP substrate.

3. 5. Experimental measurement

A picometrix T-ray 2000 THz time domain system (TDS) fitted with both a receiver and transmitter was used for the measurements. This measurement system offers the sampling period of 0.03941 ps. These results in a frequency resolution of approximately 12.5 GHz when acquiring the Fourier transform of the received time domain signals [44]. The transmitter radiates a collimated electromagnetic pulse beam in the direction of the receiver. Two measurement approaches were utilized in order to test the fabricated metamaterial absorbers. These setups were made to address many different situations emulating their use in a high frequency electronic package. The first setup comprises an electromagnetic wave impinging normally upon the absorber (Figure 3.11). In the past, most metamaterial absorbers have been tested in this fashion. Some of these tests have been conducted by varying the angle of incidence. Here, only normally incident waves are applied and tested over a wide frequency range. The success of the absorber at particular frequencies using the first setup demonstrates the feasibility of using it to absorb radiated waves from an electronic package. Using this setup, we experimentally measured the metamaterial-inspired absorbers. A reference measurement is first taken with a smooth metal plate located at the right side of the setup (1). The transmission measurement is recorded in the presence of the plate (at position (1)) by placing the sample in between the receiver and the transparent mirror (position (2)). The reflection measurement, on the other hand, is performed by placing the sample in place of the metal plate facing the transmitter across from the transparency (see Figure3.11 for more details). Also, in order to characterize the performance of different incident angles, absorbers have been measured a variety of incident angles depicted in Figure 3.12. As the absorbers patterned metamaterial structures have been measured with the different incident angles, absorbers have been verified the absorption depending on radiating angles.

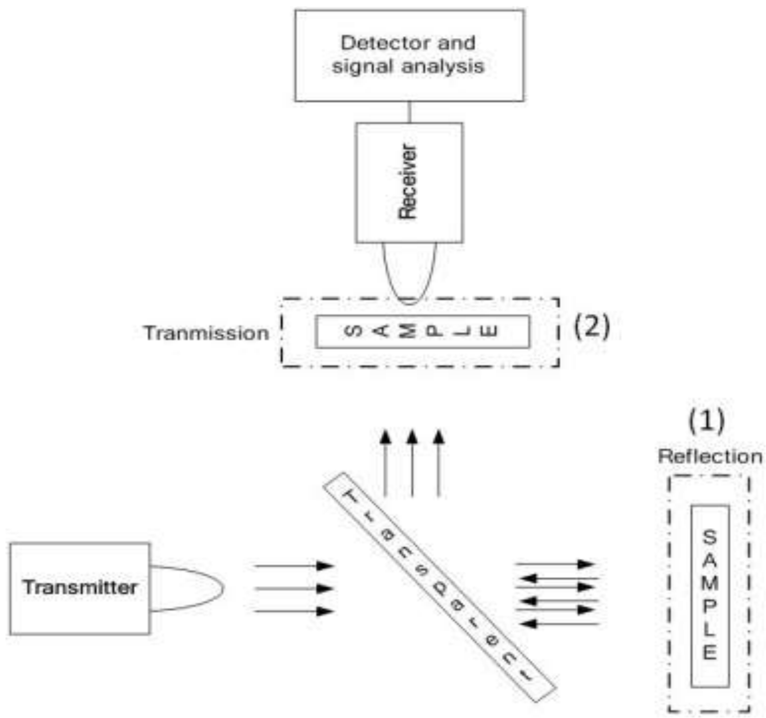

(a)

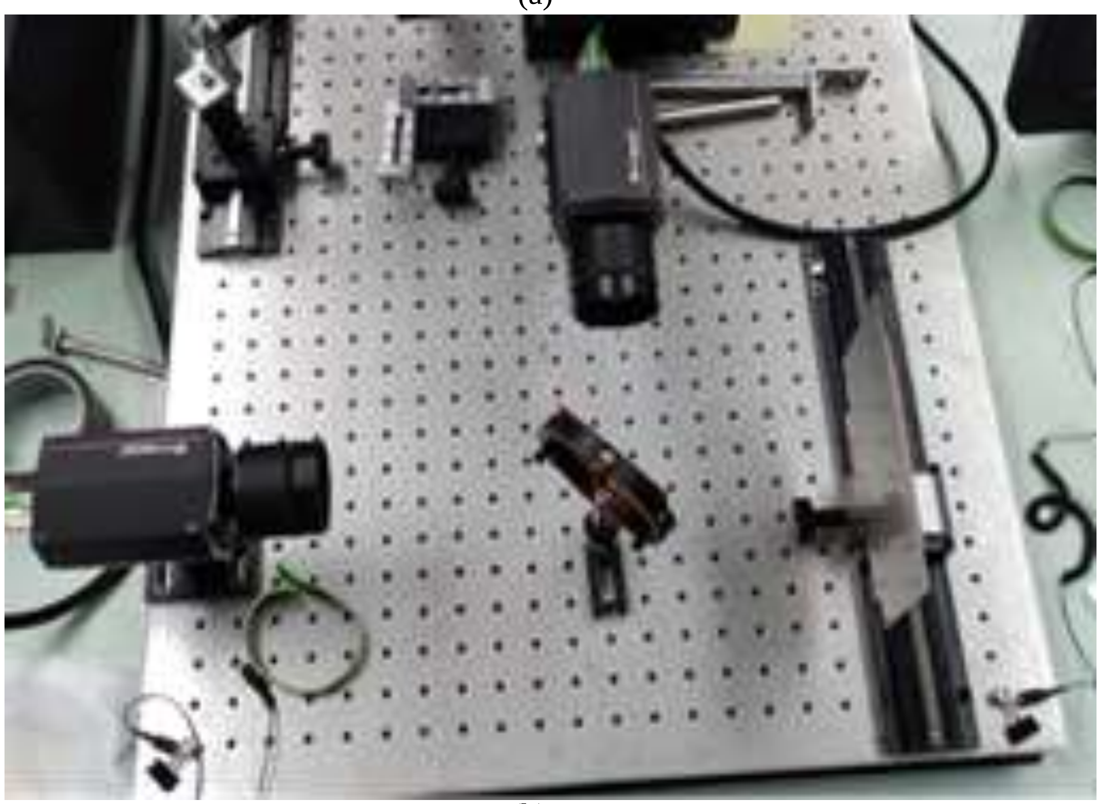

(b)

Figure 3.11 Block diagram of the reflection and transmission measurement method.

Specifically, mounting the test sample in the path of the beam would cause part of the beam to transmit through the test sample and part of it to reflect away from its interface. It is this transmission and reflection information that is utilized to characterize the absorber. This measurement demonstrates that different reflection and transmission levels will occur depending on the characteristics of the test sample. In the case of an absorber, to minimize scattering losses, reflection losses must be minimal. For the samples measured here, the reflected signal was very low, thus the absorption was calculated the same equation that was used in simulations.

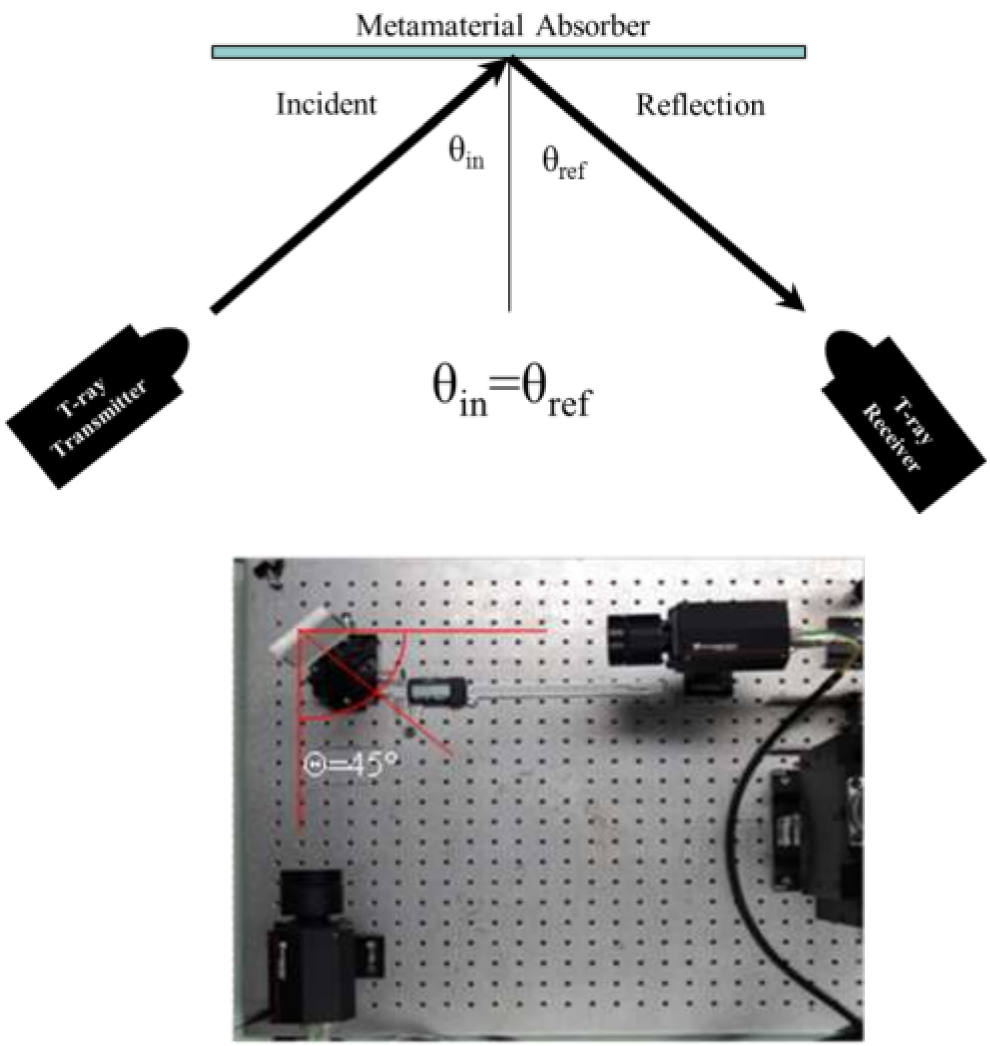

Figure 3.12 Reflection measurement setup of various incident angles.

3. 6. Measured results

3.6.1 Reflection and transmission of proposed absorbers with various incident angles

Characterized results of a 0.2 THz cross absorber have been illustrated in Figure 3.13. Figure 3.13 (a) shows the transmission measurement and a reference signal (in the absence of sample) on a time domain. As we know the time domain measurement, when the absorber under test was placed in the test setup, measured results were characterized by the magnitude and delay of the incident wave. Thus, we can analyze the electrical performance of the sample. Figure 3.13 (b) shows the calculated absorption of this sample based on these reflection and transmission measurement results. This shows a maximum absorption of 80% and the FWHM of 14.2 % (bandwidth of approximately 38 GHz centered at 0.269 THz). In Figure 13 (c), measured results and numerical analysis data are demonstrated together. In simulation, the center frequency of the designed THz cross absorber was analyzed about 0.2 THz and the FWHM was 15.6 %, however, the measured results show 0.27 THz as the peak absorption frequency(the frequency shift was computed as 70 GHz upper) compared to the simulation. This is because the surface roughness of the sample which was set in the test setup up was not evenly. As holds the sample on the metal plate, there are many air rooms located between a metal plate and a sample to obstruct the sample to be flatly. It makes the effective length of an absorber reduced. Thus, the operating frequency of the absorber can be resonated upper side. For the usable bandwidth, the measured FWHM reduced 1.4 % compared to the simulation. From different incident angles, at θ=30°, the peak absorption decreased to 68.2 % at 0.212 THz, the deviation of amount of absorption and centered frequency was 12 % and 57GHz comparing to the normal angle. The difference of amount of peak absorption was primarily from the larger beam-width of the source than the size of the absorber. It caused the misalignment and extra scattering of a path between the source, sample, and receiver. It can be improved to adjust the alignment and use the large metal plate to cover the beam-width properly.

Measured results of a circle absorber are summarized in Figure 3.14. Similarly to the cross absorber, the time domain measurement was carried out and then the frequency domain results was computed. In frequency domain results, the circle absorber shows wide absorption property significantly, from 0.2 THz to 0.4 THz.

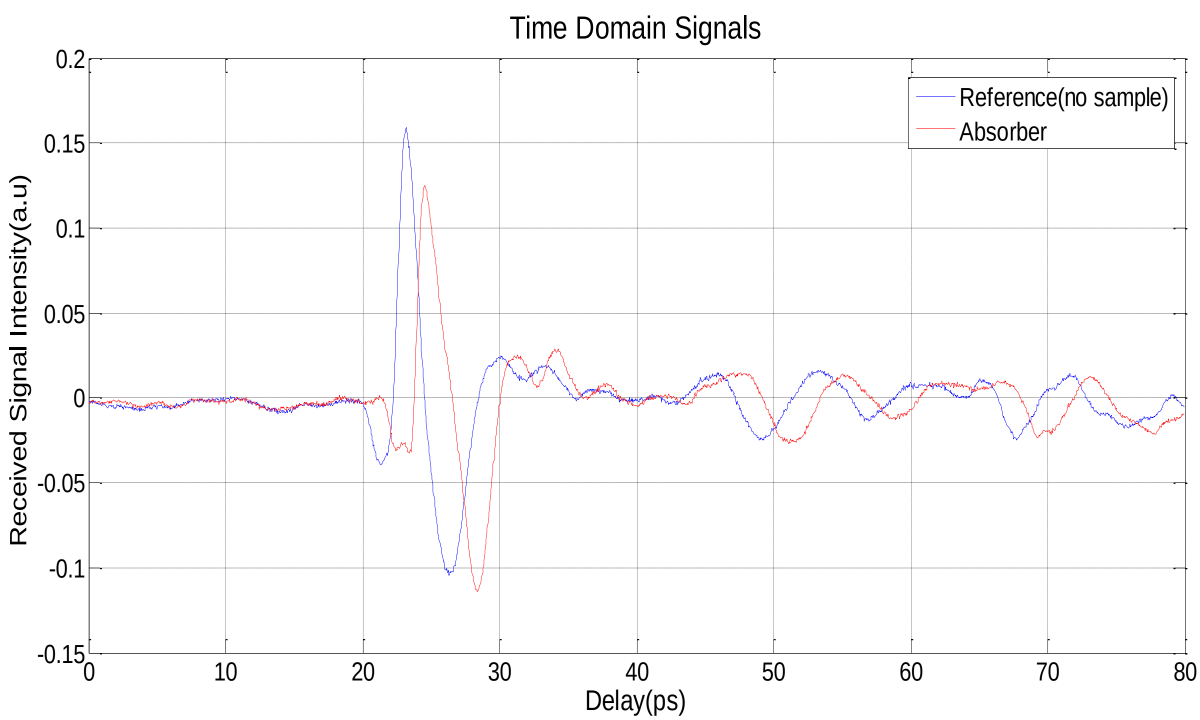

(a)

Figure 3.13 Measured transmission spectra and absorption of the 0.2 THz cross type single layer absorber, (a) time domain measurement result, (b) calculated frequency domain spectra and absorption, and (c) comparison measured results to simulations with various incident angles.

Figure 3.13 (cont'd)

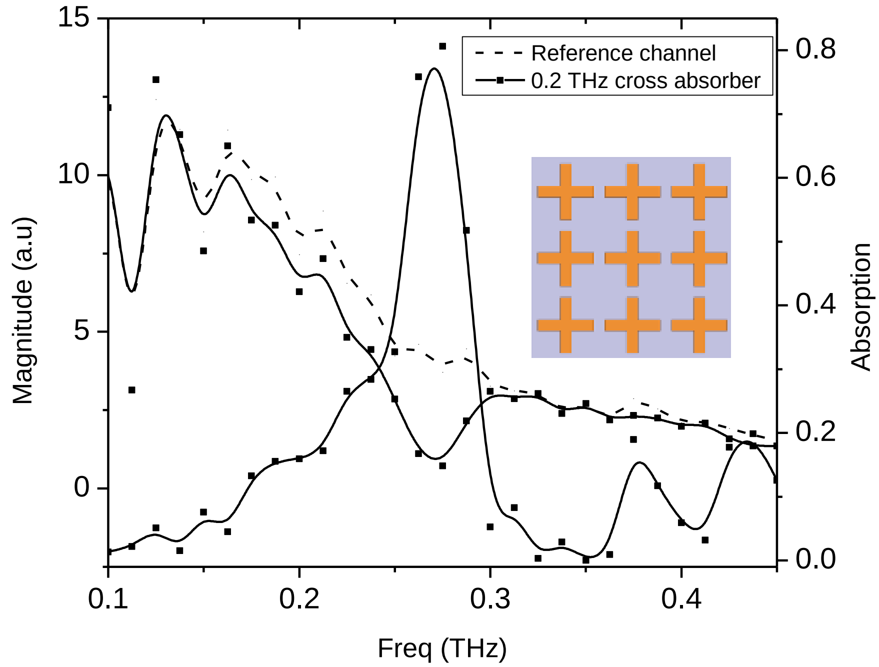

(b)

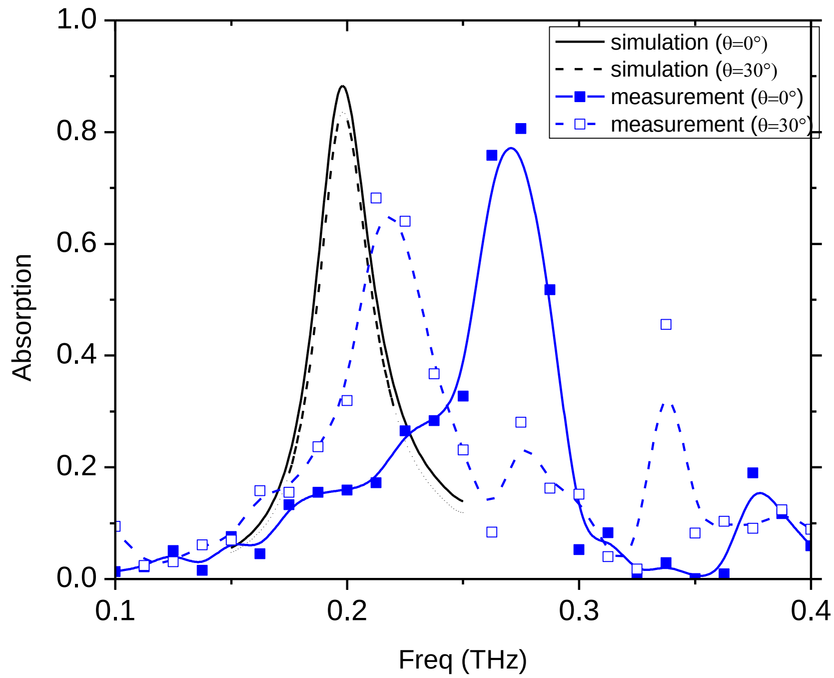

(c)

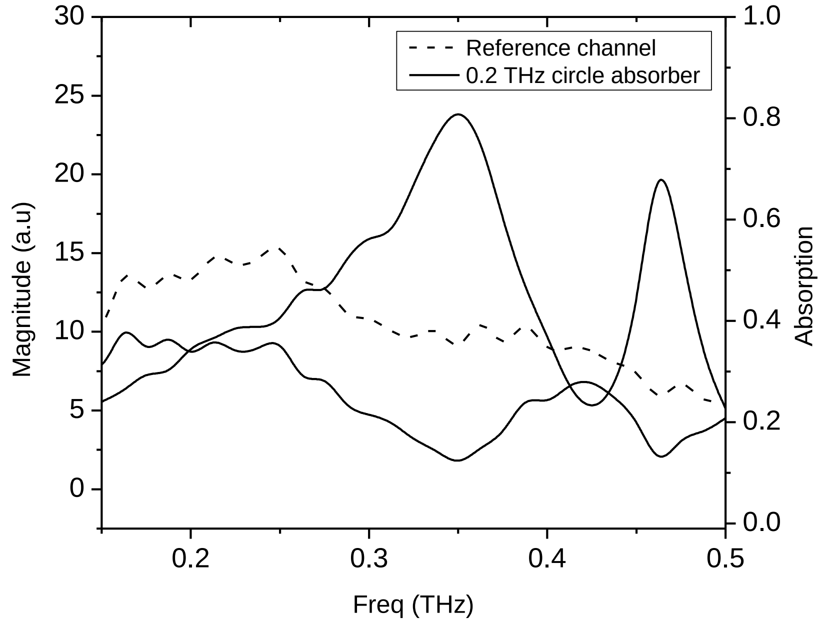

(a)

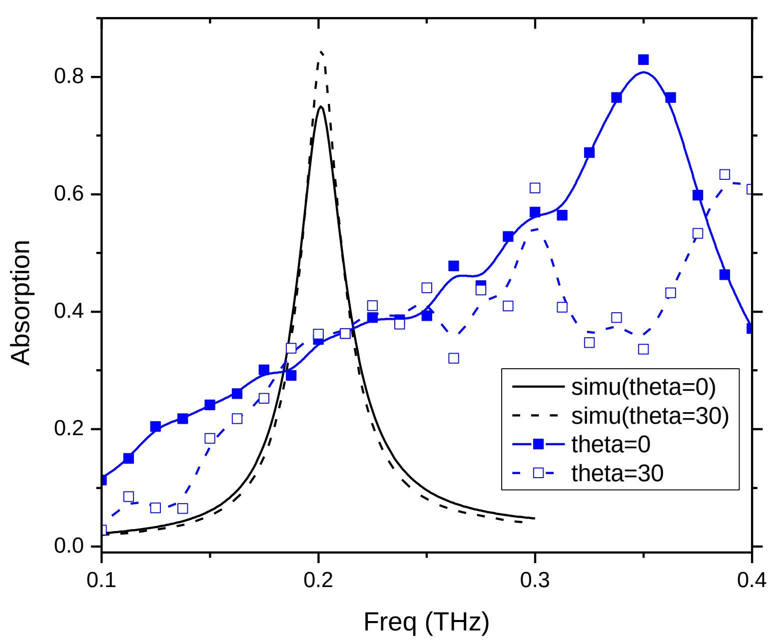

(b)

Figure 3.14 Measured transmission spectra and absorption of the 0.2 THz circle type single layer absorber.

From calculations, the occupied bandwidth above 40 % absorption was characterized to be from 0.25 THz to 0.393 THz. The peak absorption is 82.9 % at 0.350 THz as shown in Figure 3.14 (a). Also, the harmonics of the resonant frequency can be noted in measured results. Figure 3.14 (b) shows the comparison between simulations and measured results with various incident angles.

3.6.2 Waveguide measurement of proposed absorbers

Frequency domain transmission data for a 0.2 THz cross absorber using the waveguide measurement setup is provided in Figure 3.15. For this measurement, this absorber was assembled with a back metal layer. Also shown in Figure 3.15 (a) is the reference measurement that was characterized on a dielectric waveguide. This was carried out in the absence of the absorber. Figure 3.15 (b) shows the calculated absorption of this sample based on these reflection and transmission measurements. This shows the peak absorption 74.5 % at 0.212 THz and strong overall FWHM was measured 12.2 % between 0.180 and 0.26 THz. It should be noted that the measured center frequency is different for this sample design between the two measurement approaches. This is due to dielectric loading making lowering frequency in the second test setup. In this setup, the THz dielectric waveguide is touching the absorbing layer. From these measurements, it can be stated that due to the almost zero incident angle in the waveguide measurement setup (as compared to the normal incident angle using the transmission/reflection measurement setup), the scattering and reflection are decreased. Hence, this resulted in an improved absorption performance. Additionally, the maximum absorption occurs at roughly the same frequency values in both measurement cases. From these measurements, it can also be stated that the absorbers are expected to have strong absorption over a wide range of incident angles.

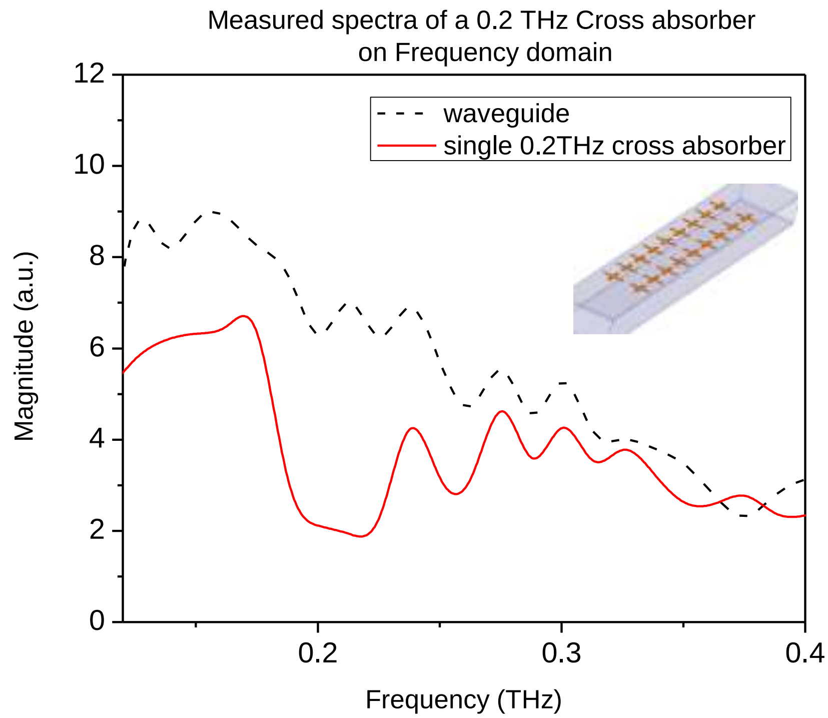

(a)

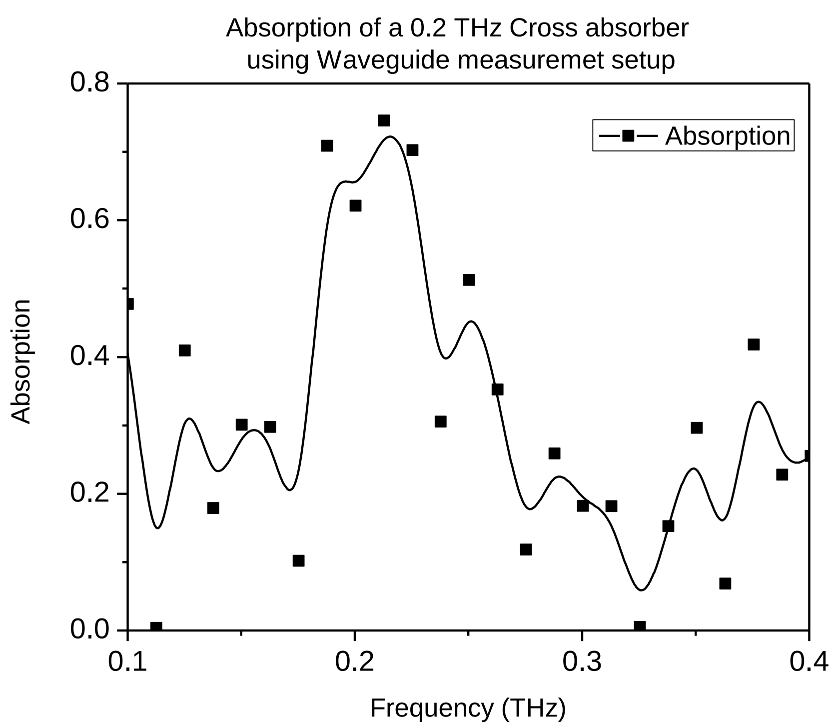

(b)

Figure 3.15 Measured frequency response (a) and absorption (b) of a 0.2 THz cross absorber using waveguide measurement.

Figure 3.16 shows the measured result obtained for a 0.2 THz circle absorber using the waveguide test setup. The waveguide measurement results of a 0.2 THz circle absorber are significantly similar to the simulation results. The peak absorption was measured as 82.2 % at 0.2 THz. The effective usable FWHM was characterized to be 25.2 % (bandwidth: 0.182 to 0.232 THz) as depicted in Figure 3.16 (b). As studied above, it was demonstrated that the single layer absorber provides strong absorption over a wide bandwidth. Further improvements can be made by double layer stacking. Stacking of a resonant structure leads to wider bandwidth and also stronger absorption. Design and experimentation were carried out for a hybrid combination of two 0.2 THz and 0.4 THz absorber layers. This was fabricated using two layers of LCP dielectrics and pressed together. There is a common solid ground plane present on the back of these structures.

Figure 3.17 shows the response obtained from a hybrid double stack of absorbers composed of a 0.2 THz cross absorber with a 0.4 THz cross absorber. Here, the 0.4 THz absorber is touching the dielectric waveguide and the 0.2 THz design is between the 0.4 THz layer and the metal backing layer. As expected, this configuration produces two usable absorption bands (Figure 3.17 (b)). The peak absorptions occur at or around the frequencies of interest (0.225 THz and 0.45 THz). To be specific, the peak absorptions of dual bands, 95.3 % and 84.3 % were measured, respectively. Moreover, the FWHM of each band is 61.4% and 21.8%. It is clear that double stacks of absorbers are proof that multi-band and ultra-wideband absorbing structure can be fabricated using this approach. This measurement shows that absorption bands can easily be tailored for different applications. In case of noise suppression, extreme bandwidth with high absorption is important.

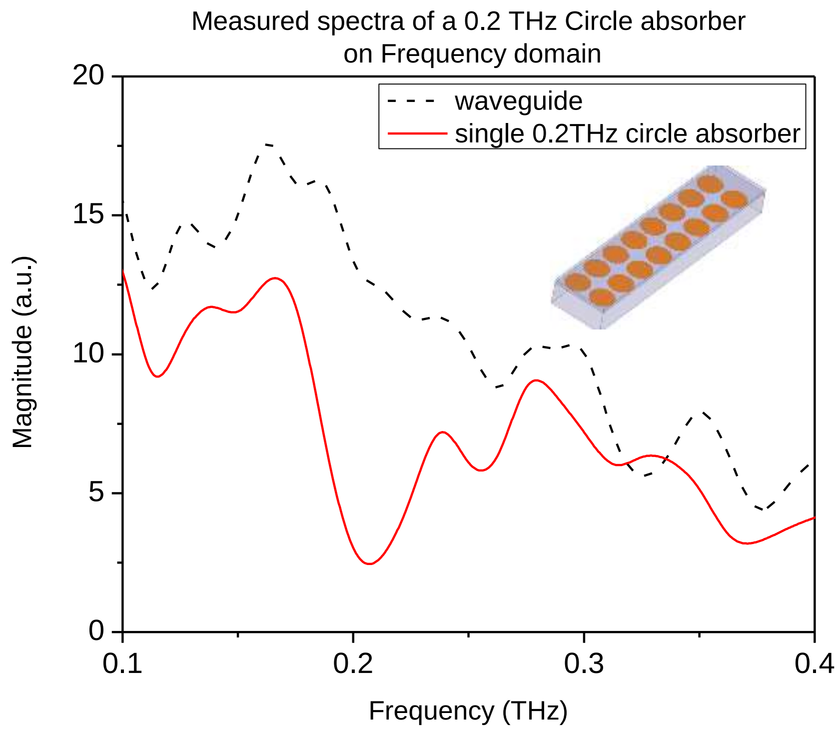

(a)

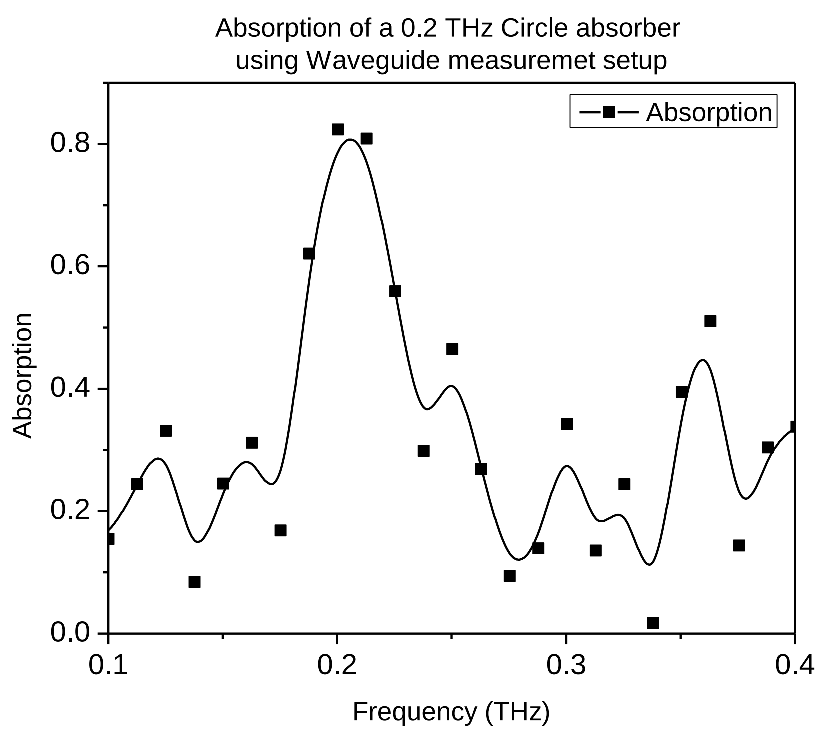

(b)

Figure 3.16 Measured response of a 0.2 THz double layer structure: (a) reference and sample signal, (b) the absorption.

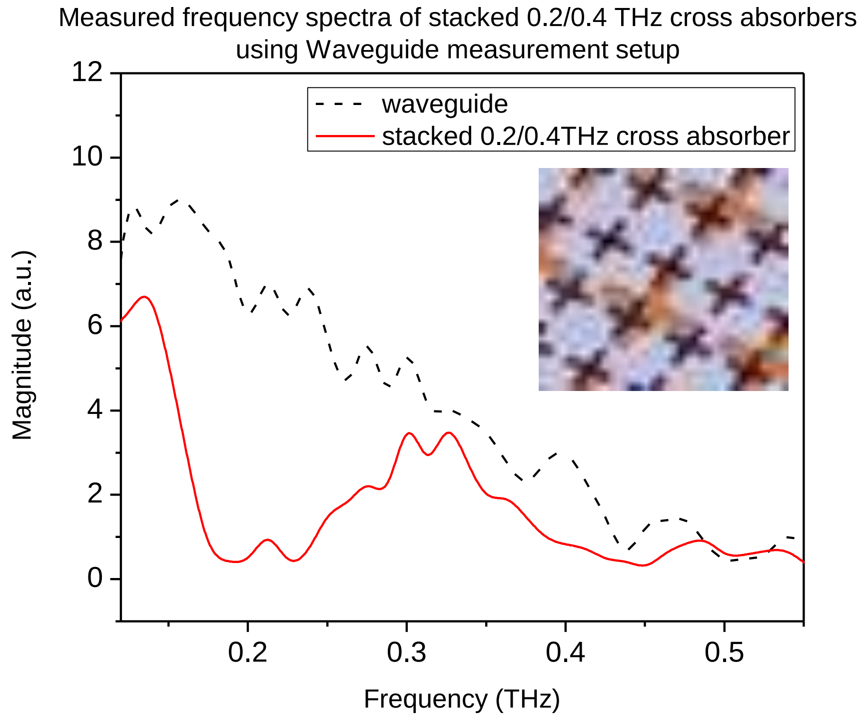

(a)

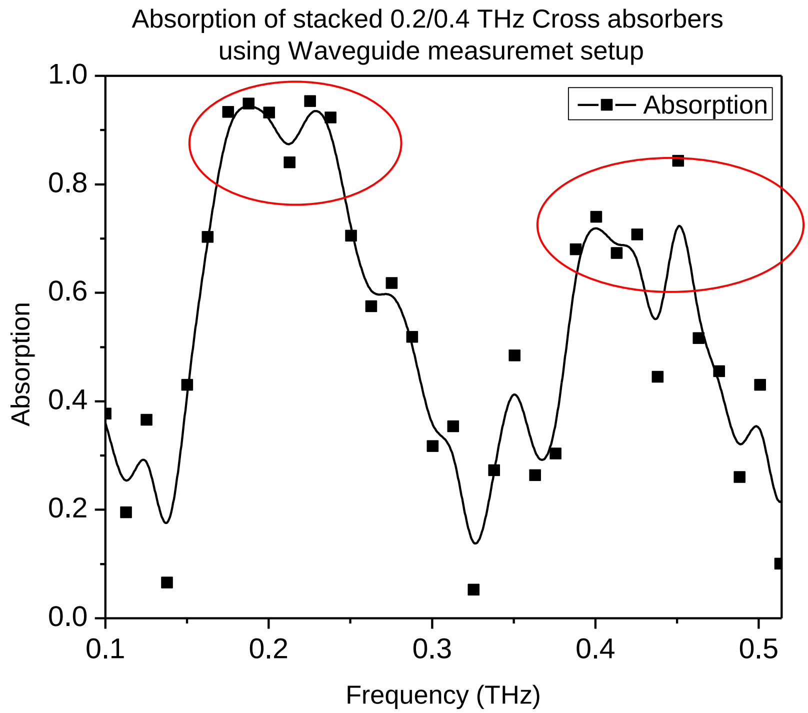

(b)

Figure 3.17 Measured response of 0.2/0.4 THz cross absorber double layer structure: (a) Measured frequency response, (b) the absorption.

3. 7. Conclusions

In this chapter, sets of metamaterial thin-film THz absorbers have been studied through EM analysis, design and fabrication. Designs having strong absorption and ultra-wide bandwidth have been demonstrated. The proposed approach takes advantage of skin-effect losses in order to make high resistivity and wide band metamaterial absorbers. Further increases in bandwidth were demonstrated through multi-stacking of metamaterial absorbers. The results of proposed metamaterial absorbers clearly demonstrate a novel approach to achieve ultra-wide band absorption with strong absorption. THz Absorbers having large FWHM can easily be designed using the proposed approach. The absorbers were tested using two types of measurement setups emulating electronic package environments. These absorbers will find applications in electronics packaging to dampen stray signals inside a package cavity. The proposed designs will also find applications in sensing and imaging applications.

CHAPTER 4. THZ POWER METER

A novel power meter operating over a frequency range of 0.1 to 0.2 THz is presented in this chapter. The power meter utilizes a thin-film metamaterial inspired absorbing layer. This absorber has the desired characteristics such as ultra-wide bandwidth and strong absorption. In a bolometer-like measurement setup, it functions as a wideband high-responsivity THz detector. The absorbing layer consists of a low loss thin dielectric membrane onto which a two-dimensionally periodic, thin metallic layers is patterned. The measured absorption coefficient is above 0.75 at 220 GHz range.

4. 1. Designs and simulations

For the first design, a cross type and Minkowski fractal resonant structure were used and details of these were discussed in earlier chapter. In order to simulate these structures, the Floquet theorem simulation method has been used same as chapter 2. The finite-element method (FEM) by commercially available software Ansoft HFSS® is performed to produce the resonance characteristics and modal field distributions of the proposed structures. The cross type structure is initially studied as planar periodic arrays. In simulation, the metallic element is defined as nickel with 5,000 Å of thickness. The elements of cross type absorber is considered on a 50 μm thick liquid crystal polymer, the length of long arm is 400μm, its short arm is 70 μm, and the gap between the unit-cell is 225 μm.

.

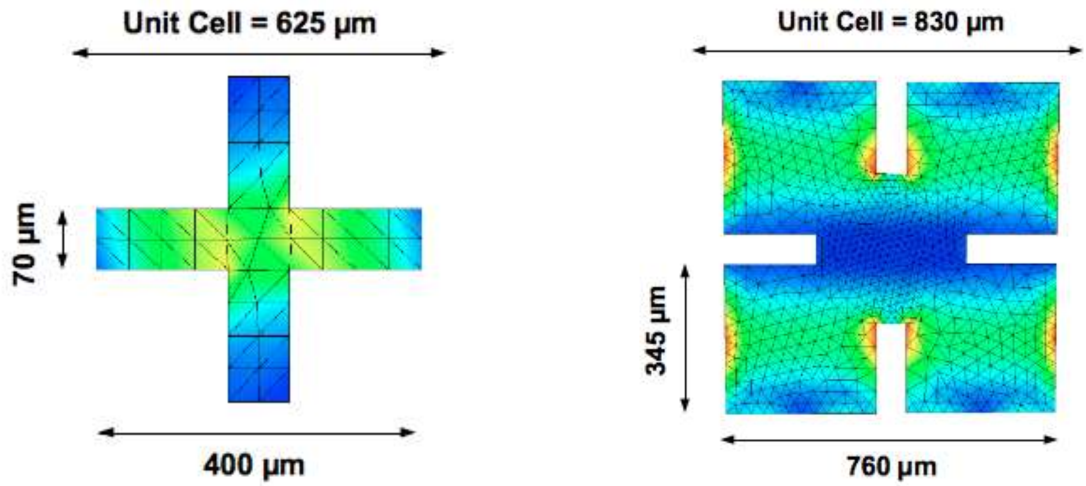

(a) Cross type (b) Minkowski fractal type

Figure 4.1 The layouts and EM field distribution of the bolometers with meta-inspired absorbers.

Figure 4.1 shows the simulated results of a Minkowski structure that is designed to operate at 0.2 THz. The frequency of strong absorption is approximately at 0.21 THz. At this frequency, 9 dB of absorption is attained. It is clear that the absolute density of absorption is higher than 80 % absorption. From simulations, the half power absorbing bandwidth is approximately 60 GHz (between 180 and 240 GHz). The bottom of Figure 4.2 shows simulated *E* and *H*-field distributions for the Minkowski structure as designed for this work. It is clear that strong *E*-field appears at the edge of structure and the EM wave penetrates the space between the metallic layers.

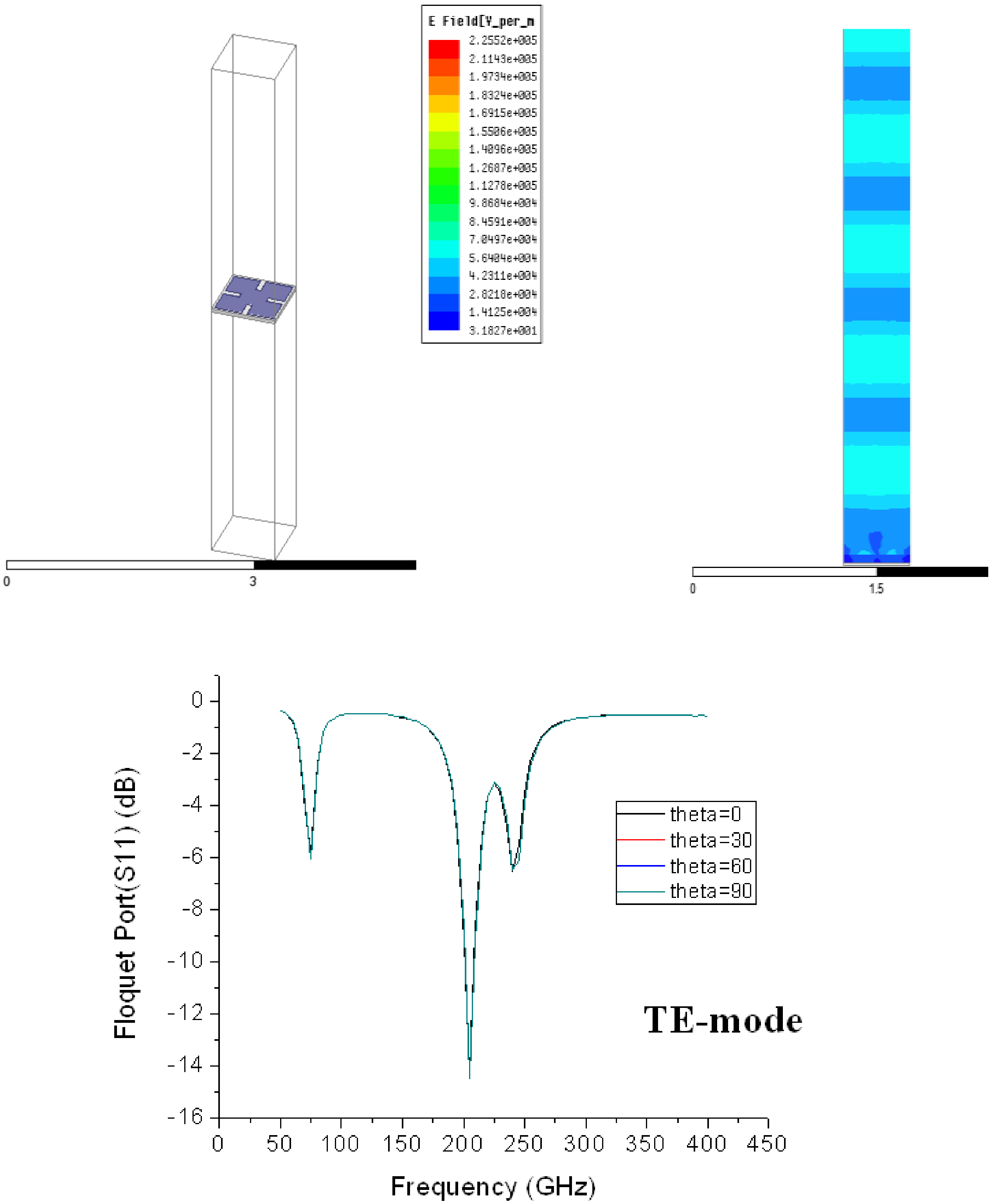

Figure 4.2 Simulation results of a 0.1/0.2 THz Minkowski absorber with various incident angles.

Figure 4.2 (cont'd)

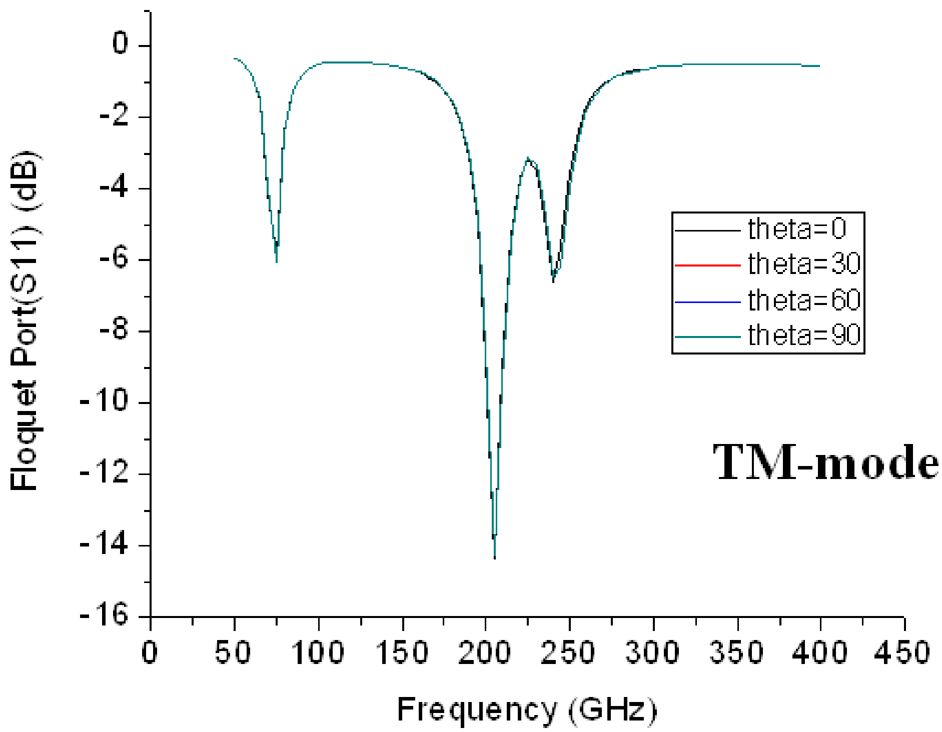

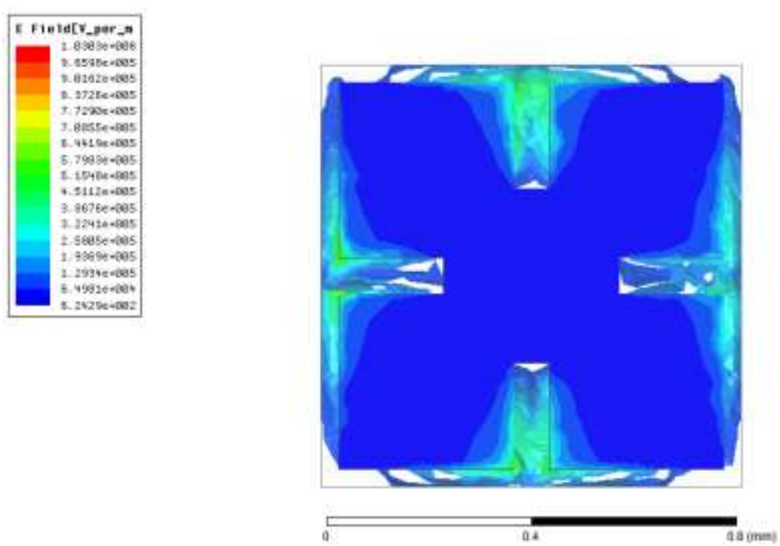

Figure 4.2 (cont'd)

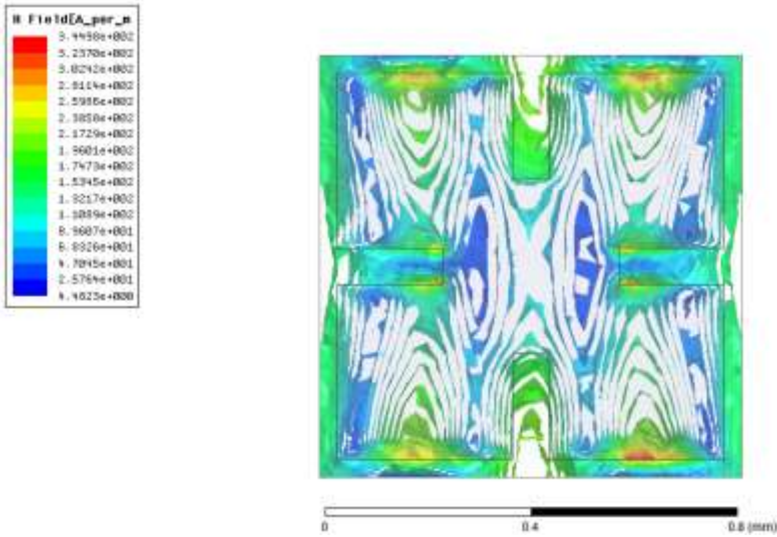

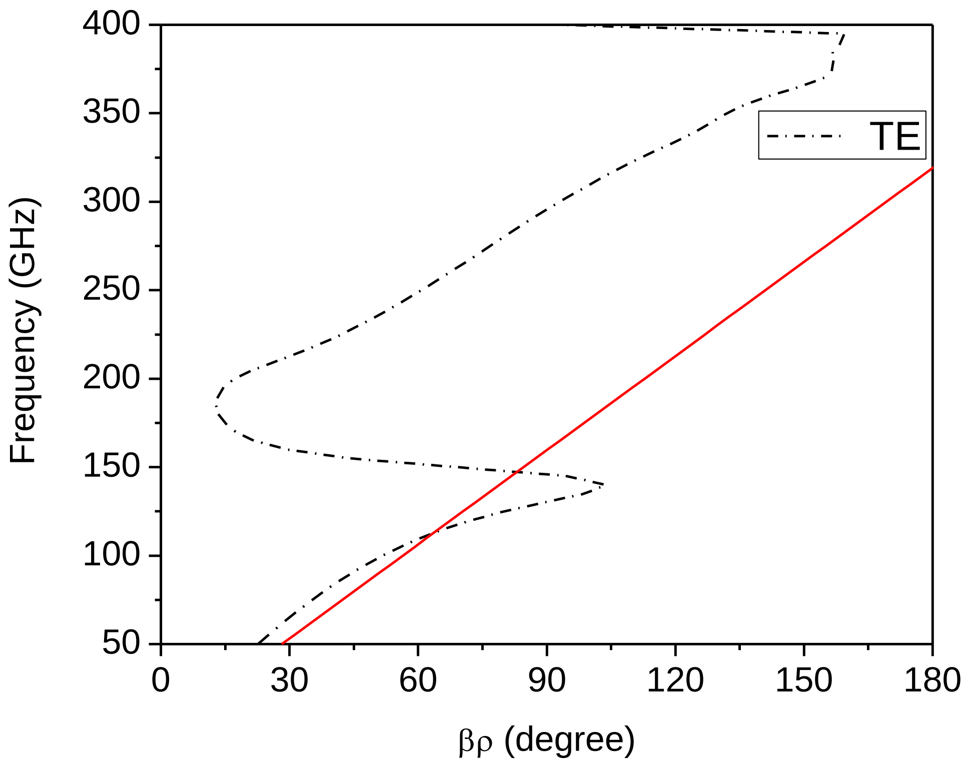

4. 2. Fabrication

The terahertz power meters were fabricated using a conventional micro-fabrication method. These power meters consist of two parts – a bolometer and a cavity. The bolometer is composed of 3-layers, Ni/Ti/Cu; 300, 20, and 300 nm, respectively. This structure was deposited on liquid crystal polymer (LCP) with the thickness of 50 μm. Figure 4.3 shows the fabrication process using conventional microfabrication method and photographs of bolometers composed of the metamaterial-inspried absorber structures. Two variations of the metamaterial unit cell were designed, a regular cross and a Minkowski fractal.

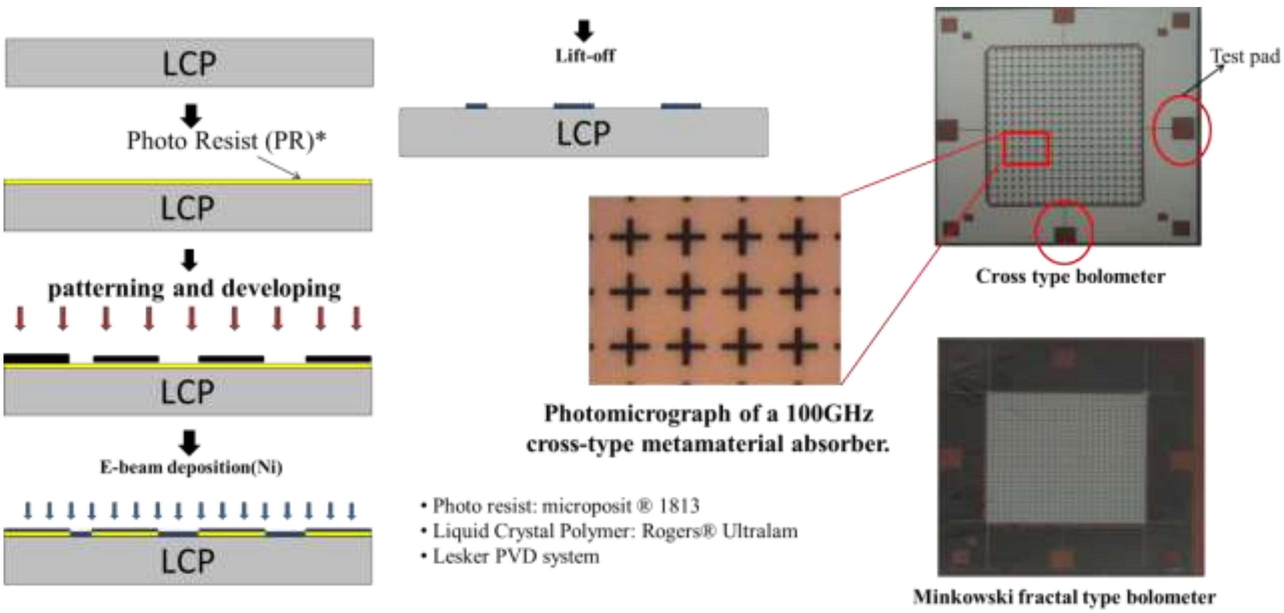

Figure 4.3 Fabrication process of absorbers designed by cross and Minkowski structures.

4. 3. Experimental setup and measurement results

The transmission measurement setup has been used to characterize the 0.1 and 0.2 THz absorbers in this work. Figure 4.4 shows the measured absorptance of proposed bolometers in frequency domain. Figure 4.4 (a) shows a maximum absorptance of 0.48 and strong overall absorptance between 0.065 and 0.18 THz. Figure 4.4 (b) demonstrates the response obtained from a Minkowski fractal type bolometer designed to have a response at two adjacent bands. This configuration produces a second absorption band (0.05 THz up to 0.25 THz). The peak absorptions occur at or around the frequencies of interest (0.05 THz and 0.22 THz). This absorber is proof that multi-band and ultra-wideband absorbing structures can be fabricated and applied to wide-band power detecting on specific frequency ranges that is willing to measure the incident power density.

In order to use it as a bolometer, the resistivity temperature coefficient is normally an important characteristic. Actually, the electrical resistance of a typical metal increases linearly with rising temperature. This is because the surface resistance changes depending on the amount of incident power being converted to heat and in turn change in the resistance of the film. The measurement setup of resistivity temperature coefficient is depicted in Figure 4.5. The thickness of metal deposition is Ni/Ti/Cu; 300, 20, and 300 nm.

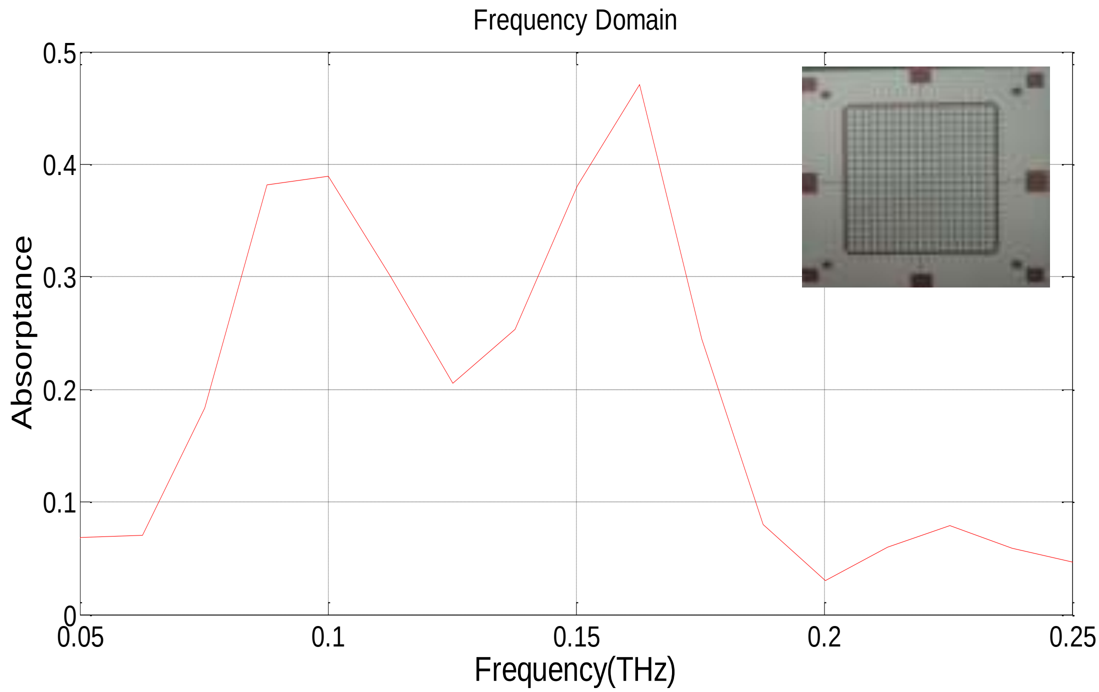

(a). Cross-type bolometer

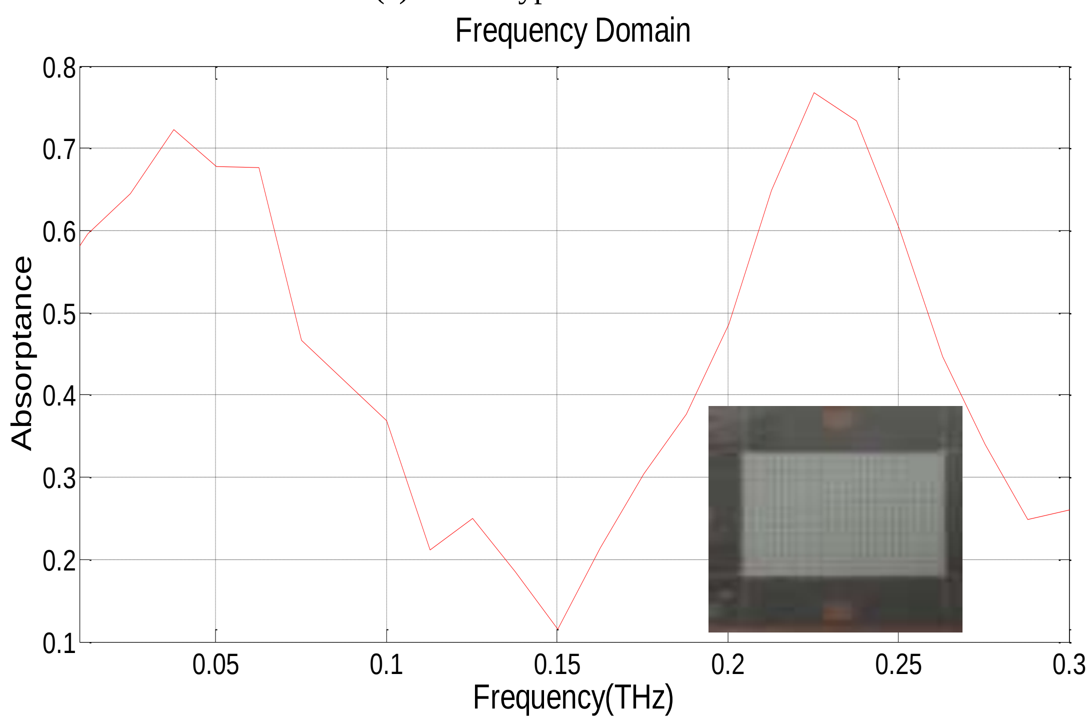

(b). Minkowski fractal type bolometer

Figure 4.4 Measured absorptance of proposed bolometers.

Figure 4.5 shows the measured temperature dependence of Ni film as a function of applied temperature measured by placing the sample in a vacuum oven and regulating the temperature. The temperature of the oven was slowly increased and the allowed to settle down before taking the measurements. A thermometer placed in the oven was used to measure the oven temperature. As the temperature increases, the resistance of the film increases linearly. Table 4.1 summarizes the measured surface resistance of bolometers using a four point probe measurement technique [45, 46].

Table 4.1 Measured resistance of proposed bolometers

Type of bolometer	Resistance(Ω)
Cross(positive)	440 Ω
Cross(negative)	15.2 Ω
Minkowski fractal	52.4 Ω

The bolometer structures were measured using a high frequency source, Backward Wave Oscillator (BWO 75~110 GHz) at 110 GHz. Figure 4.5 shows the layout of the measurement fixture. The periodic structure absorbs the incident radiation which increases the surface temperature of the metallization and increases the resistance of the aggregate structure. This variation in the resistance is measured and used to characterize the performance of the bolometers. In Figure 4.6 (a), the bolometer is located on a thick Styrofoam layer to reduce reflection and mitigate frequency change. Figure 4.6 (b) shows the equivalent circuit of testing schematic including the styrofoam used in decreasing the reflectance [47].

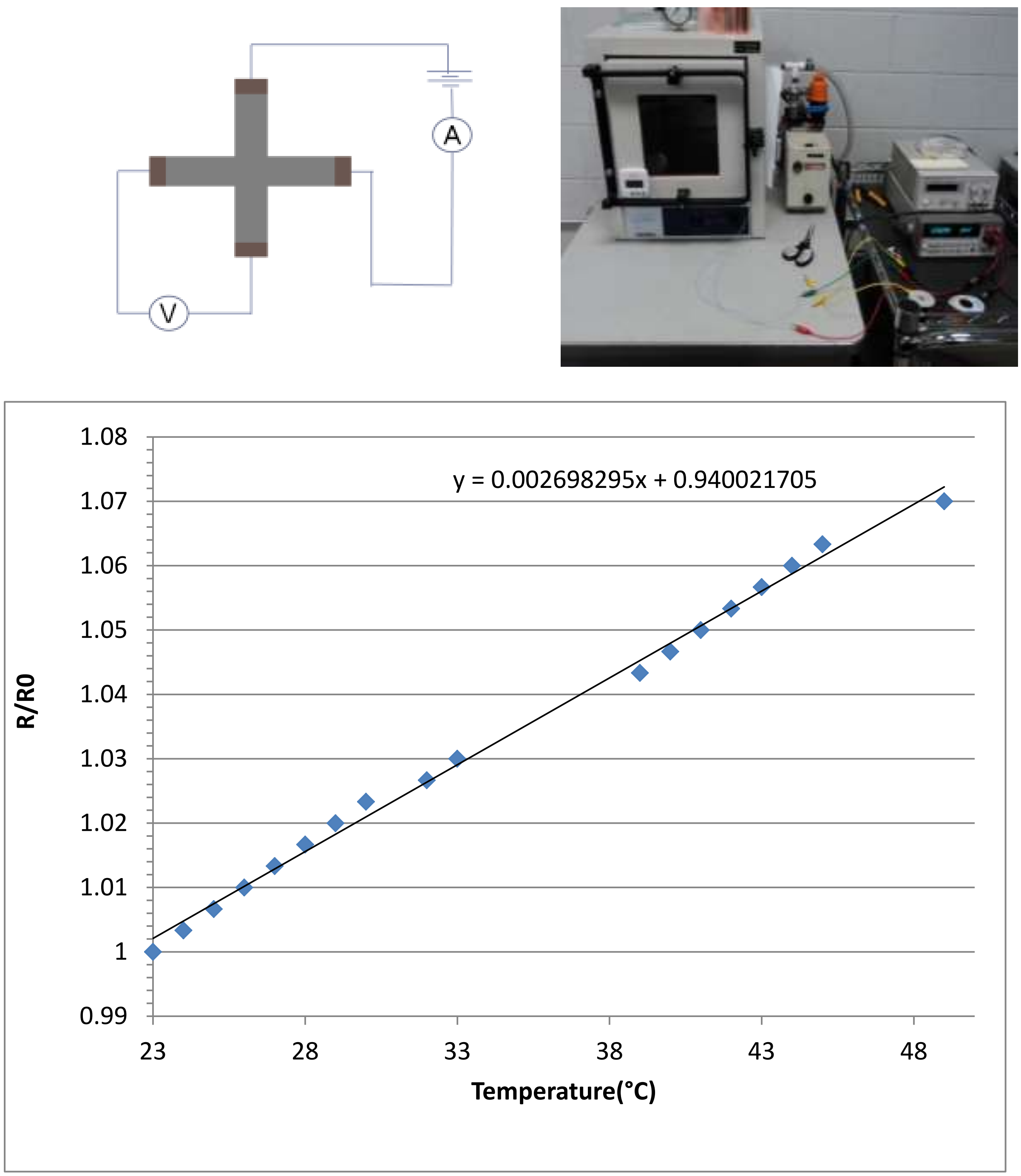

Figure 4.5 Measurement setup and measured result of resistivity temperature coefficient of nickel (Ni).

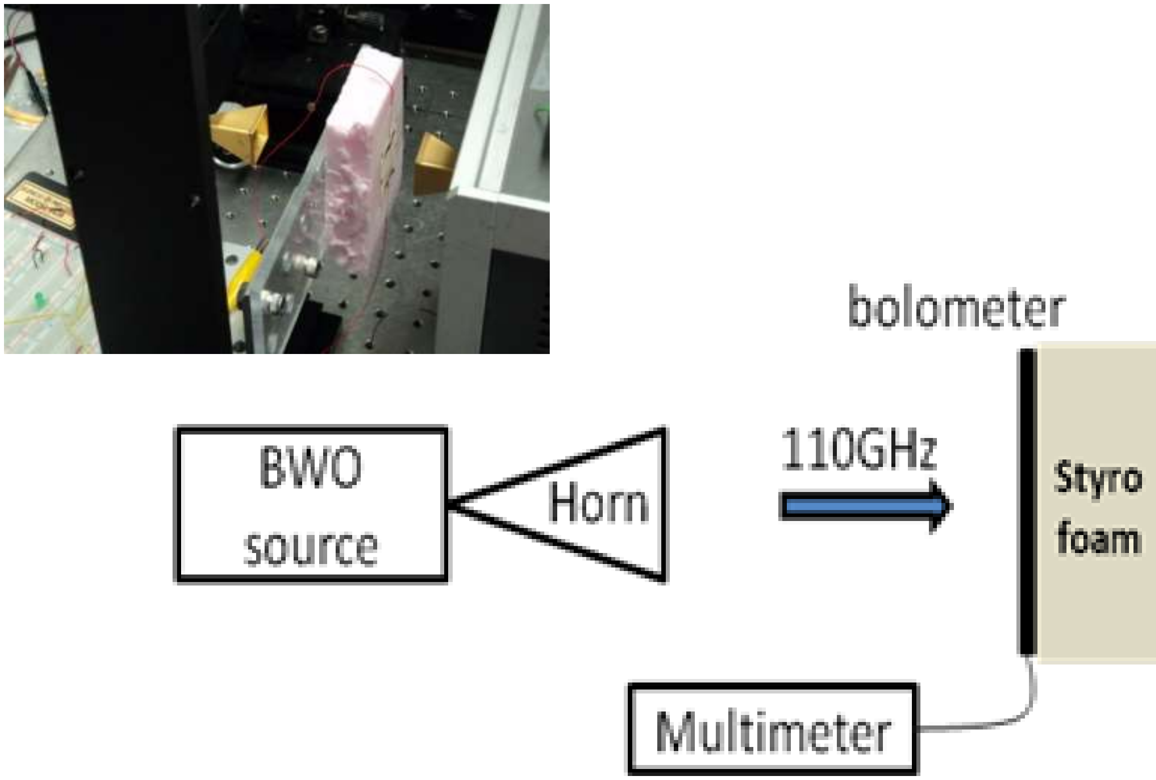

(a)

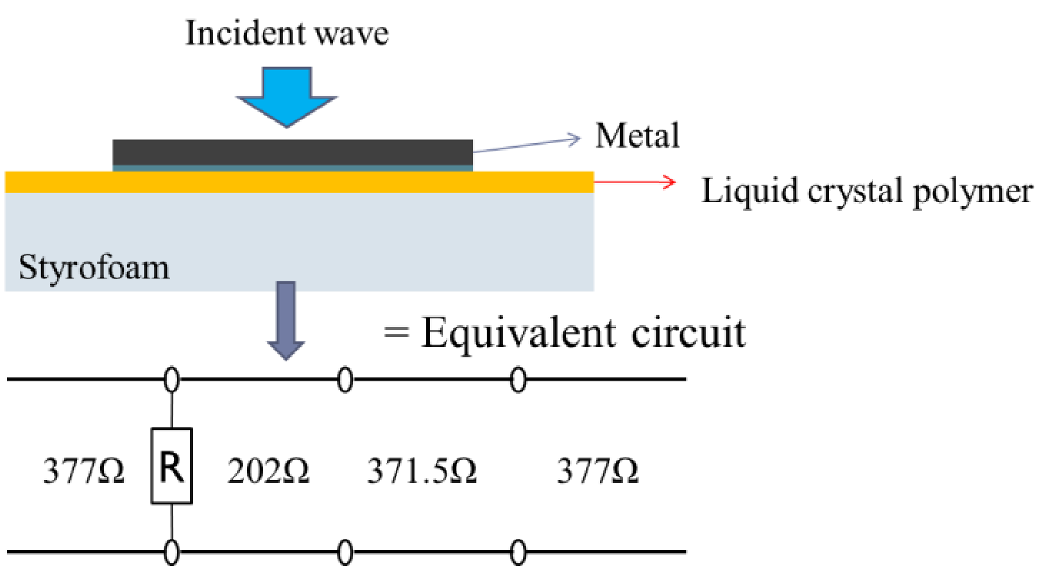

(b)

Figure 4.6 Quasi-optical measuring schematics of the bolometers using a high frequency source.

Also, we measure two different setups, one is a transmission mode which is composed of the bolometer and a styrofoam, thus the receiving power is able to measure. Another measurement is the reflection mode which comprises of the bolometer, a Styrofoam layer, and the cavity. Using this configuration, the density of incident wave arrived at the bolometer can be enhanced due to multi reflection from the cavity [47].

Figure 4.7 demonstrates the resistance variation of the bolometers, as a function of incident power. In transmission mode measurement, the variation slope of the Minkowski bolometer is the steepest among the proposed bolometers. In reflecting mode, the positive cross bolometer is more sensitive than the Minkowski bolometer.

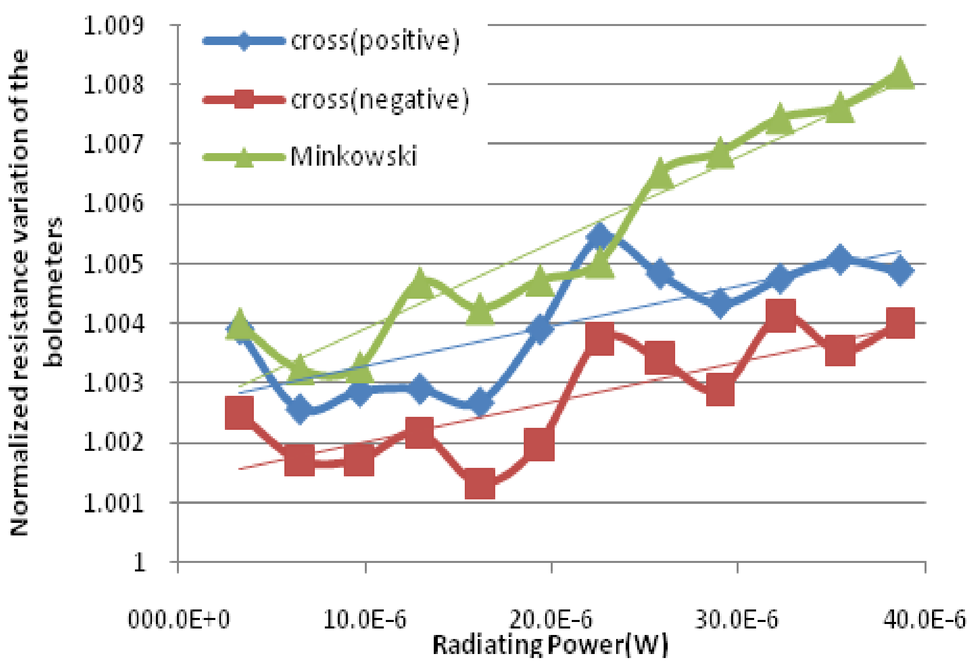

(a) Transmission mode

Figure 4.7 Measured results of normalized resistance variation of the bolometer, (a) Transmission mode, and (b) Reflection mode.

Figure 4.7 (cont'd)

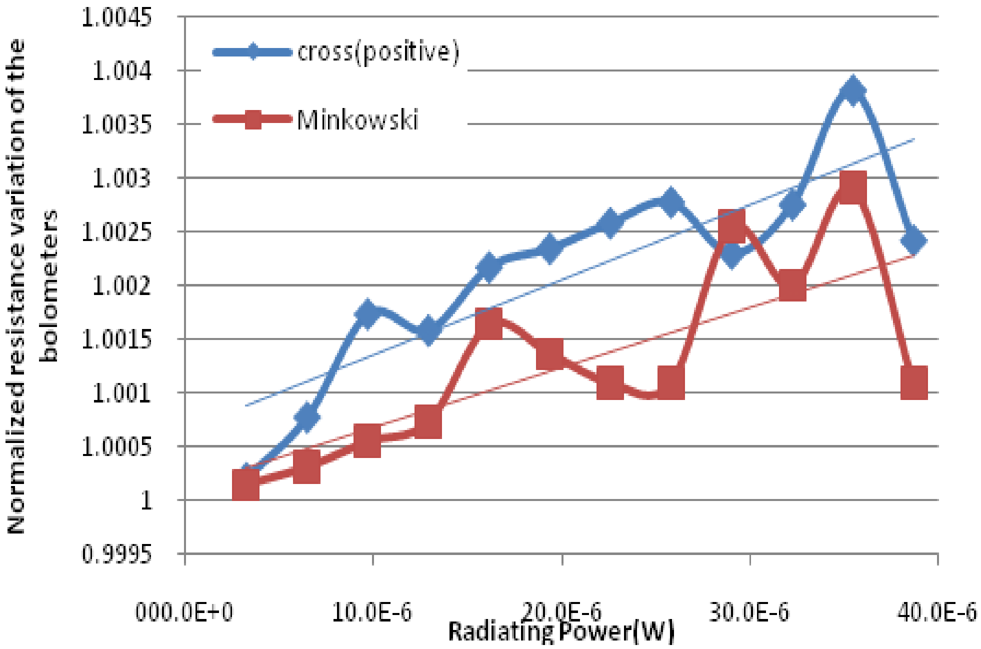

(b) Reflecting mode

4. 4. Conclusions

This chapter demonstrates the design and fabrication of a new class of power meter using metamaterial-inspired thin-film absorbers operating at millimeter and sub-millimeter wavelengths. For a cross-type bolometer, the absorption bandwidth results in approximately 0.12 THz. A Minkowski bolometer shows dual band that can be utilized to measure the power density in a multi-band system. In quasi-optical measurement results, all of proposed bolometers have shown to have high sensitivity due to the characteristic of high surface resistivity by skin-depth effect and absorbing of metamaterial-inspired structures. Compared to conventional power meters wherein the response is achieved purely due to material characteristics, these designs also utilize field enhancement due to resonance of the metallization to achieve enhanced sensitivity. In other words, resonant structures can be designed to directly absorb the incident radiation without resorting to antenna coupling or use of large area structure with back reflectors. The proposed power meters also have several advantages such as low cost, simple fabrication, and easy integration with other monolithic circuits.

CHAPTER 5. TERAHERTZ SURFACE PLASMONICS BULLS-EYE ANTENNA

5. 1. Theoretical background

Recently, plasmonic applications play a significant role in THz regime. THz absorbers introduced and discussed in previous sections basically work as the mechanism related to the THz surface plasmons at metal and dielectrics in frequency selective surfaces. In this chapter, the concept of plasmonic phenomenon will be introduced and the THz antenna, bulls-eyes type, demonstrated and characterized in order to focus the beam to improve the transmitting power to the bolometer that has been applicable to high-resolution imaging of THz spectrum.

Surface plasmon is one of physical phenomena. It is the free electrons oscillation at the boundary between a conducting and a dielectric material. Electromagnetic forces is entrapped at the boundary go with the wavering surface charge density. There is strong coupling between the electromagnetic wave and a charge density oscillation that is called a surface plasmon polariton [48]. Because of the surface charges, the electric fields have components perpendicular to the boundary, while the components of magnetic fields propagate transverse.

When the surface Plasmon travels in the x direction, the electric and magnetic fields in the two materials are described as

$$E_d(r,t) = (e_x E_{d,x} + e_z E_{d,z}) e^{-k_d z} e^{i(k_x x - \omega t)} \qquad 5-(1)$$

$$H_d(r,t) = e_y H_d e^{-k_d z} e^{i(k_x x - \omega t)} \qquad 5-(2)$$

$$E_m(r,t) = (e_x E_{m,x} + e_z E_{m,z}) e^{-k_m z} e^{i(k_x x - \omega t)} \qquad 5-(3)$$

$$H_m(r,t) = e_y H_m e^{-k_m z} e^{i(k_x x - \omega t)} \qquad 5-(4)$$

where E_d and H_d are in the dielectric layer (z > 0), and E_m and H_m in the conductor (z < 0). From these equations, the surface wave is able to be expressed by the wave-numbers k_x, k_d, and k_m for an operating frequency ω. The dispersion relations are derived by the wave equation,

$$\nabla^2 E = \epsilon\mu \frac{\partial^2 E}{\partial t^2} = \frac{1}{v^2}\frac{\partial^2 E}{\partial t^2} \qquad \text{: wave equation}$$

$$k_x^2 - k_d^2 = \epsilon_d \frac{\omega^2}{c^2} \qquad 5-(5)$$

$$k_x^2 - k_m^2 = \epsilon_m \frac{\omega^2}{c^2} \qquad 5-(6)$$

where ε_d and ε_m are the dielectric constants of the dielectric material and metal (all of material are considered nonmagnetic). Merging these two equations, it can be gotten the relation of the ratio k_d/k_m expressed in terms of k_x and ω:

$$\frac{k_d^2}{k_m^2} = \frac{k_x^2 - \epsilon_d \omega^2/c^2}{k_x^2 - \epsilon_m \omega^2/c^2} \qquad 5-(7)$$

Applying Maxwell's equation, it can be obtained the relations between E_x and H_y:

$$H_{d,y} = -i\epsilon_0 \frac{\epsilon_d \omega}{k_d} E_{d,x} \qquad 5-(8)$$

$$H_{m,y} = -i\epsilon_0 \frac{\epsilon_m \omega}{k_m} E_{m,x} \quad 5-(9)$$

E_x and H_y , which are parallel with the surface, propagate at the boundary continuously. The boundary conditions are set as

$$\frac{\epsilon_d}{\epsilon_m} = -\frac{k_d}{k_m} \quad 5-(10)$$

Substituting Equation 5-(10) into Equation 5-(5) and (6), the dispersion relation of surface plasmons can be derived,

$$k_x = \frac{\omega}{c}\left(\frac{\epsilon_d \epsilon_m}{\epsilon_d + \epsilon_m}\right)^{1/2} \quad 5-(11)$$

5. 2. Metallic Bulls-eye antenna

5.2.1 Design and simulation

It is well known that the transmission of electromagnetic waves can be enhanced when passing through subwavelength apertures at optical frequencies [49-55]. This is due to the constructive interference of resonating plasmonic modes [50]. These transmitted modes can be modified both spatially and temporally through hole arrays and periodic structures. Such systems produce enhanced, narrow-beam transmission while requiring only single wavelength geometric sizes [49, 53-55]. These apertures can be combined with gratings to couple incident electromagnetic radiation and enhance their transmission properties even further.

Numerous such plasmonic grating designs have been proposed, many of which are easily translated to the terahertz frequency spectrum [59]. In fact, several subwavelength aperture works have been published operating at terahertz frequencies [59-62]. The majority of these systems involve surrounding a central subwavelength aperture with concentric grooves, forming a spoof-surface plasmon antenna or bulls eye structure. The grooves redirect incident electromagnetic radiation toward the subwavelength aperture by exciting surface waves in the form of surface plasmons [55]. These waves are then transmitted through the aperture at enhanced levels with subwavelength focusing [49, 51 - 55]. This signal can be further shaped through the inclusion of a reciprocal grating on the backside of the system. The major advantages of the bulls eye system selected include its simpler fabrication, its planar structure, its relatively polarization-independent performance, and its behavior at terahertz frequencies spectrum is well known [60 -62].

Recently, this bulls eye structure was paired with a microbolometer for the sensing of terahertz electromagnetic waves [63]. Here the vanadium bolometer sensor was replaced with a metamaterial-inspired structure tuned to the plasmonic frequency of the bulls-eye [44, 64]. This structure is simpler to fabricate and provides high sensitivity. The incoming THz radiation is focused onto the bolometer elements using the surface plasmon antenna. The THz radiation absorbed by the metamaterial bolometer element is converted into heat which in turn heats the bolometer film. The resistance of the bolometer film is sensitive to temperature and its change in resistance is proportional to the power of the incoming signal. A THz image is formed by measuring the change in resistance at each pixel forms its reference. This coupled system is expected to not only capture a large percentage of the incident electromagnetic radiation, but also efficiently convert this energy to electrical signals at the desired frequency band.

The system was numerically simulated in stages using both finite difference and finite element electromagnetic models. First, the bulls-eye structure was characterized for its transmission properties. Then, the metamaterial bolometer was simulated for its frequency response. Three-dimensional finite element simulations were performed using the commercial software package, High Frequency Simulation Software (HFSS) at the nominal operating frequency of 100 GHz. Plane wave excitation from the top side of the bulls-eye structure was applied. Radiation boundary conditions were applied to all other domain edges. The resulting electric field plots are provided below in Figure 5.1. The wave travels along the grating and groove and travels through the centered aperture, finally converging to a small focal point.

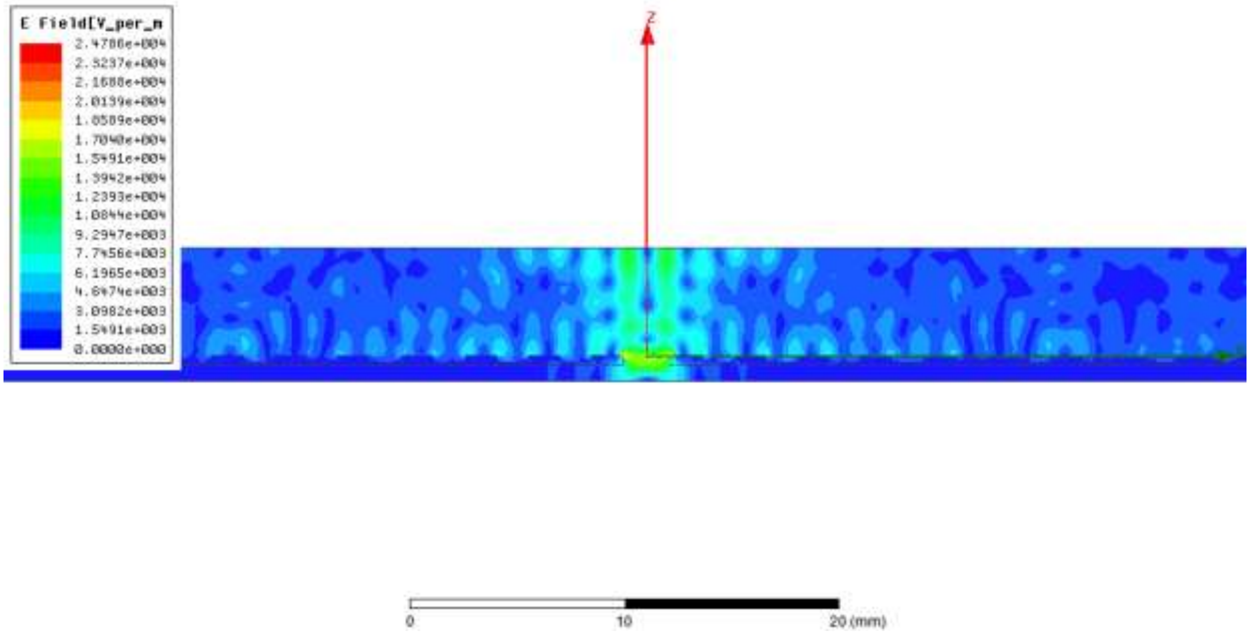

Figure 5.1 HFSS simulation result of Electromagnetic field distribution in the bulls eye structure.

This system was also numerically investigated using a two-dimensional finite-difference time domain (FDTD) simulation. Here, a consistent grid spacing of 20 μm was applied in both directions, with a Gaussian weighted exciting wave in the frequency domain. The metal structure was assumed to be a perfect electric conductor. Ten perfectly matched layers surrounded the simulation domain boundaries. Plots of the temporal and frequency domain transmitted transverse electric fields are presented in Figure 5.2. It is clear from these images that plasmonic modes reside above the bulls-eye structure and travel toward the aperture, while the transmitted field is tightly focused.

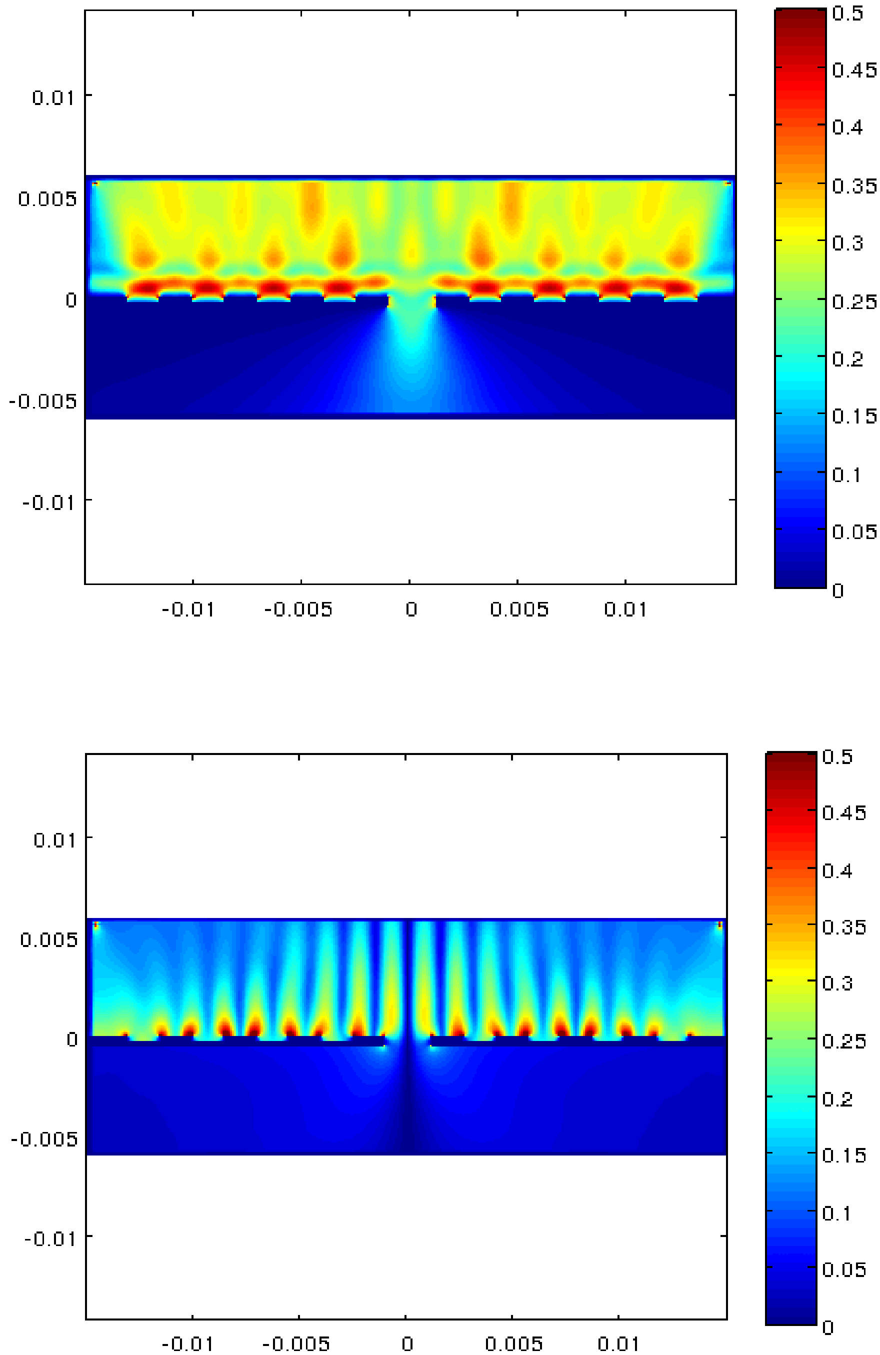

Figure 5.2 Simulated transverse electric field by FDTD.

Figure 5.3 shows the response of the plasmonic structure in both frequency and time domains. The temporal signal demonstrates the transmitted signal that is strongly dependent on the number of groove periods present. This highly periodic temporal signal leads to an enhanced frequency response at the designed frequency of slightly less than 100GHz. Moreover, the relative frequency response shows an increased response.

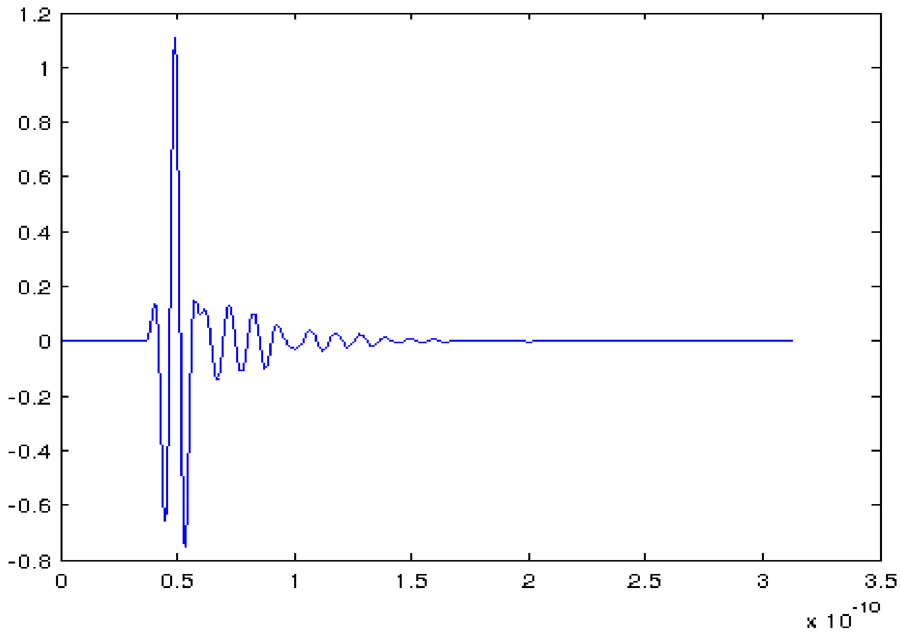

(a)

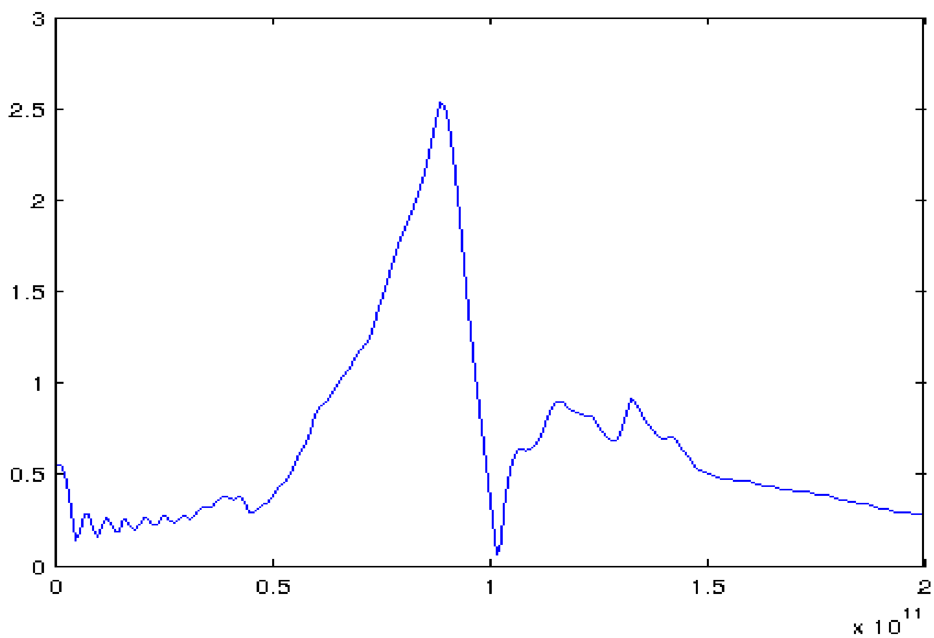

(b)

Figure 5.3 The simulation results of the bulls eye structure in time and frequency domain using FDTD. (a) Time-domain transmitted signal, (b) frequency domain transmitted signal, (c) transmitted signal (dB), and (d) incident Gaussian signal.

Figure 5.3 (cont'd)

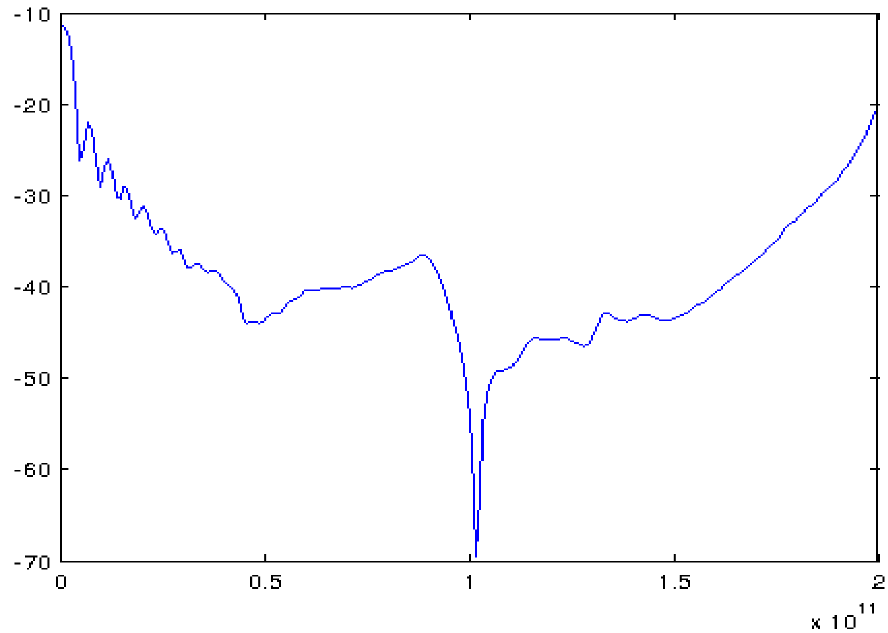

(c)

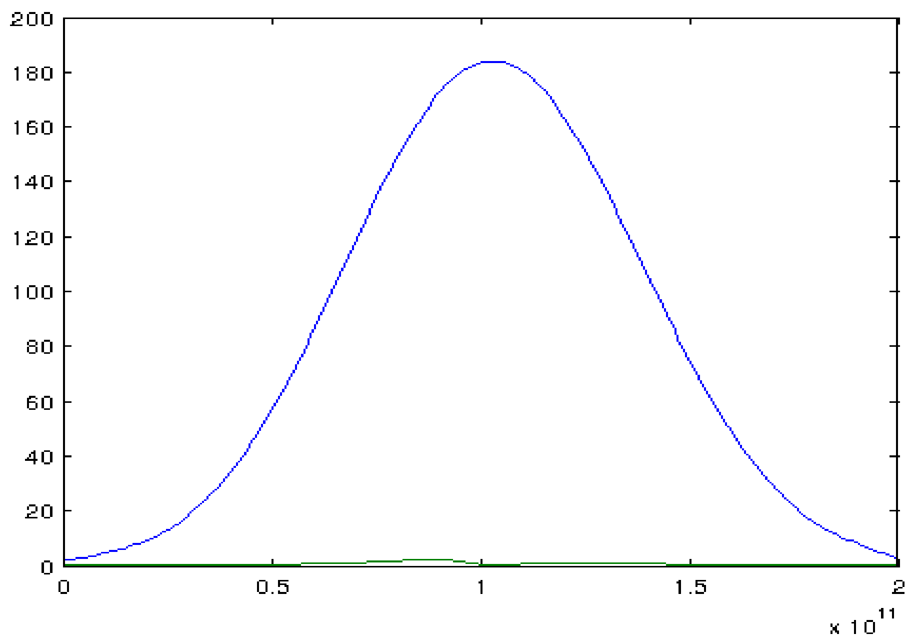

(d)

5.2.2 Fabrication

The surface Plasmon-assisted terahertz image array is composed of two-parts; the bulls eye plasmon-assisted antenna, and the metamaterial-inspired bolometer. The fabrication of these components will be described separately.

5.2.2.1. Layout of the surface plasmon-assisted THz imaging array

Figure 5.4 shows the schematic of the bulls-eye plasmon-assisted antenna. The period and width (w1 and w2) of the grating is designed to match a half wavelength at the operating frequency. The diameter (D) of the center aperture was set as three quarters of this wavelength. The detailed physical dimensions are summarized in Table 5. 1.

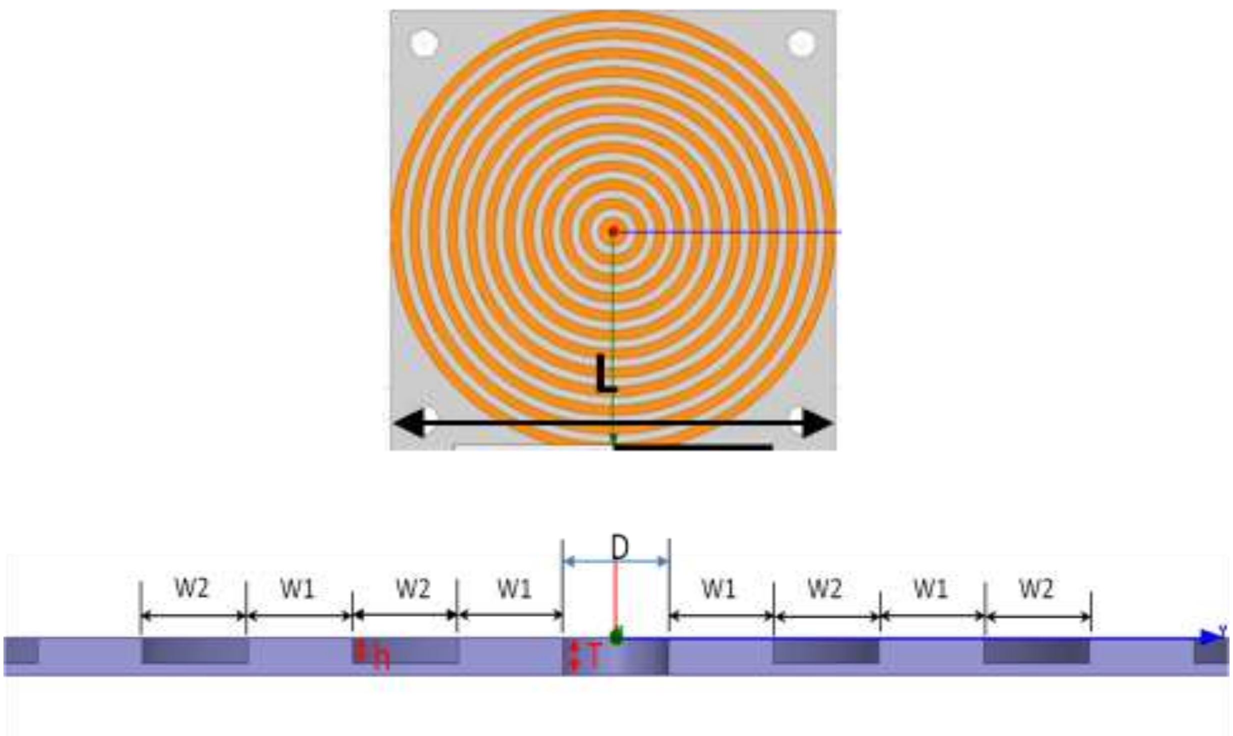

Figure 5.4 Schematics of the bulls-eye spoof plasmon antenna.

Table 5.1 Physical dimensions of the bulls-eye plasmonic-assited antenna

	Bulls-eye antenna structure	
	100 GHz	300 GHz
Width (W)	1.5 mm	0.5 mm
Diameter (D) of the aperture	2.25 mm	0.75 mm
Depth of grooves (h) and the aperture (T)	h= 300 µm	h= 100µm
	T= 450 µm	T= 150µm

5.2.2.2. Metamaterial-inspired bolometer

The metamaterial-inspired bolometer is based on design in [44, 64]. Figure 5.5 illustrates the layout and the dimensions of the metamaterial-inspired bolometer designed for operation at THz frequencies. The Minkowski fractal type pattern has been known to work at multi-band and wide band frequency ranges as a power meter [61-64].

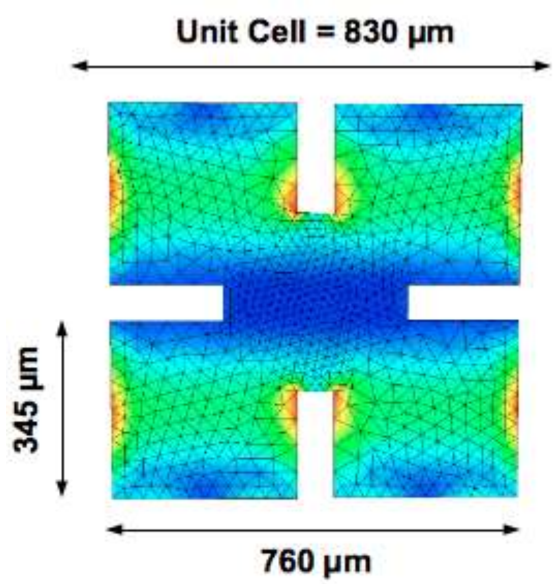

Figure 5.5 Schematic of a Minkowski fractal that forms a unit cell of a bolometer (Shown are the field strengths at resonance frequency).

5.2.2.3. Fabrication of the bulls-eye plasmon-assisted antenna

The bulls-eye plasmon-assisted antenna was fabricated using conventional metal-etching micro-fabrication process. A high purity copper plate was chosen as the base substrate for the bulls-eye structure fabrication. After photoresist patterning the Cu-plate was wet etched. Figure 5.6 shows photograph of a fabricated structure.

Figure 5.6 Photograph of the Bullseye Plasmonic-assisted antenna (100 GHz design).

5.2.2.4. Fabrication of the metamaterial-inspired bolometer

The metamaterial-inspired bolometers were fabricated using conventional micro-fabrication methods. The bolometer is composed of 3-layers, Ni/Ti/Cu :: 300/20/300 nm, respectively. Titanium (Ti) enhances adhesion, nickel (Ni) is the absorbing and the resistance layer, and Cu was used on the pad regions. This structure was deposited on a 50 µm thick liquid crystal polymer (LCP) substrate. Details of bolometer detector are discussed in [64]. Figure 5.7 shows photograph of a fabricated bolometer composed of an array of Minkowsi structures.

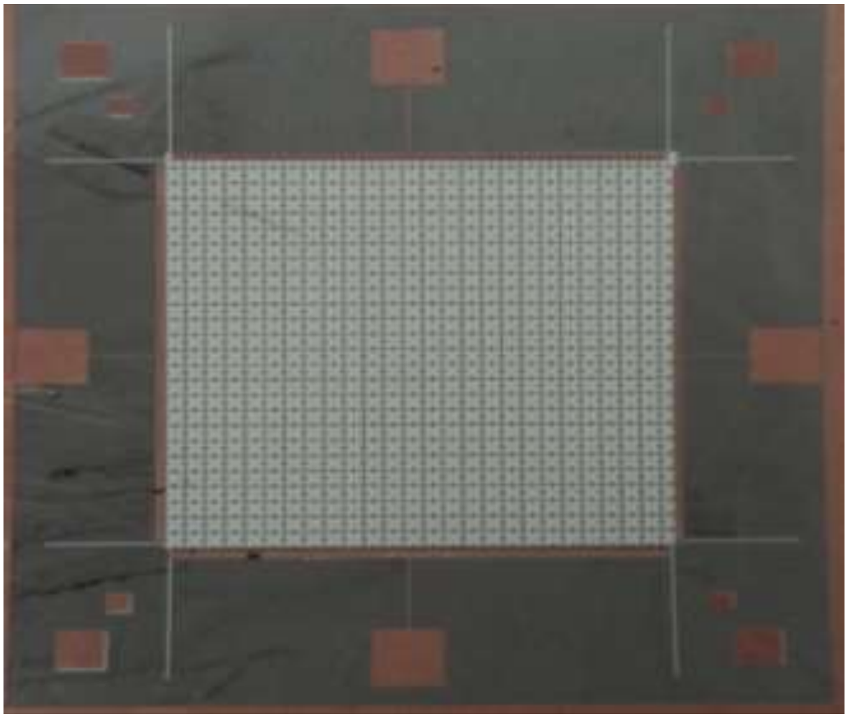

Figure 5.7 Photograph of a Minkowski fractal type metamaterial bolometer.

5.2.3 Experimental setup

In order to characterize the surface plasmonic-assisted image array, time domain and frequency domain measurement systems were both used. A time domain system, Picometrix T-ray 2000 THz time domain system (TDS) fitted with both a receiver and transmitter was used for the measurements of the bolometer and the bulls-eye plasmonic-assisted antenna. This measurement system provides a frequency resolution of approximately 2 GHz [44]. The transmitter radiates a collimated electromagnetic pulse beam in the direction of the receiver. The time domain setup excites an electromagnetic wave impinging normally upon the device under test. Using this setup, the characteristics of the bulls eye plasmonic-assisted antennas and metamaterial-inspired bolometers were measured. A block diagram of the time domain measurement setup is provided in Figure 5.8.

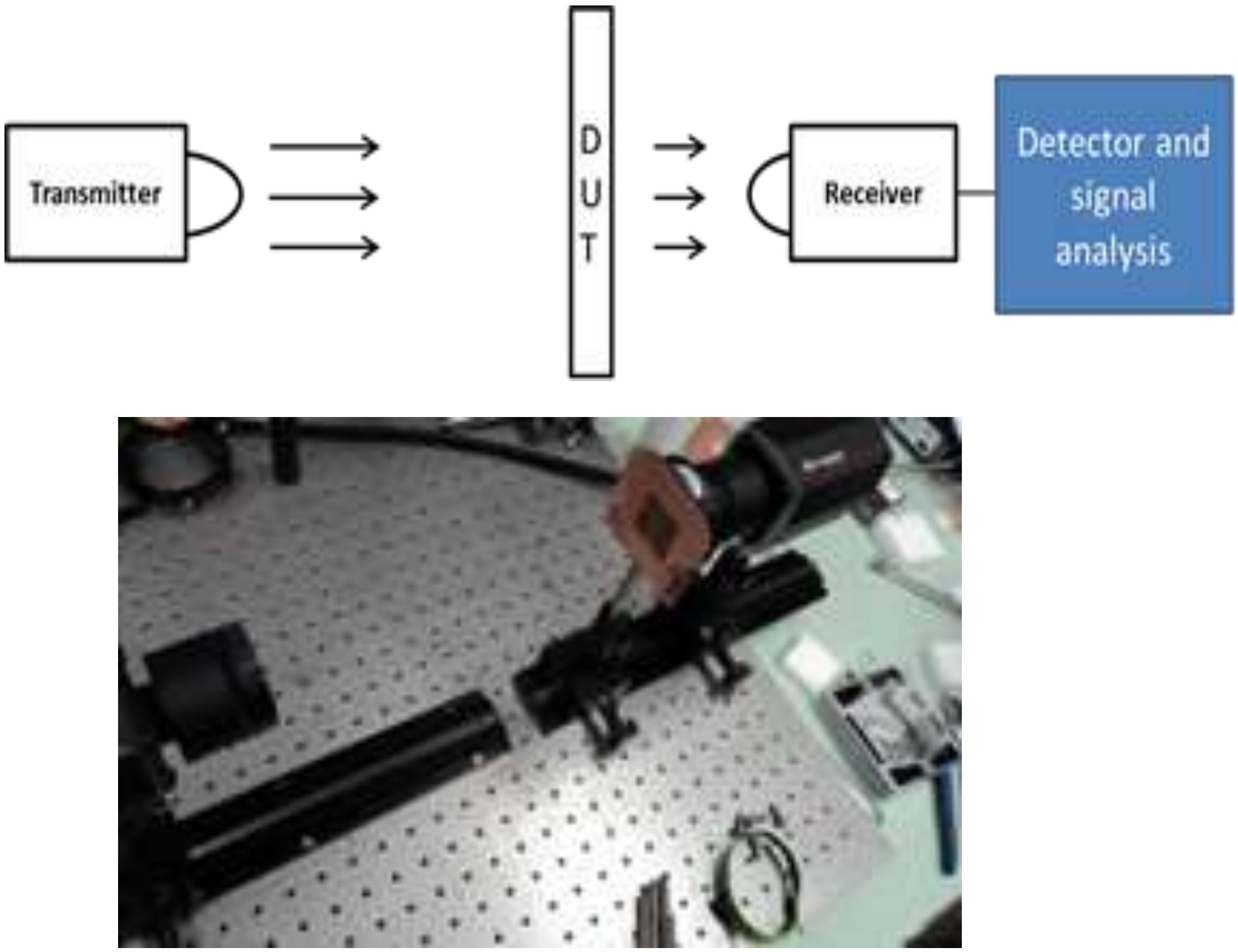

Figure 5.8 . Block diagram and photograph of the time domain measurement setup.

The frequency domain measurement setup is comprised of a spectrum analyzer and a W-band (75 – 110 GHz) backward wave oscillator (BWO). The measurement setup used is similar to a setup used in far-field test of the antenna radiation pattern [65]. In order to generate a plane wave, the transmitter and receiver were positioned within the far-filed range associated with a W-band reference horn antenna (HPBW=12°). Furthermore, to extract the properties of the plasmonic-assisted pattern, a reference signal was obtained from a pin hole of similar diameter as the bulls-eye aperture and the same metal thickness (T). Based on the measurement of the bulls-eye antenna and pin-hole, the performance of plasmonic assisted pattern may be estimated. Figure 5.9 shows the experimental setup for the frequency domain measurement system. A 3-axis manipulator was used to align the boresight of the bulls-eye plasmonic-assisted antenna.

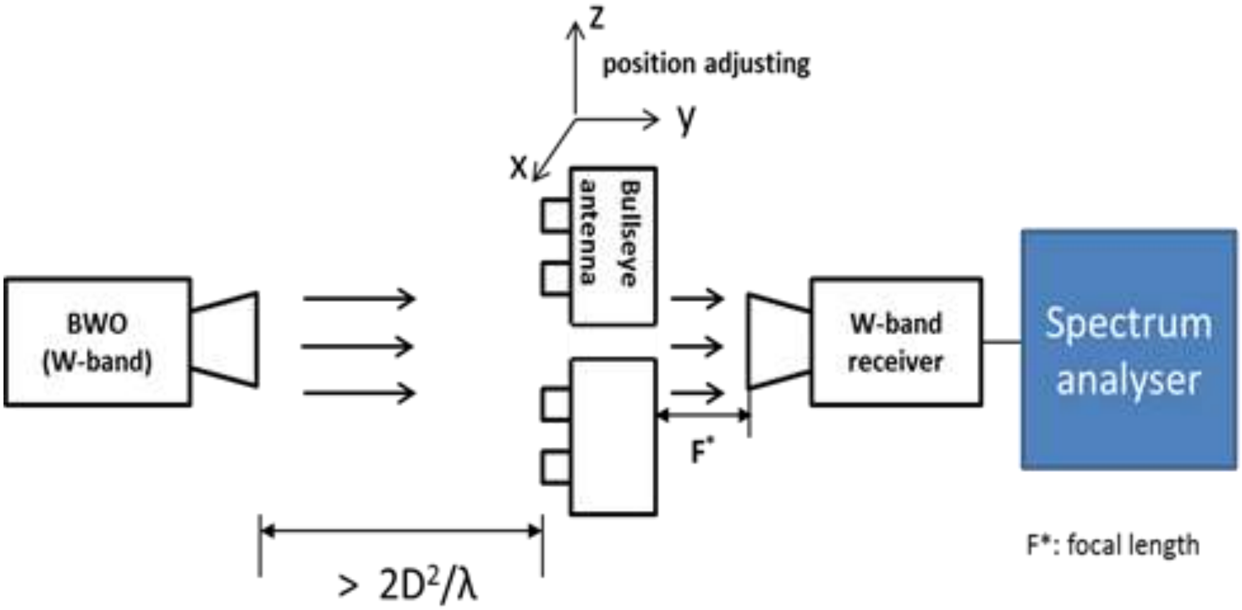

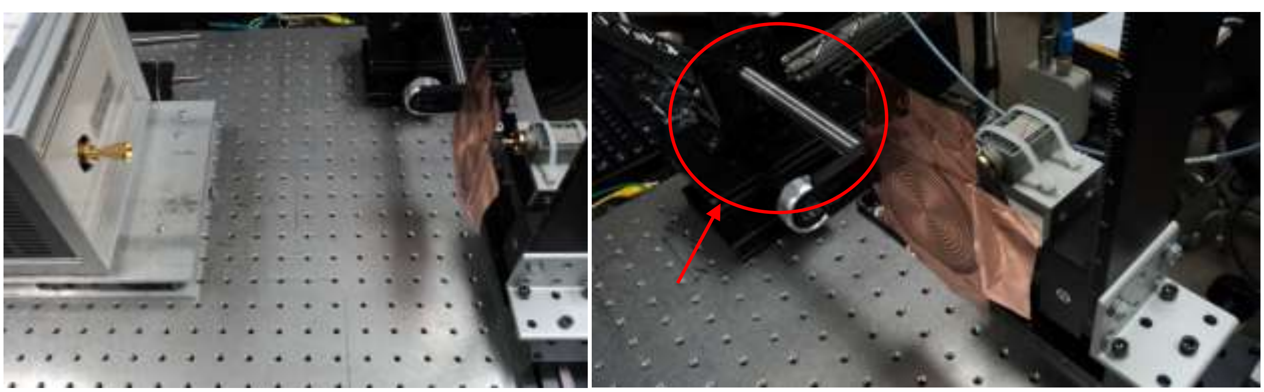

Figure 5.9 Configurations of the frequency domain measurement setup.

5.2.4 Measured results

5.2.4.1. Characterization of the bulls-eye plasmonic antenna

To verify the performance of the bullseye plasmonic-assisted antenna, the antenna was measured in both time and frequency domains. Figure 5.10 shows the characteristics of 100 GHz bulls-eye antenna in the time domain. The measured result demonstrates that the maximum transmitted frequency occurs at approximately 95GHz. Figure 5.11 shows the measured results of the reference (no antenna) and transmission antenna and pin-hole at 96 GHz. In the frequency domain, the received signal from the bulls-eye plasmonic-assisted antenna is measured -45.3 dBm and that of the pin-hole is -57.3 dBm. Background noise floor is roughly -71 dBm.

These measurement results were then converted to the signal to noise ratio (SNR). This was done by subtracting the SNR of the pin-hole from the SNR of that shown in Figure 5.12. The SNR of the bulls eye antenna is significantly higher than the pin-hole structure (approximately 16 times at 96 GHz).

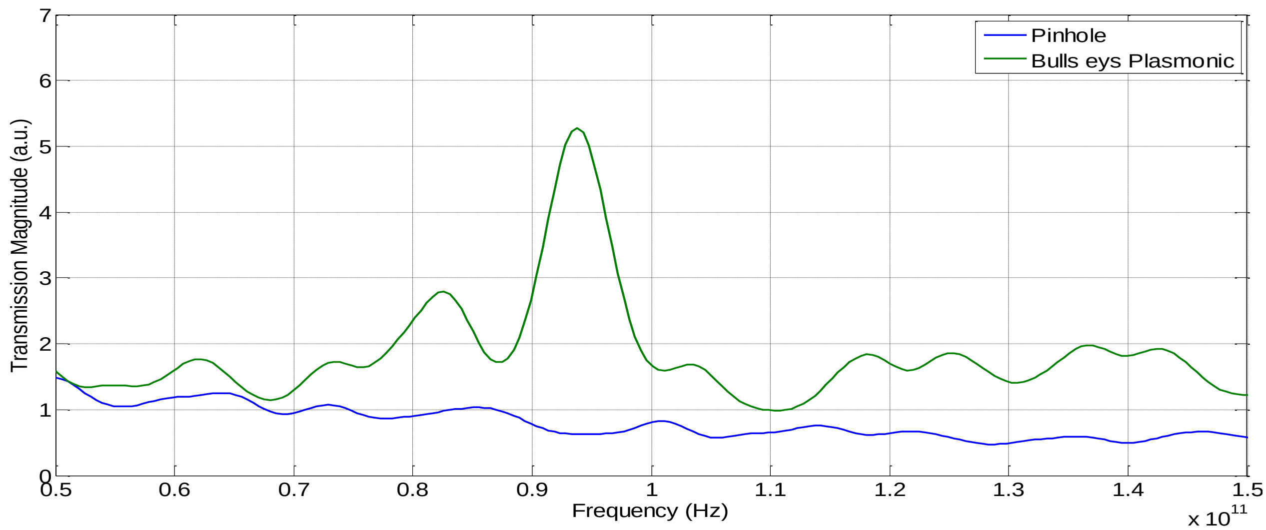

Figure 5.10 Measured results of the bulls-eye plasmonic-assisted antenna using the THz time domain measurement system.

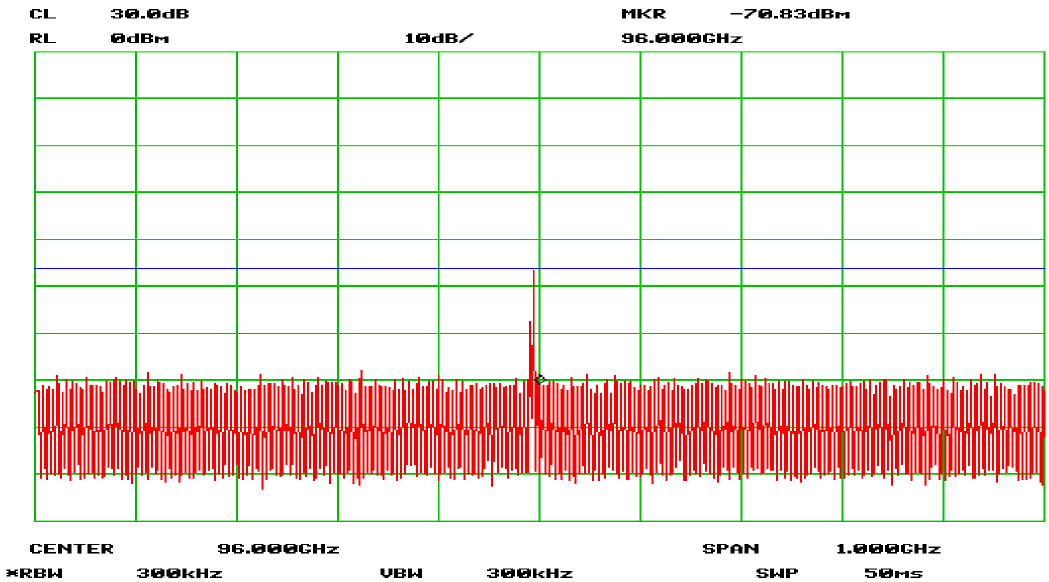

(a)

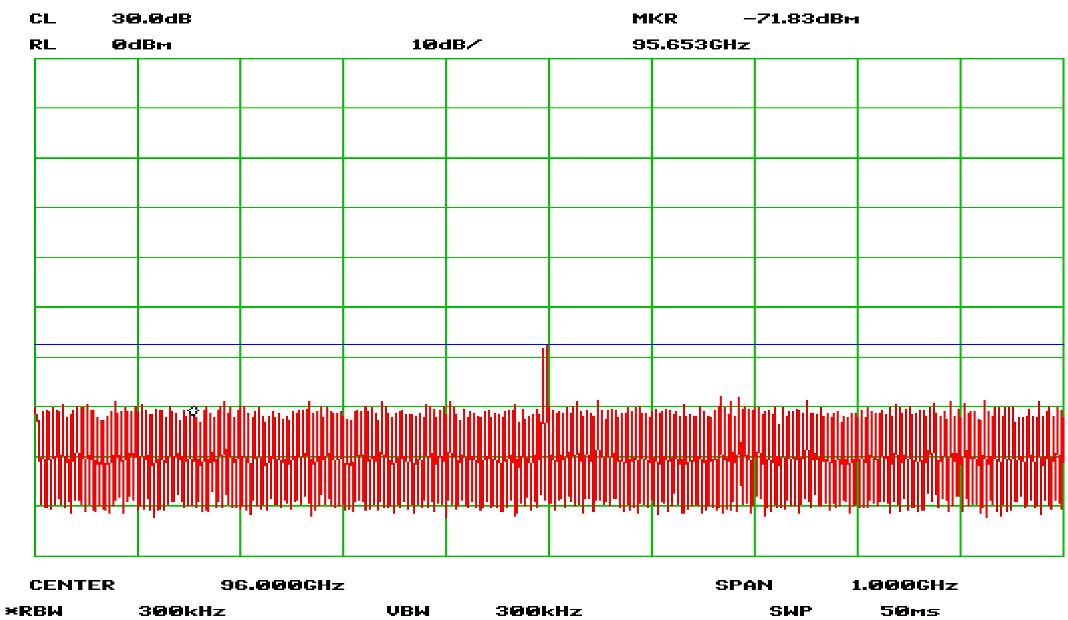

(b)

Figure 5.11 (a) Transmitted signal through the bulls-eye plasmonic-assisted antenna characterizing at 96 GHz (-45.3 dBm); (b) transmitted signal through a reference pin-hole (-57.3 dBm). Noise floor: -71 dBm at BW: 1 GHz.

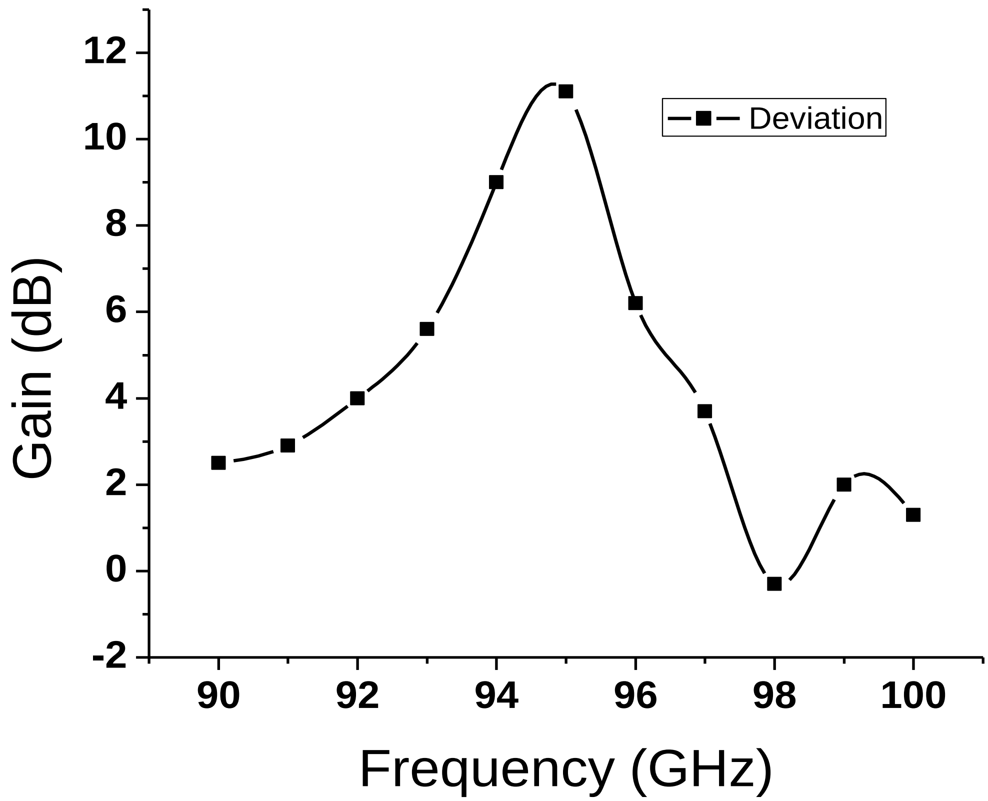

Figure 5.12 Measured signal to noise ratio (SNR) of the bulls eye structure relative to the pin hole.

5.2.4.2. Measurement results of the proposed 100 GHz imaging array

In order to further characterize the bull's eye structure, the structure was coupled to a bolometer structure. This allows in direct measurement of the transmitted power. Figure 5.13 illustrates the test setup. The bolometer structure is closely placed (~ 0.5 mm) near the aperture. A W-band antenna coupled harmonic mixer was used to calibrate the incident power from the BWO. This was carried out prior to the placement of bull's eye and bolometer structures. Figure 5 .14 shows the measured change in resistance of the bolometer as a function of frequency of the incident signal on the bull's eye structure. The measured results show a maximum detection at 96GHz. This measurement shows that the bull's eye structure can be used as a narrow band antenna. Also, it can be closely coupled to the bolometer structure while avoiding thermally loading the bolometer. The bolometer is compatible with planar fabrication and thus can be utilized in the fabrication of bolometer based THz imaging array.

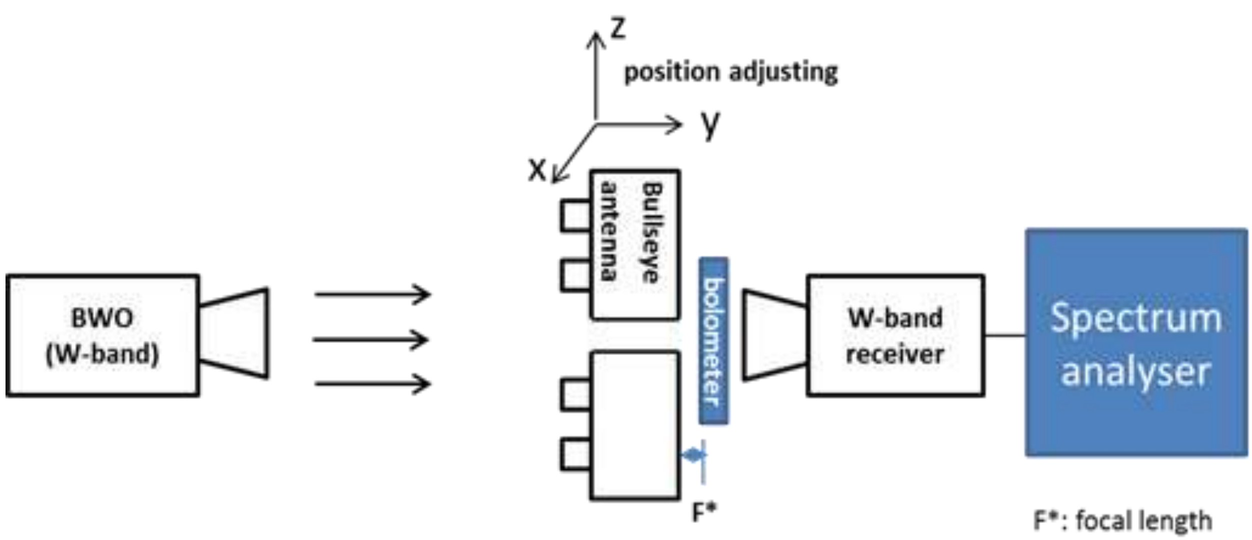

Figure 5.13 Diagram of the measurement setup for Image array.

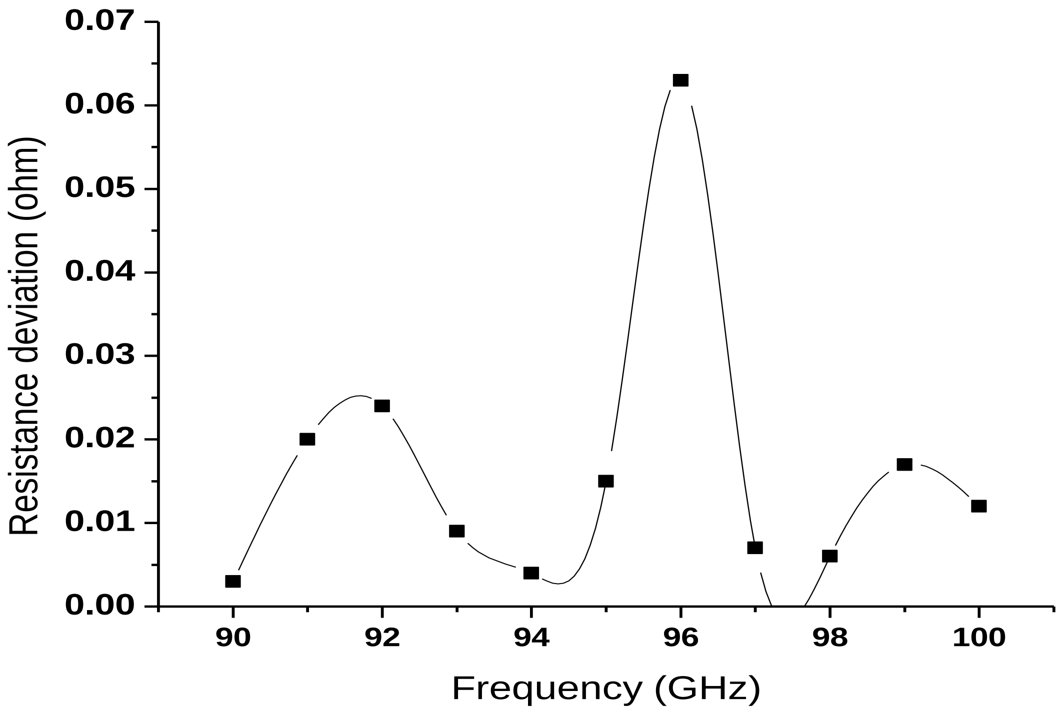

Figure 5.14 Measured resistance deviation of the bolometer detector element.

5. 3. Plastic Bulls-eye antenna

5.3.1 Design and simulation

In order to analyze and verify the behavior of the proposed bulls eye structure, numerical simulations were carried out using both the two dimensional finite difference time domain (FDTD) method and a commercial finite element method (FEM) software package (Ansoft® HFSS). Two plastic materials were analyzed in the design of antenna element; acrylic (ε_r=2.9) and high density polyethylene (HDPE, ε_r=2.37). The metal layer was approximated as a perfect electric conductor in the FDTD simulation, and assumed to be copper in the HFSS simulations. The FDTD simulation results for the transverse electric (TE) fields and transmission frequency response are provided in Figure 5.15. Here, it is clear the surface plasmons reside on the metallic groove surface located inside the plastic material. The electromagnetic wave is focused toward the center aperture by the SPs. In the frequency response plot, the operating resonance frequency is approximately 100 GHz.

FEM simulations were also carried out using the commercial EM tool, Ansoft® HFSS v.13 for the proposed antenna structure. Plane wave excitation from the top side of the bulls eye structure was applied. Radiation boundary conditions were applied to all other domain faces. The resulting wave traveled along the grating and groove through the center aperture, finally converging to a small focal point. In this simulation, the plastic material was assumed as HDPE. This simulation result is shown in Figure 5.17. Good agreement between the two simulations is observed, with the majority of the electromagnetic energy being concentrated within the plastic material at the groove surface. A significant portion of the energy also surrounds the center sub-wavelength aperture.

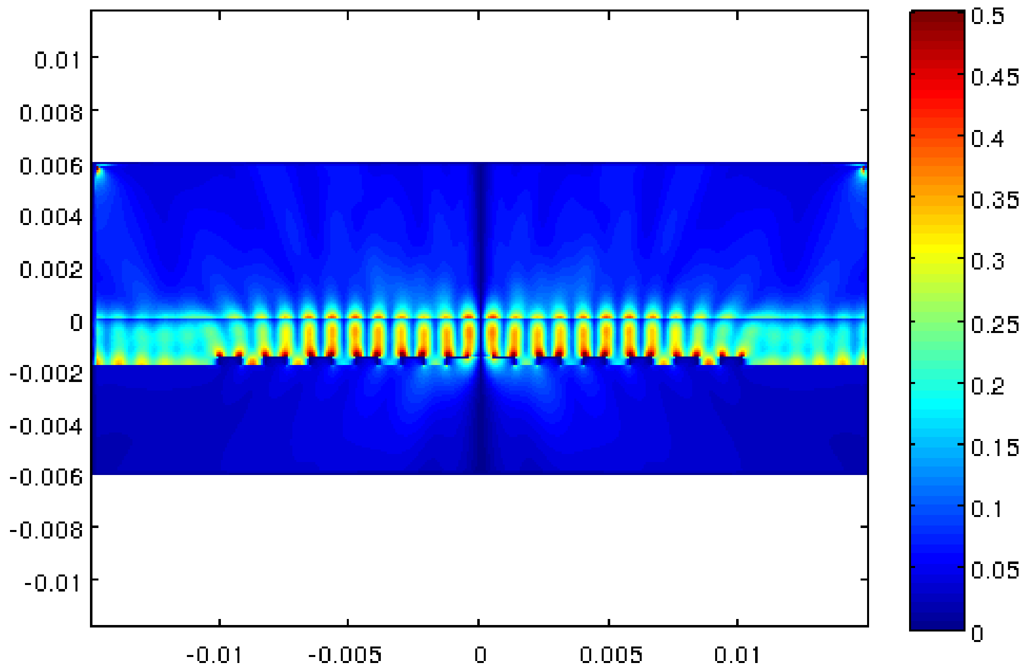

(a)

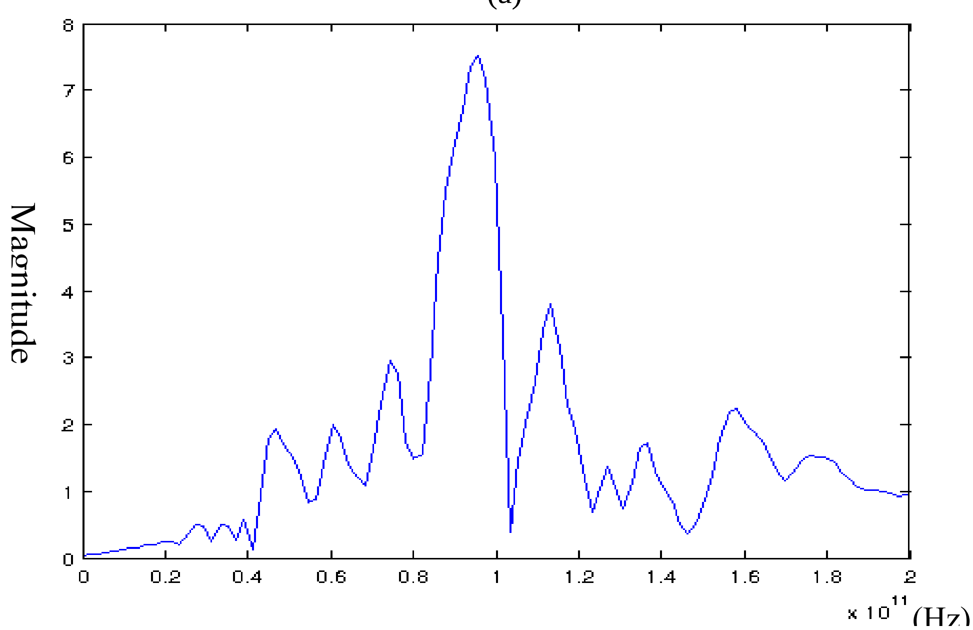

(b)

Figure 5.15 FDTD simulation results of a plastic (acrylic) bulls-eye antenna: (a) E-field distribution, (b) Transmitted signals.

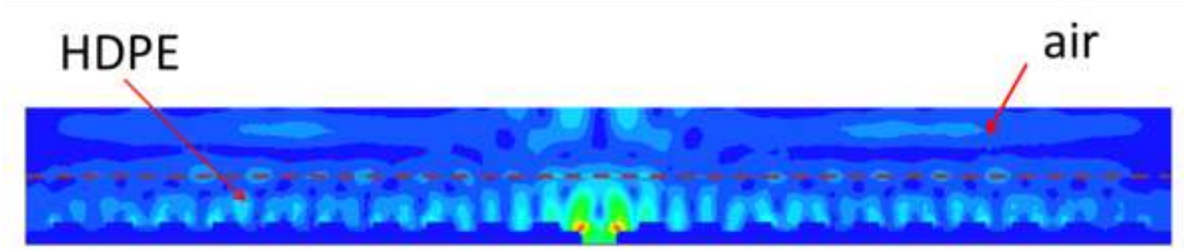

Figure 5.16 FEM (HFSS) simulation result of E-field distribution in the plastic bulls eye antenna.

5.3.2 Fabrication

A 3-D plastic printer was utilized in the fabrication of the proposed plasmon structure. The printer provides high resolution printing (resolution of ~100μm). The back side of the structure is metalized and this was achieved by sputter depositing thin titanium (Ti) and copper (Cu) layers. Titanium improves the adhesion of the Cu to the acrylic layer. Figure 5.17 shows the pictures of the fabricated bulls-eye structure.

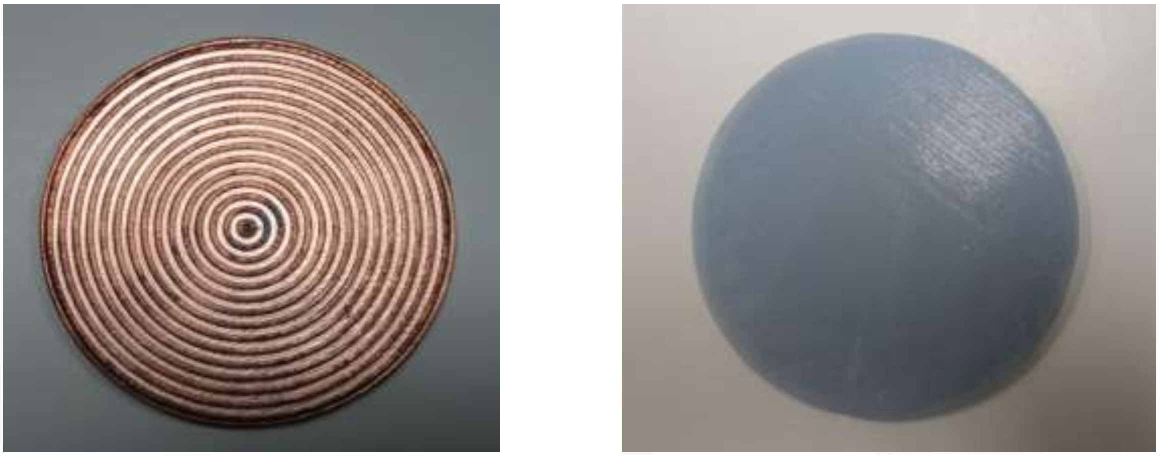

Figure 5.17 Photographs of a fabricated plastic bulls-eye antenna.

5.3.3 Measurement setup

In order to characterize the fabricated bulls eye antenna, the quasi-optic far-field measurement setup was used as shown in Figure 5.9. Also, the fabricated antenna is placed in the middle of the distance between a source (BWO) and a receiver (W-band harmonic mixer) as same measurement setup as the metallic bulls eye antenna. Figure 5.18 (a) demonstrates photographs to set up the measurement. It is to calculate the performance of the plastic antenna with trenches (leading to the plasmonic phenomenon), which a reference signal was acquired from a pin hole of same diameter as the bulls eye aperture. Using this measurement setup, we may investigate and verify the idea that how the plastic layer works to trap the EM wave and enhance the transferring power to the hole traveled through the plasmonic patterns. Also, the relative gain can be obtained to compare the received power between a pin hole and the plastic bulls eye antenna. The area of the metallic pinhole and a plastic antenna covers the receiving horn antenna entirely. This configuration helps avoid the interfering signals from the environmental sources. The diameter of aperture size of all samples (a metallic pinhole, a plastic pinhole, and a dielectric bulls eye antenna) is set as 1.5 mm (depicted in Figure 5.18 (b)).

All samples have been measured to sweep operating frequencies from 75 to 110 GHz with 1 GHz step. To tune up the operating frequency, the indicator of BWO must set as the specific value for operating frequency. The detail set values of a BWO have been summarized in Appendix B. Before measuring for samples, we need to calibrate and analyze the source (BWO and W-band horn antenna). The estimated gain and effective area of a horn antenna is 15 dBi (referring to the gain of a standard pyramid horn) and 456 mm^2 ($W \times H = 24mm \times 19mm$). The rated power of a BWO is measured 240 μW at 100 GHz. Thus, the estimated effective isotropic rated power (EIRP) is computed to be 8.8 dBm (power from the flange out of a horn antenna).

(a)

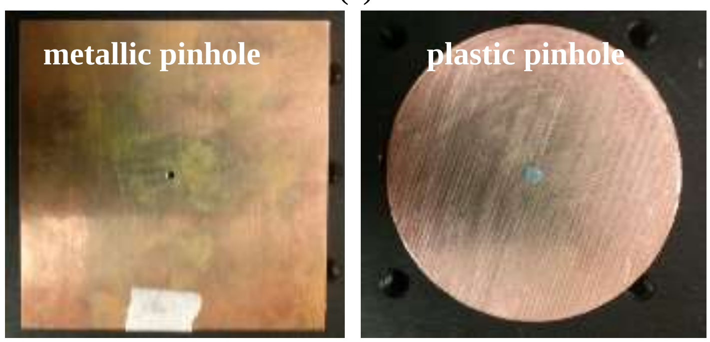

(b)

Figure 5.18 Photographs of measurement setup of a plastic bulls-eye antenna.

5.3.4 Measured results

As discussed above, in order to measure the characteristics of a plastic bulls-eye antenna, firstly, the metallic pinhole and a plastic pinhole have been measure to verify the trapping effect of a dielectric layer (ABS). Secondly, in order to evaluate the plasmonic pattern on the plastic layer, the ABS pinhole and the plastic bulls-eye antenna have been tested. As results of this measurement, the bulls eye antenna can be characterized how large the gain can be achieved comparing to the ABS pinhole. Figure 5.19 demonstrates the received power of a metallic pinhole and ABS pinhole that transmitted through the harmonic mixer of a spectrum analyzer. Over all of frequencies, the plastic pinhole shows higher (3~7dB) transmitting characteristic than a metallic pinhole. To be specific, the received power of a metallic pinhole is close to the noise level of a channel, -80 ~ -82 dBm. At 89 GHz, both of samples show similar received power, it is because the power from a BWO drops rapidly at this frequency. Around 97 GHz to 102 GHz, metallic pinhole has been measured higher amount of received power comparison to rest of frequencies range, because of the aperture size of a pinhole (a half wave length of 100 GHz).

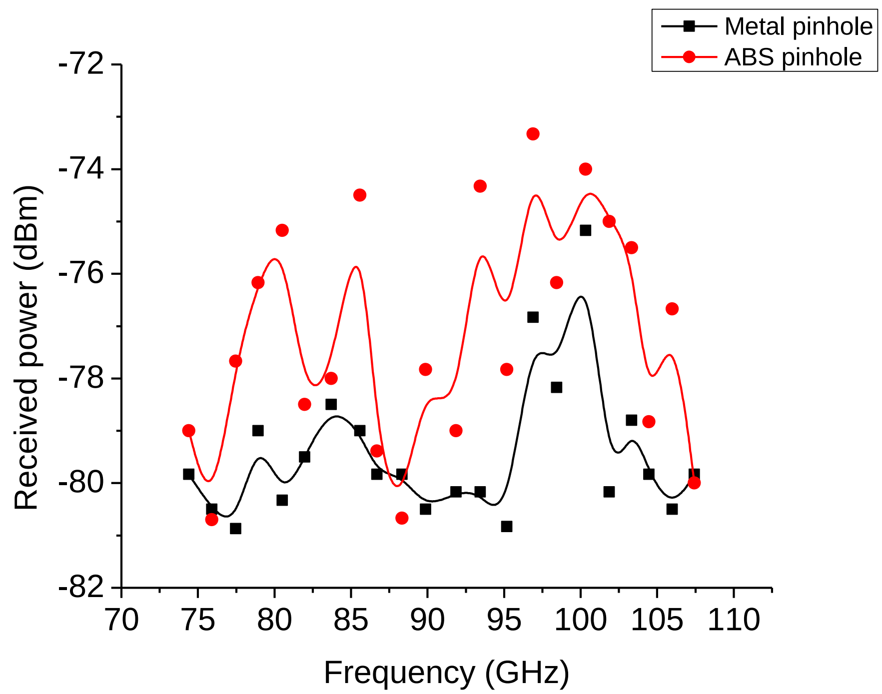

Figure 5.19 Measured received power of a metallic pinhole and plastic (ABS) pinhole.

Figure 5.20 shows the received power obtained from the ABS pinhole and a plastic bulls-eye antenna composed of plasmonic trenched pattern. Likewise the previous measurement, both of plastic samples has been measured from 75 GHz to 110 GHz. As expected, the received power of the antenna having a trenched pattern shows higher than a pinhole. In measured results, we can figure out that there is the significant usable band, from 75 GHz to 87 GHz, the bandwidth is 12 GHz. To convert to the relative gain, the plastic bulls-eye antenna is computed to be 15 dB (maximum gain at 83 GHz) compared to a pinhole.

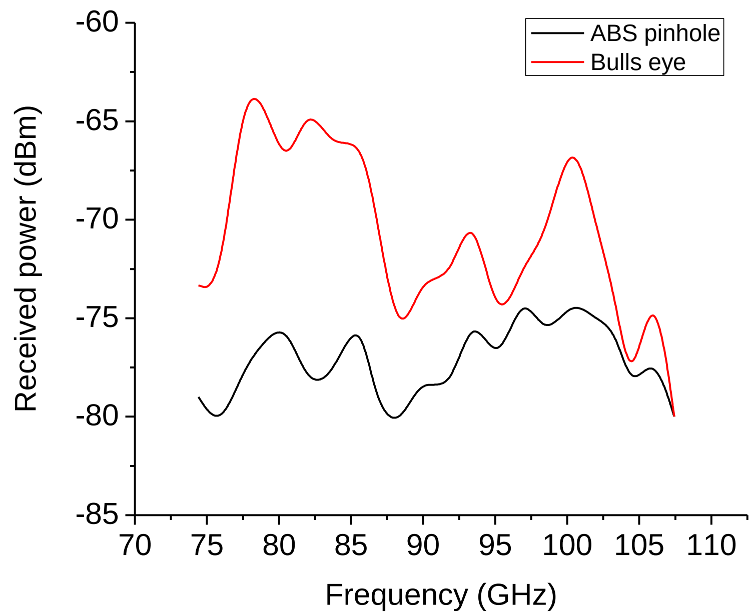

Figure 5.20 Measured received power of a plastic (ABS) pinhole and plastic bulls-eye antenna.

5. 4. Conclusions

This research provides details of simulation, fabrication, and experimental analysis of a spoof-plasmon assisted antenna coupled with a metamaterial-inspired bolometer for THz imaging. Enhanced power transmission and detection was reported at 96 GHz for the bulls eye antenna compared to a pin-hole structure. Due to its low cost and ease of fabrication, this system is expected to be easily scaled to large-scale imaging arrays. The proposed approach provides an approach to integrate a bolometer structure and the antenna element while avoiding thermal loading. Furthermore, bolometers that are subwavelength in size can be used. Small bolometer size is necessary in order to improve signal to noise ratio.

- In this chapter, a bulls eye antenna utilizing surface plasmonic enhanced transmission has been designed, analyzed and fabricated on a plastic substrate.
- The combination of surface plasmons and plastic materials help enhance the transmission power compared to similar bare metal bulls-eye antennas. Furthermore, as use the plastic material to fabricate the antenna, it can help improve the transmitting power as well.
- The proposed antenna design may be integrated with a bolometer to produce a power detector. This structure is simple to fabricate and is wafer-level processing compatible. Also, this structure can be adopted for circuit design at optical frequencies.

CHAPTER 6. DIELECTRIC MICRO LENS ARRAY FOR THZ FOCAL PLANE

6. 1. Theory of Lens

Several lens designs have been presented in literature: hemispherical, hyper/hypo-hemispherical, and extended hemispherical lenses [66-73]. The extended hemispherical lens is attractive as it offers higher directivity and can be used in imaging array systems [67]. Other advantages include higher collimating beam or sharper radiation pattern, and are interoperable with Gaussian beam systems [66]. In this paper, we studied two types of lenses: (i) extended hemispherical and (ii) hypo-hemispherical lenses. Schematics of the dielectric lenses are shown in Figure 6.1. Large diameter ($\geq 10\lambda_0$) lenses have been studied in great detail to achieve high directivity [70-72]. However, in THz focal plane systems designs, there is a need to meet the higher density integration challenge and thus smaller diameter lenses are needed.

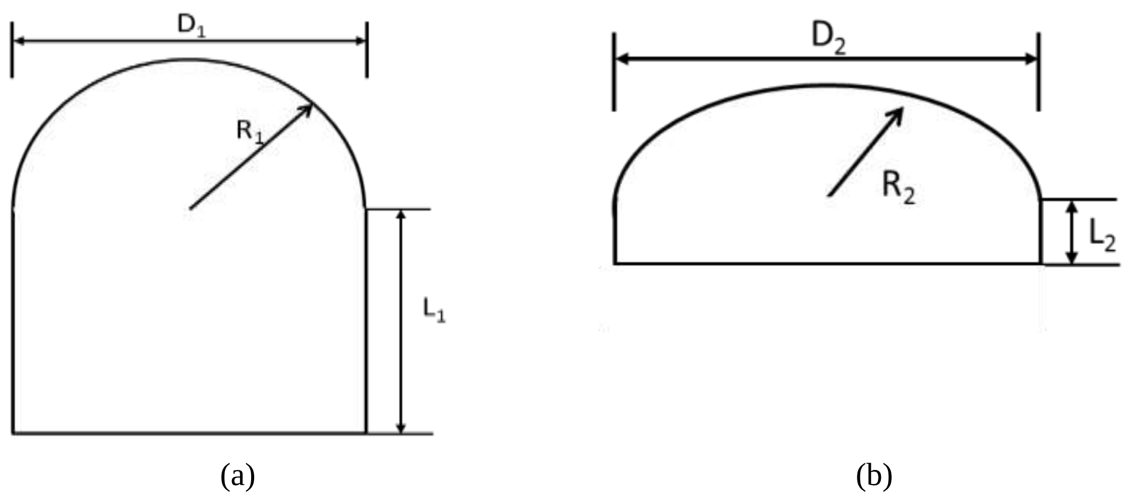

Figure 6.1 The schematics of proposed dielectric lenses: (a) extended hemispherical, (b) hypo-hemispherical.

In order to design the extended hemispherical lens, the hemispherical radius and extended length must be calculated. For this calculation, the ellipse equation is utilized [68]:

$$\left(\frac{x}{a}\right)^2 + \left(\frac{y}{b}\right)^2 = 1 \qquad 6-(1)$$

Where, the foci are at ± c and $c = \sqrt{b^2 - a^2}$

The eccentricity (e) of the ellipse can be analyzed with the refractive index, n, that is characterized by the optics:

$$e = \frac{\sqrt{b^2 - a^2}}{b} = \frac{1}{n} \qquad 6-(2)$$

$$b = \frac{a}{\sqrt{1 - \frac{1}{n^2}}}, \quad c = \frac{b}{n} \qquad 6-(3)$$

For analyzing electrical path lengths of dielectric lenses, the following Fermat's principle was used [72],

$$\frac{R}{\lambda_0} = \frac{F}{\lambda_0} + \frac{R\cos\theta - F}{\lambda_d} \qquad 6-(4)$$

$$R = \frac{(n-1)F}{n\cos\theta - 1} \qquad 6-(5)$$

where R is the radius from radiating source to the lens surface, F is the focal point, and λ_o and λ_d are wavelength of free-space and guided wavelength in a dielectric material, respectively. Based on these equations, the dielectric ellipsoidal structure can be calculated. However, practically a perfect elliptical lens can be hardly produced. Thus, the extended hemisphere lens where the feeding or bolometers are slightly offset from the center of a designed hemisphere can be analyzed by a desired dielectric material extension of thickness, L_{ext}. The optimal ratio of the radius of a designed hemisphere and the length of extended part was referred $L_{ext}/R=0.39$ that is suitable to the ellipse with eccentricity ($\varepsilon=1/\eta=0.65$) for HDPE, $\eta=1.543$ [74].

6. 2. Simulation

THz lenses are to be made out of dielectric materials, specifically, high density polyethylene (HDPE, $\varepsilon_r=2.35$), and Acrylonitrile Butadiene Styrene (ABS, $\varepsilon_r=2.79$). These materials are cost effective, easy to produce, and show low dielectric loss in the THz frequency range [43, 75]. Dielectric properties of HDPE in the THz frequency range are presented in [75]. In this paper ABS material is characterized using a method presented in [43]. The measured results will be presented in detail in chapter 6.5. Physical dimensions, such as the diameter and the extended length of the extended hemispherical dielectric lens, are calculated by the equations explained above. Table 6.1 details the key physical dimensions.

Ansoft High Frequency Simulation Software (HFSS®) was used to simulate the proposed THz lens design based on three-dimensional Finite Element Method (FEM). In order to analyze the proposed lenses, simulations of the lenses were divided into two categories: (i) field simulations of electromagnetic waves and (ii) radiation pattern simulations such as near-field and far-field which are typically used in antenna design analysis.

Table 6.1 Physical dimensions of extended hemispherical lenses

	HDPE Lens(ε_r =2.35)	Acrylic Lens(ε_r=2.79)
$D = 1.6 \times \lambda_0$	R_1 = 0.80mm	R_1 = 0.80mm
	L_1 = 1.02mm	L_1 = 0.93mm
$D = 5 \times \lambda_0$	R_1 =2.50mm	R_1 = 2.50mm
	L_1 = 3.19 mm	L_1 = 2.93 mm
Hypo	R_2 = 1.25 mm	R_2 = 1.25 mm
	L_2 = 0.65mm	L_2 = 0.60mm

Figure 6.2 shows the E-field distribution for two extended hemispherical lenses ($D = 1.6 \times \lambda_0$, $5 \times \lambda_0$) and a hypo-hemispherical lens. In the field simulation, plane waves were simulated starting from the bottom side of dielectric lens to analyze the E-field distribution. While passing through the lens structure, the electromagnetic wave focuses on a point, the focal point, which shows a high intensity of the traveling wave. Figure 6.2 (a) shows that the collimating beam is broad compared to the lens diameter and the focal point is located 1.33 mm away from the plane wave source. Figure 6.2 (b) and (c) illustrate the simulated E-field distribution of a large diameter ($D = 5 \times \lambda_0$) lens and a hypo-hemispherical lens. In both of the simulated results, the main beam is narrower and enhances the transmission intensity more than a smaller diameter lens. This is predicted by theory and results from an increased effective lens diameter [64].

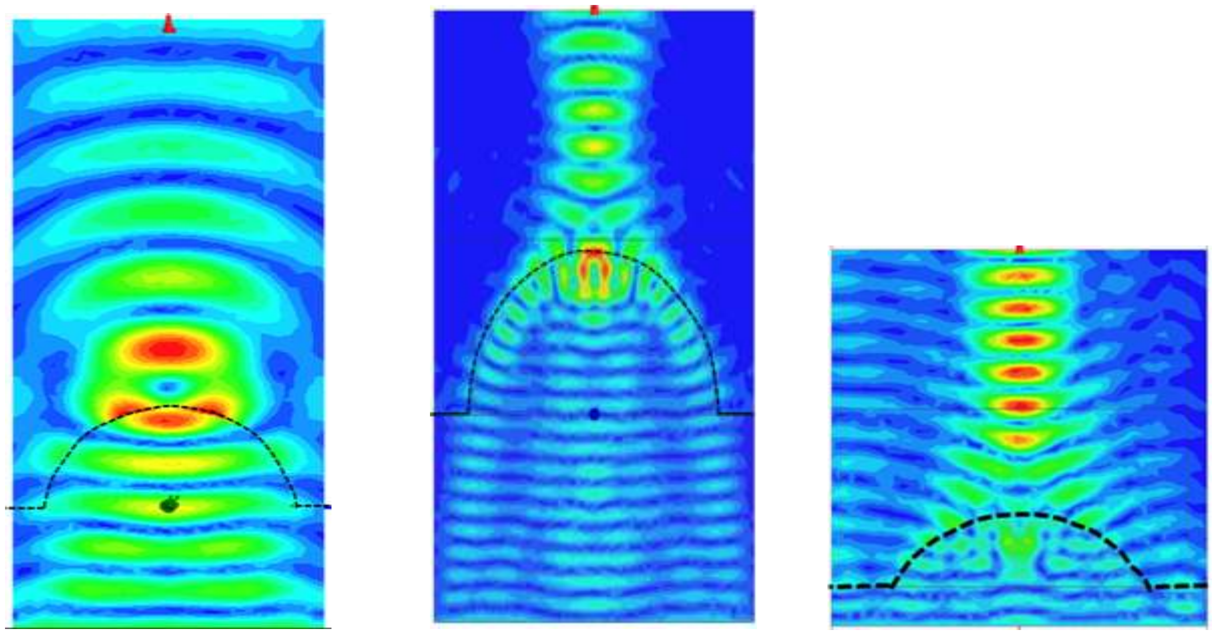

(a) (b) (c)

Figure 6.2 Results of incident wave field analysis for extended hemispherical lenses (a) D = 1.6 × λ_0, (b) D = 5 × λ_0, and (c) hypo-hemispherical lens.

For the near field simulations, the boundary is located on the focal point of each lens where the power intensity of travelling wave is concentrated. Figure 6.3 shows the near field simulation results of two hemispherical lenses (D = 1.6 × λ_0 and 5 × λ_0) and a hypo-hemispherical lens. All simulated radiating beam shapes clearly demonstrate the typical Gaussian beam distribution. Among the simulation results, a hypo-hemispherical lens has a narrow beam and low side lobe. However, the focal point of the hypo-hemispherical lens is located 3.61 mm away from the plane wave source, which is three times further away than the simulated small diameter hemispherical lens (D = 1.6 × λ_0).

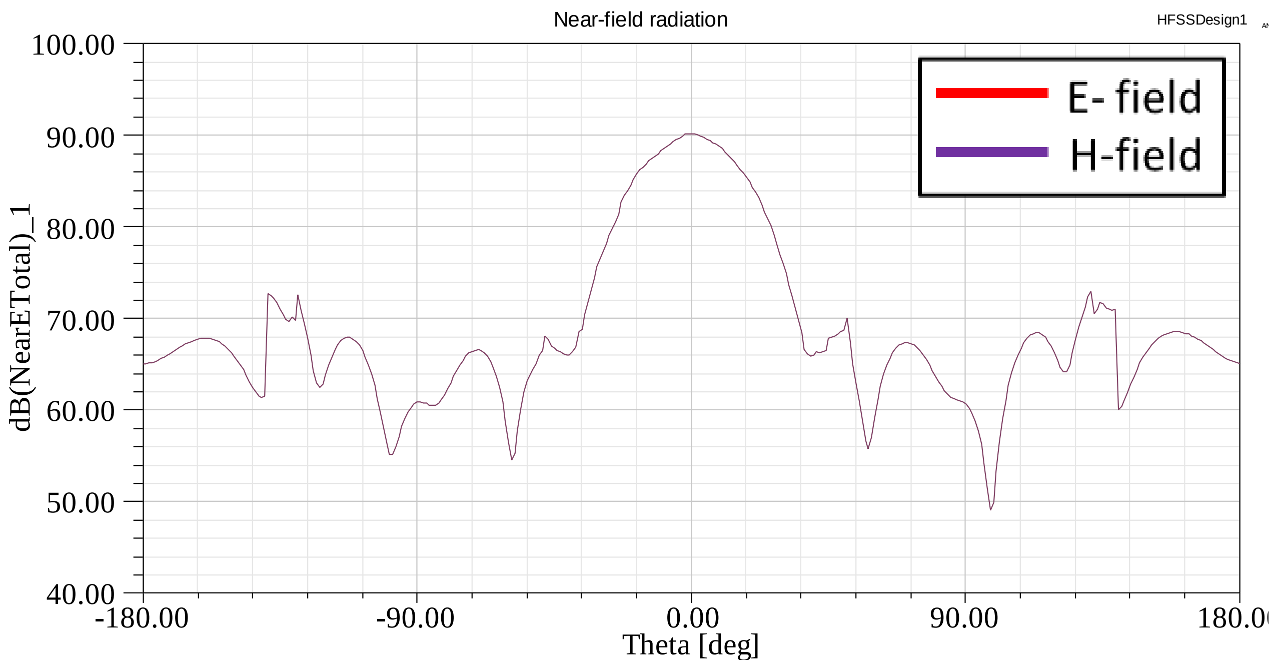

(a)

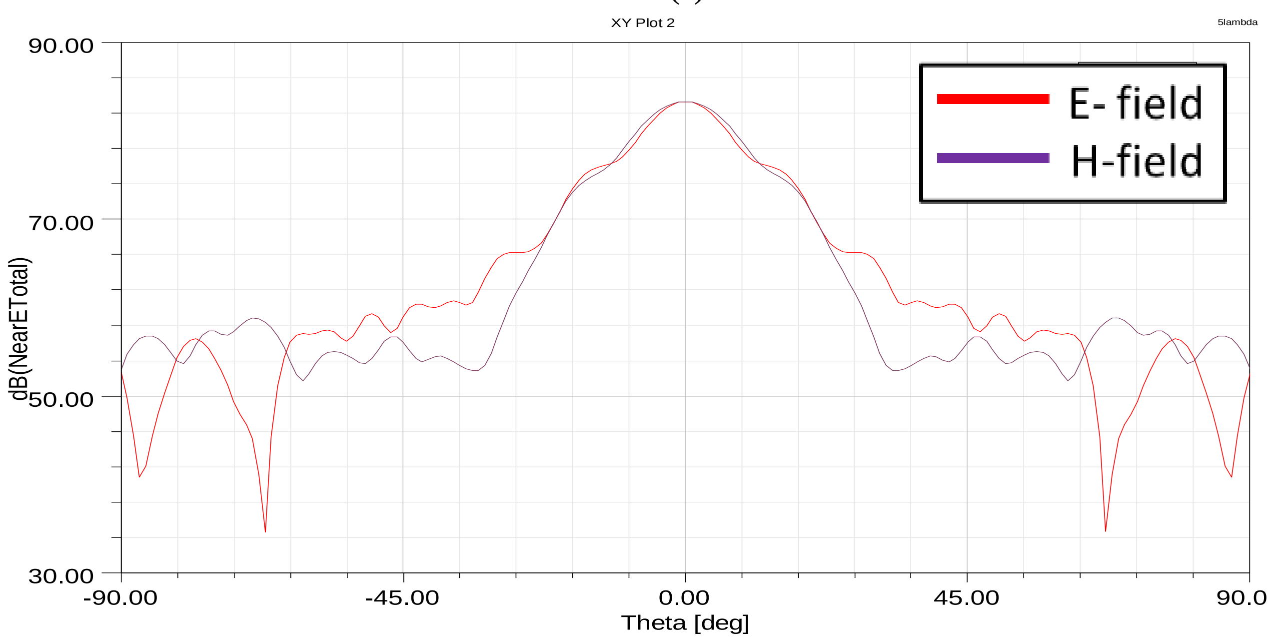

(b)

Figure 6.3 Simulated near field (E-field) radiation patterns of extended hemispherical lenses: (a) D = 1.6 × λ_0, (b) D = 5 × λ_0, and (c) hypo-hemispherical lens.

Figure 6.3 (cont'd)

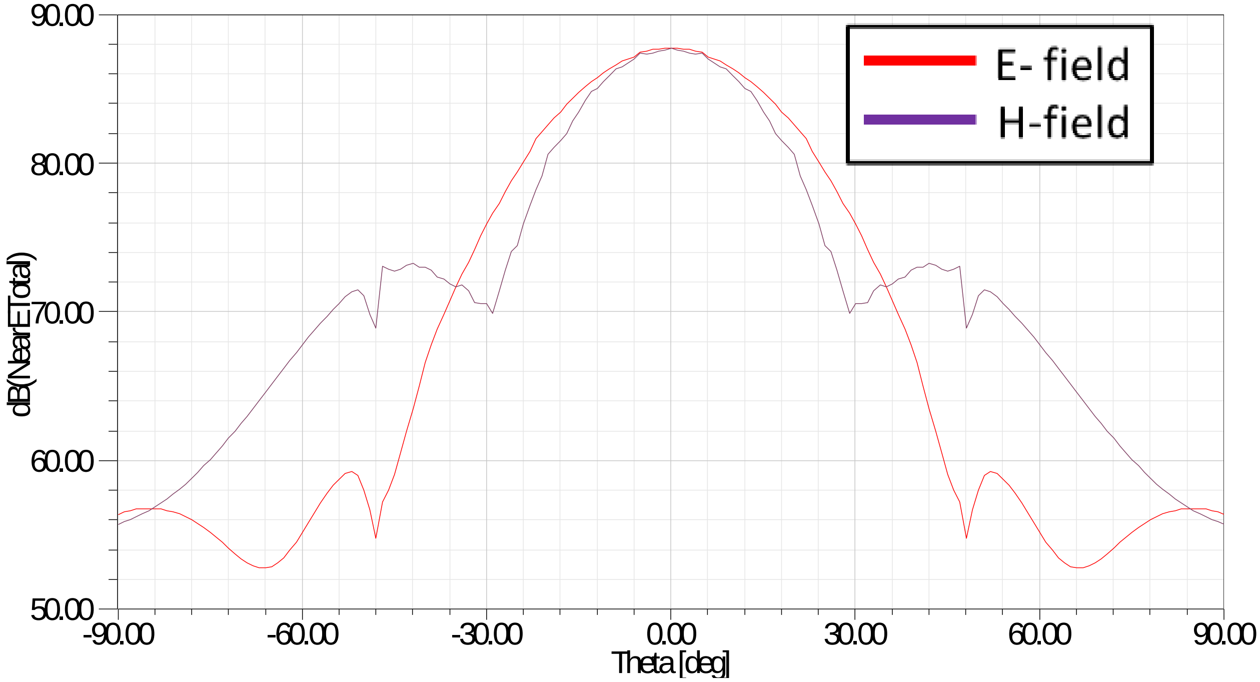

(c)

Figure 6.4 demonstrates the far-field radiation patterns (directivity of E-plane) which were calculated using HFSS. In this simulation, all of lenses have high directivity (> 15 dB) at the target frequency. In addition, as the diameter of a given lens increases the directivity improves. The maximum directivity of a hemispherical lens (D = 5 × λ_0) is computed as 23.5 dB at 300 GHz with HFSS while that of a hemispherical lens (D = 1.6 × λ_0) is 16.1 dB at same operating frequency. It is clear, then, that the large diameter lens has a higher directivity than the small diameter lens. A hypo-hemispherical lens shows similar performance characteristics to a large hemispherical lens when both lenses have the same radius (1.6 × λ_0).

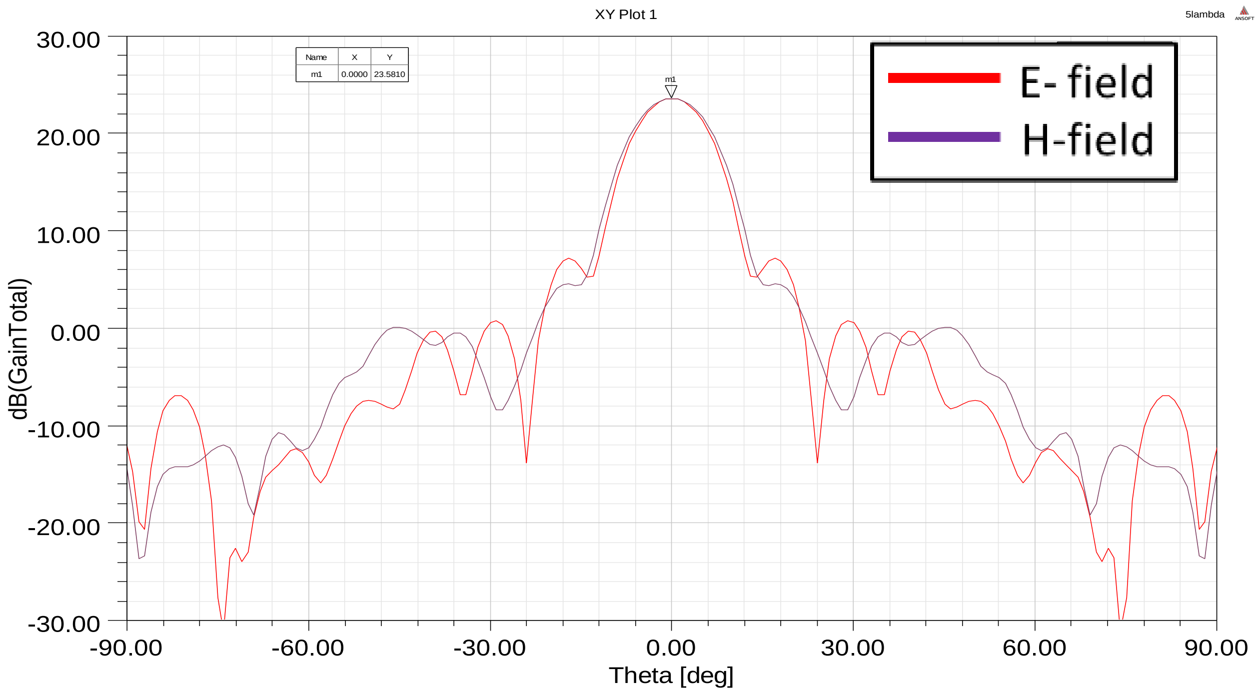

(a)

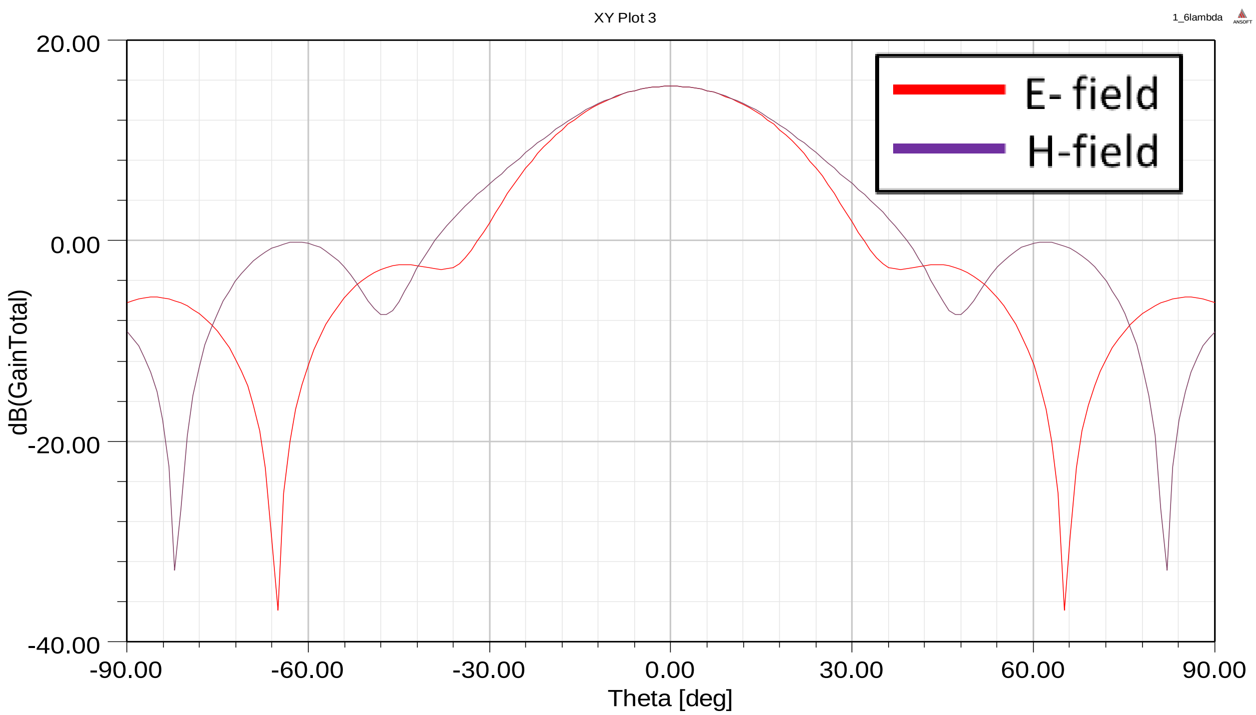

(b)

Figure 6.4 Simulated far field pattern of the two extended hemispherical lenses: (a) D = 5 × λ_0, (b) D = 1.6 × λ_0, and (c) hypo-hemispherical lens.

Figure 6.4 (cont'd)

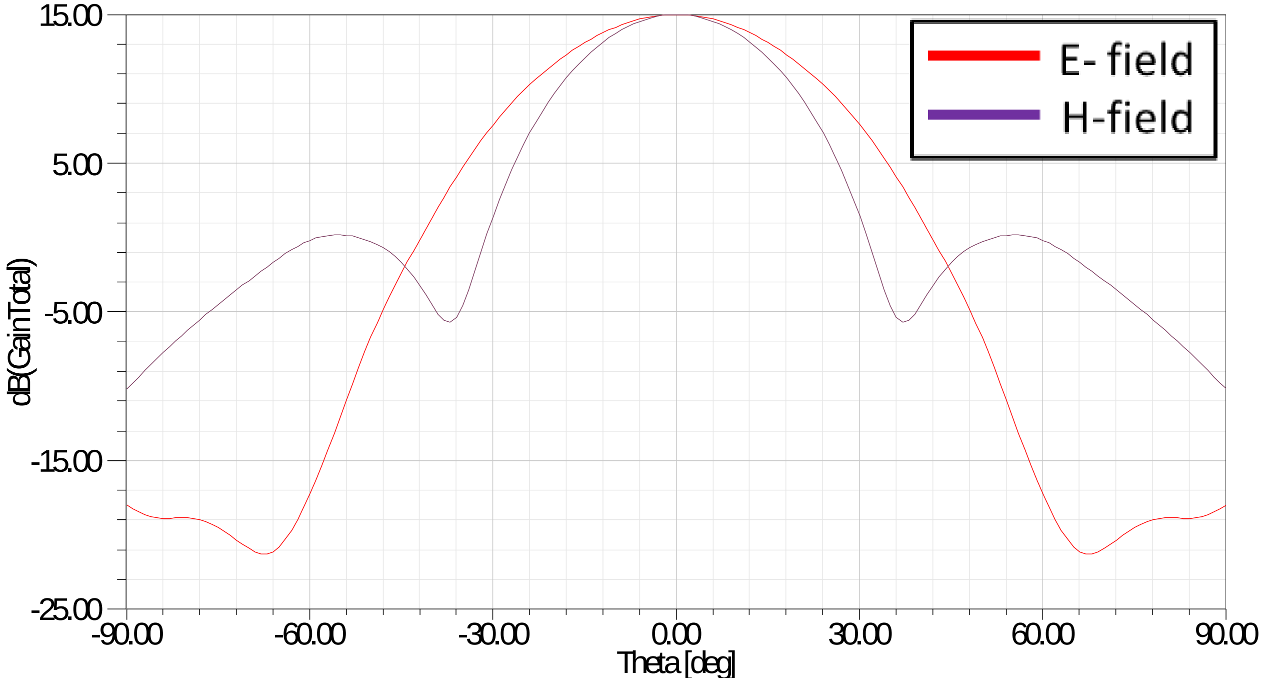

(c)

The radiated electric field has been demonstrated in Figure 6.5. Electromagnetic waves have been exited from the bottom port. In order to analyze the field distribution, the wave port has been set the waveport in HFSS. On a simulated result of a $5\times\lambda_0$ lens, after transmitting the lens, the propagating wave was transformed to the plane wave. Similarly, the small diameter (1.6 $\times$ λ_0) of a lens shows the propagating plane wave.

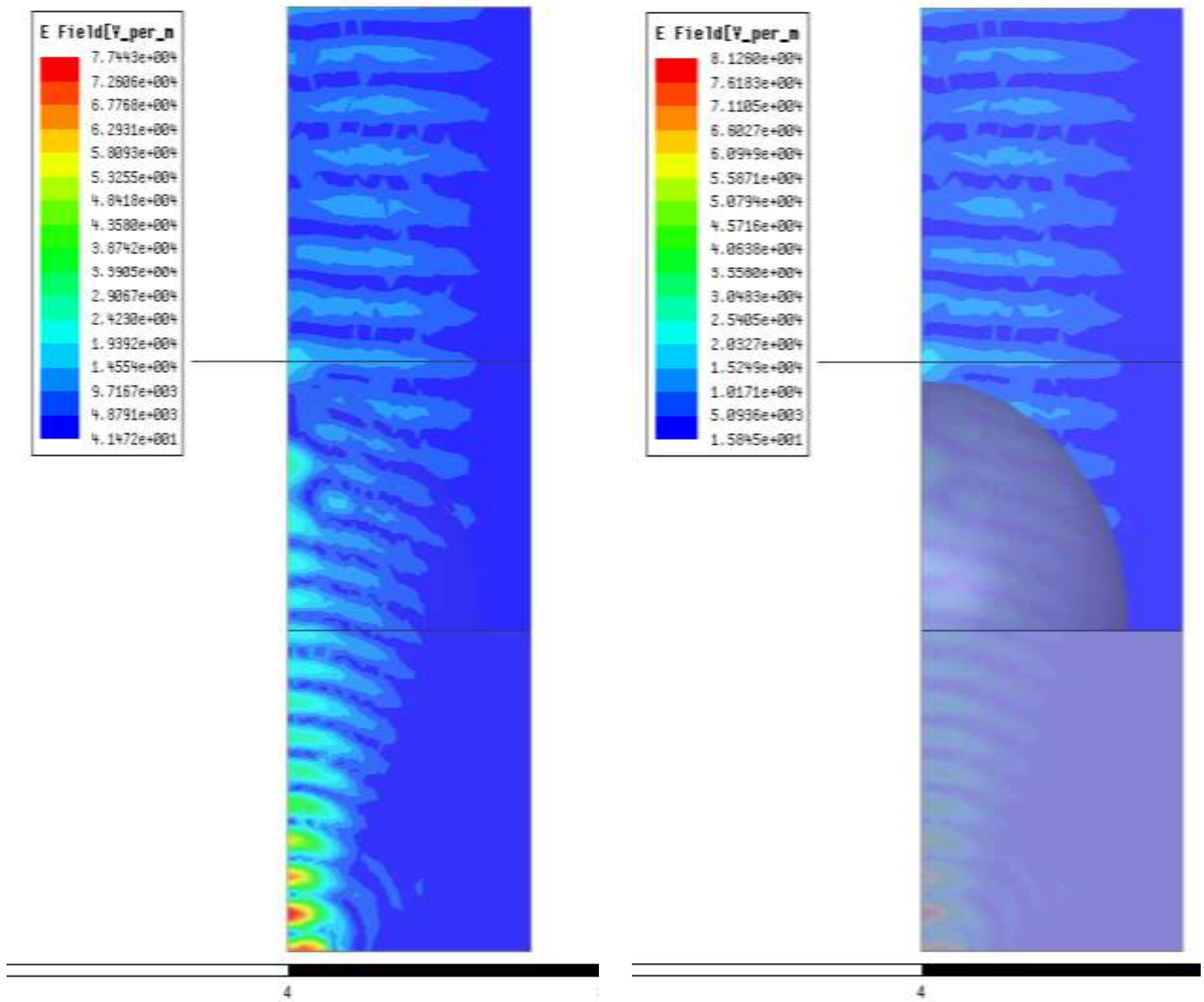

(a)

Figure 6.5 The electric far-field radiation pattern of $5 \times \lambda_0$ (a) and $1.6 \times \lambda_0$ (b) lenses.

Figure 6.5 (cont'd)

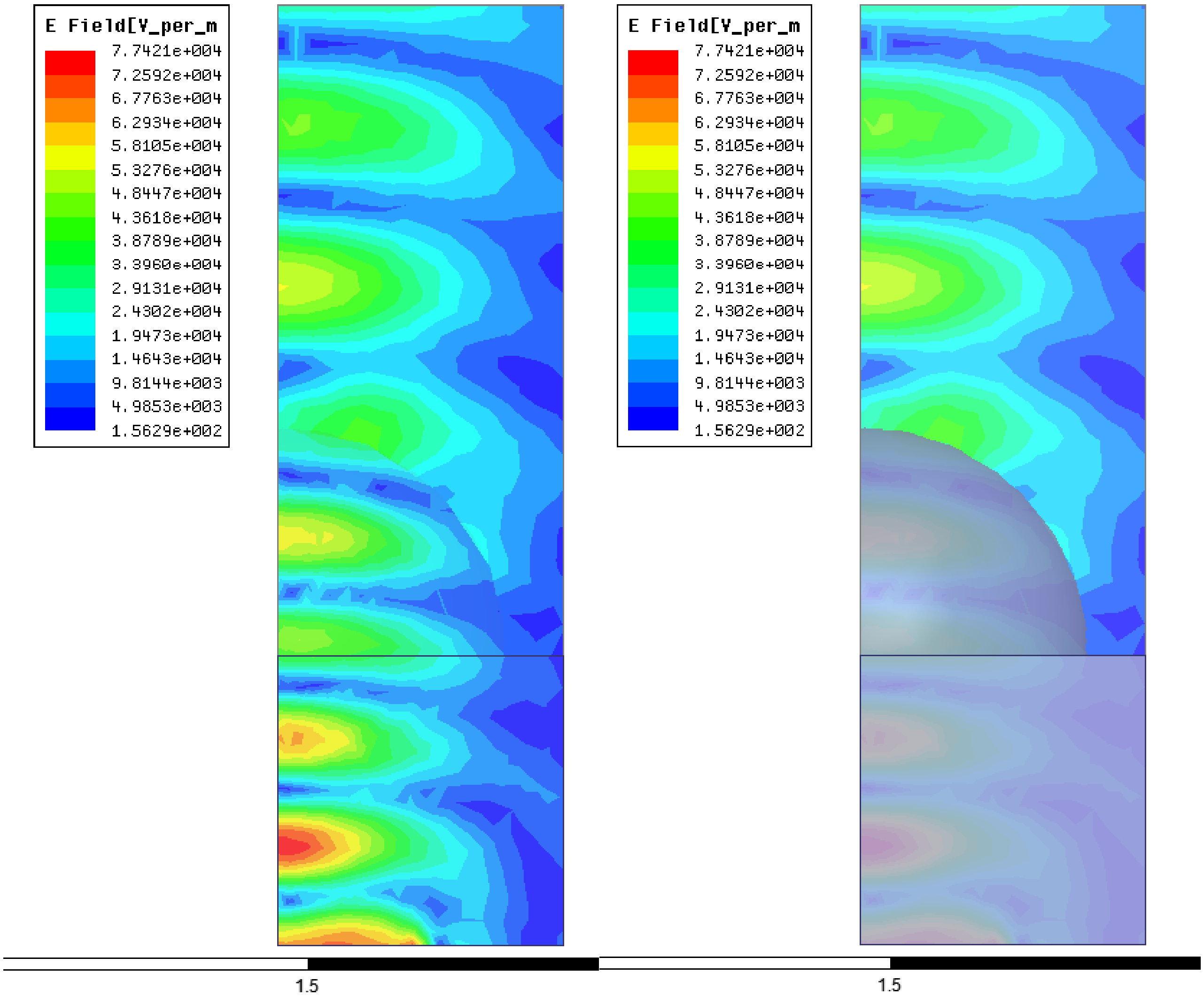

(b)

6. 3. Fabrication

Two methods were studied for the fabrication of micro-lens array. First, a 3-D plastic printer was utilized in the fabrication. The printer provides high resolution printing (resolution up to 30 μm). ABS is used as the dielectric material (detail measured material properties are presented in chapter 6.5). This fabrication method has several advantages: time-saving fabrication, good reproducibility, and allows prototype fabrication in a short cycle time. Figure 6.6 shows photographs of fabricated lenses using this approach. The micro molding was used in a second fabrication process. Details of this process will be presented at the conference. This method is desirable when mass production of a design is required. Furthermore, this method allows larger flexibility in use of dielectric materials (thermoplastic materials) as compared to 3D printing. Generally, in order to use the micro molding process, the metallic mold must be produced. For this, normally, micro-machining or micro fabrication has been used [72]. In this manuscript, a new cost effective way to manufacture the mold structure using 3D printing and metal plating was utilized. As a first step, starting with the 3D printed structure, the 3D structure is coated with thin titanium (Ti) and Cu seed layers for electroplating. Bulk metal plating was used to build up the thick metal layer (up to mm level). The base 3D plastic structure is dissolved, using solvents, leaving behind a thick Cu mold structure. This mold structure is mounted on a Cu plate through soldering and used as the mold for fabrication of HDPE based micro-lens array.

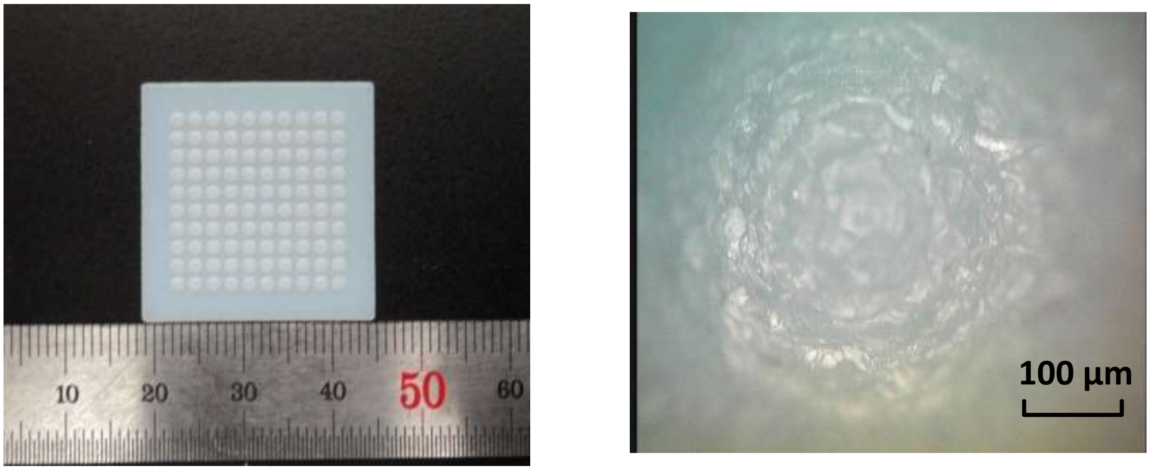

(a)

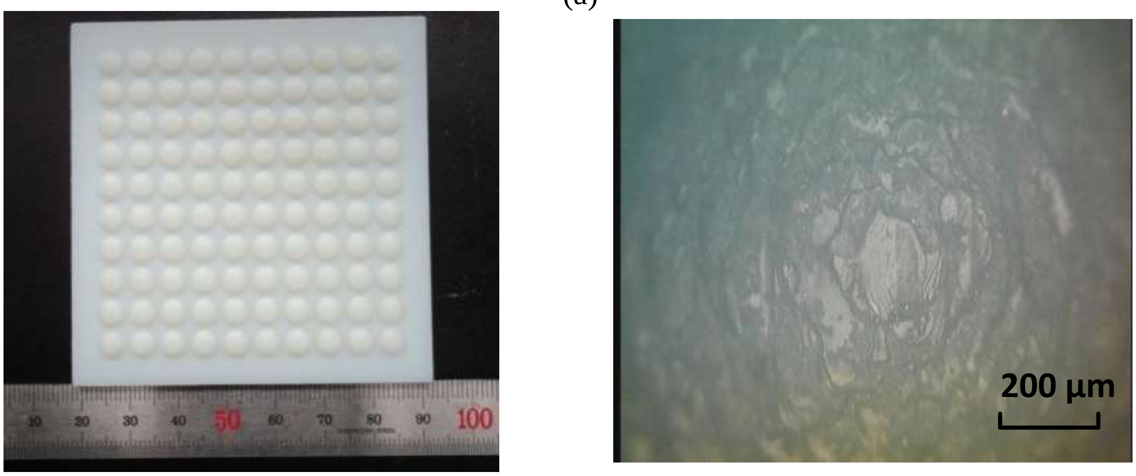

(b)

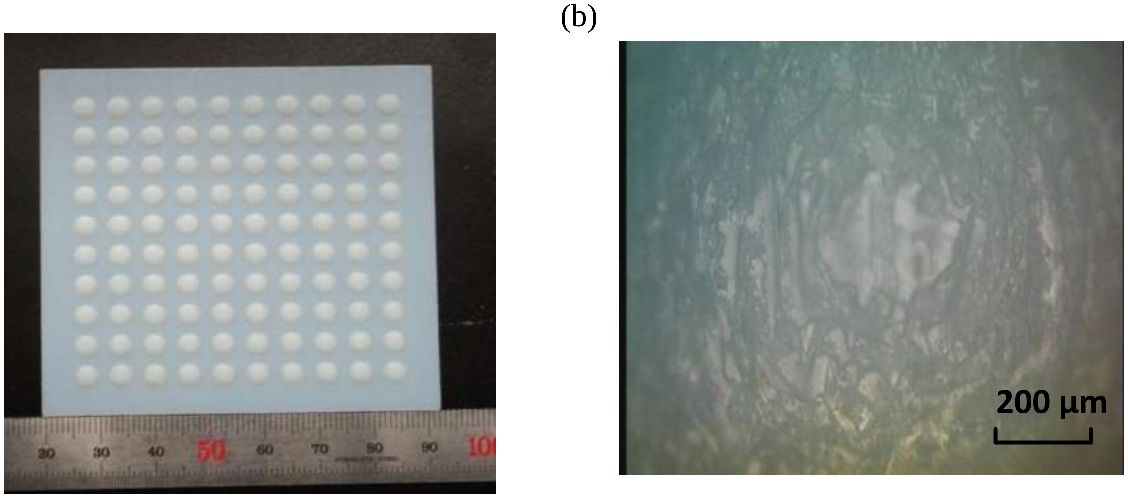

(c)

Figure 6.6 Photographs of fabricated THz lenses (left: lens array, right: microphotographs of lens surface).

6. 4. Experimental measurement setups

In order to measure the fabricated THz lenses, we used two measurement methods; near-field and far-field testing. Both measurements utilized the time domain measurement system (Picometrix T-ray 2000 THZ TDS). This measurement system offers a sampling period of 0.03941ps [44]. This result in a frequency resolution of approximately 12.5 GHz when acquiring the Fourier transform of the received time domain signals. The transmitter radiates a collimated electromagnetic pulse beam in the direction of the receiver.

The block diagram of far-field measurement setup is demonstrated in Figure 6.7. In order to apply the plane incident wave, the distance between the transmitter and a THz lens was set as 30 cm (>> $2d^2/\lambda$) in far-field range [65]. At this distance, the main beam of a transmitter covers up approximately 2.5 inches diameter on the substrate, which is enough to illuminate an array of THz lenses. To detect the transmitted power, a receiver is placed just behind the lens in order to minimize losses. Using this measurement setup, several of the lenses fabricated were characterized. To verify the lens performance, we first measured the far-field setup without a lens to collect reference data. The transmission characteristics of lens are recorded by placing the lens array in between the transmitter and the receiver.

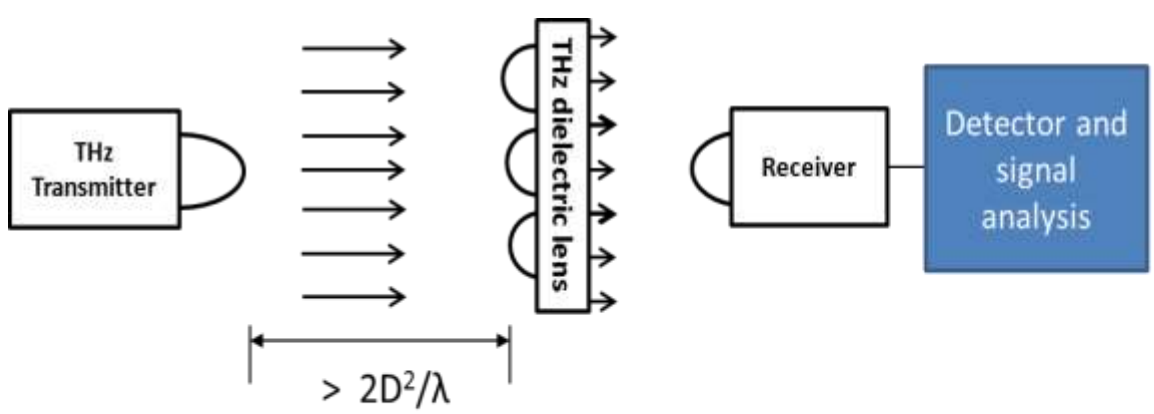

Figure 6.7 Block diagram of far-field measurement setup.

A second setup, near-field measurement, was used to characterize individual lens elements. Figure 6.8 shows the layout of the near-field measurement setup. In order to measure the position of high received power intensity, planar scanning method was adopted. To limit the transmission, the metal plate (Cu, t=450 μm) with aperture, was placed in between a lens and a receiver. The diameter of the aperture was designed to have a cut-off frequency below the design frequency (f = 300 GHz). This metallic aperture structure plays a role as a near-field probe, because it can scan and measure the power density on the surface of a lens. An absorbing aperture material instead of Cu would be desirable to minimize multiple reflections. This will be utilized in future experiments. A 2-axis robotic manipulator was used allowing a step resolution of 200 μm on each axis. The receiver behind the metallic aperture measures the received power density passing through the dielectric lens. The lens was fixed, whereas the aperture was attached to the robotic arm. The receiver was also fixed at it has a wide capture window and not necessary to move. Through this setup, spatial power density across the lens array was measured. For the first measurements, on scanning in one axis was carried out with a resolution of 1 mm between the data points.

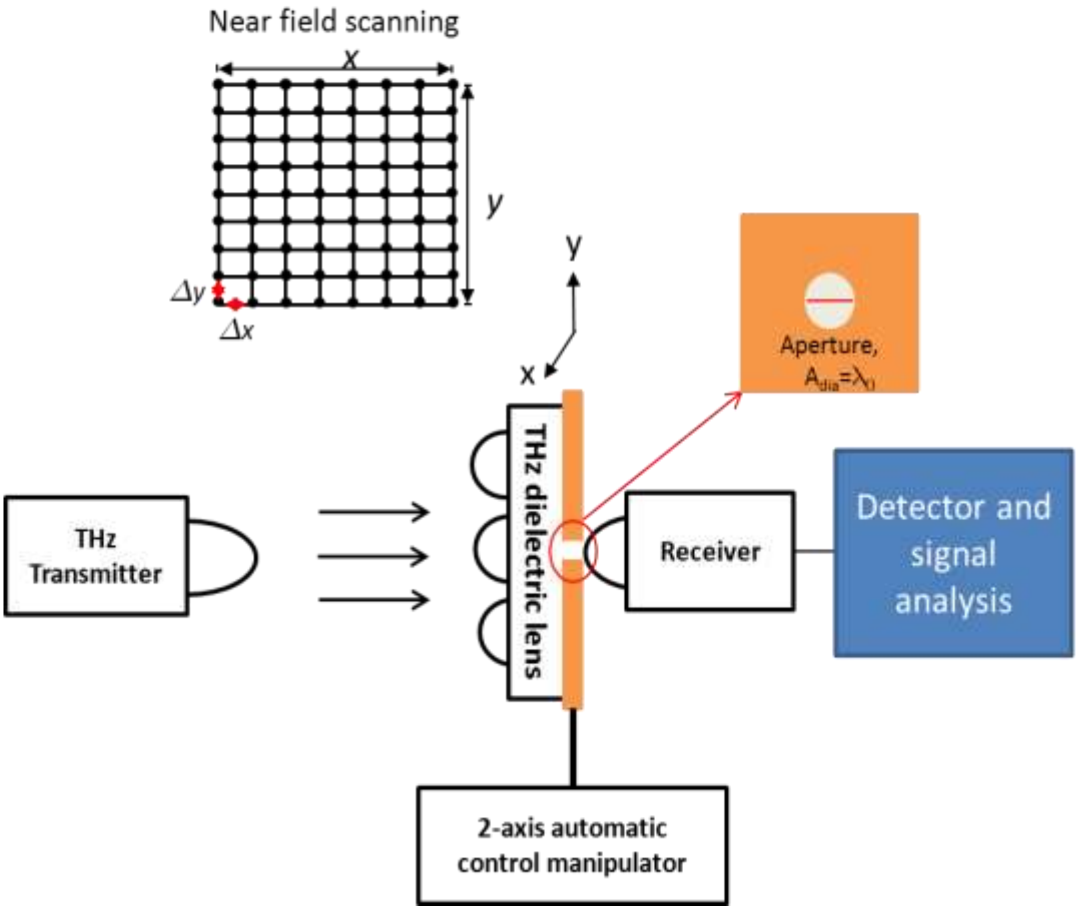

(a)

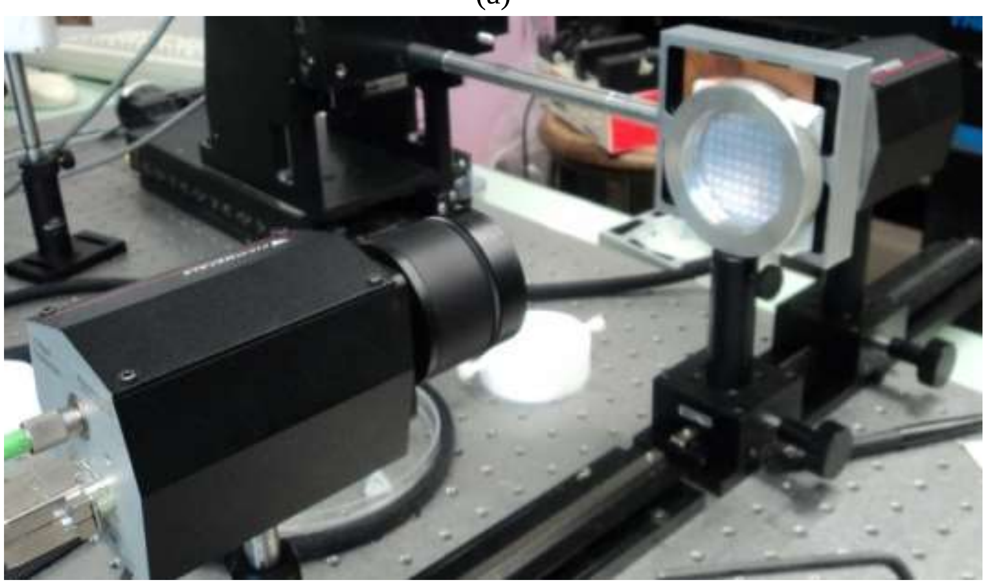

(b)

Figure 6.8 Block diagram and a photo of planar scanning for near-field measurement setup.

6. 5. Measurement results

In order to characterize the electrical properties of a dielectric material that was used in the fabrication lenses at THz frequencies; this paper adopts and utilizes the material characterization method as described in [43]. The measured properties for a candidate material are shown in Figure 6.9. The dielectric constant of the material ranges from 2.73 to 2.81 in THz frequency range (up to 0.8 THz). Loss tangent (tan δ) of the material increases linearly from 0.012 to 0.05 from 0.1 THz to 0.8 THz, respectively.

The measured result of near-field planar scanning is shown in Figure 6.10. The step size of axis-movement is set to a millimeter unit (d=1 mm) and the total scan length is 11 mm with a metallic aperture (A_{dia}=1 mm). The data shown in Figure 6.11 is based on the measured results of near-field scanning of an extended hemispherical lens ($D=5 \times \lambda_0$). The two strongest hot spots were examined in measured results. The result shows that the distance between two hot spots is equal to the distance between the unit lenses, 5mm. This suggests that the hot spot of the individual lens, as simulated above, are arrayed similarly as the lenses. The focal spot is smaller than the aperture window and thus the measured result is spread of over a large window than calculated through simulations. Actual intensity difference between the higher peak and valley region will be higher if measured using a smaller aperture window.

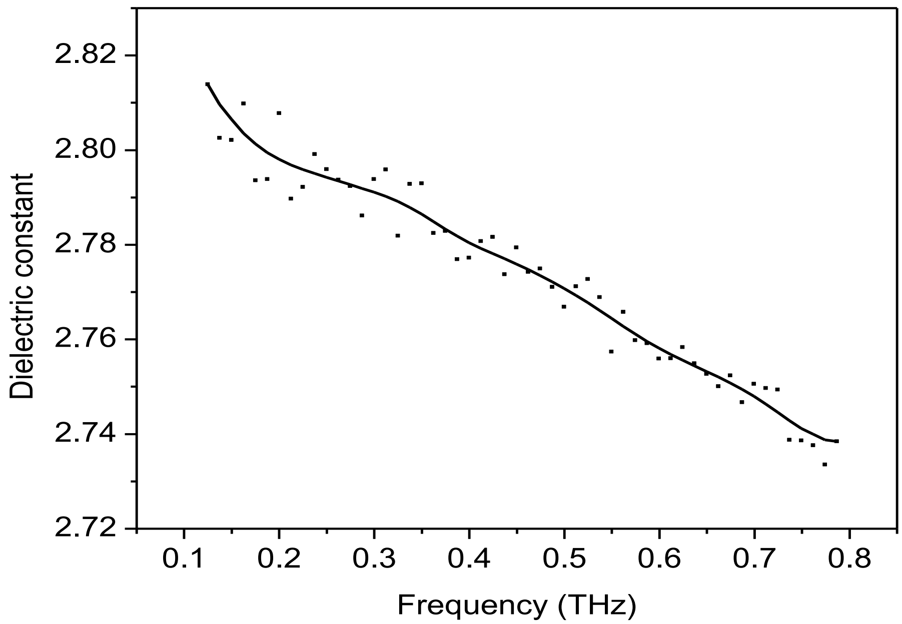

(a)

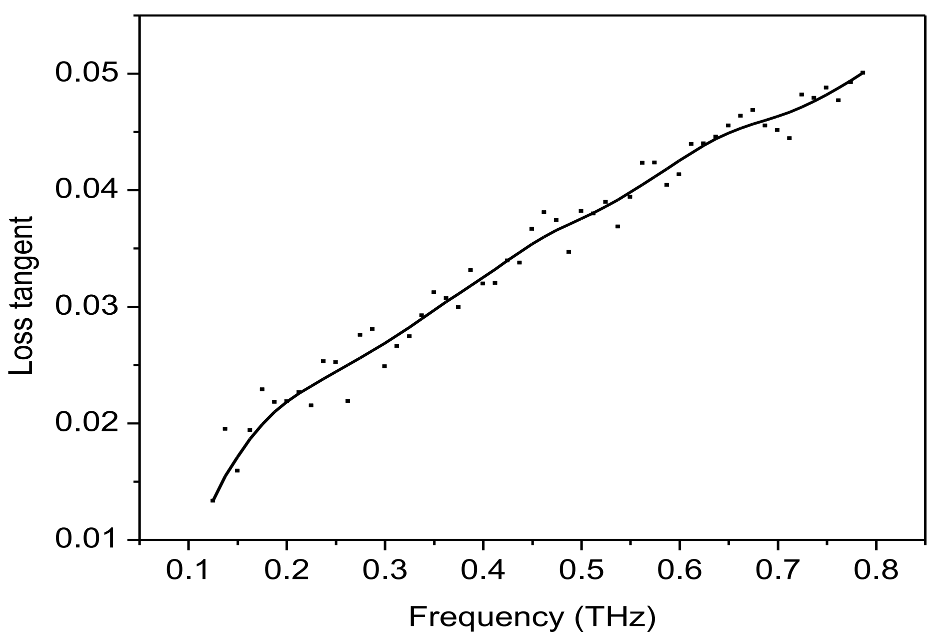

(b)

Figure 6.9 The (a) dielectric constant and (b) loss tangent of ABS material used in the fabrication of lenses.

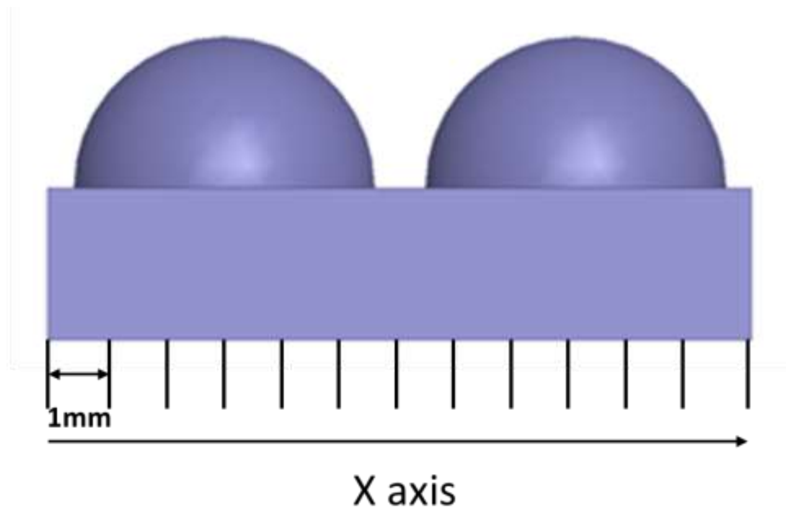

(a)

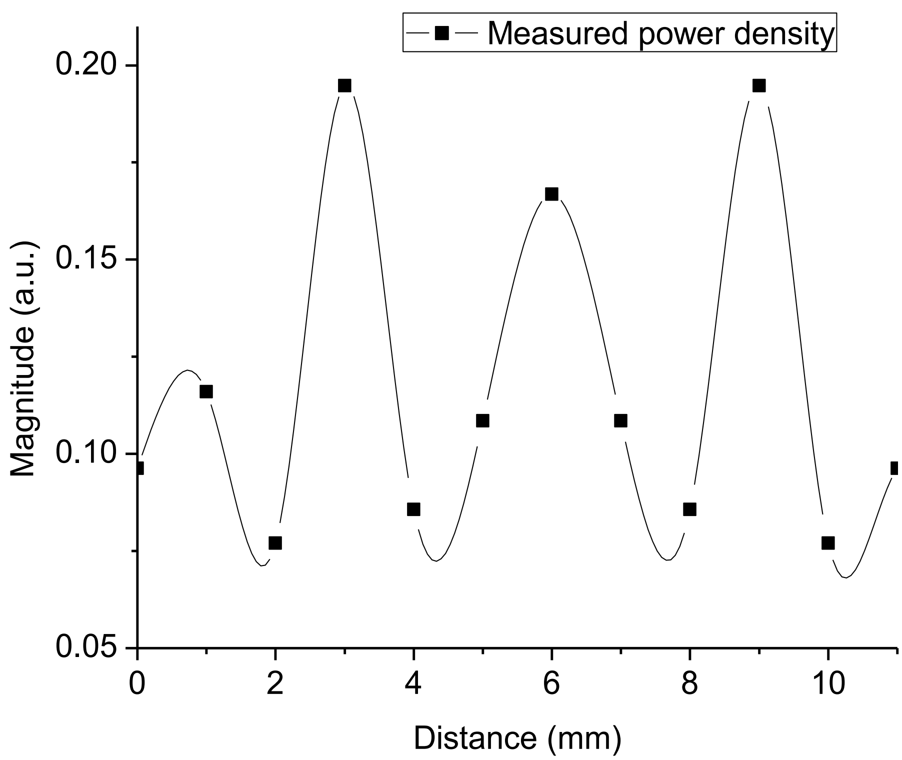

(b)

Figure 6.10 Measured results of Near-field planar scanning: (a) Schematics of scanning, (b) Measured intensity plot across the lens array (across two lenses).

Figure 6.11 shows the measured transmission coefficient of an extended hemispherical lens (D=5 $\times$ λ_0) using the far-field measurement setup. In order to compute the normalized transmission coefficient with a given lens, a reference coefficient is obtained first, defined by the far field characteristics of the testing configuration without a lens. Then the far-field properties of fabricated lenses were examined. In Figure 6.11 (a), it is clear the maximum transmission coefficient is 0.48 and an overall transmission coefficient (> 0.3) is presented between 0.13 and 0.28 THz, suggesting a 0.15 THz usable bandwidth. Figure 6.11 (b) shows the response obtained from another fabricated extended hemispherical lens (D=10 $\times$ λ_0) showing that the measured usable bandwidth for this lens is 0.1 to 0.18 THz. It should be noted that the measured center frequencies are different from the desired center frequencies of both of designed THz lenses. This is due to the receiver being placed on a slightly different position compared to the calculated focal point.

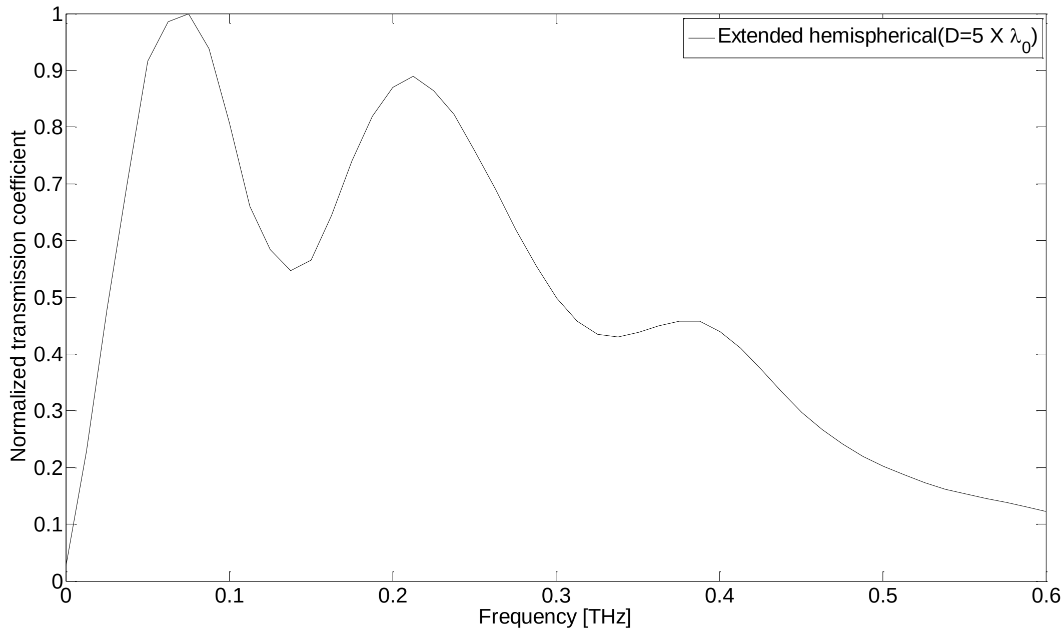

(a)

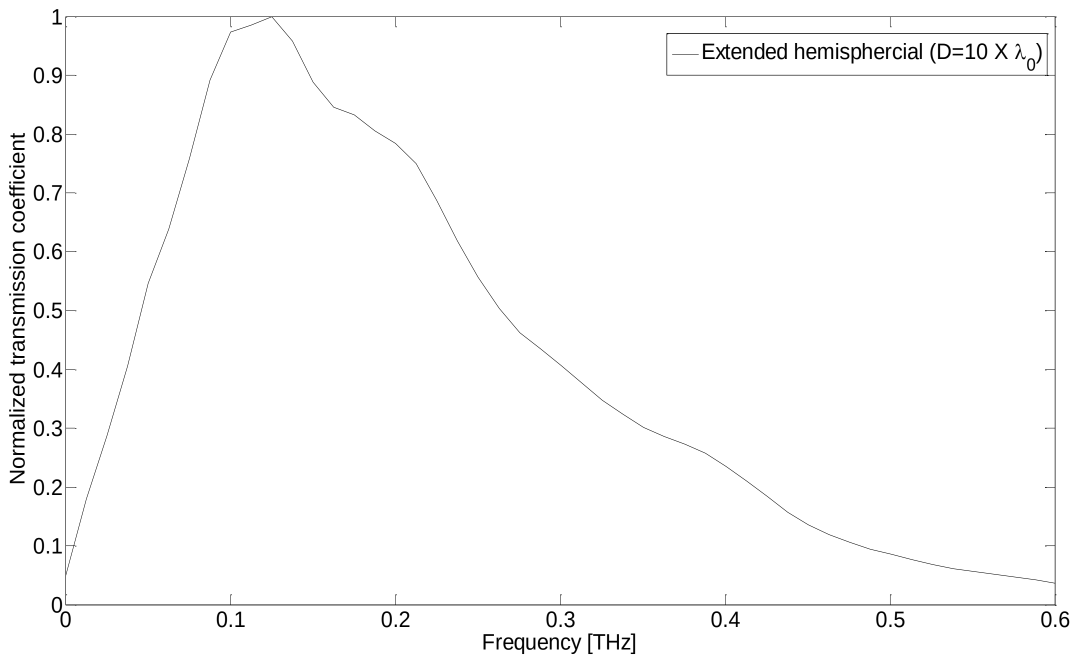

(b)

Figure 6.11 Far-field measurement results of extended hemispherical lenses; (a) D=5 × λ_0, (b) D=10 × λ_0.

Figure 6.12 shows the transmission responses obtained from an extended hemispherical lens and a hypo-hemispherical lens with same diameter, D=5 $\times$ λ_0. In this measurement, both of the lenses show analogous transmission patterns. This is because the curvilinear contour of both lenses was designed with the same diameter. Above 0.3 THz, the hypo-hemispherical lens showed more high transmission coefficient. This is because a hypo lens is thinner than that of an extended hemispherical lens. This degradation of transmission can be improved by using low loss polymer materials such as HDPE and LDPE instead of ABS.

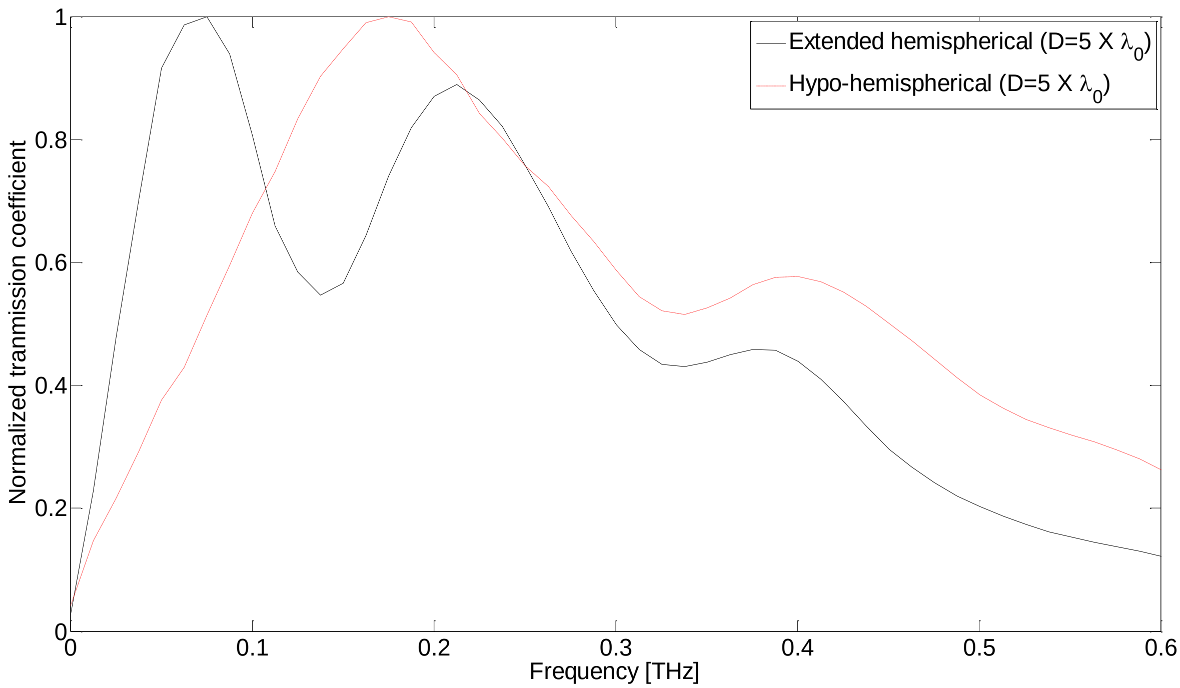

Figure 6.12 Measured transmission coefficients of two different lenses with the same diameter.

6. 6. Conclusions

In this work, THz dielectric lens array have been designed, fabricated and characterized over a wide frequency range. Fabrication was carried out using a 3D plastic printer using ABS dielectric material. This process is suitable for the fabrication of lens array. It can be utilized in the direct fabrication of lens at the wafer level. Fabricated lenses have been characterized using a simple near and far field measurement setup. Measured results clearly exhibit the expected transmission characteristics of lenses. The proposed approach can reduce complexity in assembly and is simple to implement.

CHAPTER 7. THZ IMAGING ARRAY SYSTEM

7. 1. Design and simulation

7.1.1 Microbolometer based on metamaterial structure

One of the key advantages of using metamaterials is that the frequency of operation can be changed arbitrarily through manipulation of geometry of a unit cell. Here a modified slit ring resonator (SRR), [77 - 79], is adopted in the design of unit cells operating at 0.1 and 0.4 THz. These cells are scaled version of each other. Geometry of each unit cell is optimized to achieve a compact sub-wavelength size structure. Figure 7.1 shows the design layout of the unit cells. Figure 7.1 (a) is the basic model of the SRR, it is disjointed from its neighboring cells. Figure 7.1 (b) and (c) shows the unit cell which is composed of interconnected metamaterial unit cells. The unit cells are connected together so that the resistance change can be directly measured across these groups of cells. These unit cells are connected together using two approaches: straight and zigzag. In the straight connection approach, the top sections of the unit cells are connected together. In the zigzag approach, the diagonals of the unit cells are connected together. The zigzag approach provides higher resistance path. Table 1 summarizes the physical dimensions of the unit cell and array. The periodicity of the unit cells is approximately one sixth of the free space wavelength at these design frequencies.

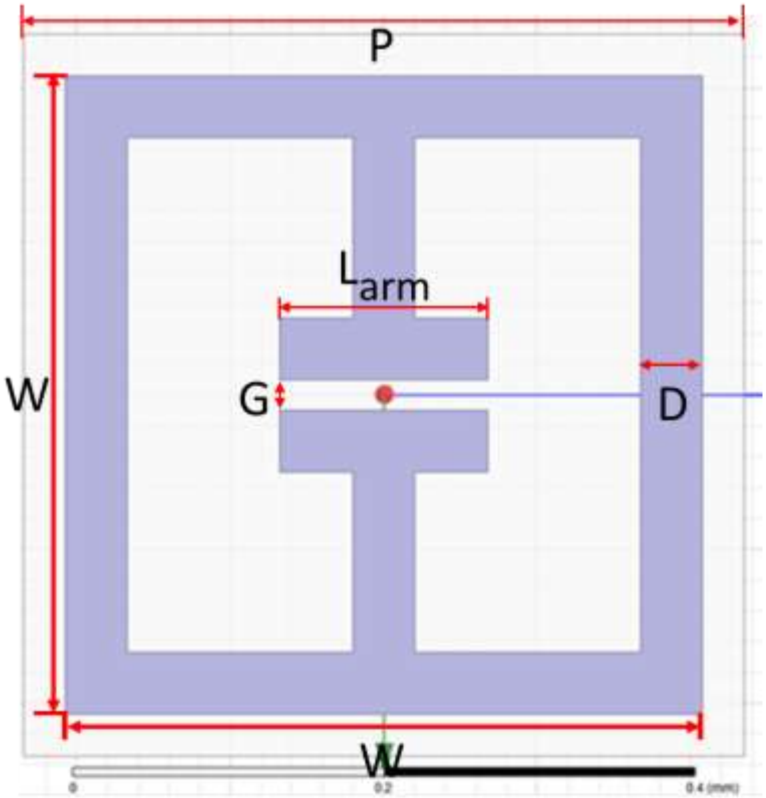

(a)

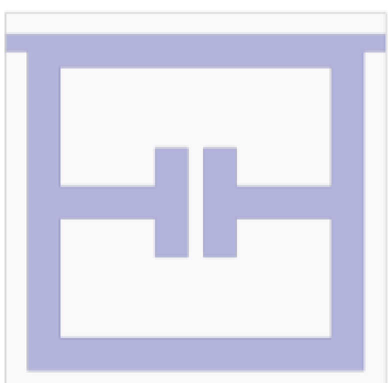

(b)

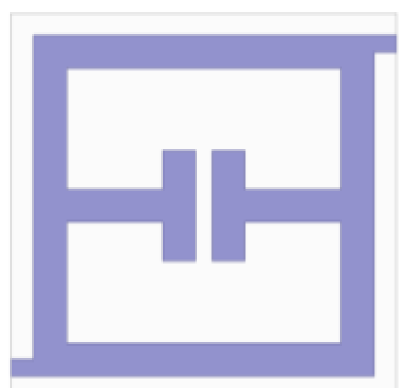

©

Figure 7.1 The geometry of SRR structure, (a) a modified SRR unitcell, (b) a straight connection unitcell, and (c) a zigzag connection array of unitcells.

Table 7.1 Dimensions of a unitcell of designed microbolometers

Parameters	Dimensions		Remarks
	0.1 THz	0.4 THz	
Periodicity (P)	0.47 mm	0.115 mm	- $\lambda_{0.1\ THz}$= 3 mm ($\lambda_{0.1\ THz}$ /P=6.38) - $\lambda_{0.4\ THz}$=0.75 mm ($\lambda_{0.4\ THz}$ /P=6.52)
Width (W)	0.415 mm	0.105 mm	
length of arm (L_{arm})	0.135 mm	0.035 mm	
Width of arm (D)	40 μm	10 μm	
Gap (G)	20 μm	5 μm	

Ansoft HFSS v.14, a full wave EM simulator based on finite element method (FEM), was utilized in the design of unit cell structures. A low loss polymer substrate, PEEK (polyether ether ketone), is used as a substrate material. The substrate thickness is 250 μm and its electrical properties in the THz spectral region are presented in [43]. The dielectric properties of PEEK are: dielectric constant, ε_r=3 and loss tangent, tan δ = 0.05 over a frequency range of 0.1 to 0.6 THz [43]. PEEK is inert to most chemicals used in microfabrication, has low moisture absorption and low thermal conductivity. A solid ground plane (Cu, 1 μm thick with thin Ti adhesive layer) is e-beam deposited on one side of the substrate. A 500 nm thick e-beam deposited nickel (Ni) is used in the patterning of the absorbing structures. The thickness of this conductor is less than the wavelength at 0.1 THz and it is a few times thicker than its skin depth.

Figures 7.2 (a) and (b) shows the simulation results of unit cells of microbolometer operating 0.1 and 0.4 THz, respectively. The proposed SRR is dependent on the polarization of incident waves. Simulations are carried out for both vertical (V-pol) and horizontal polarization (H-pol) incident waves. For the analysis, the array is assumed to be infinite in periodicity and thus Floquet's theorem analysis is carried out on HFSS.

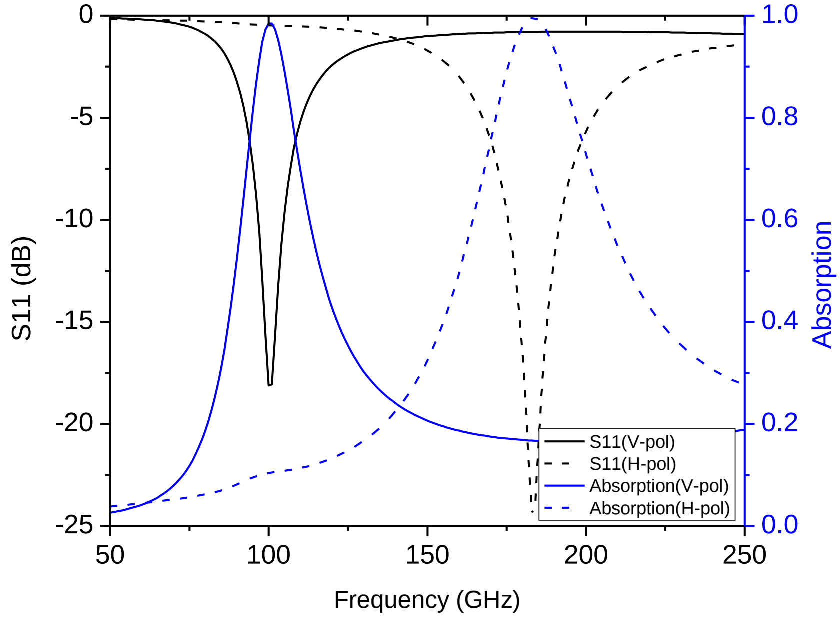

(a)

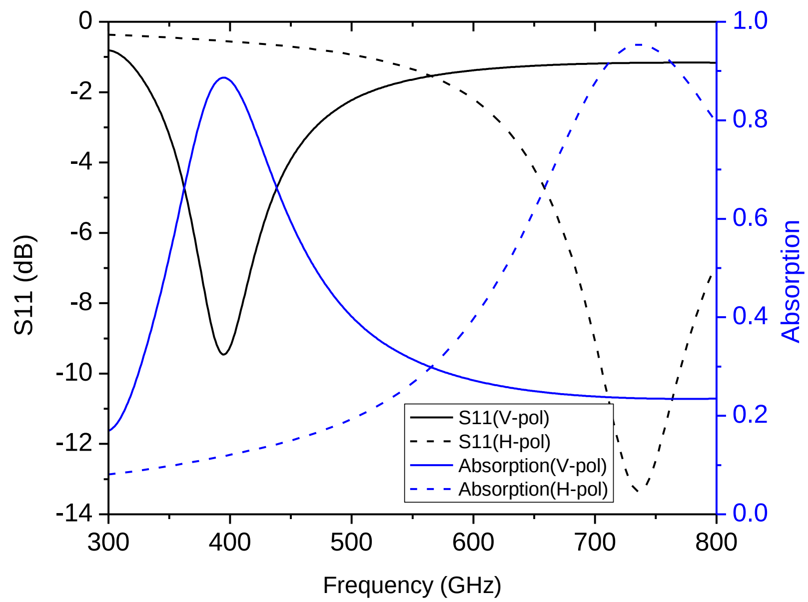

(b)

Figure 7.2 Simulation results (reflectivity and absorption) of a proposed unit cell of imaging array, (a) V- and H-polarization of 0.1 THz unit cell and (b) V- and H-polarization of 0.4 THz unitcell.

In case of vertical incident wave, the resonant frequency of the structure is excited at 0.1 THz. The reflected signal (S11) is approximately -18 dB and this translates to 98.5 % absorption. The absorption is simply calculated by subtracting the reflected power from unitary incident power. The power transmitted through the sample is negligible as there is a solid ground plane present on the opposite side. The usable bandwidth (above 50 % of absorption) of the unit cell (V-pol) is 26 GHz (90 to 116 GHz). In the case of H-pol incident wave, the resonant frequency is excited at 0.183 THz. This is different from the excitement of V-pol resonance frequency because of difference in electrical lengths (shown in Figure 7.3 of surface current distributions).

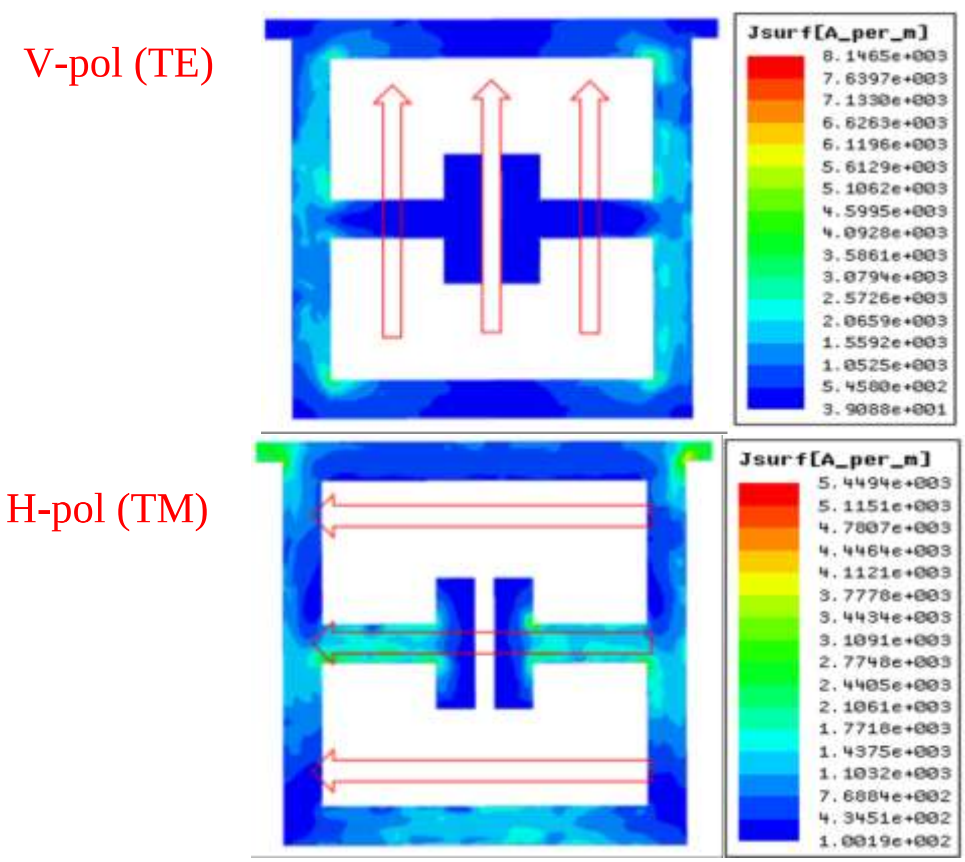

(a)

Figure 7.3 Surface current distributions of each excited mode, (a) Magnitude and (b) Vector of surface currents, V- and H-pol (from up and down).

Figure 7.3 (cont'd)

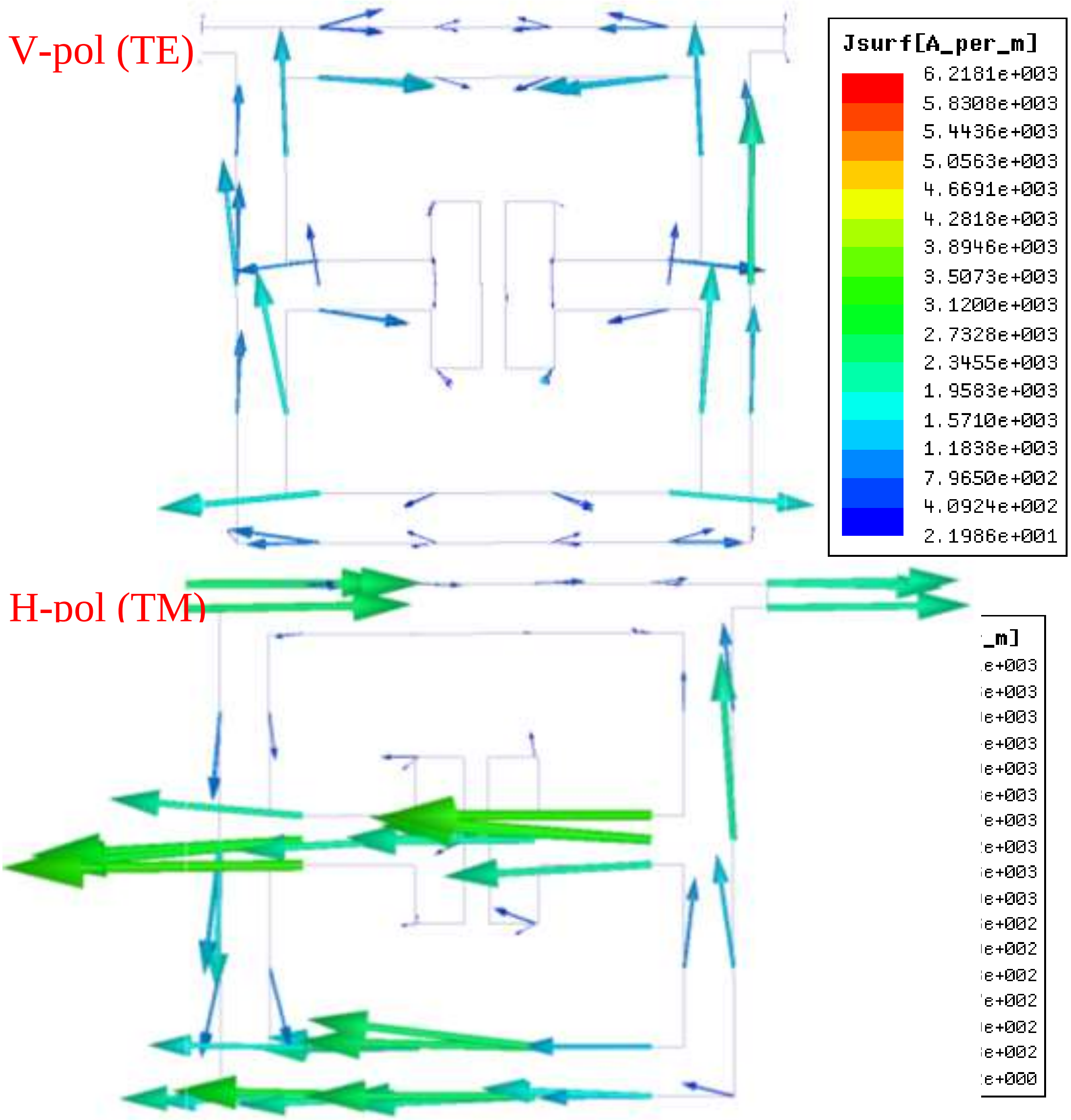

(b)

The minimum S11 was calculated to be -24 dB at resonant frequency of 0.183 THz. The maximum calculated absorption is 99.5 % at this resonance frequency. The usable half power absorption bandwidth was calculated to be approximately 54 GHz (between 0.16 to 0.214 THz).

Similar design and analysis was carried out for a scaled 0.4 THz unit cell structure. For the physical parameters tabulated in Table 1, a 0.394 THz resonance frequency is calculated for

V-pol mode excitation. The reflected signal, S11, is determined to be -9.5 dB. This translates to absorption of 88.7 % at the resonant frequency. The bandwidth of 0.4 THz unit cell (V-pol) is 127 GHz (between 0.350 to 0.47 THz).   For H-pol mode excitation, the resonant frequency was calculated to be 0.736 THz and the reflected signal (S11) is approximately -13.4 dB.

7.1.2 Beam focusing element- dielectric lens

The lens designs were carried out using the design approach outlined in Chapter 6. The operating frequency is chosen to be 0.1 THz, same as the operating frequency of the microbolometer. The simulated results of the lens are shown in Figure 7.4. The lens is composed of the hemispherical part and the extended part. As mentioned in the previous chapter, this configuration has an advantage that it can easily be integrated with microbolometers. Figure 7.4 (a) shows the layout of the extended hemispherical dielectric lens. The physical dimensions of the extended lens are the radius (R) = 9.88 mm and the extension length (L) = 3.85 mm, respectively. For the fabrication, plastic material (Acrylic, ε_r=2.7) was considered. This material is not only suitable for three dimensional printing, but also shows the low loss at THz frequency range. All physical values of the lens are designed to integrate this structure with the microbolometer array. The lens diameter is six times larger than the wavelength of the operating frequency. Figure 7.4 (b) shows the simulated far-field radiation of E-field. The radiation shows the planar wave through the lens on the exciting wave. The waveport is referred to the dimension of a W-band waveguide, the size of a port is 1.6 mm × 1.6 mm, because the wanted frequencies travels well through the waveport and excites and couples to the lens. Also, as increases the port size same as the initial designed array size (area of 3 × 3 array =5.4 mm × 5.4 mm), about 0.55 cm × 0.55 cm, the radiation wave shows the good pattern as expected. Figure 7.4 (c) demonstrates the simulation result of the far-field gain of a dielectric lens. The calculated gain was obtained as 15.5 dB. This performance is similar with lenses to analyze and characterize the chapter 6. The radiation patterns of the lens are described in Figure 7.4 (d). Both radiation patterns of E- and H-plane are well matched with the typical pattern of the dielectric lens with a square wave radiating port.

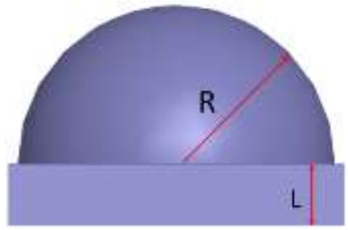

(a)

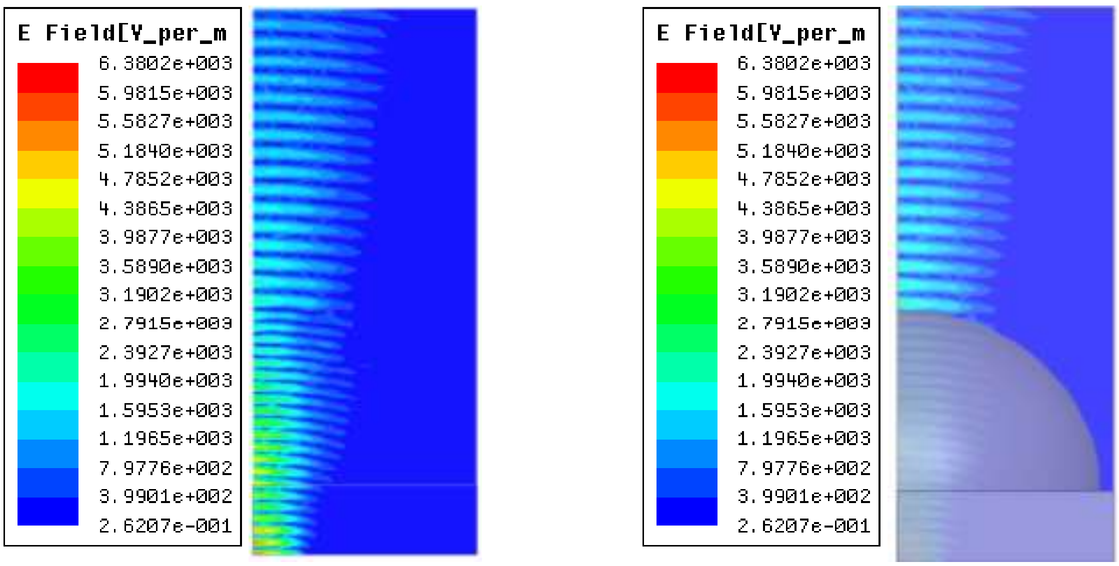

(b)

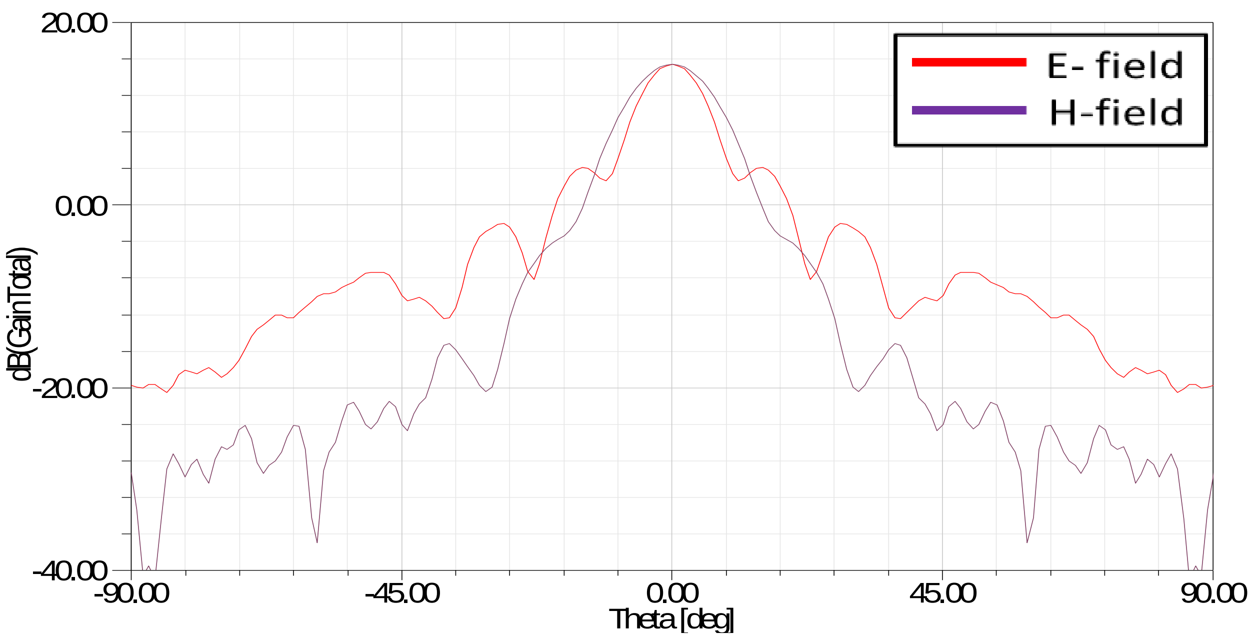

(c)

Figure 7.4 Schematics and simulation results of designed dielectric lens, (a) layout, (b) far-field radiation (E-field), (c) gain, and (d) radiation pattern of the lens.

Figure 7.4 (cont'd)

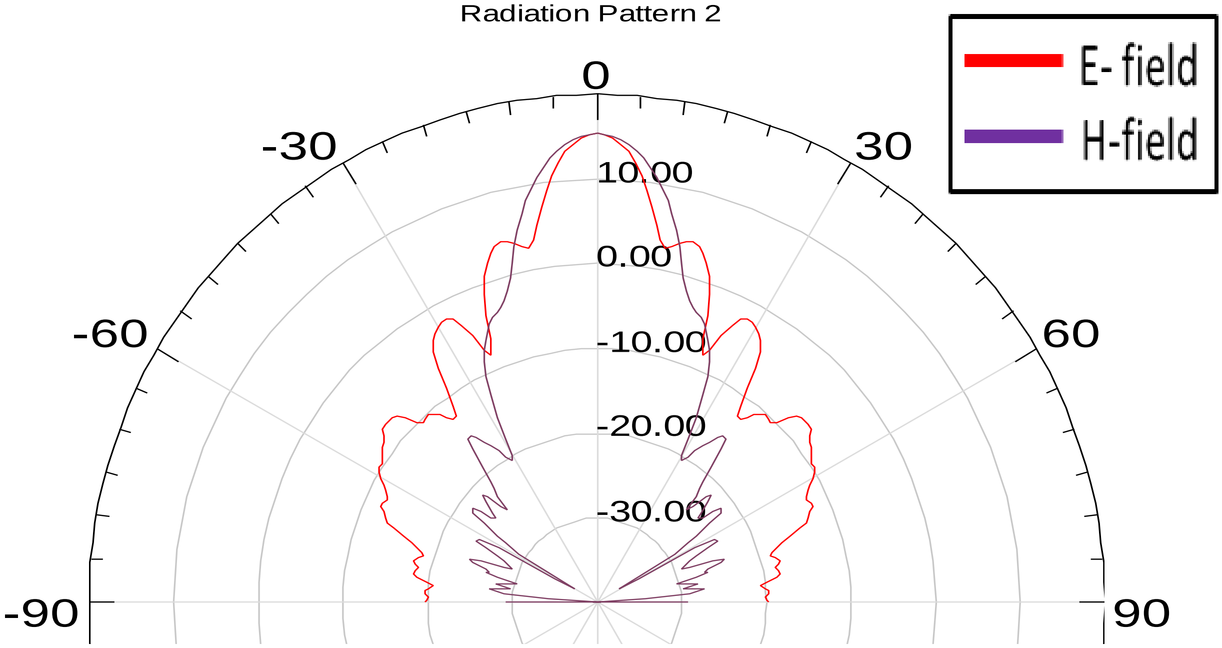

(d)

7. 2. Imaging array layout design

Previous sections, the frequency dependent unitcell for detecting the incident power and beam focusing element, the dielectric lens have been investigated. The goal of this dissertation is to be introduced the multi-unitcell array for imaging system. Thus, the array design must consider the arrangement of proposed microbolometer based on metamaterials working at THz range. Figure 7.5 shows the unitcell alignment to construct the imaging array system. Each pixel is composed of 4 by 4 unitcells. The design of a pixel helps the detecting capability improve because the total resistance of pixel can increase to connect series. The geometry of a pixel is also considered to measure the variation of resistance. One side connects to the signal pad located on outer, and the other side goes to the ground pad shown in Figure 7.5 (a). Figure 7.5 (b) and (c) demonstrate the total layout of proposed THz imaging array systems. The straight connection array consists of nine microbolometers, nine signal pads, and two common ground pads as shown in Figure 7.5 (b). The zigzag connected imaging array, shown in Figure 7.5 (c) is the layout same as the straight connection array.

Pads shown in above figures are composed of copper having a good electrical conductor. The square shape of a pad is for measuring the alteration of surface resistance each pixel. The ground plane is produced in two circular pads on the designed layout. Total size of the 3 × 3 THz imaging array is 2 cm × 2cm (including test pads), the detecting area where is placed pixels is approximately 7.5 mm × 7.5 mm. Fabrication of this structure requires two mask layers. The first mask layer is to pattern the Ni layer and the second mask is needed to pattern the Cu pads and traces.

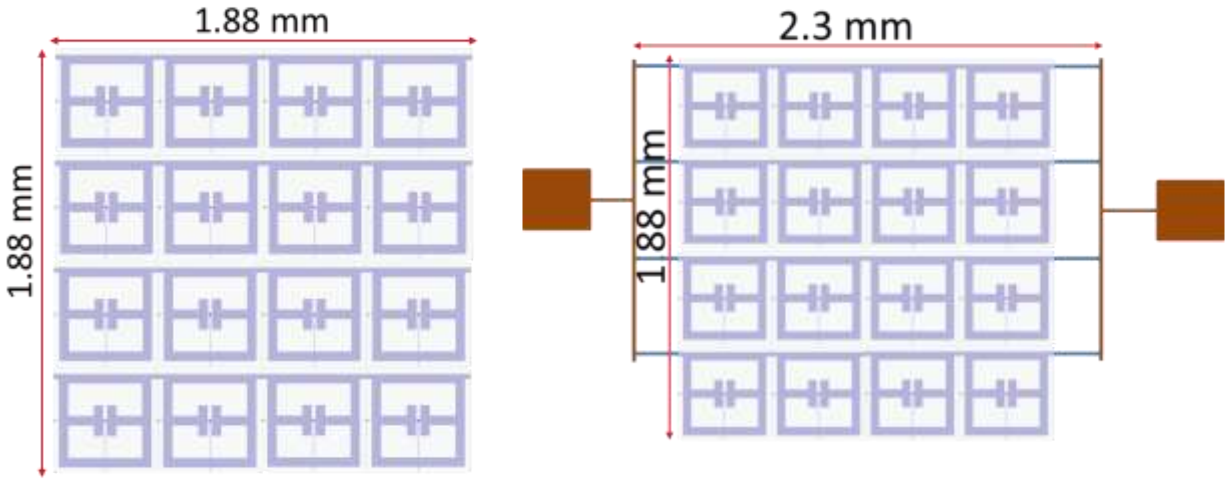

(a)

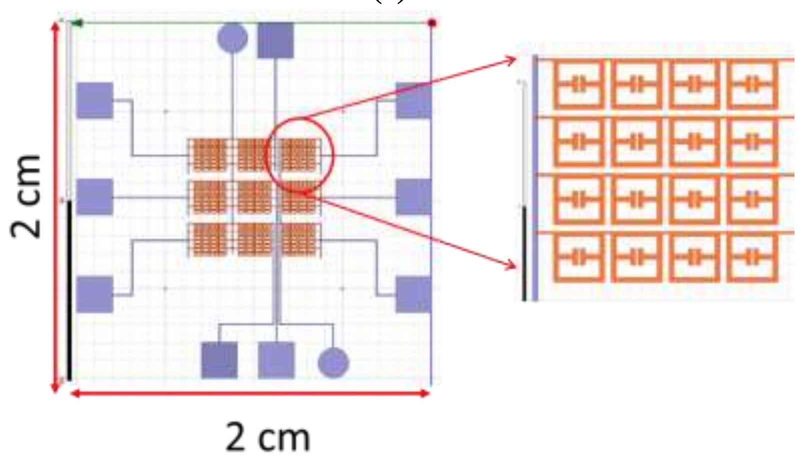

(b)

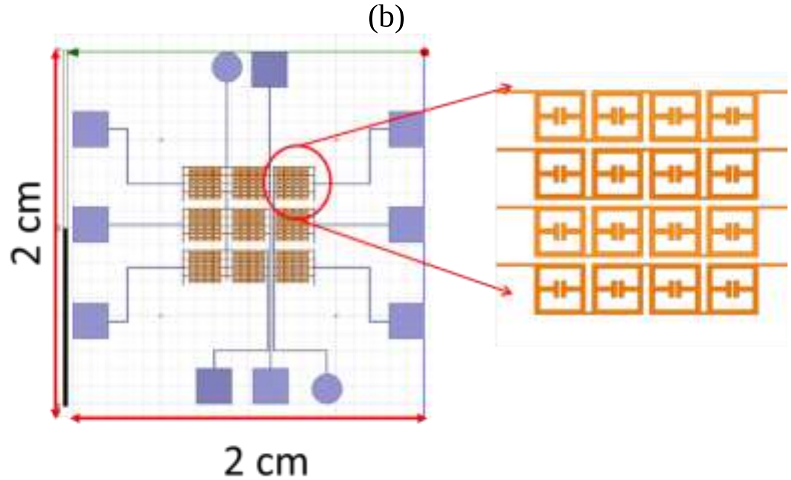

(c)

Figure 7.5 Layouts of 0.1 THz imaging array pixels, (a) configuration of a pixel, (b) the straight connected imaging array, and (c) the zigzag connected imaging array.

7. 3. Fabrication

In order to fabricate designed THz imaging array, the microfabrication process was used to implement the THz imaging pixel array. First step of the process, using acetone, methanol, and isopropanol, the substrate that used same as the simulation considered, LCP and PEEK should be cleaned to remove the residual particle and dust on. After drying in an oven, photoresist, Shipley 1813 positive photoresist, is deposited on the substrate to use a spin-coater. The speed of the spin-coater is set as 4000 rpm, and the time set as 30 sec. This can be achieved with 1.5 μm of the photoresist thickness. After deposit the photoresist, the baking should be conducted in the hot oven or on the hot plate for 10 minutes (hot oven) or 1 min (hot plate). Then, using UV source, the lithography has been carried out for 1.1 min. In development process, to immerse the illuminated sample in MF 321 developer for 25 sec and 10 sec in a row, also in order to get the best results, the brief oxygen plasma “de-scum” was used between lithography and metal deposition [80 - 82]. This de-scum process will remove any thin photoresist residue that could cause poor metal adhesion or contact. A 120W, 30 second oxygen plasma at 100% O_2 flow rate (all other gases off) should be sufficient. The e-beam evaporator was utilized to deposit the first layer metal, nickel on top of the photoresist. Metallic layers are composed of double layers using different metals. In order to enhance the adhesive metal deposition, titanium has been used for an adhesive layer (t= 300 Å). The deposition ratio of nickel was set as 0.5 Å/sec to metallize the nickel pattern to make even surface roughness and 5,000 Å of final thickness of nickel was achieved. The metal liftoff was performed with a sonicator. The sonicator help decrease the lift-off time required for the acetone soak. However, the sonicator doesn’t use over 5 min to avoid the metal stress due to thin (< 1 μm) metal film. Once the lift-off is completed, washing it with isopropanol and agitate for 1 minutes and rinse with DI water and dry out with

N_2 gas. To produce second layer of the THz imaging array, follow the same procedures such as spinning coating, lithography, and developing. On photoresist deposition, to adjust the spinning speed 4,000 to 2,000 rpm, this setting helps the thickness of photoresist deposit up to 2 μm. This thickness supports to help the second metal lift-off process. The sputtering has been used to deposit the second metal layer (copper) on top of the first layer. Also, using the lift-off process mentioned above, the unwanted pattern metal layer is removed. The detail process is described in Figure 7.6.

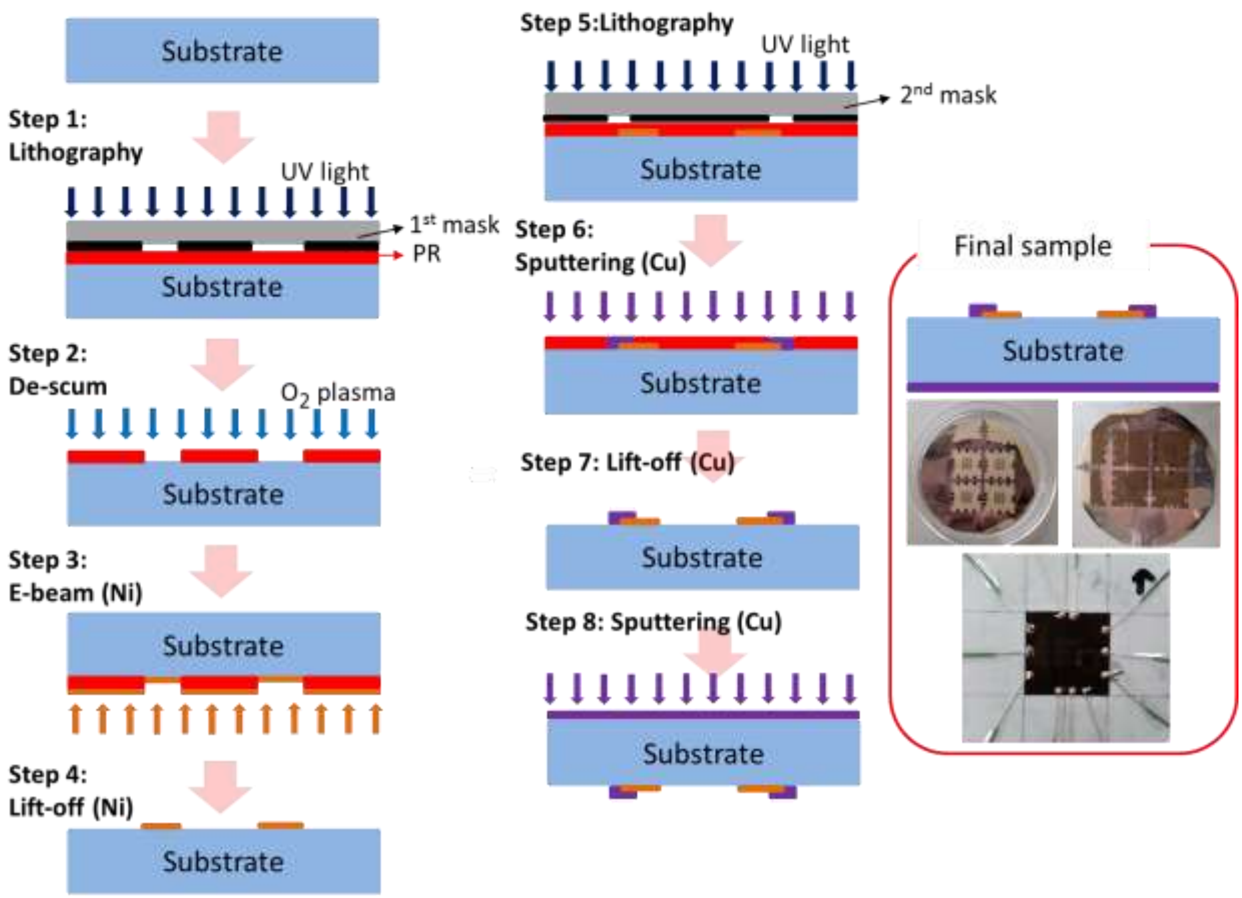

Figure 7.6 Microfabrication process of a proposed THz imaging array.

Figure 7.7 shows example photographs of the fabricated THz imaging array. The physical dimension of the fabricated nickel microbolometer pixel array was inspected using a microscope. As shown in pictures, the metal patterns and interconnections were well aligned the exact positions that designed on mask layouts.

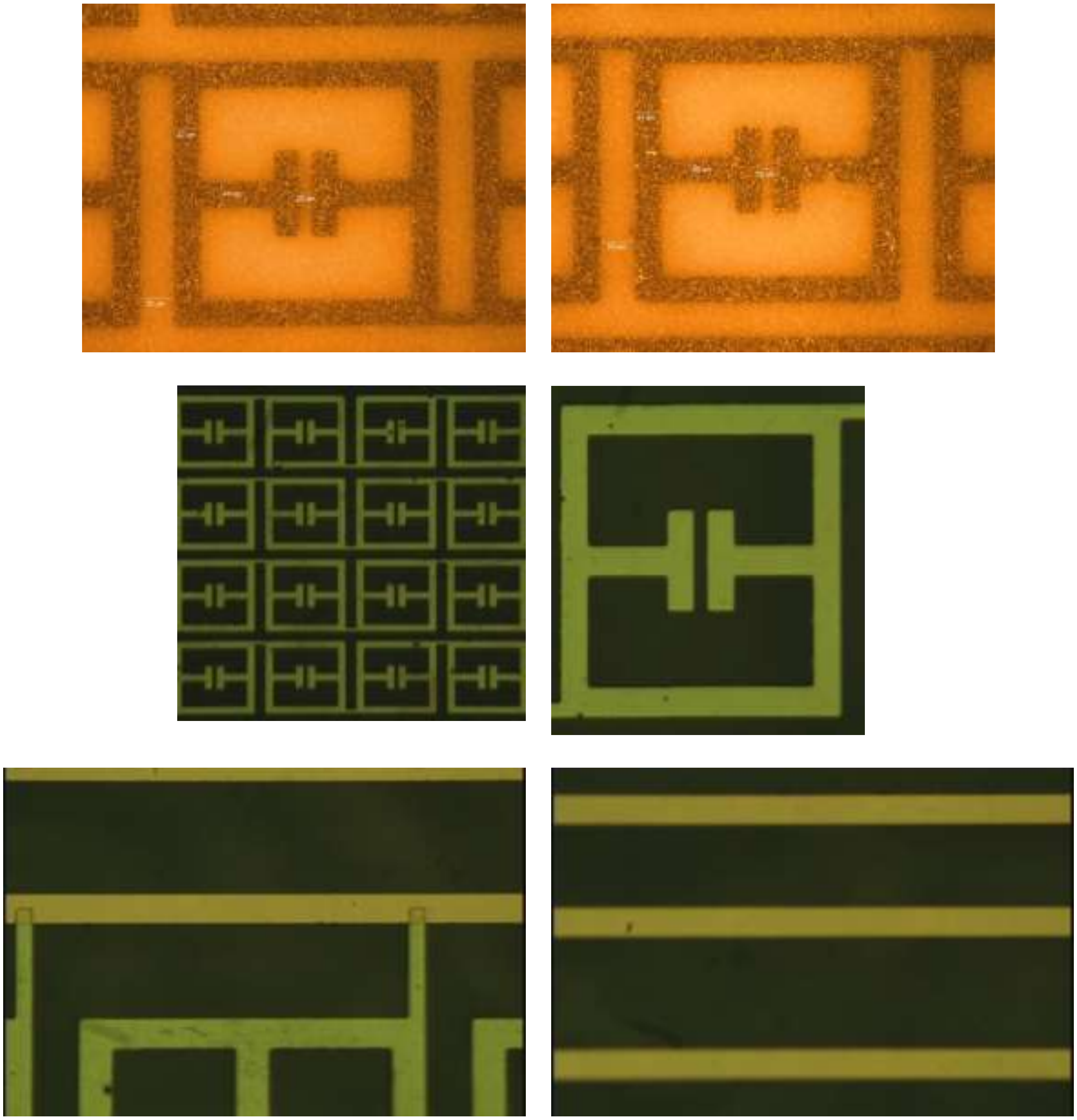

Figure 7.7 Microphotographs of manufactured THz imaging array.

7. 4. Experimental measurement setups

Two measurement setups are used in the characterization of the pixel elements and the imaging array. First setup is made to determine the absorbed power by the pixel elements and the second setup is made to characterize imaging characteristics of the fabricated devices.

The setup for the measurement of power absorbed depicted in Figure 7.8 (a). In this setup, an array of absorbing elements is placed in front of the horn antenna. A W-band directional coupler is attached between the horn antenna and the backward wave oscillator (BWO, W-band source). A W-band receiver (a calibrated harmonic mixer) attached to the directional coupler was used to measure the reflected power. For calibration, a flat metal sheet was used that was placed at the same distance as the absorbing elements. The reflected signal from the reference and the array elements was measured and the difference in signal is used to calculate the absorbed power.

An open-ended W-band waveguide was used to illuminate the object to be imaged. Measurement was setup for capturing the image in the transmission mode depicted in Figure 7.8 (b). Since the array is composed of 3×3 array, a 2-axis robotic manipulator was used with step resolution of 200 μm on each axis to raster the sample to be able to capture a complete image of the sample. A multimeter along with data acquisition was used to measure the resistance across the individual pixel elements. The THz imaging array was fixed, whereas the object under scan was attached to the robotic arm. Through this setup, change of surface resistance of each pixel across the array was measured to capture the image.

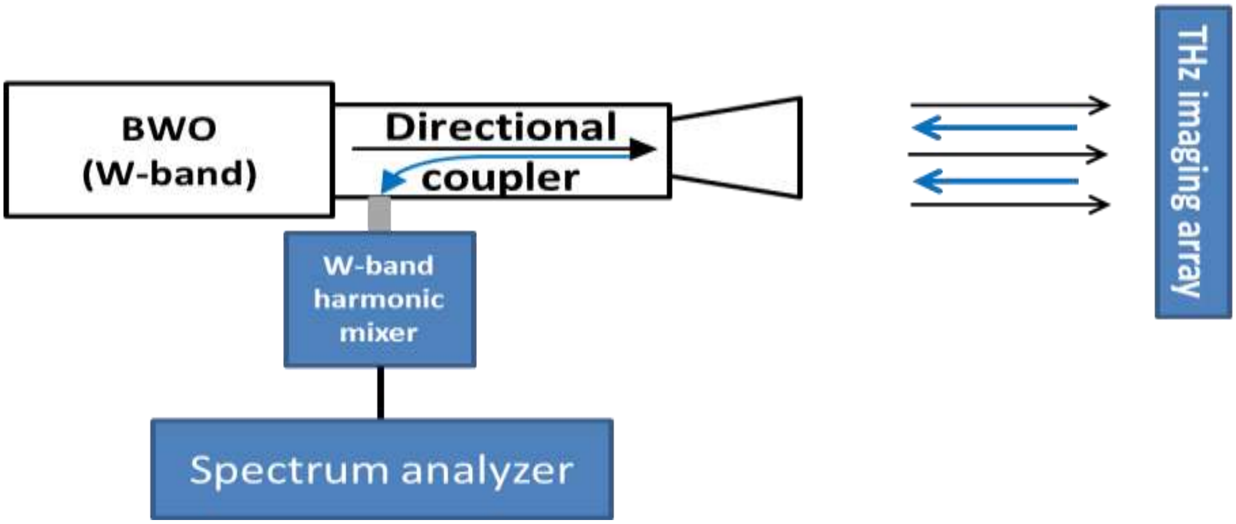

(a)

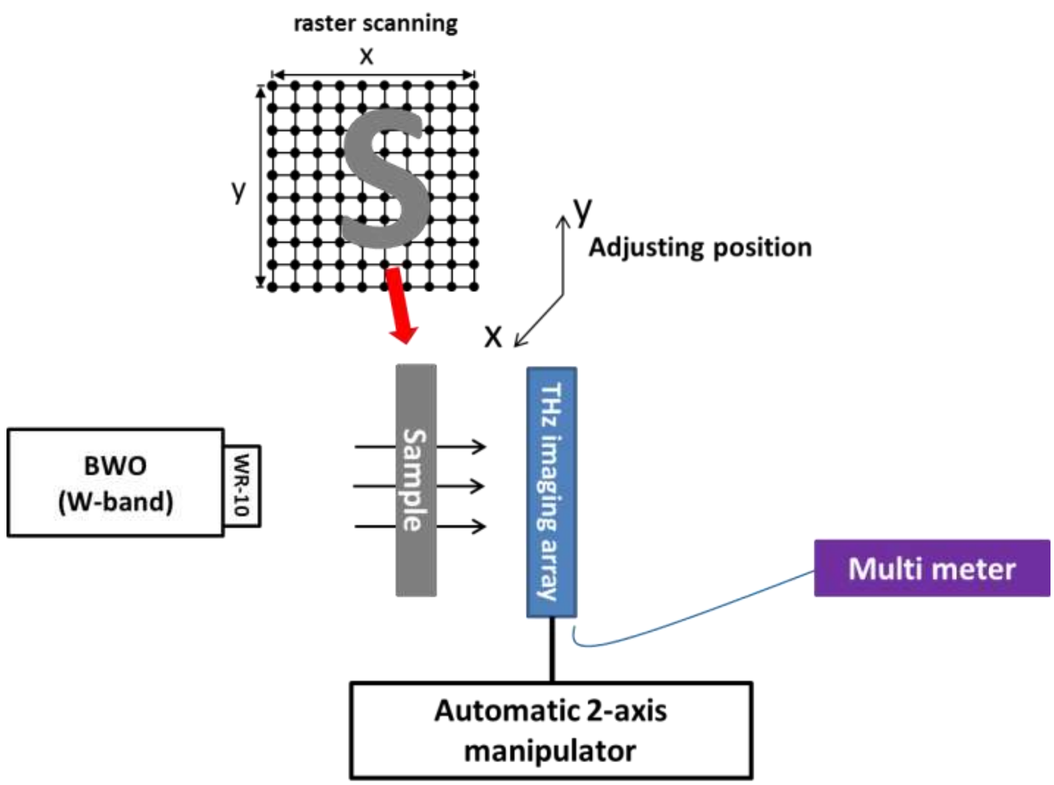

Figure 7.8 Measurement setup block diagrams, (a) Absorption measurement setup, and (b) Imaging measurement setup.

Generally, the noise equivalent power (NEP) of a bolometer is defined as the power needed to achieve a signal to noise ratio of unit at 1 Hz bandwidth [83]. To indirectly measure the intrinsic NEP of the bolometer, a bias circuit with a DC voltage and a load resistor was used. In this configuration [28, 29], a voltage is applied across the series connected bolometer and fixed temperature insensitive resistor. A voltage drop is measured across the bolometer as a function of applied current. The detail layout of a measured setup is shown in Figure 7.9.

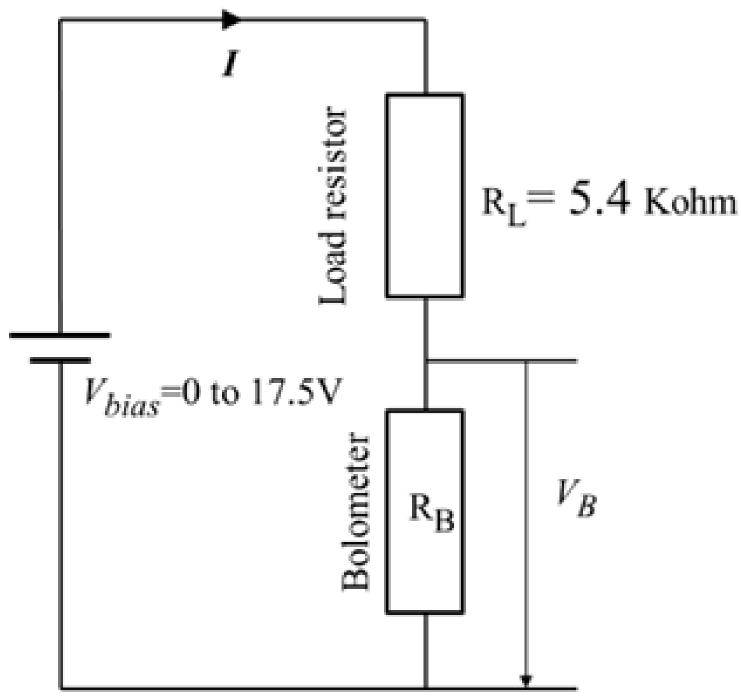

Figure 7.9 Measuring setup of noise equivalent power.

7. 5. Measurement results

Absorption measurements were carried out from 85 to 105 GHz with step resolution of 1 GHz. Figure 7.10 shows the measured result of the proposed THz microbolometer array. In order to characterize the absorption of the bolometer array, the main orientation of polarization, vertical polarization was excited. The measured results matches closely with the simulation results (V-pol: 0.1 THz at Figure 7.2 (a)). The results show strong absorption for V-pol from 87 GHz to 107 GHz (shown in Figure 7.10). The absorption is determined to be 9.8 dB at 102 GHz. It is lower than the simulated absorption of 18 dB. Rest of frequency range could not be measured as the source frequency is limited to 110 GHz. However, we can estimate that the performance of rest of frequencies will have similar results as the simulation results shown in Figure 7.2 (a).

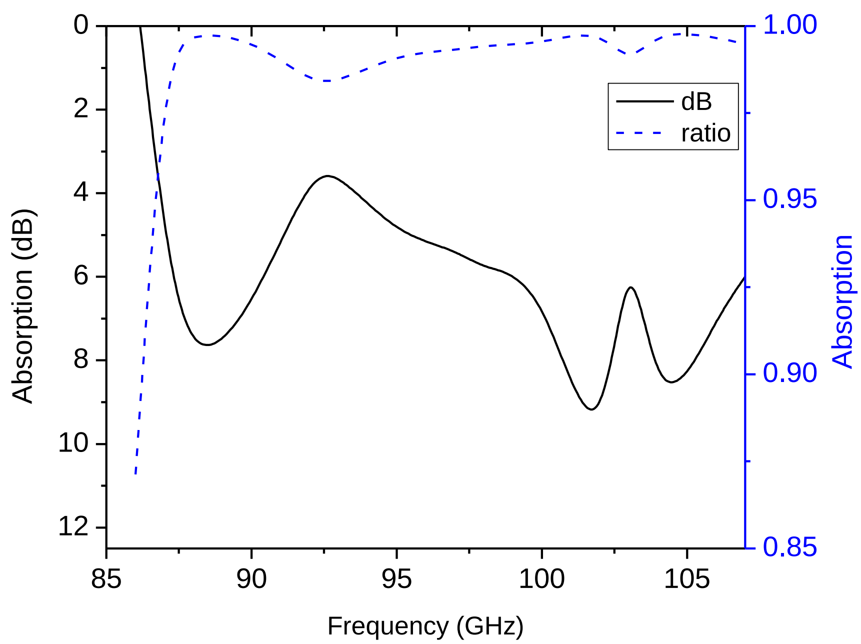

Figure 7.10 Measured result of power absorption of THz imaging array.

Figure 7.11 shows the measured resistance of a bolometer versus applied current while the environment temperature is fixed (T=296 ^{o}K). The power drop across the bolometer converts to heat and which in turn increases the resistance of the bolometer as seen in Figure 7.11 (a). This can be plotted as a function resistance versus power drop across a bolometer as shown in Figure 7.11 (b). The slope of Figure 7.11 (b) gives the sensitivity of the bolometer. NEP of the bolometer can be calculated using the slope (sensitivity), TCR of the film and Johnson noise [29, 83, 84]. The TCR of Ni was introduced in Figure 4.6 with similar thickness processed using e-beam (α=2.7×10^{-3} grad^{-1}). Using these measure results and supposing the Johnson noise is the only parameter defining the radiation equivalent to the power of the NEP, the calculated intrinsic NEP of a bolometer is 1.652×10^{-9} W/Hz$^{1/2}$. Considering to the absorption property of the bolometer, the estimated the NEP of a sample can be analyzed 8.26×10^{-9} W/Hz$^{1/2}$ at 100 GHz due to the frequency shifting. The detailed parameters that used to calculate the NEP are shown in Table 7.2.

Table 7.2. NEP calculated parameters

Parameters	value	Remarks
Resistance (R)	R_0=49.153 Ω	No bias
	R_1=166.3 Ω	I=17 μA V=13V
Power (W)	82.5 μΩ	
Responsivity (S)	0.997 V/W	$S = I * \frac{dR}{dW}$
$NEP^2 = \frac{4kTR}{S^2}$		

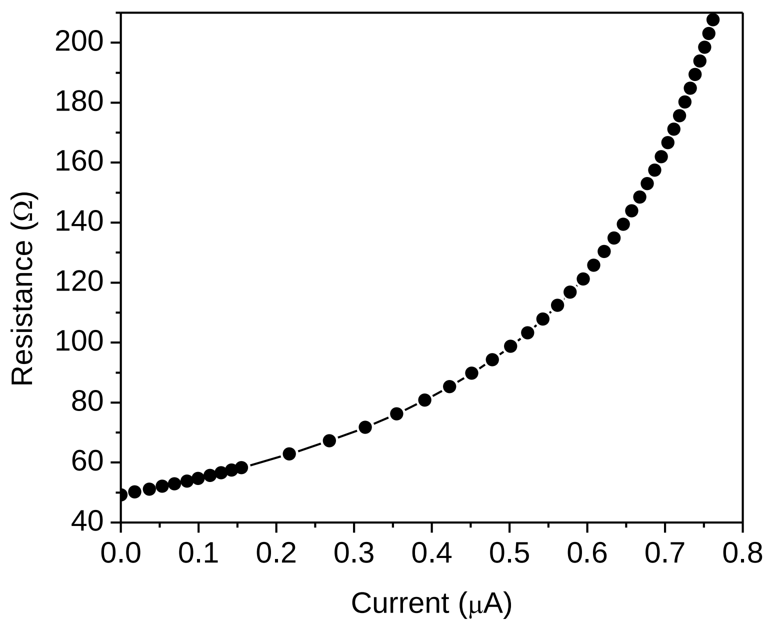

(a)

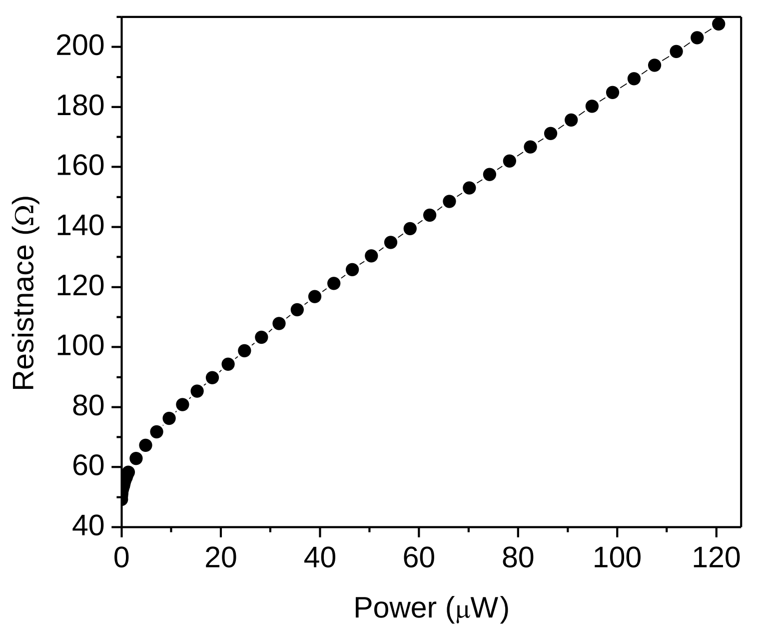

(b)

Figure 7.11 Measured resistance versus (a) current and (b) power.

In order to demonstrate the viability of the proposed imaging array, an imaging scan was carried using the fabricated structures. Figure 7.12 (a) shows a photograph of a sample with punched holes in a metallic sheet. The minimum size of holes is 0.9 cm × 0.9 cm which is approximately twice the size of a pixel element on each side. Figure 7.12 (b) shows the transmitted signal as a function of position across the sample. The measurement step of X- and Y-axis robotic arm set at 6mm in each direction. A total of 11 × 11 = 121 points are measured over the XY plane and the spacing between the source and the detector was set to approximately 7cm.

The setup shown in Figure 7.12 (b) can be used in transmission measurements and shapes of structures can be resolved using a bolometer pixel element. Scattering at the edge of punched holes makes the holes appear larger than their actual size. For the measurement of an actual sample hidden in a paper envelope the setup shown in Figure 7.13 (a) was used. Here, to minimize scattering and to attain a close to a plane wave impinging on a sample an open ended WR-10 waveguide at the source end was used in place of the horn antenna. Furthermore, the raster steps were decreased to improve resolution. Measured image of a metalized sample placed in an optically opaque envelope between the source and the imaging array is shown in Figure 7.13. In this picture, colors represent the density of the signal after passing through the sample. Blue color represents low-transmission and red color represents regions with high transmitted signal. The physical size of the sample is approximately 2.8 cm × 2.5 cm. In this measurement, the axial step size is set as 2mm per step. A total of 21 × 21 = 441 points are collected in the XY plane. The image scanned clearly shows the hidden object. This clearly shows that proposed imaging array of this paper can be used in high sensitivity imaging applications.

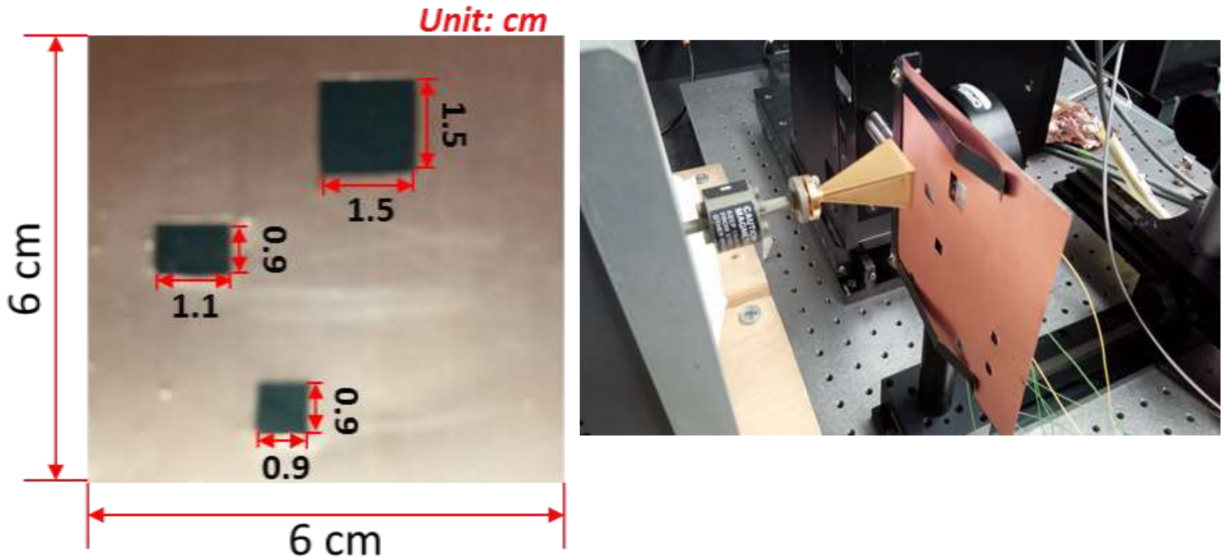

(a)

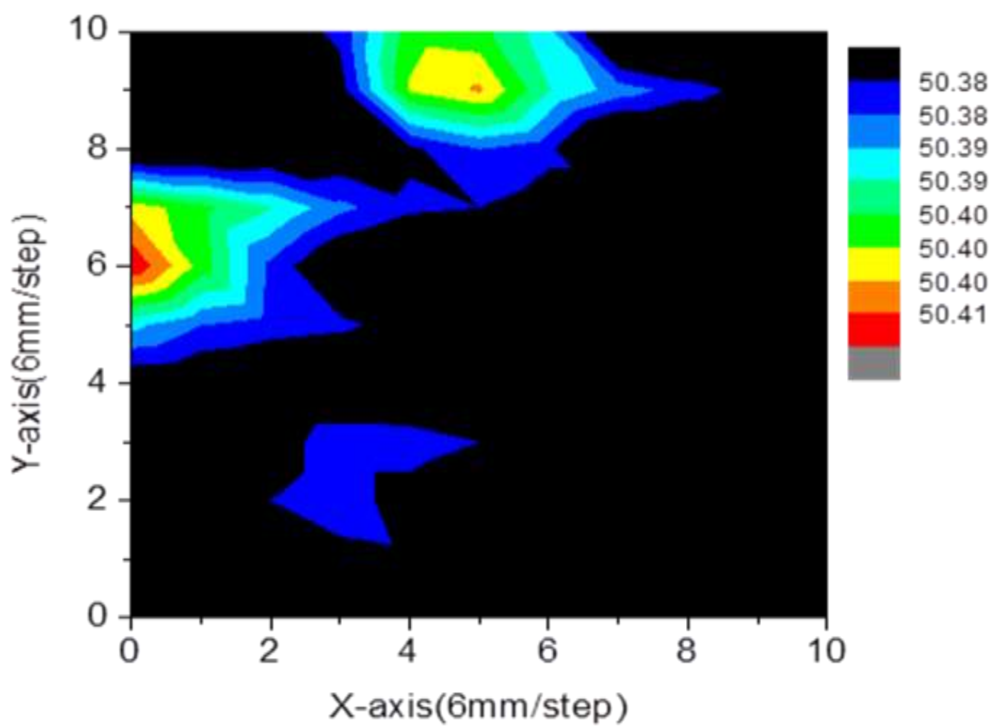

(b)

Figure 7.12 Measurement setup (a) and scanned result (b) of punched holes on the metallic sheet.

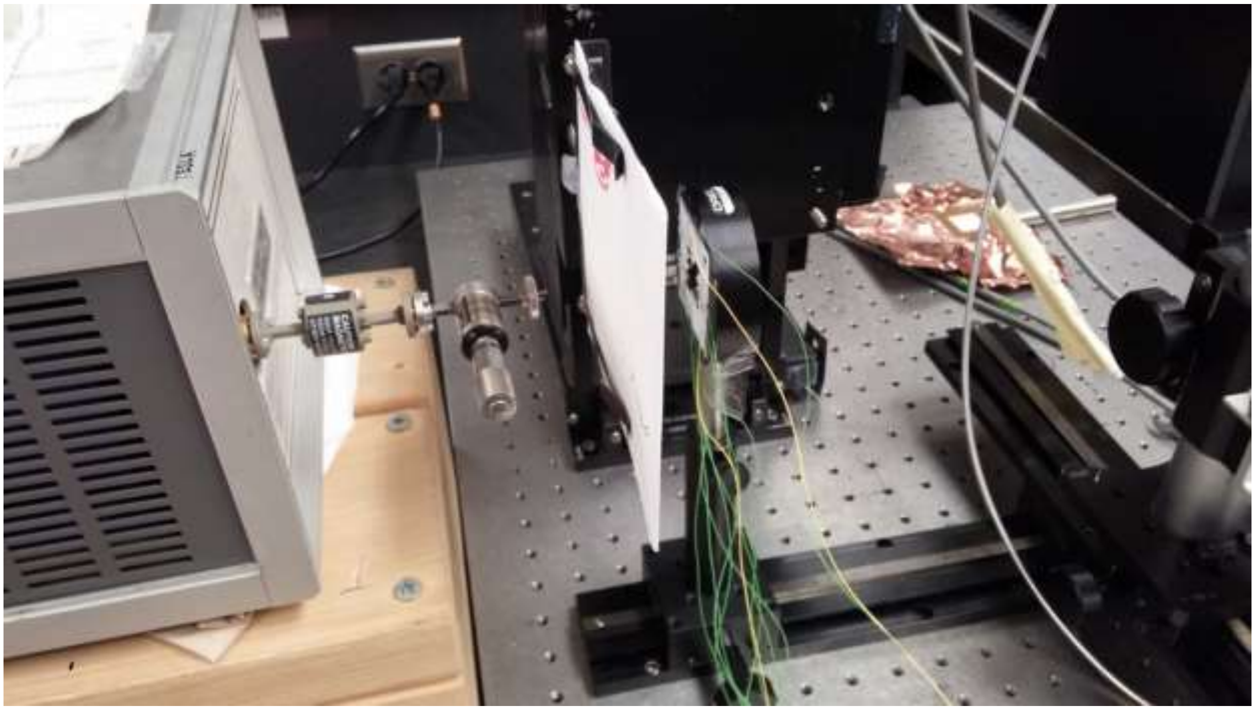

(a)

(b)

Figure 7.13 Scanning layout and results of concealed S-shaped metal, (a) scanning layout, (b) scanned metallic S-shape pendant, (c) and (d) scanned results with different scanning resolution.(set raster scanned resolution: (c) 4mm/step and (d) 2mm/step).

Figure 7.13 (cont'd)

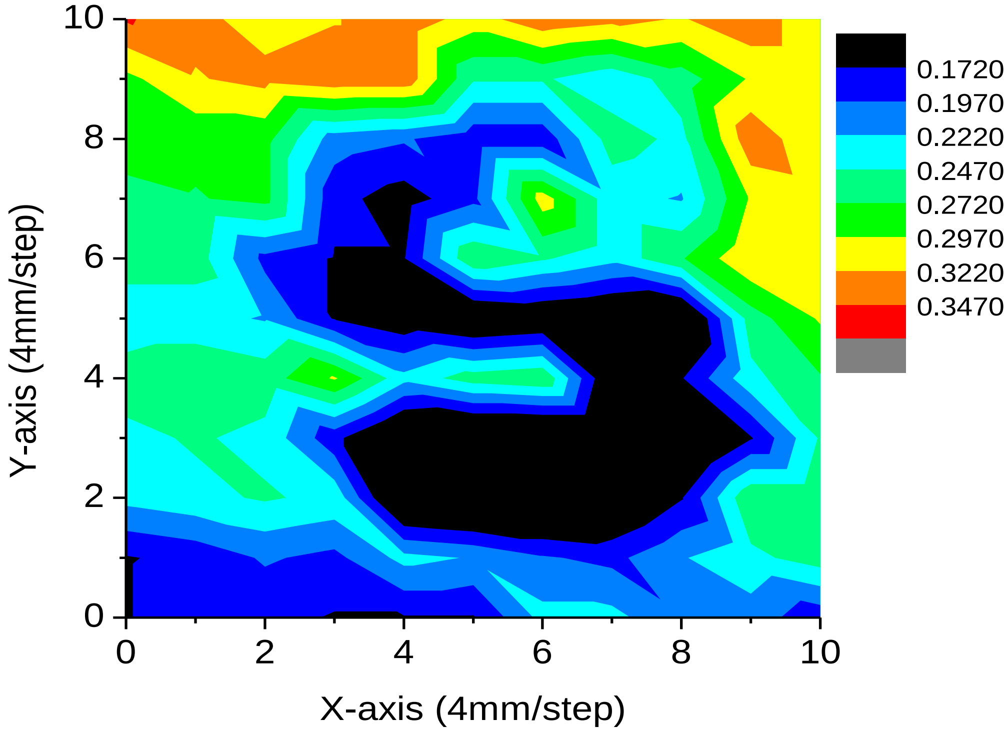

(c)

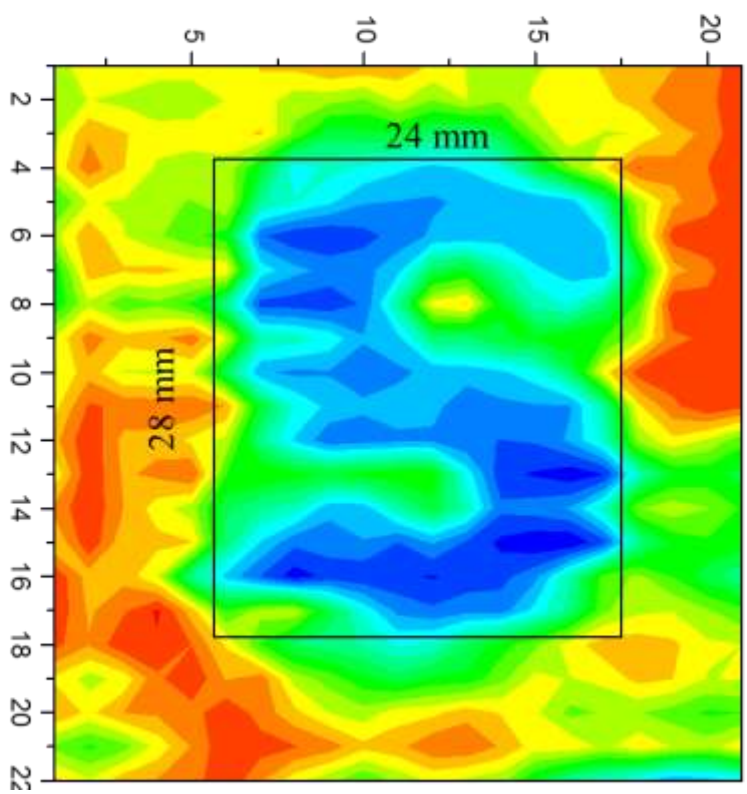

(d)

7. 6. Further improving NEP of the bolometer

We discussed about the new THz imaging array in previous sections. The most important parameter, the NEP of the bolometer which is mainly composed of the imager, must be considered to develop the imaging array. In this section, we would introduce the way to improve the NEP of the bolometer further. Normally, the thermal bolometer has a noise that is only related to the variation of the heat loss to the heat sink, and the thermal coupling radiates purely [28, 29, 83]. Thus, the NEP is derived by

$$NEP = \sqrt{\frac{16A\sigma kT^5}{\epsilon}} \qquad 7-(1)$$

Where A is the area of a pixel (m^2), σ is Stefan-Boltzmann constant ($=5.67\times10^{-8}$ $J/(m^2 \cdot S \cdot K^4)$), k is Boltzmann constant ($=1.374\times10^{-23}$ J/K), T is the temperature (°K), and ϵ is the emissivity [83]. From this equation, the NEP could be manipulated by adjusting parameters of the equation. For example, as decreasing the effective area of a pixel or increasing the absorptance of a bolometer, the value of NEP goes smaller, it can be achieved the higher sensitivity of the bolometer.

Our approach originates from miniaturizing the effective area of a pixel. As similar as the proposed metamaterial bolometer, other candidating models based on modified slit ring resonator (SRR) structure are considered to build up the low NEP compact bolometer [85].

7.6.1 NEP analysis

In this section, the intrinsic NEP of the bolometer will be introduced. From the equation, 7 – (1), we can estimate the intrinsic NEP of the ideal bolometer. This computed NEP is used as a reference value to compare the performance of practical bolometers. It has been indicated that this reference to assume a perfectly noiseless environment of the bolometer [86]. Here is an example to analyze the NEP of a bolometer. Assume a blank metal layer that is composed of an absorbing layer on a typical infrared bolometer. The amount of absorbing incident wave by the bolometer is considered as 0.5 (equal to 3dB of the reflectivity). Figure 7.14 (a) shows the calculated intrinsic NEP according to different physical size of a bolometer. In this computation, we assume that the bolometer is operated at room temperature and the physical size is a 50 μm × 50 μm of a bolometer. The intrinsic NEP of it would be calculated as 3.16×10^{-13} W/Hz$^{1/2}$ at room temperature. Under same condition, when the dimension has been changed, the NEP is analyzed to increase the NEP. It means the performance of the bolometer to degrade. Another example, there are two bolometers to have same physical dimension (300 μm × 300 μm), only difference between two samples is the absorption (ϵ), one is 0.5 and the other is 0.95. In this case, the higher absorption (ϵ = 0.95) bolometer shows the lower NEP (=1.37×10^{-12} W/Hz$^{1/2}$, depicted red dot in Figure 7.14 (a)) compared to the lower absorption (ϵ = 0.5) bolometer (=1.9×10^{-12} W/Hz$^{1/2}$), approximately 72 % degradation. Through, this analysis, we can say that higher absorption bolometer is able to work better performance than the lower and verify our approach, high absorption and small effective area to enhance the bolometer performance by this analysis.

Figure 7.14(b) shows the relationship between temperature and the NEP. Compared to the variation of NEP dependent on dimension, it of NEP dependent on temperature changes rapidly, roughly seven order of the calculated value. It is because the main factor of the equation, 7-(1) is temperature (T) having the variation of temperature to the fifth power.

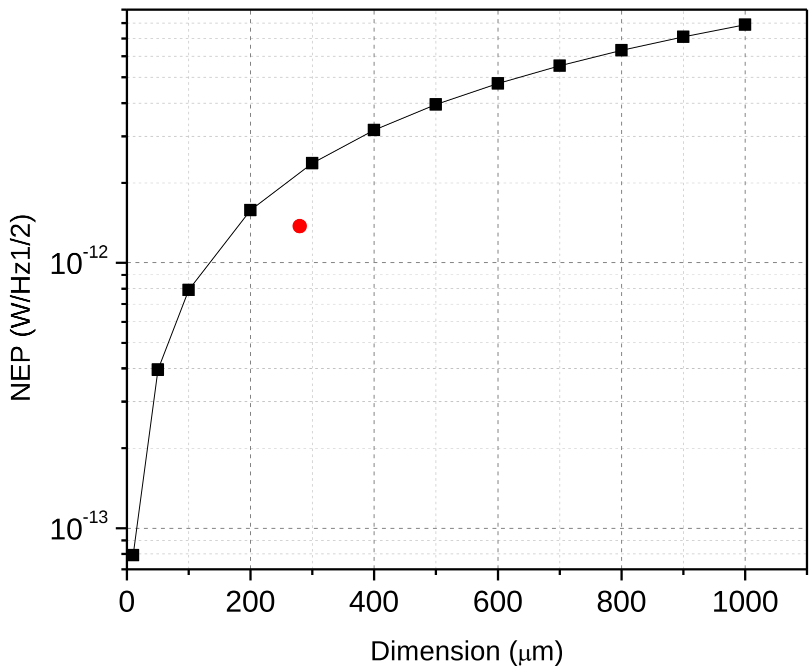

(a)

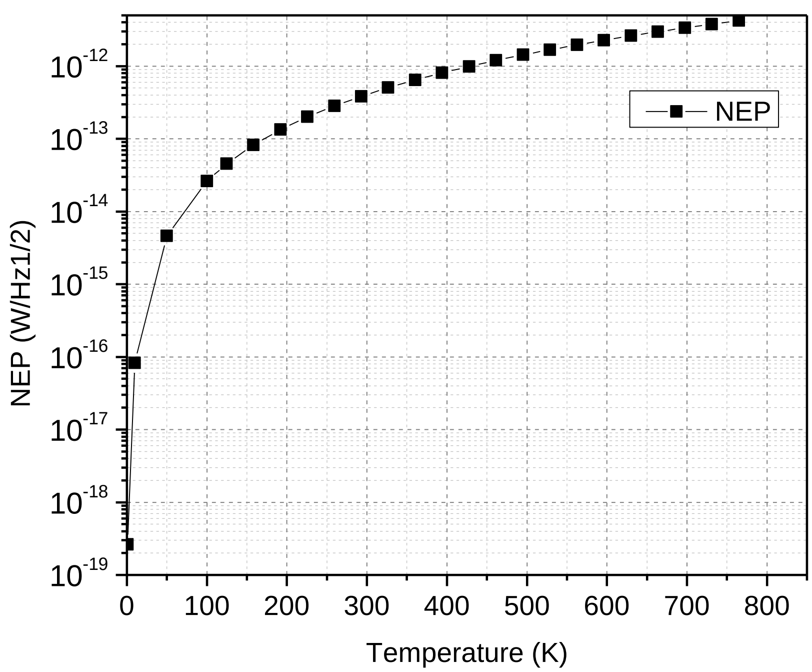

(b)

Figure 7.14 Analysis result of NEP, (a) dimension dependent and (b) temperature dependent.

7.6.2 Miniaturized metamaterial (U-shape) bolometer

The physical dimensions of a miniaturized bolometer are the periodicity (P) of a unitcell is 360 μm, the length (L) of a unitcell is 298.6 μm shown in Figure 7.15 (a) [85, 87 - 90]. In order to improve the absorption of the proposed bolometer, we investigate the relation between the number of the arm and the amount of absorption. The width (w) and gap (g) of a unitcell are designed as 20 μm and 18 μm, respectively (depicted in Figure 7.15 (a)). The spacing (S) between arms is set as 10μm. Schematics of absorbers that are adjusted the number of arms are described in Figure 7.15 (b), (c), and (d). The detail physical information of the unitcell is summarized in Table 7.3. The entire geometry of the proposed bolometer is composed of a patterned conductor layer (top layer), dielectric substrate (middle layer), and ground plane in side of a substrate (bottom layer). PEEK is adopted as a substrate same as introduced sample discussed in previous sections. The conductor material is considered as nickel (Ni) to simulate and fabricate the proposed absorber.

Table 7.3 Physical dimensions of the miniaturized (U-shape) bolometer

Physical dimensions	values	Remarks
P	360 μm	- Frequency: 100 GHz - Material: PEEK - Metal: nickel (Ni, 500 nm) - $\lambda/P = 8.33$ @ $\lambda = 3mm$
L	298.6 μm	
g	18 μm	
W	20 μm	
S	20 μm	

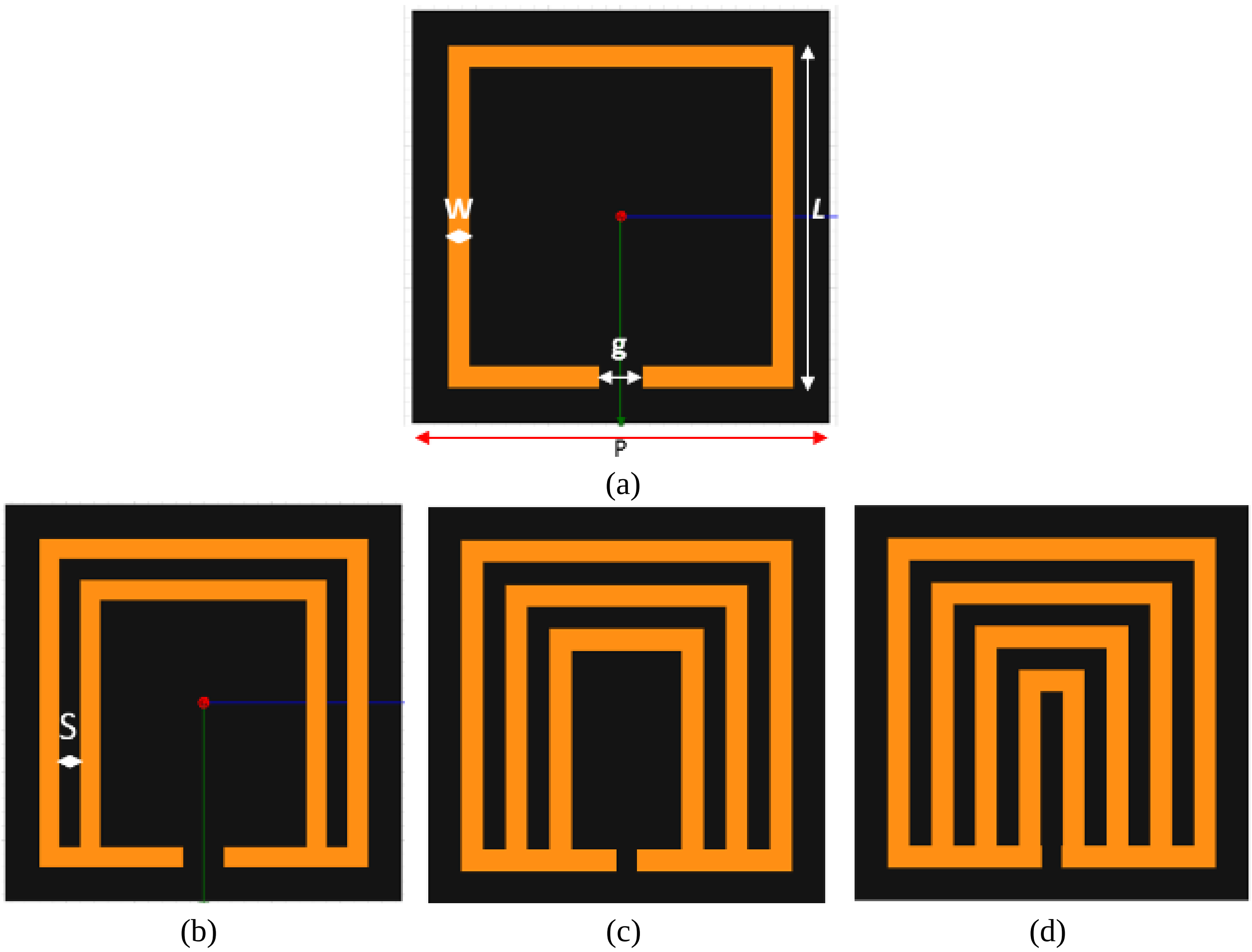

Figure 7.15 Schematics of the miniaturizing (U-shape) bolometer structure, (a) single arm, (b) double arms, (c) triple arms, and (d) quad arms.

The proposed bolometer is analyzed EM properties by using HFSS as the same manner as absorber that studied in previous chapters. Figure 7.16 and 7.17 demonstrate simulated absorption properties of a U-shaped bolometer with vertical and horizontal E-polarization, respectively. In Figure 7.16, the reflectivity of a single arm is computed as 3.15 dB at 103.1 GHz that is equivalent to the converted absorption, approximately 0.52. In case of a U-shape bolometer having quad arms, the reflectivity shows -14 dB at 109.7 GHz (absorption = 0.96). Simulated results of the bolometer having double and triple arms describe high absorption (0.92 and 0.95).

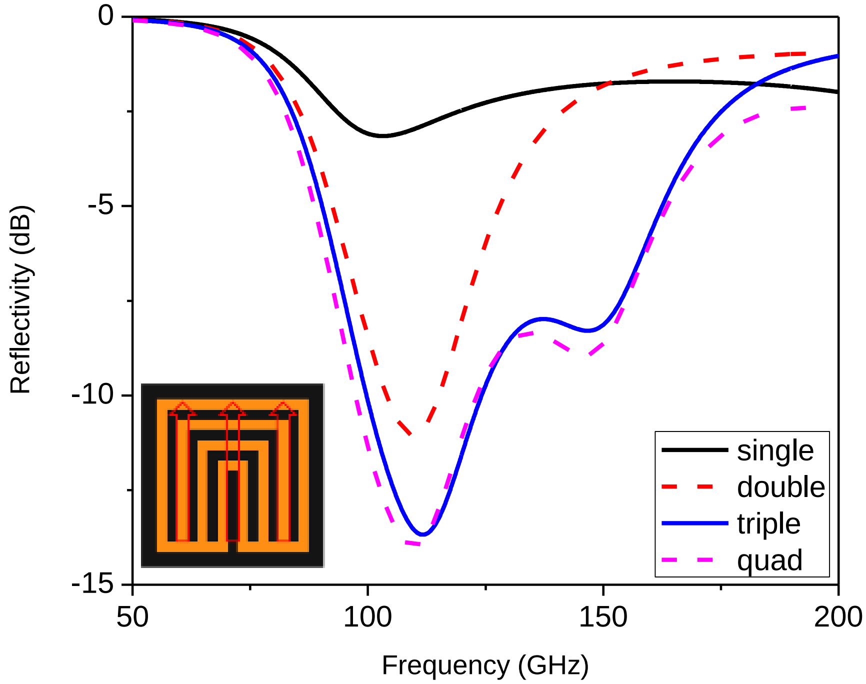

(a)

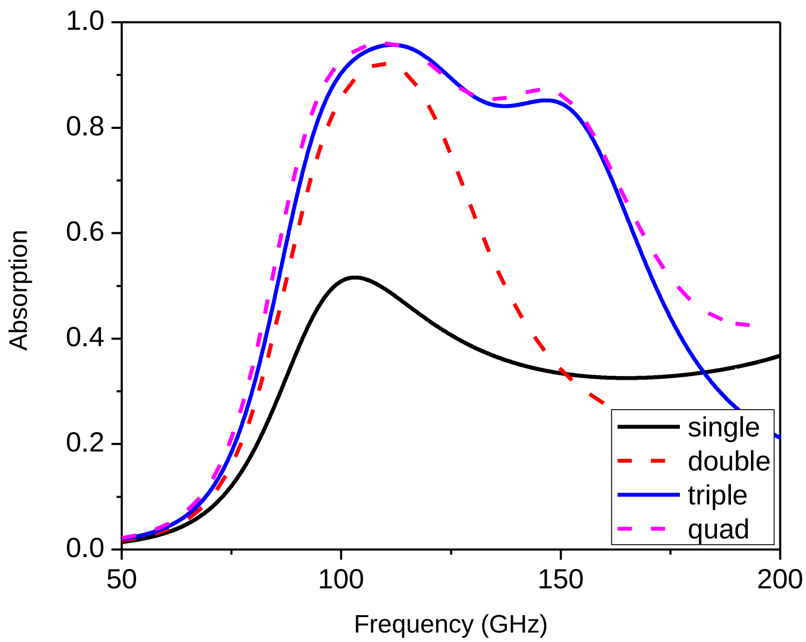

(b)

Figure 7.16 Simulated results of a miniaturized (U-shape) absorber (V-pol.), (a) reflectivity and (b) absorption.

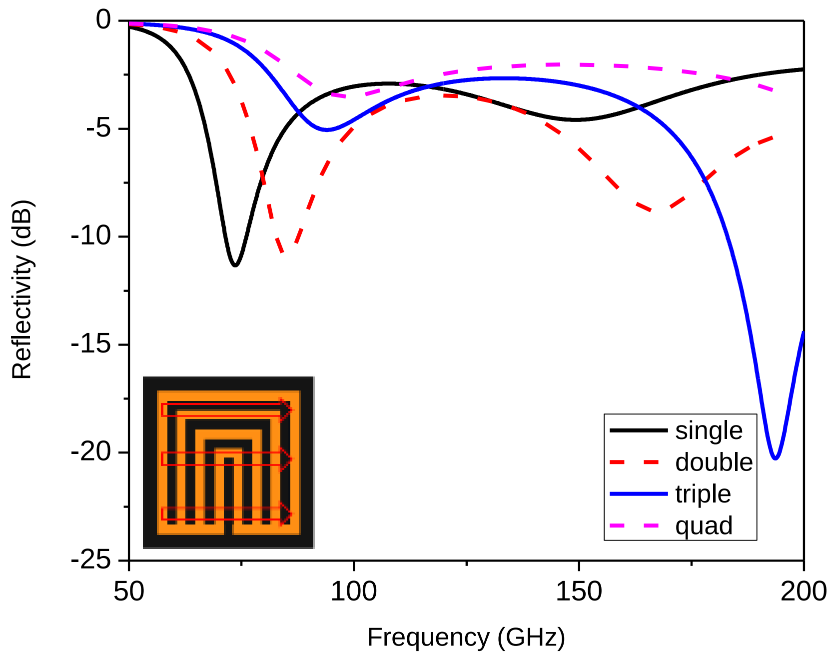

(a)

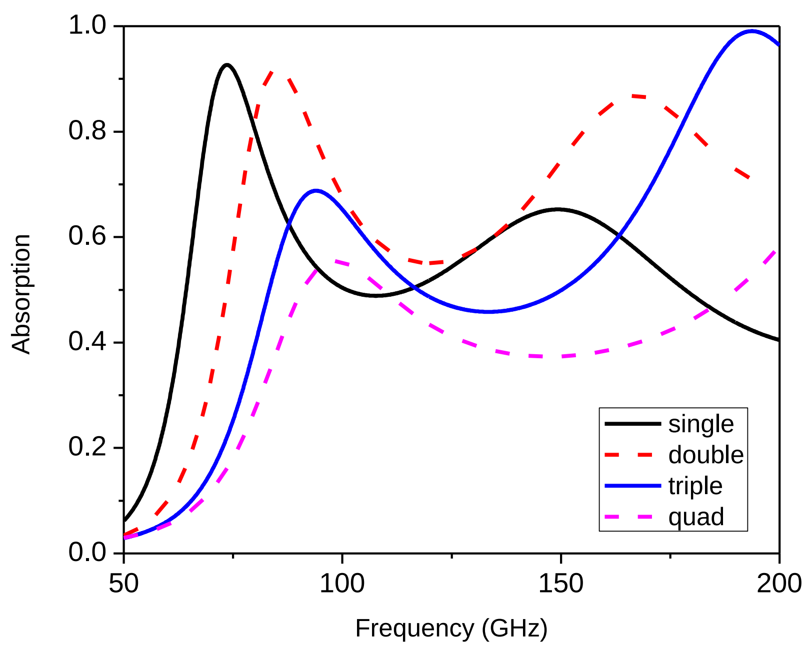

(b)

Figure 7.17 Simulated results of a modified absorber (H-pol.), (a) reflectivity and (b) absorption ratio.

Usable absorbing half power bandwidth of each absorber with designed arms (single to quad) are computed as 10.1 GHz (98.5 ~ 108.6 GHz), 50.1 GHz (87.2 ~ 137.3 GHz), 86.1 GHz (85.4 ~ 171.5 GHz), and 92.4 GHz (84 ~ 176.4 GHz), respectively. According to this analysis, we could conclude the relationship between numbers of arms, to increase the number of arm, to enhance the absorption at vertical E-polarization. It is because the enlarging effective resistant area helps produce higher surface resistance with increasing the number of arms. For horizontal E- polarization, Figure 7.18 describes the computed results for reflectivity and absorption. Compared to V-pol, the results demonstrate that increasing the number of arms makes the operating frequency shift to higher frequency and reduces absorption.

7.6.3 Miniaturized metamaterial (hybrid serpentine/spiral) bolometer

In this section, we introduce a different type of metamaterial bolometer by modifying the U-shaped structure discussed in the previous section. The schematic of this bolometer resembles a hybrid of serpentine and spiral inductor structure. Dimensional information of a miniaturized unitcell is the periodicity (P) of a unitcell is 194 μm, the length (L) of a unitcell is 180 μm shown in Figure 7.18 (a). The width (w) and gap (g) of a unitcell are designed as 12 μm and 11 μm shown in Figure 7.18 (a). The spacing (S) is set at 11μm. Figure 7.18 (b) and (c) shows the simulated results of a miniaturized structure that is designed to operate at 0.1 THz. It shows strong absorption peak at approximately 98.4 GHz (in case of H-polarization). At this frequency, the return loss (magnitude of S_{11}) is approximately 12.4 dB. This translates to an absolute absorption density of 94.3 %. From the simulations, the half power bandwidth (HPBW) of the absorbing peak range from 71.4 GHz to 200 GHz. This structure provides a wide band absorption which is desirable for many applications.

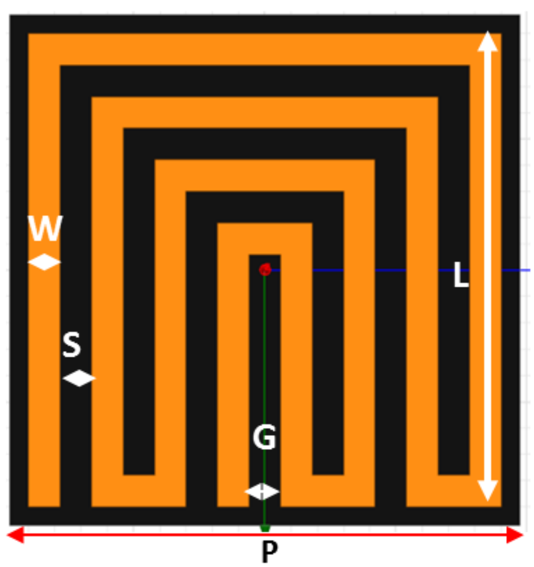

(a)

Figure 7.18 Simulated results of a proposed serpentine absorber, (a) schematic, (b) reflectivity, and (c) absorption ratio.

Figure 7.18 (cont'd)

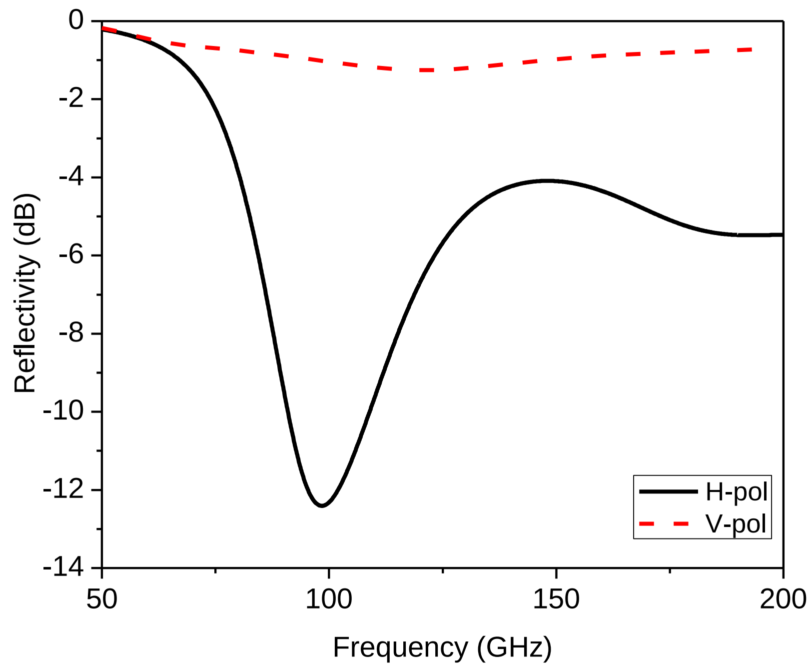

(b)

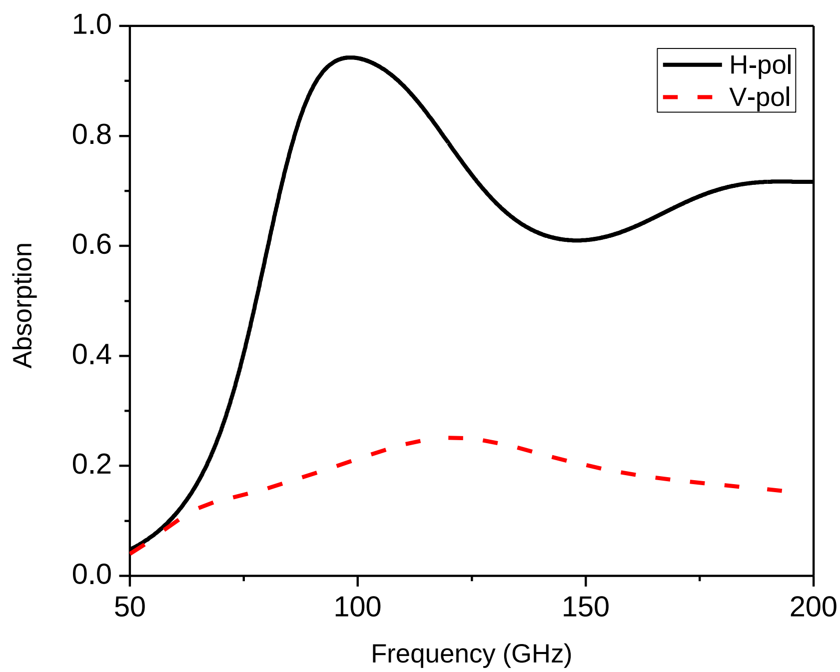

(c)

7.6.4 Fabrication

In order to fabricate the designed miniaturized absorbers, fabrication processes discussed in section 7.5 is utilized here again. Figure 7.19 (a) shows the mask layout of fabricated bolometers having different numbers of unit cells per pixel element, 1 unit cell to 4 × 4 unit cells. Additionally, there are four different designs, based on U-shaped unitcell and hybrid serpentine/spiral unitcell mentioned in the previous section. Fabricated bolometers and its assembly is shown in Figure 7.19 (b). This configuration allows ease of soldering of wires between bolometers and a testing die. This approach protects the bolometer and holds it flat. A test –die produced on FR-4 substrate is used to complete the assembly [91].

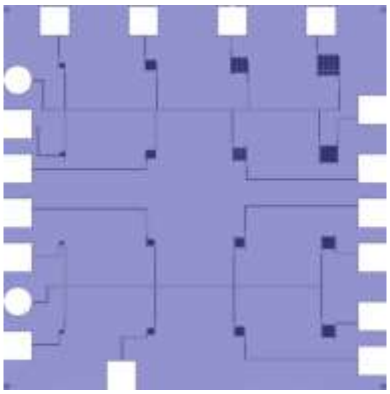

(a)

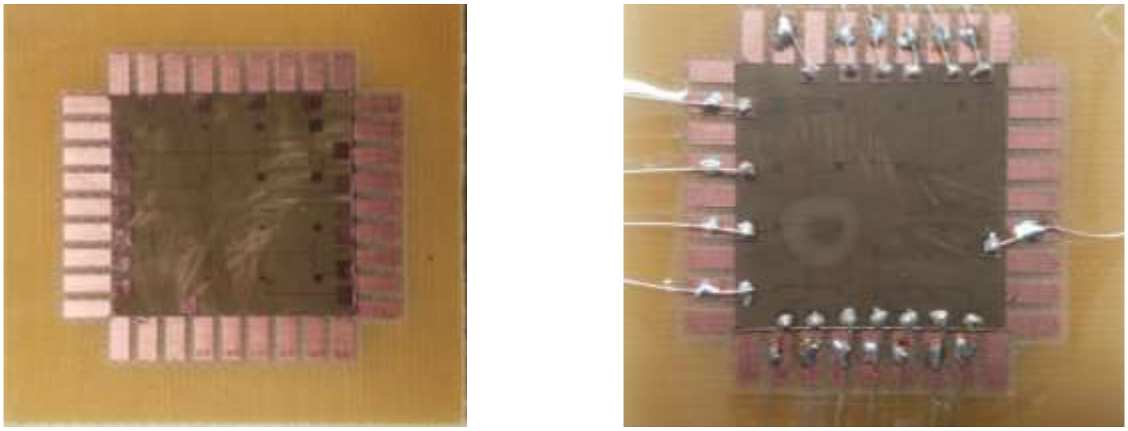

(b)

Figure 7.19 Mask layout (a) and photographs of fabricated bolometers (b).

The lens array has been designed to enhance the density of incident power and also to characterize the performance of the bolometer designs. Detail physical dimensions are the diameter which is 6 mm, and the extension length is 0.7 mm. In order to achieve good alignment between a bolometer and lens and connected wires, the leg (spacer) of a lens array has been drawn to a height of 1 mm. This length is optimum for focusing as confirmed through the EM simulation and allows assembly of the system. The effective receiving area, where is 1mm away from a lens, is calculated as 1×1 mm^2. Designed lens array has been fabricated using 3-D plastic printing (ABS plastic). Figure 7.20 demonstrates the layout and photographs of a lens array and EM simulation results of the lens.

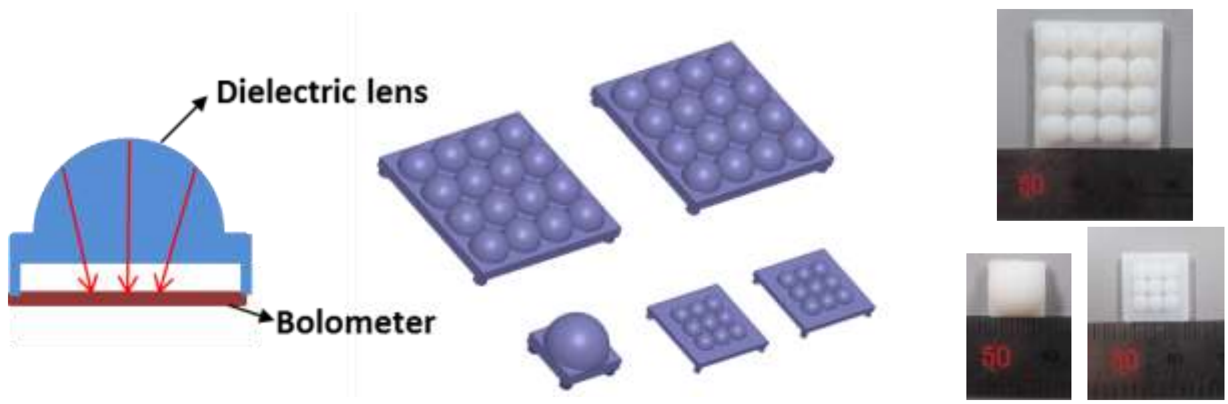

(a)

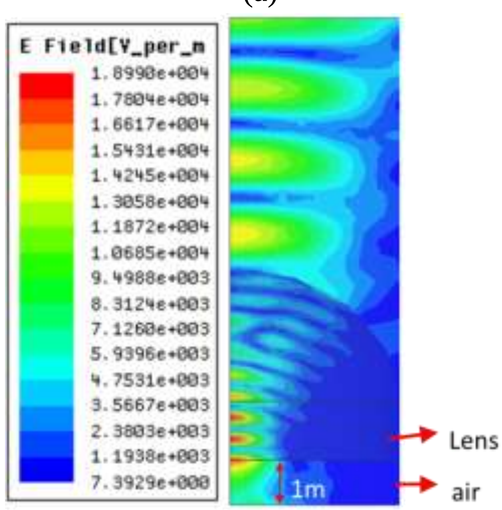

(b)

Figure 7.20 Layout and photographs of a lens array (a) and E-field simulation (b).

7.6.5 Measurement

In order to measure the bolometer and lens array, the near-field radiation setup is used. The setup for near-field radiation measurement setup is shown in Figure 7.21 (a). Through this measurement, the sensitivity of a bolometer has been characterized. Moreover, the sensitivity of the integrated system, a bolometer and a lens array has been measured. First, the sensitivity of a bolometer is tested using the configuration without a lens array. In this setup, each bolometer is measured for variation in resistance under illumination using a multimeter. It is measured again by the lens array, the lens array sits on top of a bolometer. Resistance change was measured several times and the average values are presented.

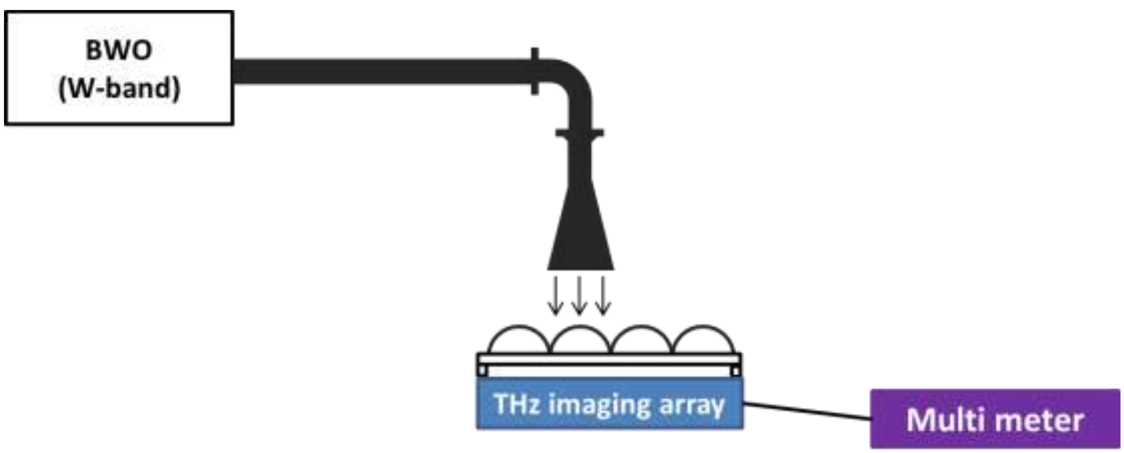

(a)

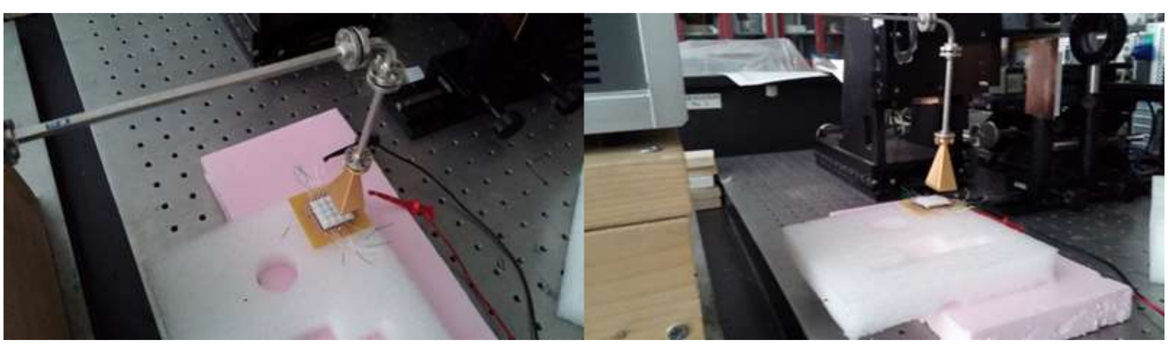

(b)

Figure 7.21 Measurement setup for the assembly of a bolometer and a lens array.

Figure 7.22 demonstrates the measured result obtained using setup shown in Figure 7.21. As shown in Figure 7.22, the graph plots the number of unitcell array versus the variation of resistance. Also, it shows the effect of a polarization of incident wave and its effect on resistance change upon illumination. As the number of unitcell increases per pixel the change in resistance gets bigger for V-polarization illumination. The change in resistance increases when a lens is introduced on top of the bolometer structure. The lens focuses larger amount of power onto the bolometer structures.

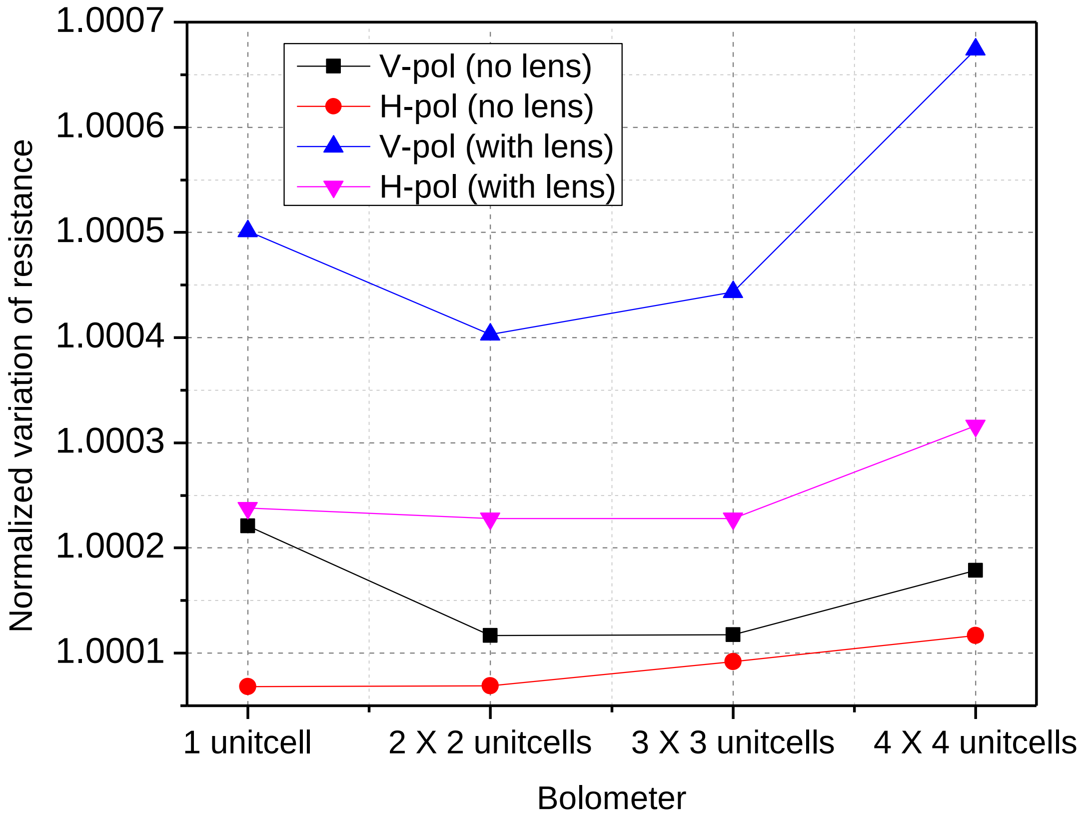

Figure 7.22 Measured results of resistance variation.

CHAPTER 8. CONCLUSIONS AND FUTURE WORK

8. 1. Conclusions

In this dissertation, a novel THz imaging array has been proposed and presented. The design of a bolometer is based on the use of frequency dependent periodic structures (FSS and metamaterials) and high surface resistivity adopting the skin effect. Combining these properties, high absorbing bolometers have been developed to replace the scheme of conventional imaging arrays. In order to improve the density of incident wave, micro-optics has been utilized to be suitable to integrate with planar bolometers. Plasmonic bulls-eye antenna and lens antenna have been investigated to use new cost effective fabrication processes of the use of a wet etching and 3D printing manufacturing method. Based on these research achievements, the novel THz imaging array system has been introduced and discussed about the integration way and the characterization of the imager.

Various groups of thin-film THz absorbers using metamaterials have been investigated through EM analysis, design and fabrication in chapter 3. Designs of THz absorber show strong absorption and ultra-wide bandwidth at terahertz frequency ranges. The proposed approach takes advantage of skin-effect losses in order to make high resistivity and wide band metamaterial absorbers. To enhance sensitivity high resistivity metal (nickel) is utilized in the fabrication of the absorbing structure. Further enhances in operating bandwidth were exhibited through multi-stacking of metamaterial absorbers. The results of proposed metamaterial absorbers clearly describe a new way to achieve ultra-wide band absorption with strong absorption. THz Absorbers having large usable bandwidth can easily be designed using the proposed approach.

The absorbers have been measured to use frequency and time domain measurement setup. These absorbers can be applied in sensing and imaging systems.

Based on this research achievement, the new type of a power meter has been introduced in chapter 4. Proposed periodic structures is to use to build up the power detector and sub components such as interconnection between periodic structure and pads to connect with test apparatuses to measure the characteristics of a power meter have been designed. Proposed power meter designs have been analyzed to perform the EM simulation using HFSS. In order to evaluate the detecting power sensitivity of a power meter, measurements are carried out to use W-band high power BWO, largely restricted by existing measurement setup. Temperature coefficient of resistance (TCR) of the nickel film is measured and shows high sensitivity to change in temperature.

One of the advantages of decreasing the effective area of the bolometer is decrease in noise and increase in sensitivity. However, with decrease in area the effective capture area decreases. To overcome this challenge, micro-optics are used to focus the incoming radiation onto the bolometer. Two types of micro-optics focusing elements are studied: i) dielectric lens antenna and ii) bulls eye surface plasmonic antenna. The use of bulls-eye antenna element for imaging array is demonstrated here for the first time. Details of the micro-optics are presented in Chapters 5 and 6. Simulations of beam focusing elements were carried out using Ansoft HFSS. For the fabrication of bulls eye structure was carried out using two approaches: i) wet-etching, ii) 3D plastic molding (printing). The dielectric lens antenna was fabricated using 3D plastic printing. Integration of micro-optics at the wafer level is demonstrated using these fabrication approaches. Measurements of the micro-optics are carried out in both far- and near-field regions.

In chapter 7, a new THz imaging array is proposed and demonstrated. The proposed imaging array is based on high resistivity metamaterial that provides high absorption of incident signal. The imaging pixel element is composed of an array of sub-wavelength metamaterial unit cells. The unit cells can be scaled to design detector element in the desired band of operation. Furthermore, the size of the unit cells can be reduced down into subwavelength size. These subwavelength structures directly absorb THz radiation and this can be utilized as a detector through a change in the resistance across the pixel element. An intrinsic NEP of 1.6×10^{-9} $W/Hz^{1/2}$ is demonstrated at 0.1 THz. This can further be improved by optimizing thermal isolation, TCR of the film and effective resistance of the film.

The entire results of this dissertation clearly demonstrate and verify that a novel THz imaging array system, which is composed of new types of high resistivity frequency dependent metamaterial absorbers, three dimensional high concentrating antenna elements (bulls eye and lens) with various fabrication materials, and system level integrations, can be utilized to design cost effective and simple THz imager applications.

8. 2. Future work

Future work could include further explorations in the development of miniaturizing the unitcell, reducing the thermal loading between the absorber and substrate, utilizing high TCR materials, and integration of the read-out circuitry. In this section, we would suggest the ways to implement and improve the performance of a THz imaging array.

8.2.1 Genetic Algorithm

Recently, the use of genetic algorithms (GA) has become quite popular to optimize and miniaturize antennas and RF/microwave circuits designs because GA well matched with existing EM analysis techniques, and generally produces results that satisfy the given requirements [92-94]. Many researches have already been carried out furthering both the computational maturity of GA optimization in electromagnetics, as well as in expanding the domain of applications including quite sophisticated designs [93], [95]–[96]. These research with GA optimization have led many distinct results are novel configuration of cells and broadband/multiband operation. Thus, in order to miniaturize the unitell, GAs can be utilized in future work.

Here is an example of GA optimization, filling beehive- cell (FBC) method, one of the advanced structural design methodologies, originated from filling square-pixel (FSP) [94]. This FBC can improve to organize several latticed shapes such as diagonal and rhomboidal. In this analysis, using this GA method, the configuration of the cell can be manipulated as a variety of filling shapes. Figure 8.2 demonstrates the samples of cell configurations based on FBC method [94]. In order to generate the plotting function, FBC runs several iterations to optimize the requirement using GA steps such as reproduction utilizing the biological operators came from the theory of evolution, selection, survivor of the fittest position.

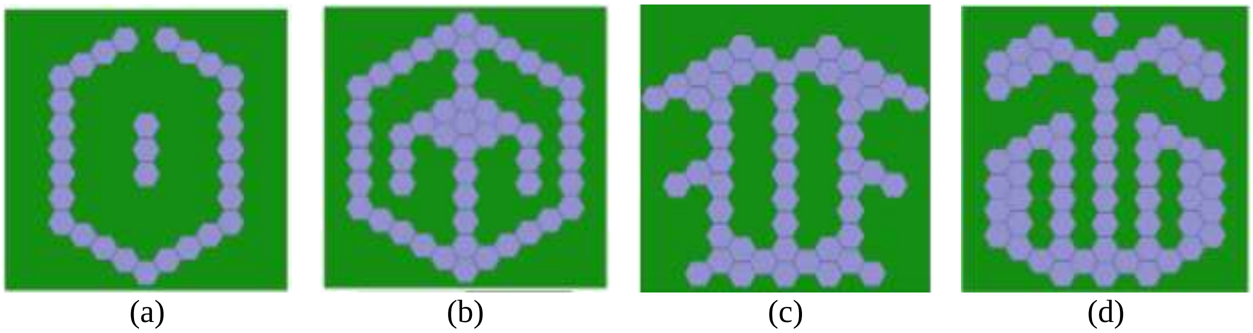

Figure 8.1 Various schematic of unicells generated from GA [94].

8.2.2 Thermal loading

Conventionally, for example, the infrared and mmW uncooled bolometers comprise of thermally isolated layers deposited temperature sensitive materials on top [30]. Mostly, materials can be utilized VO_X, α-Si or poly-SiGe [83]. These thermal detecting layers are implemented to use the microfabrication process directly on CMOS circuits. In this integrating configuration, for optimum performance, the detectors must be thermally isolated from their auxiliaries [97]. Otherwise, the detecting element would become thermally loaded that it would harmfully affect to degrade the function of power detection as thermal detectors.

Likewise, our bolometer consists of thin-film absorbers and a dielectric substrate. Absorbers directly deposited on top of the substrate by using e-beam deposition. In this configuration, despite of using low thermal conducting material, PEEK, there is large interfacing area between absorbers and a substrate to worsen the sensitivity of a bolometer. Here are alternative ways to improve the thermal loading. Firstly, the suspended scheme, well known as RF-MEMS cavity, can be used instead of a substrate. To fabricate the cavity and a thin membrane layer such as silicon nitride (Si_3N_4), the bolometer can be produced on top of a silicon nitride layer and it help isolate thermal loading from surroundings. The other way is to use a special material, Aerogel has the low thermal conductivity. Normally, Aerogel works as a good thermal insulator because of their own characteristics to invalidate heat transfer methods such as convection, conduction, and radiation [98]. Thus, the cavity can be filled with aerogel to build up the thermal isolation layer. Figure 8.2 shows conceptual pictures of thermal isolation for a bolometer. Figure 8.2 (a) demonstrate the scheme a suspended bolometer on the membrane and a cavity fulfilled with air. The integrated pixel demonstrates in Figure 8.2 (b). A pixel consists of 2×2 unitcells on top of an aerogel cavity or silicon nitride membrane, and a readout circuit. Also, there is a wire bonding to interconnect a bolometer and a readout circuits, which is needed to measure the resistance variation of the detector element, which preclude from thermal leakage of the absorbed radiation.

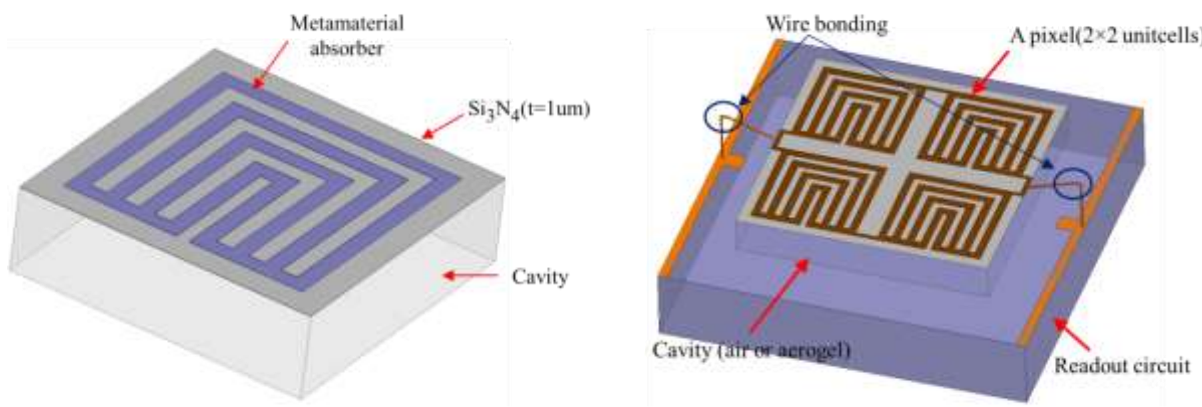

(a) (b)

Figure 8.2 Conceptual pictures of thermal isolation, (a) cavity, and (b) integration a bolometer with a readout circuit.

8.2.3 Readout circuits

Normally, the readout circuits are designed to assist a good interface between detecting elements and the digital domain part such as signal processing [99]. In our case, we can adopt two approaches here, Firstly, using commercial switching matrix (MUX), the readout circuit can be built up easily. Figure 8.3 shows the proposed readout circuit to be able to measure a 3×3 THz imaging array. It consists of a preamp to amplify the signal from a pixel, time division based switching matrix, and data acquisition component. Using measured raw data, a scanned image appears on display.

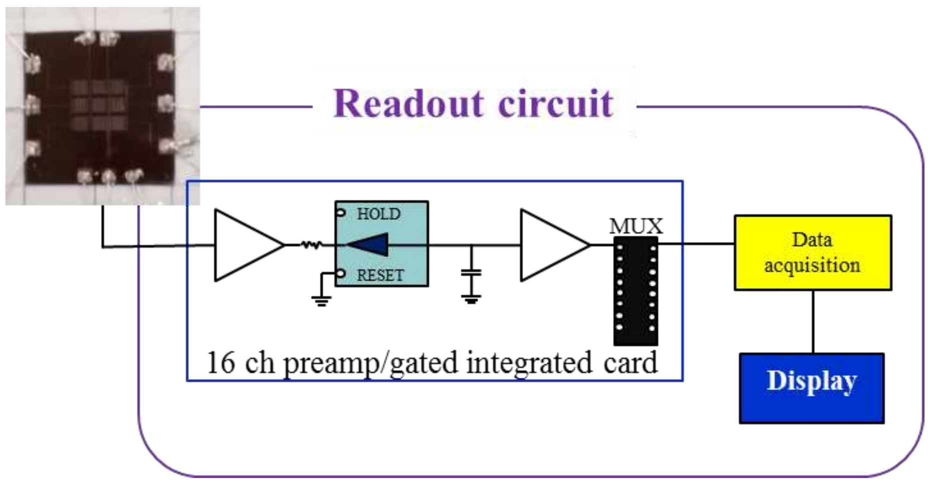

(a) Read-out circuitry

Figure 8.3 Proposed system level assembling methods and readout circuit.

Another approach is to use a variety of CMOS readout techniques such as source-follower per detector (SFD), direct injection (DI), and gate-modulation input (GMI) [99]. These readout circuits can assist to develop the imaging system having large number of pixel, for instance 100 × 100 array.

8.2.4 Temperature Coefficient of Resistivity (TCR)

We could use high TCR material to improve the sensitivity of the bolometer. Some materials, for examples, nickel alloys, amorphous Si, and antimony (Sb) have higher TCR than nickel. With this property, the bolometer can work more sensitive at the same amount of incident power. It could assist lower NEP bolometer. Table 8.1 summarizes the TCR of various materials [100,101].

Table 8.1 Temperature coefficient of resistance (TCR) of materials

Material	Temperature Coefficient of Resistance (TCR, $\%K^{-1}$)
Copper	0.003862
Gold	0.0034
Nickel	0.006
Vanadium oxide (VOx)	0.021
Poly SiGe	0.02
α-Si:B:H	0.028
α-Si:H	0.039
$GeSiO_x$	0.042
α-SiGe:HF	0.049

8.2.5 THz spectroscopy

Recently, spectroscopy is one of the most interesting applications of terahertz regimes which grow from the strength of the signal source or absorption specification for a specimen such as molecules [6].

We introduced many types of absorbing structure in this dissertation. From this, the sensor for THz spectroscopy can be developed to modify and combine absorbing structure together. Figure 8.4 (a) demonstrates the idea of the THz spectroscopy. In this combination of a unitcell, there is two different size of double slit ring resonators, has yielded the multiple high absorbing peaks. In order to verify this idea, the EM simulation has been carried out to use Ansoft HFSS. Figure 8.4 (b) and (c) shows the simulation layout and the simulation results. Especially, in Figure 8.4 (c), the multiple absorption peaks (above 70% absorption) are observed at 0.1, 0.16, and 0.215 THz, respectively. In spectroscopy application, if the specimen is loaded to the proposed sensor, the magnitude and frequency of absorption should change depend on the material properties of the specimen.

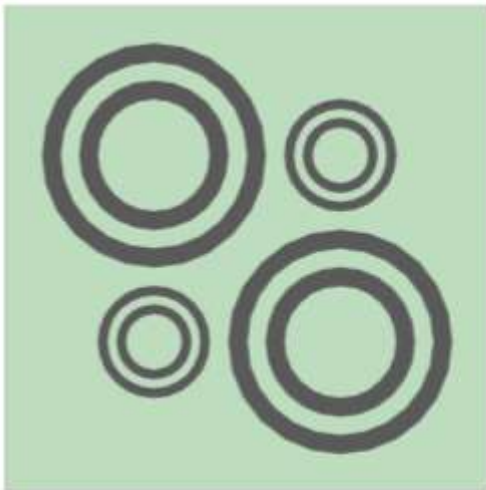

(a)

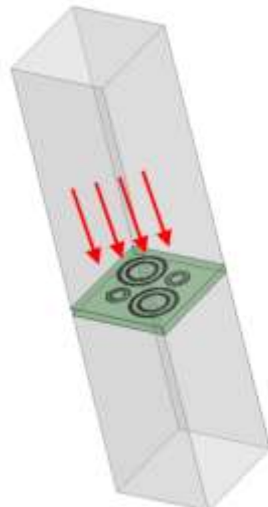

(b)

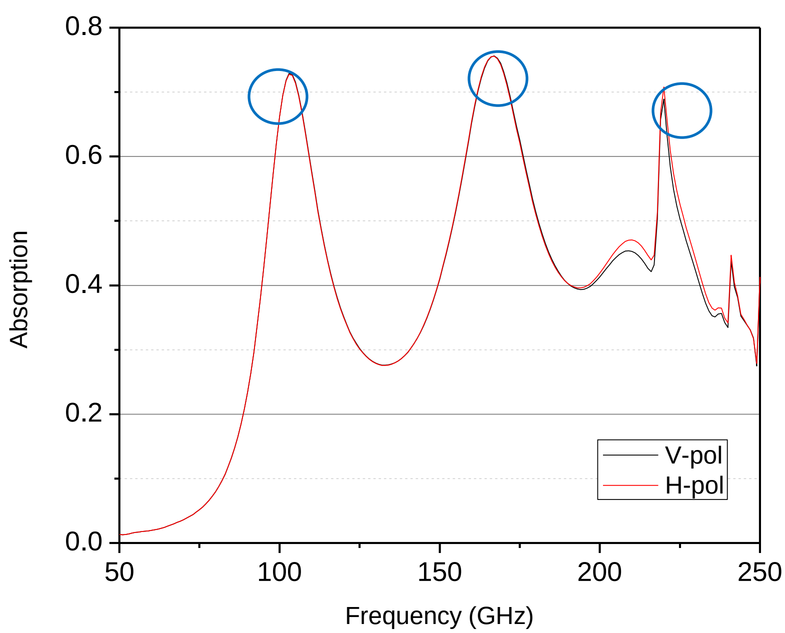

(c)

Figure 8.4 Simulation result for a muti-band unitcell, (a) layout of a unicell and (b) the preliminary simulation result of absorption.

APPENDICES

APPENDIX A

Operative Microfabrication Procedures

A.1 Deep copper wet etching process

This etching process is a recipe of copper wet etching that developed by Terahertz System Lab (Tesla) at Michigan State University. Using this proposed etching process, microwave circuits, metallic bulls eye antennas and metallic molds of microfluidic capillaries having the height of several tens to hundreds of micrometers have been fabricated.

Etching procedure steps are as follows:

1. Prepare the metallic plate or the substrate.
2. In order to remove contaminations on the surface of the substrate, standard RCA cleaning or simple surface cleaning process (details to be introduced) are carried out.
3. Place the substrate in basket.
4. Spray and submerge the basket with the substrate in a beaker containing acetone for 20 seconds.
5. Remove the basket and the substrate from the acetone beaker and spray and immerse them in a beaker containing Methanol for 20 seconds.
6. Remove the basket and the substrate from the acetone beaker and spray and immerse them in a beaker containing deionized water (DI) for 1 min.
7. After cleaning the substrate, blow dry substrate with nitrogen gas (N2). The substrate should be no stains on the surface.
8. Put the substrate in the hot oven at 95 °C for 5 min or bake the substrate at 105 °C for 1 min on the hot plate (this will assist to drive off remaining surface moisture to help enhance the adhesion of photoresist (PR) to the substrate).

9. Using a plastic dropper, the substrate is coated with positive PR (Shipley 1813 in ERC cleanroom).
10. Spin the PR coated substrate for 30 seconds at 4,000 rpm (t=1.2 μm).
11. Bake the substrate at 95 °C for 1 min on the hot plate or put the substrate in the hot oven at 95 °C for 5 min.
12. Inspect the quality of coated PR. If there are some dusts or particle on the surface of PR, go back to step 3 and redo the steps.
13. Use a mask aligner or photolithography machine to expose the PR under the set parameters (275W, 1.1 min on Karl Suss MJB 3 mask aligner in ERC).
14. Submerge the substrate in the developer (MF-319) agitating continuously for 40 ~ 45 seconds.
15. Spray and immerse the substrate in a DI beaker in 1min.
16. Blow dry the substrate with N2.
17. Mix the wet etchant, DI: Sodium persulfate ($Na_2O_8S_2$, MG Chemicals) =3:1(normally 1,000 ml: 330 g).
18. Heat up the wet etchant on the hot plate at 80 °C and measure the temperature of the etchant up to 45 °C. After reaching the etchant temperature up to 45 °C, and then adjust the temperature of the hot plate to maintain the etchant temperature 45 °C.
19. Immerse the exposed substrate into the etchant slowly.
20. The etch rate for copper by the mixed etchant is approximately 3.2 μm/min (Detail measured etching rate shown in Figure A.1). After etching for the wanted amount of time, remove the substrate from the wet etchant.
21. Rinse the substrate in DI water beaker for 1 min and blow dry it with N2.

22. Inspect the etched substrate under the microscope to investigate the etching pattern. If the pattern has not been fully etched, go back to step 19.
23. Spray acetone on the substrate to remove the PR.
24. Rinse the final sample with methanol and DI water.
25. Finally, blow dry with N2.

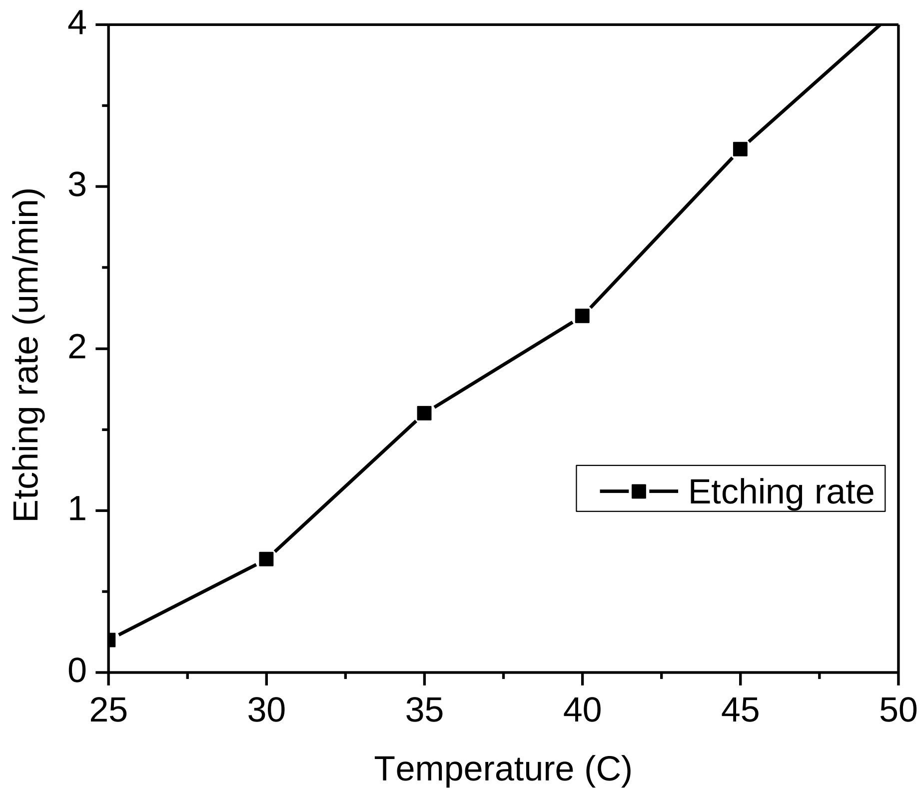

Figure A.1 The etching rate of the copper wet etchant.

A.2 De-scum process

This process will help prepare wafers and substrates for photolithography process may need to remove photoresist residue in normally patterning (trenched) areas [102]. Usually, de-scum process is limited to the removal of photoresist by an oxygen or fluorine plasma, the products being vapors or reactive species with photoresist to form ash which are volatile and pumped out by the vacuum system. At MSU cleanroom, there is a RIE machine, Nordson March RIE-1701(shown in Figure A.2).

Figure A.2 Nordson March RIE-1701.

Descum process steps are as follows:

1. Set parameters on a RIE front panel described below.

Table A.1 Set parameters of a RIE

Parameters	O_2 flow rate	Power	Pressure	Time
Set values	10 sccm	120 W	30 mTorr	30 seconds

2. After setting parameters, press ‘Vacuum’ to pump down until the pressure goes to the setting pressure.
3. Press ‘Gas’ button and turn to green light, and then press ‘RF’ to turn to green.
4. After 30 seconds for etching, then press ‘Purge’, and ‘Bleed’.
5. Press ‘Stop’ and ‘Chamber close’. And then, remove the sample from the chamber.

APPENDIX B

Indicator values of a W-band BWO to set the operating frequency

Table B.1 Indicator values of a BWO

Indicator value	Operating frequency
20.2	74.412 GHz
23.4	75.919 GHz
26.3	77.470 GHz
29.7	78.927 GHz
32.4	80.515 GHz
35	81.969 GHz
38.3	83.710 GHz
42.2	85.582 GHz
44.4	86.688 GHz
48	88.328 GHz
50.7	89.868 GHz
54.3	91.867 GHz
57.4	93.450 GHz
60.8	95.180 GHz
64.2	96.900 GHz
67.2	98.433 GHz
70.6	100.322 GHz
73.8	101.868 GHz
76.7	103.342 GHz
79.3	104.462 GHz
82.5	105.977 GHz
85.6	107.435 GHz

BIBLIOGRAPHY

BIBLIOGRAPHY

[1]. Ferguson, B. and Zhang, "Material for terahertz science and technology", *nature material*, vol. 1, pp. 26-33, Sep, 2002.

[2]. Siegel, P. H, "Terahertz Technology", *IEEE Transactions on Microwave Theory and Techniques*, Vol. 50, No.3, pp.910-928, March, 2002.

[3]. Advanced Millimeter-wave technologies, *1st* edition, Wiley, 2009

[4]. A. Markelz, *et al*., "Pulsed terahertz spectroscopy of DNA, bovine serum albumin and collagen between 0.1 and 2.0 THz," *Chem. Phys. Lett*. 320, pp.42–48, 2000.

[5]. T.G. Phillips and J. Keene, "Submillimeter astronomy," *Proc. IEEE* 80, pp.1662–1678, 1992.

[6]. A, Rostami, *et al*., "Terahertz Technology Fundamentals and Applications,", Springer, 2011.

[7]. http://www.nist.gov/pml/data/xraytrans/index.cfm

[8]. D. Woolard, "Terahertz electronic research for defense: novel technology and science.", 11th Int. *Space Terahertz Tech. Symp*., Ann Arbor, MI, pp. 22–38, 2000.

[9]. Y. C. Shen, et al., "Detection and identification of explosives using terahertz pulsed spectroscopic imaging", *Applied Physics Letters*, 86(24), 2005.

[10]. K. Yamamoto, "Noninvasive inspection of C-4 explosive in mails by terahertz time-domain spectroscopy", *Japanese Journal of Applied Physics* 43(3B), pp. 414–417, 2004.

[11]. H.-B. Liu, Y. Chen, G. J. Bastiaans and X.-C. Zhang, "Detection and identification of explosive RDX by THz diffuse reflection spectroscopy", *Optics Express* 14(1), pp. 415–423, 2006.

[12]. T. S. Hartwick, D. T. Hodges, D. H. Barker and F. B. Foote, "Far infrared imagery", *Applied Optics* 15(8), pp. 1919–1922, 1976.

[13]. B. B. Hu and M. C. Nuss, "Imaging with terahertz waves", *Optics Letters* 20(16), pp.1716–1718, 1995.

[14]. L. Yujiri, M. Shoucri and P. Moffa, "Passive millimeter wave imaging", *Microwave Magazine*, IEEE 4(3), pp. 39–50, 2003.

[15]. J. E. Bjarnason, T. L. J. Chan, A. W. M. Lee, M. A. Celis and E. R. Brown, "Millimeter wave, terahertz, and mid-infrared transmission through common clothing", *Applied Physics Letters* 85(4), pp. 519–521, 2004.

[16]. R. Olsen, S. Clark, J. Galliano, Chung-Ta Hseih, J. Lovberg, C. Martin and C. Phillips, “Video rate passive millimeter-wave imager”, in *Proceedings of the 18th Conference on Digital Avionics Systems*, 1999. vol. 1, pp. 3.C.1-1-8, Nov. 1999.

[17]. Razeghi, M., *Technology of Quantum Devices*. Springer, New York, 2010.

[18]. Weinreb, S., Kerr, A.R., “Cryogenic cooling of mixers for millimeter and centimeter wavelengths”, *IEEE J. Solid-State Circuits* 8, pp.58–63, 1973.

[19]. McColl, M., Millea, M.F., Silver, A.H., “The superconductor–semiconductor Schottky barrier diode detector”, *Appl. Phys. Lett*. 23, pp.263–264, 1973.

[20]. D. M. Sheen and D. L. McMakin, “Three-dimensional millimeter-wave imaging for concealed weapon detection”, *IEEE Transactions on Microwave Theory and Techniques* 49(9), pp. 1581–1592, 2001.

[21]. McGrath, W.R., “Hot-electron bolometer mixers for submillimeter wavelengths: an overview of recent developments,” *6th Int. Space Terahertz Technol. Symp*., Pasadena, CA, pp. 216–228, 1995.

[22]. E. M. Gershenzon, G. N. Goltsman, I. G. Gogidze, Y. P. Gusev, A. I. Elantev, B. S. Karasik, and A. D. Semenov, “Millimeter and submillimeter range mixer based on electronic heating of superconductive films in the resistive state”, *Superconductivity*, vol. 3, no. 10, pp. 1582–1597, 1990.

[23]. W. R. McGrath, B. S. Karasik, A. Skalare, R. Wyss, B. Bumble, and H. G. LeDuc, “Hot-electron superconductive mixers for THz frequencies,” in *SPIE Terahertz Spectroscopy Application. Conf*., vol. 3617, pp. 80–88, Jan. 1999.

[24]. Langley, S.P., “ The bolometer,” *Nature* (London) 25, pp.14–16 (1881)

[25]. Byrd, J.: THz Detectors, Accelerator-Based Sources of Coherent Terahertz Radiation. UCSC, Santa Rosa (2008)

[26]. http://cmb.physics.wisc.edu/detectors/index.html

[27]. http://qmciworks.ph.qmw.ac.uk/index.php?option=com_content&view=article&id=109&Itemid=533

[28]. W.Holland, “Bolometers for Submillimeter and Millimeter Astronomy”, *Single-Dish Astronomy: Techniques and Applications, ASP Conference proceedings*, vol.278, 2002.

[29]. R.K. Bhan, R.S. Saxena, C.R. Jalwania, and S.K. Lomash, “Uncooled Infrared Microbolometer Arrays and their Characterization Techniques”, Defense Science Journal, vol.59, No.6, pp. 580-589, Nov. 2009.

[30]. The Optical Society of America, *Handbook of optics. Volume II, Design, fabrication, and testing; sources and detectors; radiometry and photometry, 3rd Edition*. McGraw-Hill, 2009.

[31]. A. Luukanen, A.J. Miller, and E.N. Grossman, "Active millimeter-wave video rate imaging with a staring 120-element microbolometer array", *Proceedings of the SPIE*, vol. 5410, pp. 195-201, 2004.

[32]. B.A. Munk, *Frequency-selective surfaces: Theory and design*, Wiley, New York, 2000.

[33]. T. K. Wu, *Frequency-selective surface and grid array*, Wiley, New York, 1995.

[34]. J. C. Vardaxoglou, "Frequency-selective surfaces: Analysis and design," *Research Studies Press, Ltd*., Taunton, UK, 1997.

[35]. R. Mittra, C. Chan, and T. Cwik, "Techniques for analyzing frequency selective surfaces-a review," *IEEE Proc*., 76(23), pp.1593-1615, 1988.

[36]. C. H. Tsao, R. Mittra, "Spectral-domain analysis of frequency selective surfaces comprised of periodic arrays of cross dipoles and Jerusalem crosses," *IEEE Trans. Antennas Propag*., AP-32(5), pp.478-486, 1984.

[37]. Christopher L. Holloway, *et. al*., "An Overview of the Theory and Applications of Metasurfaces: The Two-Dimensional Equivalents of Metamaterials", *IEEE Antennas and Propagation Magazine*, vol.54, No.2, pp.10-35, April, 2012.

[38]. J. P. Montgomery, "Scattering by an infinite periodic array of conductors on a dielectric sheet," *IEEE Trans. Antennas Propag*., AP-23(1), pp.70-75, 1975.

[39]. M. Mrejen, A. Israel, H. Taha, M. Palchan, and A. Lewis, "Near-field characterization of extraordinary optical transmission in sub-wavelength aperture arrays," *Optics Express*, 15:9129, July 2007.

[40]. David Pozar, *Microwave Engineering, 4th Edition*, Wiley, 2011.

[41]. H. A. Wheeler, "Formulas for the Skin Effect", *Proceedings of I.R.E*, pp.412-424, Sep. 1942.

[42]. *International Union of Pure and Applied Chemistry*, IUPAC handbook definition. 2009

[43]. Jose Hejase, *et al*., "Terahertz characterization of dielectric substrates for component design and nondestructive evaluation of packages," *IEEE Transactions on Components, Packaging and Manufacturing Technology*, vol. 1(11), pp.1685-1694, 2011.

[44]. K. Y. Park, *et al*., "Metamaterial-inspired absorbers for terahertz packaging application", *61st Electronic Components and Technology Conference (ECTC)*, pp. 2107-2113, May, 2011.

[45]. L.J. van der Pauw, "A Method of Measuring Specific Resistivity and Hall Effects of Discs of Arbitrary Shape", Philips Technical Review, vol.20, No. 8, pp.220-224, 1958/59.

[46]. KEITHLEY, "Four-Probe Resistivity and Hall Voltage Measurements with the Model 4200-SCS", *Application Note series*, No. 2475.

[47]. Curtis C. Ling, and Gabriel M. Rebeiz, "A wide-band monolithic quasi-optical power meter for millimeter-and sybmillimeter-wave applications", *IEEE Transactions on Microwave Theory and Techniques*, vol.39, No.8, Aug, 1991, pp.1257~1261.

[48]. Yun-Shik Lee, *Principles of Terahertz Science and Technology*, Ch. 5, Springer, 2009

[49]. T. Thio, *et al*., "Enhanced light trans. through a single subwavelength aperture," *Optics Lett*., 26(24):1972, 2001.

[50]. J. Lindberg, K. Lindfors, T. Setala, M. Kaivola, and A. T. Friberg, "Spectral analysis of resonant transmission of light through a single sub-wavelength slit," *Optics Express*, 12(4):623, February 2004.

[51]. T. W. Ebbesen, H. J. Lezec, H. F. Ghaemi, T. Thio, and P. A.Wol, "Extraordinary optical transmission through sub-wavelength hole arrays," *Nature*, 391(6668): pp.667-669,February 1998.

[52]. M. Beruete, M. Sorolla, I. Campillo, J.S. Dolado, L. Martin-Moreno, J. Bravo-Abad, and F.J. Garcia-Vidal, "Enhanced millimeter wave transmission through quasioptical subwavelength perforated plates," *IEEE Transactions on Antennas and Propagation*, 53(6), pp.1897-1903,2005.

[53]. Degiron, H. J. Lezec, W. L. Barnes, and T. W. Ebbesen, "Effects of hole depth on enhanced light transmission through subwavelength hole arrays," *Applied Physics Letters*, 81(23):4327, 2002.

[54]. M. Mrejen, A. Israel, H. Taha, M. Palchan, and A. Lewis, "Near-field characterization of extraordinary optical transmission in sub-wavelength aperture arrays," *Optics Express*, 15(15):9129, July 2007.

[55]. L. Martn-Moreno, F. Garca-Vidal, H. Lezec, A. Degiron, and T. Ebbesen, "Theory of Highly Directional Emission from a Single Subwavelength Aperture Surrounded by Surface Corrugations," *Physical Rev. Lett*., 90(16), 2003.

[56]. G. Brolo, R. Gordon, B. Leathem, and K. L. Kavanagh, "Surface Plasmon Sensor Based on the Enhanced Light Transmission through Arrays of Nanoholes in Gold Films," Langmuir, 20(12): pp. 4813-4815, June 2004.

[57]. H. Ghaemi, *et al*., "Surface plasmons enhance optical transmission through subwavelength holes," *Physical Review B*, 58(11):pp.6779-6782, Sept. 1998.

[58]. K. Azad, *et al*., "Ultrafast optical control of terahertz surface plasmons in subwavelength hole arrays at room temperature," *Applied Physics Lett*., 95(1):011105, 2009.

[59]. B. Lee, S. Kim, H. Kim, and Y. Lim, "The use of plasmonics in light beaming and focusing," *Progress in Quantum Electronics*, 34(2): pp.47-87, March 2010.

[60]. Agrawal, H. Cao, and A. Nahata, "Time-domain analysis of enhanced transmission through a single subwavelength aperture," *Optics Express*, 13(9):3535, May 2005.

[61]. Agrawal, H. Cao, and A. Nahata, "Excitation and scattering of surface plasmon-polaritons on structured metal films and their application to pulse shaping and enhanced transmission," *New Journal of Physics.* 7:249, 2005.

[62]. Agrawal, H. Cao, and A. Nahata, "Shaping terahertz pulses using structured metal films," *Lasers and Electro-Optics Society*, October 2005.

[63]. C. Meierbachtol and P. Chahal, "A Novel Subwavelength Microbolometer for Terahertz Sensing," *International Journal of High Speed Electronics and Systems*, vol. 20, no. 3, pp. 611-619, 2011.

[64]. K. Y. Park, N. Wiwatcharagoses, A. Baczewski, and P. Chahal, "A novel terahertz power meter using metamaterial-inspired thin-filme absorber," *36th International conference on Infrared, Millimeter and Terahertz Waves (IRMMW-THz)*, Oct, 2011.

[65]. Constantine A. Balanis, *Antenna Theory*, 3rd edition, Wiley, 2005.

[66]. G. M. Rebeiz, "Millimeter-wave and terahertz integrated circuits antennas," *Proc. IEEE*, vol.80 (11), pp. 1748-1770, 1992

[67]. D.F. Filipovic, *et al*., "Double-slot antennas on extended hemispsherical and elliptical silicon dielectric lenses," *IEEE Transaction on Microwave Theory and Techniques*, vol.41, no.10, pp.1738-1749, 1993.

[68]. D.F. Filipovic, *et al*., "Off-axis properties of silicon and quartz dielectric lens antenna," *IEEE Transaction on Antennas and Propagations*, vol.45, no.5, pp.760-766, 1997.

[69]. W.B. Dou, *et al*., "Pattern prediction of extended hemispherical-lens/objective-lens antenna system at millimeter wavelengths," *IEE Proc.-Microw. Antenna Propag*., vol.145, no.4, pp.295-298,1998.

[70]. Fernandes and J. G. Fernandes, "Performance of lens antennas in wireless indoor millimeter-wave application," *IEEE Transaction on Microwave Theory and Techniques*, vol. 47, no. 6, pp. 732–737, Jun. 1999.

[71]. K. W. Leung, "Complex resonance and radiation of hemispherical dielectric-resonator antenna with a concentric conductor," *IEEE Transaction on Microwave Theory and Techniques*, vol. 49, pp. 524–531, Mar. 2001.

[72]. G. Godi, *et al*., "Performance of reduced size substrate lens antennas for millimeter-wave communications," *IEEE Transaction on Antennas and Propagation*, vol.53, no.4, pp.1278-1286, April, 2005.

[73]. Ajoy Ghatak, *Optics*, *3rd* Edition, McGraw-Hill, 2005.

[74]. R.C. O'Brient, "A Log-Periodic Focal-Plane Architecture for Cosmic Microwave Background Polarimetry", *Doctoral dissertation*, UC Berkeley, 2010.

[75]. K. Y. Park, N. Wiwatcharagoses, and P. Chahal,"Surface plasmon-assited terahertz imaging array", *62nd Electronic Components and Technology Conference (ECTC)*, pp.1846-1851, May, 2012.

[76]. K. Y. Park, N. Wiwatcharagoses, and P. Chahal, "Plastic injection micromachining of millimeter and sub-millimeter rectangular waveguide filters", *36th International conference on Infrared, Millimeter and Terahertz Waves (IRMMW-THz)*, Oct, 2011.

[77]. H.T, Chen, W.J.Padilla, *et al*, 'Active terahertz metamaterial devices', *nature letters*, vo.444, pp.597-600, Nov. 2006.

[78]. D. Schurig, J.J. Mock, and D.R. Smith, "Electric-field-coupled resonators for negative permittivity metamaterials", *Applied Physics Letters*, 88:041109, 2006

[79]. J. B. Pendry, A. J. Holden, D. J. Robbins, and W. J. Stewart, "Magnetism from Conductors and Enhanced Nonlinear Phenomena", *IEEE Transactions on Microwave Theory and Techniques*, vol.47, No.11, pp.2075-2084, Nov. 1999.

[80]. Mohamed Gad-el-Hak, *MEMS Design and Fabrication, 2nd Edition*, CRC press, 2006.

[81]. https://snf.stanford.edu/SNF/processes/process-modules/etching/dry-etching/resist-stripping-including-descum/resist-stripping-descum-and-polymer-removal-in-drytek2-semi-clean

[82]. http://nanolab.berkeley.edu/labmanual/chap4/4.32matrix.pdf

[83]. R. J. Keyes, *Optical and Infrared Detectors*, 2nd Edition, Springer, 1980.

[84]. R. Novak and J.Hrbek, "Nickel bolometers", Czech Journal of Physics, B.18, No.11, pp.1423-1432, 1968.

[85]. D.R. Chowdhury, R. Singh, M. Reiten, H.T. Chen, A. J. Taylor, J.F. O'Hara, and A.K. Azad, "A broadband planar terahertz metamaterial with nested structure", *Optics Express*, vol.19, No.17, pp.15817-15823, Aug.2011.

[86]. E.H. Putley, "The ultimate sensitivity of sub-mm detectors", *Infrared Physics*, vol.4, pp.1-8, 1964.

[87]. S. Linden, C. Enkrich, M. Wegner, J. Zhou, T. Koschny, and C. M. Soukoulis, "Magnetic response of metamaterials at 100 terahertz", *Science* 306, pp.1351-1353, 2004.

[88]. J. F. O'Hara, R. Singh, I. Brener, E. Smirnova, J. Han, A. J. Taylor, and W. Zhang, "Thin-film sensing with planar terahertz metamaterials: sensitivity and limitations," *Opt. Express* 16(3), pp. 1786–1795, 2008.

[89]. I. A. I. Al-Naib, C. Jansen, and M. Koch, "Thin film sensing with planar asymmetric metamaterial resonators," *Appl. Phys. Lett.* 93(8), 083507, 2008.

[90]. 7. R. Singh, C. Rockstuhl, C. Menzel, T. P. Meyrath, M. He, H. Giessen, F. Lederer, and W. Zhang, "Spiral-type terahertz antennas and the manifestation of the Mushiake principle," Opt. Express 17(12), pp. 9971–998, 2009.

[91]. http://www.onsemi.com/pub_link/Collateral/AND8086-D.PDF

[92]. F. J. Villegas, T. Cwik, Y. Rahmat-Samii, and M. Manteghi, "A parallel electromagnetic genetic-algorithm optimization (EGO) application for patch antenna design," *IEEE Trans. Antenna Propagation*, vol.52, pp. 2424-2435, 2004.

[93]. D.J. Kern and D. H. Werner, "A genetic algorithm approach to the design of ultra-thin electromagnetic bandgap absorbers", *Microwave and Optical Tech. Letters*, vol.38, no.1, pp. 61- 64, July, 2003.

[94]. P. Y. Chen1, C. H. Chen, H. Wang, J. H. Tsai, and W. X. Ni, "Synthesis design of artificial magnetic metamaterials using a genetic algorithm", *Optics Express*, vo.16, no.17, 12806, 2008.

[95]. R. Zentner, Z. Sipus, and J. Bartolic, "Optimum synthesis of broadband circularly polarized microstrip antennas by hybrid genetic algorithm," *Microwave and Optical Technol. Lett.*, vol. 31, no. 3, pp. 197–201, Nov. 2001.

[96]. R. L. Haupt and S. E. Haupt, "Optimum population size and mutation rate for a simple real genetic algorithm that optimizes array factors," *Applied ComputationalElectromagn. Soc. J.*, vol. 15, no. 2, pp. 94–102, July 2000.

[97]. http://www.xenics.com/en/infrared_technology/uncooled_bolometer.asp

[98]. http://en.wikipedia.org/wiki/Aerogel

[99]. C.C. Hsieh, C-Y Wu, F-W Jih, and T-P Sun, "Focal-Plane-Arrays and CMOS Readout Techniques of Infrared Imaging Systems", *IEEE Transactions on Circuits and Systems for Video Technology*, vol.7, No.4, Aug. 1997.

[100]. http://en.wikipedia.org/wiki/Electrical_resistivity_and_conductivity

[101]. R. Ambrosio, A. Torres, A. Kosarev, A.S. Abramov, A. Heredia, M. Landa, and M. Garcia, “Amorphous Si1-YGeY:H, F films obtained by Low Frequency PECVF for uncooled microbolometers,” *Mat. Res. Soc. Symp. Proc*. Vol. 808, A4.29.1-6, 2004.

[102]. Quorum Technologies Ltd., Plasma Etching/Ashing Technical Brief, application notes.